Geofluids

Advances in Enhancing Coalbed Methane and Shale Gas Recovery 2021

Lead Guest Editor: Yong Li
Guest Editors: Zhejun Pan, Jian Shen, Yanjun Meng, Haijiao Fu, and Songqi Pan

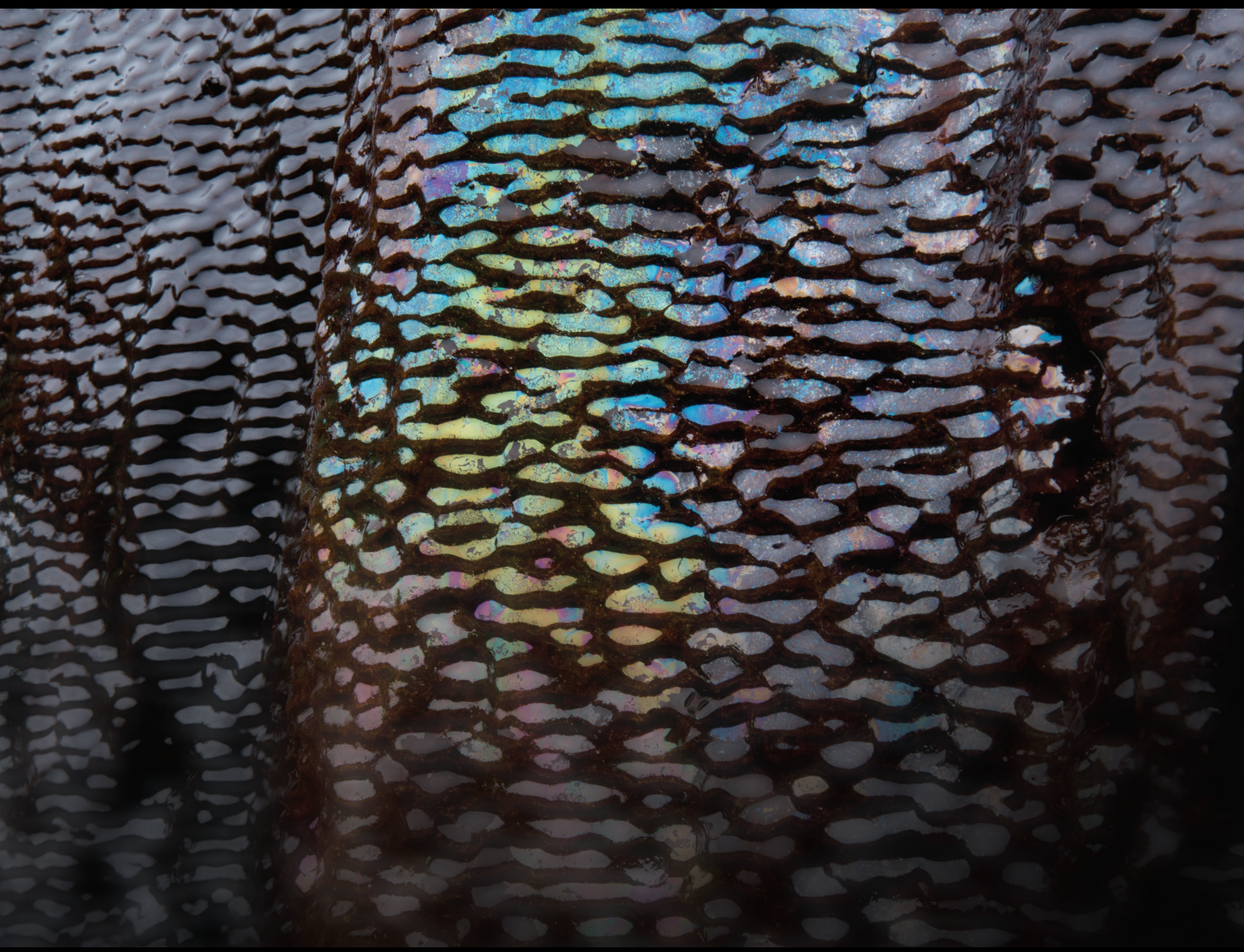

Advances in Enhancing Coalbed Methane and Shale Gas Recovery 2021

Geofluids

Advances in Enhancing Coalbed Methane and Shale Gas Recovery 2021

Lead Guest Editor: Yong Li
Guest Editors: Zhejun Pan, Jian Shen, Yanjun Meng, Haijiao Fu, and Songqi Pan

Chief Editor

Associate Editors

Academic Editors

Contents

Methane Adsorption in Anthracite Coal under Different Pressures and Temperatures—A Study Combining Isothermal Adsorption and Molecular Simulation
Tieya Jing, Jian Zhang, Mingyu Zhu, Wentao Zhao, Juan Zhou, and Yulong Yin
Research Article (15 pages), Article ID 8528359, Volume 2023 (2023)

Optimal Injection Parameters for Enhancing Coalbed Methane Recovery: A Simulation Study from the Shizhuang Block, Qinshui Basin, China
Du Liu, Longyong Shu, Yanbin Wang, Zhonggang Huo, Shihu Zhao, and Xing Xiong
Research Article (13 pages), Article ID 3311827, Volume 2022 (2022)

Spatial and Temporal Distribution of Groundwater in Open-Pit Coal Mining: A Case Study from Baorixile Coal Mine, Hailaer Basin, China
Wenfeng Du, Lei Chen, Yunlan He, Qiangmin Wang, Peiqiang Gao, and Quansheng Li
Research Article (17 pages), Article ID 8753217, Volume 2022 (2022)

Extension Limit of a Straight-Swirling Mixed Jet Bit and Its Influential Factors in Radial Jet Drilling
Peng Du, Weikang Xia, and Chaoxiong Yu
Research Article (10 pages), Article ID 3078233, Volume 2022 (2022)

Study on the Effect of Salinity and Water Content on CBM Adsorption/Desorption Characteristics of Coal Reservoir in Baode Block
Wei Zhang, Yanxiang He, Qingfeng Zhang, Yanjun Meng, Tuo Liu, Wenhui Meng, Yun Zuo, and Hongbo Fan
Research Article (9 pages), Article ID 5055273, Volume 2022 (2022)

Coalbed Methane Industry Development Framework and Its Limiting Factors in China
Rui Li and Guofu Li
Review Article (10 pages), Article ID 8336315, Volume 2022 (2022)

Imbibition Retention in the Process of Fluid Replacement in Tight Sandstone Reservoir
Xiong Liu, Yang Zhang, Desheng Zhou, Le Yan, Hai Huang, and Xinru Li
Research Article (8 pages), Article ID 3028969, Volume 2022 (2022)

Main Factors of Mesozoic Tectonic Deformation in the Erlian Basin, Inner Mongolia, China: Insights from Physical Modelling
Yue Zhao, Qiang Xu, Yongchen Li, Xiujia Bai, Rong Ding, Jianxin Wang, and Tao Hou
Research Article (15 pages), Article ID 8130349, Volume 2022 (2022)

Multiscale Fracturing in Medium- to Low-Rank Coals and Its Implications on Coalbed Methane Production in the Baode Area, Eastern Ordos Basin, China
Wei Zhang, Baoshan Zhao, Qingfeng Zhang, Jikun Zhang, Ziling Li, Xiaoguang Sun, and Mingming Yan
Research Article (12 pages), Article ID 4549153, Volume 2022 (2022)

Hindawi
Geofluids
Volume 2023, Article ID 8528359, 15 pages
https://doi.org/10.1155/2023/8528359

Research Article

Methane Adsorption in Anthracite Coal under Different Pressures and Temperatures—A Study Combining Isothermal Adsorption and Molecular Simulation

Tieya Jing, Jian Zhang, Mingyu Zhu, Wentao Zhao, Juan Zhou, and Yulong Yin

Beijing Key Laboratory of CO_2 Capture and Treatment, China Huaneng Clean Energy Research Institute, Beijing 102209, China

Correspondence should be addressed to Mingyu Zhu; 18133801859@163.com

Received 23 June 2022; Revised 24 August 2022; Accepted 1 October 2022; Published 10 May 2023

Academic Editor: Yong Li

In situ gas content is an important parameter associating coalbed methane, while the influence of pressure and temperature on methane adsorption and desorption still needs to be revealed. In this study, the molecular structure and methane adsorption capacity of anthracite coal collected from Diandong Coalfield (China) were studied based on ^{13}C nuclear magnetic resonance (^{13}C NMR), Fourier transform infrared spectroscopy (FT-IR), and methane isothermal adsorption experiment. The results show that the carbon skeleton of coal sample is mainly composed by aromatic carbon (72%), followed by aliphatic carbon structure (14.2%). Carbons connected to the oxygen atoms contribute 13.7% of the total carbons in coal molecule, and the oxygen atoms are mainly in the form of carbonyl. The 2-dimension structure and 3-dimension molecular structure of coal sample was also reconstructed. The average chemical formula of the coal molecule is $C_{200}H_{133}O_{21}N_3$. The experimental methane adsorption isothermal data of the coal sample under different temperatures shows that with increasing the temperature, the methane adsorption amount at each pressure decreases obviously. At 7 MPa and 20°C, the methane adsorption amount of the coal sample is 28.5 cm^3/g. Comparably, at 100°C and 7 MPa, the methane adsorption amount is only 15.9 cm^3/g, decreasing by 44%. In mesopores, temperature has stronger influence on methane adsorption under higher pressure than that of lower pressure. On the contrary, in micropores, temperature has weaker effects on methane adsorption at higher pressure than that at lower pressure. The results can be beneficial for understanding methane adsorption characteristics of deep coal.

1. Introduction

Coalbed methane (CBM) is clean energy and has been widely extracted and utilized with huge potential in China [1–5]. The accumulation mechanism of CBM is quite different from other types of natural gas as CBM is mainly stored as absorbed state [6–8]. Thus, methane adsorption mechanism in coal is considered to be one of the most important factors to realize CBM production [9–12]. In previous studies, it was found that the adsorption behavior of methane in coal is caused by intermolecular interaction forces between methane molecules and coal matrix [11, 13]. In addition, the coal maturity, composition, pore structure, pressure and temperature all have effect on the methane adsorption capacity [8, 14–18]. However, the pore system in coal is complex, and this makes the methane adsorption mechanism in coal is still unclear [19–21].

Methane adsorption isothermal experiment (gravimetric method or volumetric method) is commonly used to test the methane adsorption capacity of coal reservoir [15, 22]. The adsorption behavior has been widely studied under different pressure and temperature conditions [23, 24]. It was found that with increasing methane pressure, the adsorption capacity increases, which can be simulated by the Langmuir equation [23, 25, 26]. Besides, with increasing temperature, the methane adsorption capacity decreases. When the

vitrinite reflectance of the coal sample increases from 0.5% to 3.7%, the methane adsorption capacity decreases firstly and then increases [17, 24, 27]. In general, the anthracite coals have strong adsorption capacities [24, 28]. The in-situ CBM contents in many anthracite coalfields were found much higher than other coal seam [29].

Molecular simulation has been applied in studying the methane adsorption mechanism as molecule simulation could provide molecule-scale information about the methane adsorption behavior in coal [30–32]. The density distribution of adsorbed methane, the location of the adsorbed methane, and the methane adsorption behavior of different size pores in coal can be directly provided by the molecule simulation [13, 33, 34]. Therefore, the molecule simulation has received extensive attention in coalbed methane studies. The graphite-slit pore models are used to represent the adsorption behavior of methane in slit pores [13]. However, the coal molecule structure is significantly different from graphite [32, 35].

In the studies of CBM, it is important to evaluate the in situ methane content in coal. As the depth of the coal is different in different coalfields, the pressure and temperature of underground coal seams are different. The increase of burial depth of the coal seam can lead to temperature and pressure increment. However, it is unclear how temperature and pressure affect methane adsorption behavior. In this study, the influence of pressure and temperature on methane adsorption behavior is investigated by both physical experiments and molecular simulation methods.

2. Methodology

2.1. Samples. The coal samples used in this study are collected from No. 2 coal seams in Yuwang coal mine in East Yunnan (Diandong coalfield), China. Yuwang coal mine is an underground coal mine with high gas content. The average thickness of No. 2 coal seams is 1.13 m. The vitrinite reflectance of these coal samples is about 2.4%. The ash content of the coal sample is 23.66% and the volatile content is 9.99% under air-dry basis.

2.2. Experiments

2.2.1. ^{13}C Nuclear Magnetic Resonance (^{13}C NMR). The ^{13}C NMR experiment was conducted by JNM-ECZ600R in Nuclear Magnetic Resonance Center of Tsinghua University. The powder coal samples were used and resonance frequency was set to 150 MHz. During the experiment, the mass frequency was set to 12 kHz with the total scan time of one hour (1200 times) [36].

2.2.2. Fourier Transform Infrared Spectroscopy (FT-IR). When performing the FT-IR experiment, PerkinElmer spectrum (Frontier FT-IR) was used. About 2 g powder coal samples were used in the experiment. Before the experiment, atmospheric correction was performed. The scanning range was set from 450 cm^{-1} to 4000 cm^{-1}. The scanning speed is 0.2 s^{-1}. The analysis of the FT-IR is based on the previous study [37].

2.2.3. Methane Isothermal Adsorption Experiment. The Methane isothermal adsorption experiment was performed in Unconventional Natural Gas Laboratory, China University of Mining and Technology, Beijing. Before the experiment, the Yuwang coal samples were pulverized to about 60-80 mesh and were dried at 80°C for 24 hours. Methane adsorption experiments were carried out by the 3H-2000PH methane adsorption instrument by volumetric method. For the instrument, the pressure can be set to as high as 690 bar (69 MPa).

2.3. Simulation Methods

2.3.1. Coal Molecule Reconstruction. The reconstruction process of coal molecular model contains several steps. Firstly, the molecular information of the model was obtained by statistical analysis of the experimental data such as industrial analysis, elemental analysis, ^{13}C NMR, and FT-IR. Then, the initial model satisfying the structural information is drawn by ACD/ChemSketch. After that, the ^{13}C NMR of initial model was calculated and compared to the experimental data. The initial model wall was corrected based on the comparing results to obtain the objective two-dimensional model structure. The two-dimensional model will be imported for model optimization to obtain the three-dimensional model with the lowest energy configuration. Finally, the periodic boundary is added to truly restore the microstructure of coal samples. The details of the molecule reconstruction process can be also seen in previous studies [38, 39].

2.3.2. Simulation of Methane Adsorption in Coal. The methane adsorption in coal is physical adsorption, and the interaction forces are mainly Van de Waals forces. In the simulation, the Van de Waals forces are calculated by Lennard-Jones potential energy function. The simulation was carried out at different temperature and different pressure. The maximum pressure is 7 MPa. The temperature and pressure conditions are set according to the experimental conditions.

3. Results

3.1. Results of ^{13}C NMR. According to the previous studies, the ^{13}C NMR spectrum of the Yuwang coal sample can be divided into four parts: aliphatic carbon peaks (chemical shift = 0 − 60 ppm), ether oxygen carbon peaks (chemical shift = 60 − 90 ppm), aromatic carbon peaks (chemical shift = 100 − 165 ppm), and carbonyl and carboxyl carbon peaks (chemical shift = 165 − 250 ppm) [40, 41]. Peak fitting of the ^{13}C NMR spectrum was performed by using the software origin. The fitting results were shown in Table 1 and Figure 1.

According to the peak fitting results, the carbon skeleton structure of YW coal sample is mainly composed by aromatic carbon structure (72%), followed by aliphatic carbon structure (14.2%). Carbons connected to the oxygen atoms contribute 13.7% of the total carbons in coal molecule. In addition, the aromatic carbon structure is mainly composed by benzene rings and naphthalene rings. There are less anthracene rings and phenanthrene rings. The structures of

Table 1: ^{13}C NMR peak attribution and relative content of YW samples.

Serial number	Peak type	Half peak width (ppm)	Chemical shift (ppm)	Relative area (%)	Peak position attribution
1	Gaussian	8.0	19	2.4	Aromatic methyl
2	Gaussian	11.2	32	3.51	Methylene, methylene
3	Gaussian	14.4	45	8.3	Seasonal carbon
4	Gaussian	4.1	107	0.5	Protonated aromatic carbon
5	Gaussian	15.4	126	63.7	Bridged aromatic carbon
6	Gaussian	9.3	141	7.8	Alkyl substituted aromatic carbon
7	Gaussian	9.5	200	5.2	Carboxyl carbon
8	Gaussian	7.4	208	5.5	Carbonyl carbon
9	Gaussian	10.0	215	3.0	Carbonyl carbon

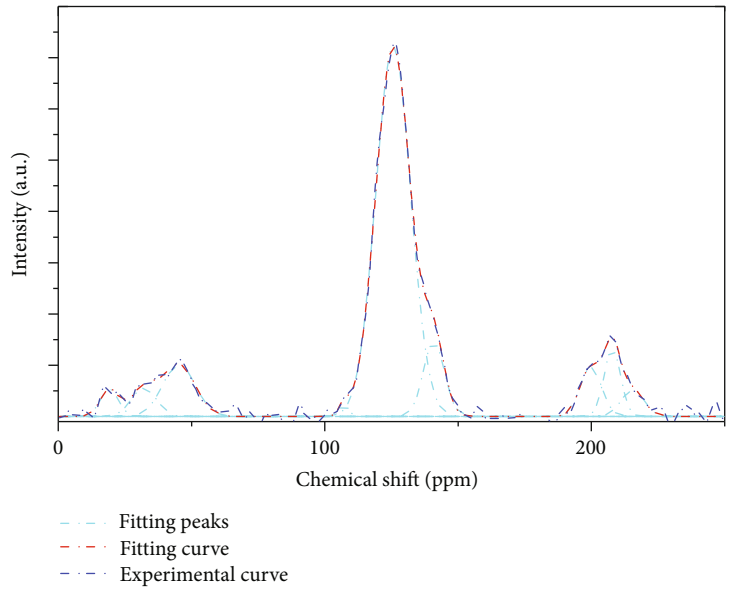

Figure 1: ^{13}C NMR data of the YW coal samples with the peak fitting results.

aliphatic carbon on the side chain are mainly composed by methyl and methylene. The oxygen-containing functional groups are mainly ether bonds. According to elemental analysis and ^{13}C NMR data, the aromaticity rate is 74.5%, and the total carbon in coal molecular structure unit is 200. The ratio of benzene : naphthalene : anthracene : phenanthrene : pentacene in YW sample is 5 : 5 : 3 : 0 : 2 (Table 2).

3.2. Results of FT-IR. The peak fitting results of FT-IR are shown in Figure 2. The assignment of each peaks are according to Tables 3–6. The region between 2800 and 3000 cm^{-1} of FT-IR spectrum is the aliphatic carbon region. The infrared spectrum of this region shows that the side chain alkyl is mainly methylene and there is a small amount of methyl (Table 6).

3.3. Coal Molecular Construction. The ^{13}C NMR and FT-IR data are used to reconstruct the chemical molecular structure of anthracite, and the average chemical formula of the anthracite coal molecule is $C_{200}H_{133}O_{21}N_3$, as shown in Figure 3(a). In addition, it can be seen that the oxygen atoms are mainly in the form of carbonyl groups, which can be also found from the ^{13}C NMR spectrum. The nitrogen atoms are in the form of pyrrole rings. After annealing and geometrically optimizing the 2D molecule, it can be found that the aliphatic side chain is obviously elongated and the aromatic carbon structure is distorted, as shown in Figures 3(b) and 3(c). Simultaneously, 14 optimized anthracite molecules put into the unit cell to construct a 3D structure of anthracite coal as shown in Figure 3(d). The size of the 3D molecular structure is 3.345 nm × 3.345 nm × 3.345 nm.

Table 2: Forms of aromatic carbon with different molecular configurations of coal samples.

Existing forms of aromatic carbon	Numbers
Benzene	5
Naphthalene	5
Anthracene	3
Phenanthrene	0
Pentacene	2
Pyrrole	3

3.4. Methane Adsorption Isothermal Data. Figure 4 illustrates the experimental methane adsorption isothermal data

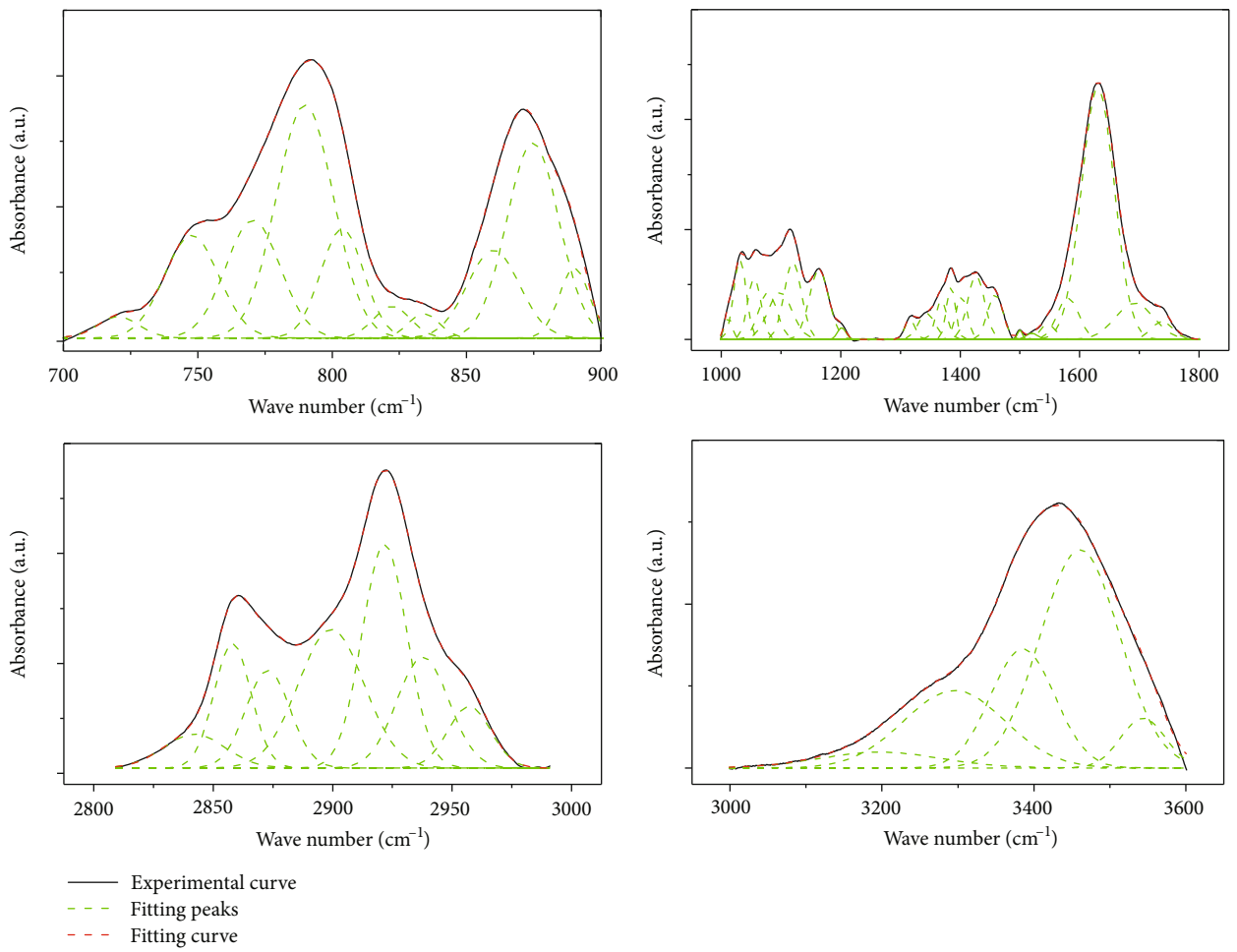

Figure 2: The peak fitting results of FT-IR of YW coal samples.

of the YW coal sample under different temperatures. It can be seen that the adsorption capacity of methane increases significantly with increasing the pressure under the same temperature. This phenomenon demonstrates that it is conductive to the adsorption of methane under higher-pressure conditions. With increasing temperature, the methane adsorption amount is significantly weakened. At the pressure of 7.0 MPa, the methane adsorption capacity of the YW coal sample is 28.5 cm^3/g under the temperature of 20°C. Comparably, the methane adsorption amount under the temperature of 100°C is only 15.9 cm^3/g, decreasing by 44%. At the pressure of 1 MPa, with the temperature increases from 20°C to 100°C, the methane adsorption amount decreases from 10.0 cm^3/g to 7.1 cm^3/g.

3.5. Simulation of Methane Adsorption in Micropores of Coal Sample. The pores of the model are calculated based on the 3D YW coal molecule, as shown in Figure 5. It can be seen from there are many pores in the coal matrix. These pores are very small in size, and the pore size ranges from 0.34 to 1.0 nm. In addition, the shape of these micropores is irregular. We employed methane adsorption simulation by using the 3D YW coal molecule and these methane molecules are adsorbed in the micropore (Figure 5). Figures 6(a) and 6(b) illustrate the simulation adsorption capacity of methane under different pressures and temperatures. With the methane pressure increasing from 1 MPa to 7 MPa at 100°C, the absolute adsorption amount of methane increases from 7.52 cm^3/g to 14.50 cm^3/g, and the excess adsorption amount of methane increases from 7.30 cm^3/g to 12.91 cm^3/g. While, when the pressure reaches critical value, the absolute adsorption amount is found saturated, then the excess adsorption amount will show downward trend. Compared with pressure, temperature has a negative effect on methane adsorption. With temperature increasing, the adsorption capacity of methane gradually decreases. When the temperature is 20°C, the absolute methane adsorption amount and excess methane adsorption amount is 25.2 cm^3/g and 23.0 cm^3/g under 7 MPa pressure. When the temperature increases to 100°C, the absolute methane adsorption amount and excess methane adsorption amount decreases from 14.50 cm^3/g to 12.91 cm^3/g at 7 MPa pressure, decreasing by 42.4% and 43.9%, respectively.

3.6. Simulation Methane Adsorption in Mesoporous. Figures 7(a) and 7(b) demonstrated the simulation results of the methane adsorption behavior in mesopores. When the temperature increases, the methane adsorption capacity

Table 3: Regional content of aromatic hydrocarbons (the assignments of the FT-IR is according to [37]).

Chemical shift (cm^{-1})	Relative area (%)	Peak position attribution
720	1.79	Skeleton vibration of (CH_2) $n \circ > 4$ on the side chain of n-alkanes
748	11.28	Out of plane deformation vibration of CH in aromatics (4-5 adjacent H atoms)
771	12.29	
790	26.87	
804	9.24	Out of plane deformation vibration of CH in aromatics (3 adjacent H atoms)
822	20.48	
834	4.14	
860	2.34	Out of plane deformation vibration of CH in aromatics (2 adjacent H atoms)
875	1.51	
890	9.43	

Table 4: Regional content of oxygen-containing functional groups (the assignments of the FT-IR is according to [37]).

Chemical shift (cm^{-1})	Relative area (%)	Peak position attribution
1012	0.77	C-O-C telescopic vibration
1031	4.54	
1055	3.72	
1078	3.95	
1099	5.22	C-O-C symmetric telescopic vibration
1120	6.11	
1164	6.14	R-O-C telescopic vibration
1202	0.46	Ar-O-C telescopic vibration
1316	0.92	
1344	2.02	
1369	2.16	CH_3 symmetrical bending vibration
1385	2.28	
1402	4.91	
1427	3.13	Asymmetric deformation vibration of CH_3 and CH_2
1459	0.20	
1500	1.06	
1520	4.07	
1547	37.83	Aromatics C°=°C skeleton vibration
1580	1.77	
1631	2.06	
1692	0.33	Stretching vibration of C°=°O in quinone and anhydride
1738	6.36	

Table 5: Regional content of aliphatic carbon (the assignments of the FT-IR is according to [37]).

Chemical shift (cm^{-1})	Relative area (%)	Peak position attribution
2836	5.37	CH_2 telescopic vibration
2853	11.92	CH_3 telescopic vibration
2870	23.69	
2899	26.00	CH telescopic vibration
2924	14.99	CH_2 asymmetric telescopic vibration
2942	6.86	
2963	11.18	CH_3 asymmetric telescopic vibration

Table 6: Regional content of hydroxyl group (the assignments of the FT-IR is according to [37]).

Chemical shift (cm^{-1})	Relative area (%)	Peak position attribution
3197	5.14	Ring stretching vibration
3295	21.28	OH-O stretching vibration
3385	20.72	OH-OH stretching vibration
3461	46.97	
3544	5.90	OH-Π telescopic vibration

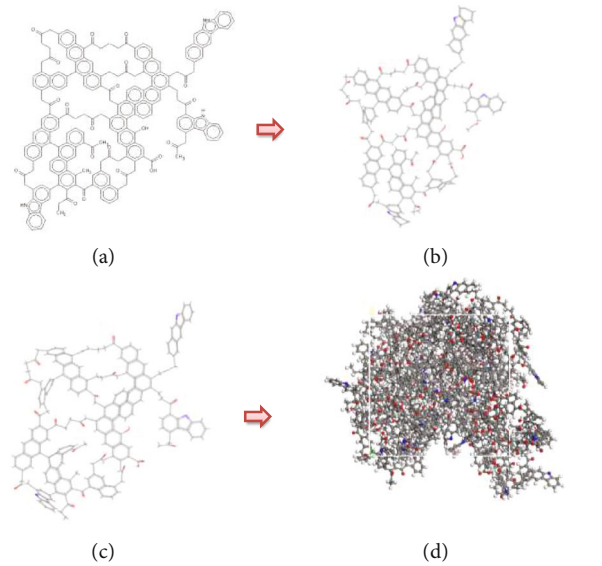

Figure 3: Molecular structure model of YW anthracite. ((a) 2D molecular model; (b) 3D structure optimization results; (c) 3D structure after anneal treatment; (d) 3D molecule structure with 14 molecules).

decreases significantly in 3°nm pore. This phenomenon is consistent with the adsorption of methane in micropores and experimental data. With pressure increasing from 1°MPa to 7°MPa at temperature of 100°C, the absolute adsorption amount of methane increases from $6.23 \times 10^{-3} \circ cm^3/g$ to $4 \times 10^{-2} \circ cm^3/g$, and the excess adsorption amount of methane increases from $2.70 \times 10^{-3} \circ cm^3/g$ to $1.43 \times 10^{-2} \circ cm^3/g$, respectively. When temperature increases from 20°C to 100°C, the absolute adsorption amount of methane decreases from $6.6 \times 10^{-2} \circ cm^3/g$ to $4 \times 10^{-2} \circ cm^3/g$, and the excess adsorption amount of methane decreases from $2.98 \times 10^{-2} \circ cm^3/g$ to $1.43 \times 10^{-2} \circ cm^3/g$ under 7°MPa pressure. With the temperature rising from 20°C to 100°C, the absolute adsorption amount and excess adsorption amount decreases by 33.33% and 52.01%, respectively (at 7°MPa pressure).

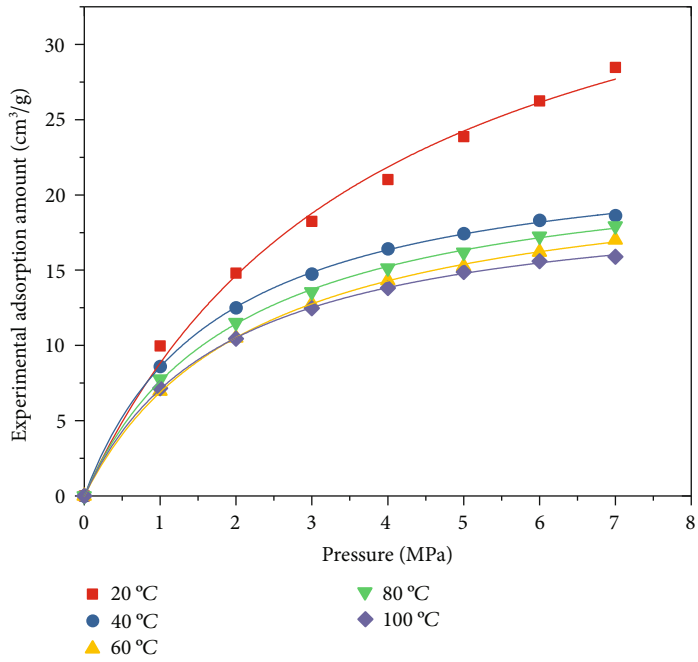

Figure 4: Experimental methane adsorption isothermal data of YW coal samples under different temperatures.

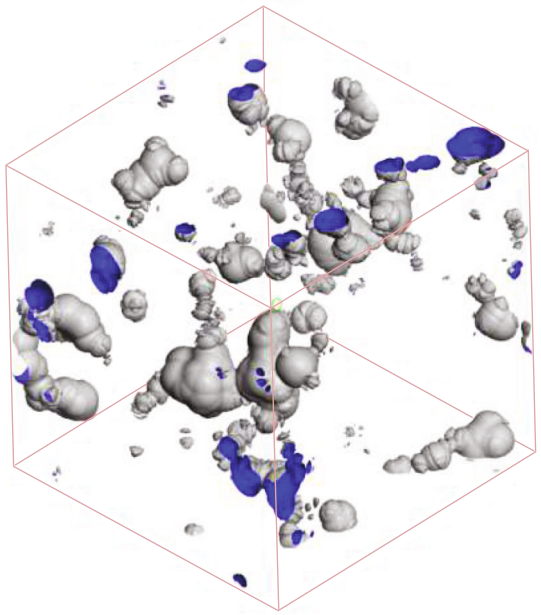

Figure 5: Pore distribution in YW anthracite coal molecule (3.345 nm × 3.345 nm × 3.345 nm).

4. Discussion

4.1. Methane Adsorption Density at Different Pressure and Temperature. Figures 8(a) and 8(b) show the methane density distribution in 3 nm pores under different temperature and pressure. The adsorbed methane molecule is mainly located near the pore walls, and the methane adsorption density near the pore surface is much larger than that in the center of the slit pore. In addition, the methane density in the center of slit pore increases linearly with increasing the pressure. The density of adsorbed layers near the pore wall firstly increases significantly, and then increases slowly when the pressure is larger than 4 MPa. Figure 8(b) shows the methane density distribution at different temperatures. It can be found that with increasing the temperature, the methane density near the pore walls and in the center of the pore both decreases. However, the decrease of methane density in the center of pore is not obvious with increasing the temperature. Comparably, the methane density on the pore surface decreases significantly. It indicates that the temperature significantly affects adsorbed methane molecules. In Figures 8(a) and 8(b), the density near the pore surface is more sensitive to the pressure and temperate compared to the methane in the center of the pores. In addition, it can be seen that as the pressure increases, the methane density on both sides of the pore wall increases. While, as the temperature increases, the density of methane on both sides of the pore decreases. The reason is that the pores provide enough space in anthracite coal molecules, and as the pressure increases, more methane will be adsorbed on the pore surface. However, as the temperature increases, the methane molecules adsorb thermal energy and convert it into kinetic energy, thereby breaking the adsorption force of the pore wall and escaping from the pores. These simulation results are consistent with the experimental results of methane adsorption isotherm.

4.2. The Effect of Temperature on Methane Adsorption Amount of Coal. Figure 9 shows the experimental methane adsorption data at different temperature. It can be seen that the methane adsorption amount of coal sample at 20°C is significantly larger than those at larger temperature. Based

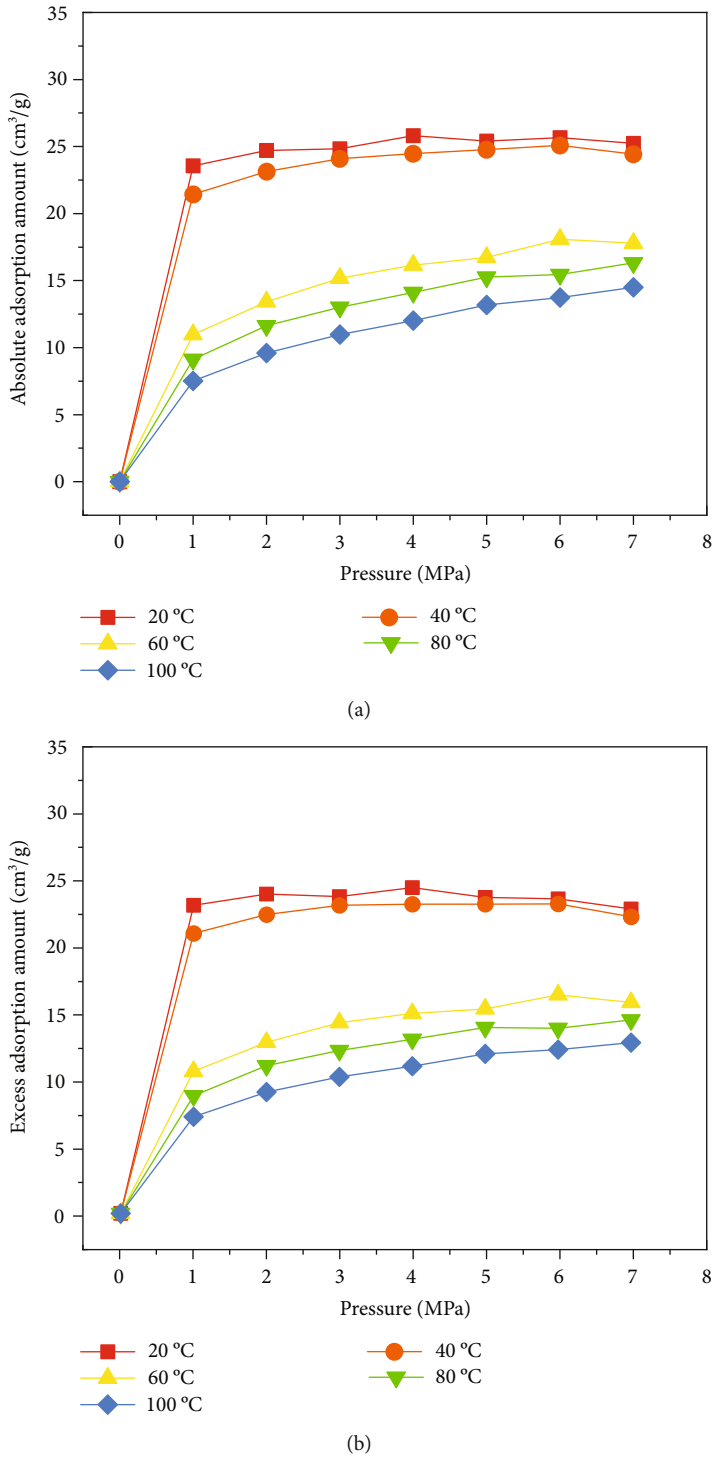

Figure 6: Simulation methane adsorption under different temperatures ((a) absolute adsorption amount under different temperatures; (b) excess adsorption amount under different temperatures).

on Figure 9, it can be seen that when the pressure is larger, the temperature has larger effect on the methane adsorption amount. At 7 MPa, the methane adsorption amount is 28.5 cm^3/g under 20°C, and decreases to 15.9 cm^3/g under 100°C, decreasing by 44%. However, at 1 MPa, the methane adsorption amount is 10.0 cm^3/g under 20°C, and decreases to 7.1 cm^3/g under 100°C, decreasing by 28%.

Experimental data illustrate the overall methane adsorption amount in all pores of coal sample including micropores, mesopores, and macropores. As shown in Figures 6 and 7, methane adsorption in micropores is different from that in mesopores. Thus, it should be discussed separately. Figure 10 shows the relationship of temperature and methane adsorption amount in micropores under different

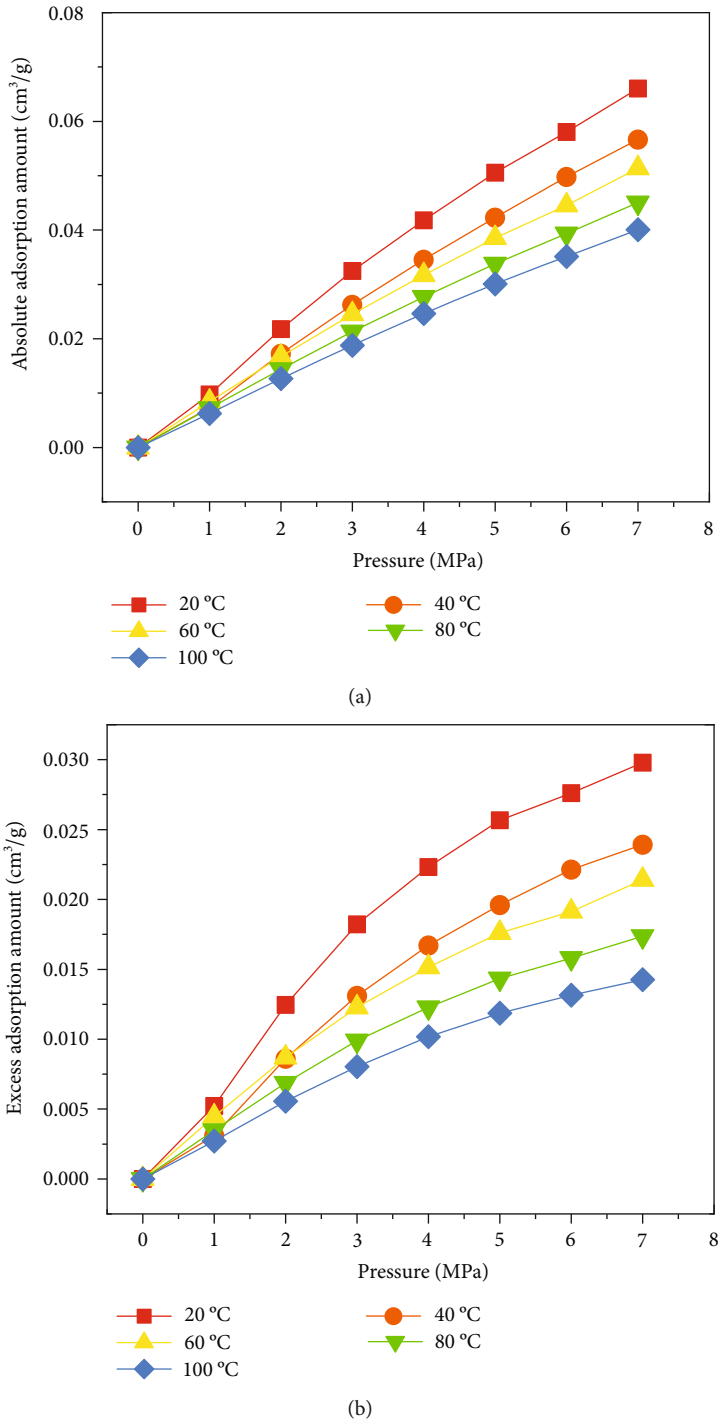

Figure 7: Simulation methane adsorption in 3 nm pore under different temperatures (a) absolute adsorption amount under different temperatures; (b) excess adsorption amount under different temperatures).

pressure. It can be found that at 20°C the adsorption amount in micropores at different pressure is similar, but at 100°C, the methane adsorption amount is micropores at lower pressure is obviously smaller than that at high pressure. It means, in micropores, temperature have larger effects on methane adsorption at low pressure than that at high pressure.

Figure 11 shows the influence of temperature on methane adsorption in mesopores under different pressure. With increasing the temperature, the methane adsorption amount decreases, which is consistent to the experimental data (Figure 9). It is also obvious that temperature has larger effect on methane adsorption amount at higher pressure than that at lower pressure. At 1 MPa, the

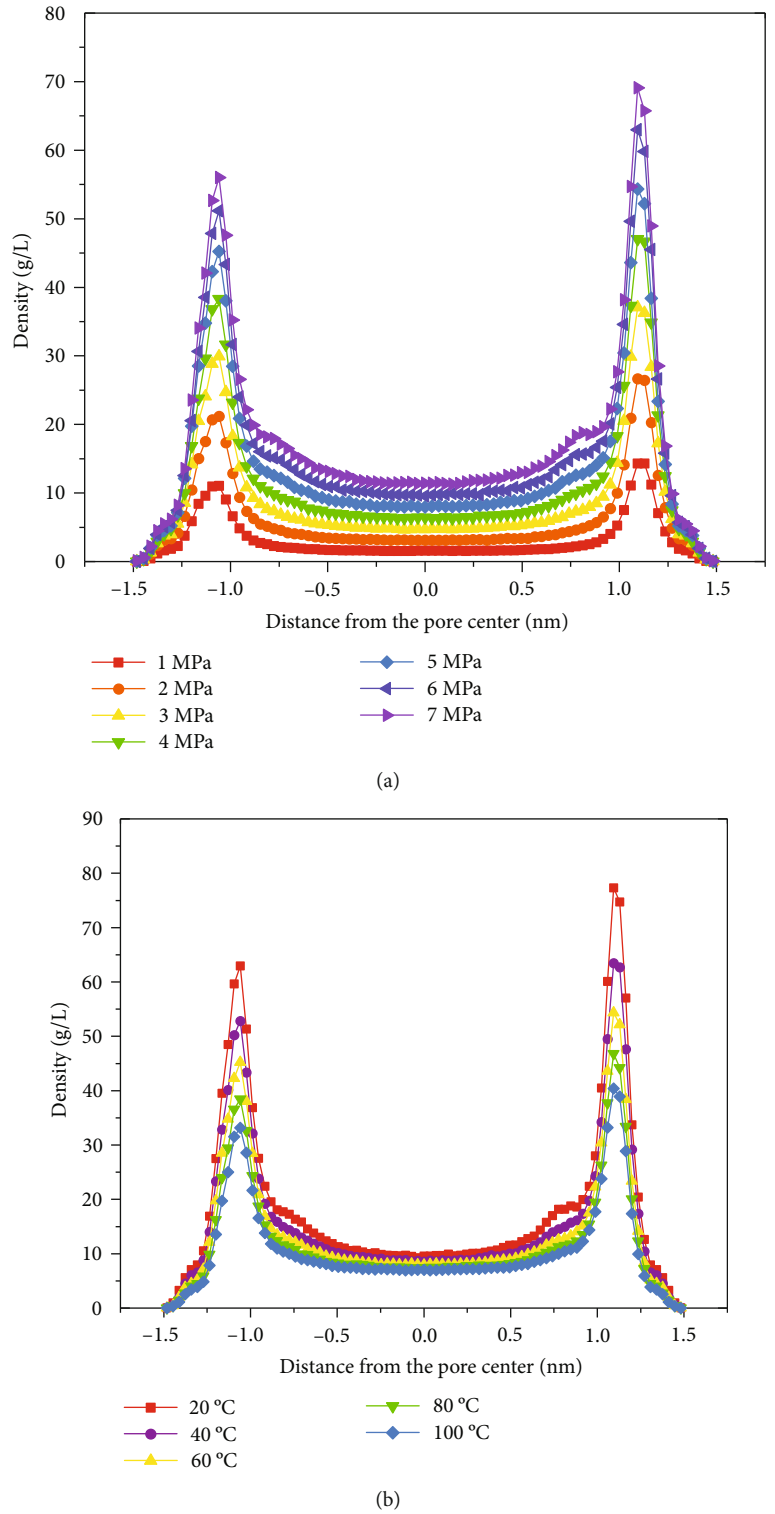

Figure 8: Characteristics of methane density variation in 3 nm slit pore at different pressures (a) and different temperatures (b).

methane adsorption amount at 20°C is 0.01 cm^3/g, and decreases to 0.0027 cm^3/g at 100°C, decreasing by 48%. Comparably, at 7 MPa, the methane adsorption amount at 20°C is 0.066 cm^3/g, and decreases to 0.014 cm^3/g at 100°C, decreasing by 78%. By comprehensively analyzing that the methane behavior in micropore, mesopore, and macropores, when the pressure is higher, temperature has larger effects on methane adsorption in mesopores and macropores, and has weaker effects on methane adsorption in micropores. The experimental data show

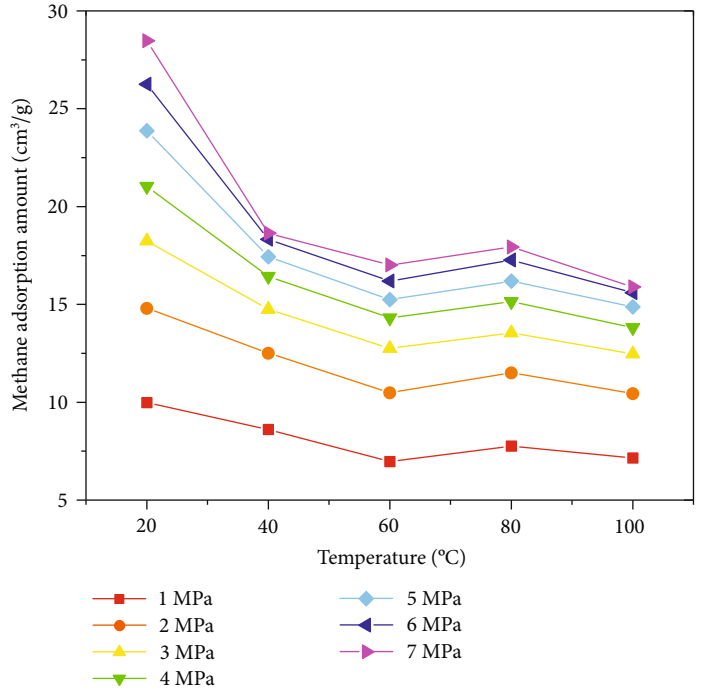

Figure 9: The effect of temperature on methane adsorption amount of coal (experimental data).

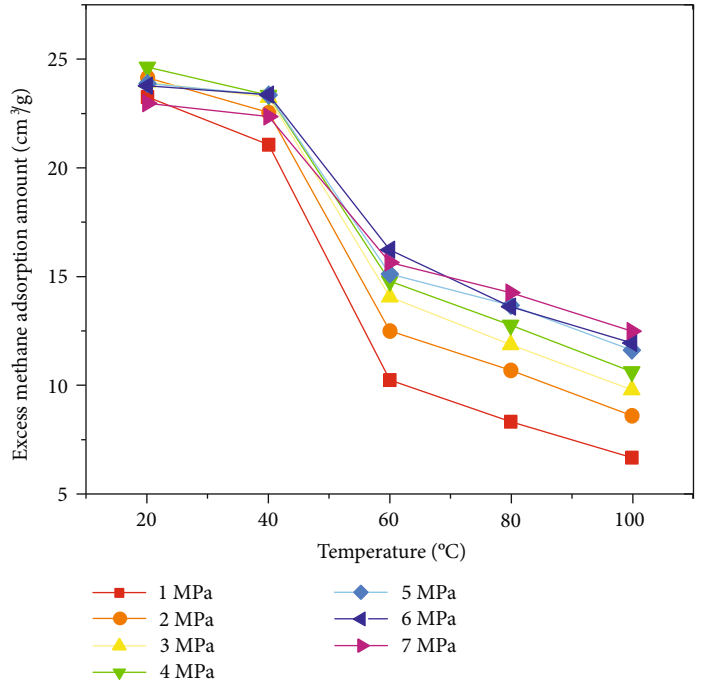

Figure 10: The effect of temperature on methane adsorption amount in micropores (simulation data).

that in YW coal sample, the temperature has larger effects on methane adsorption methane adsorption at high-pressure stage, which is consistent to the phenomenon of methane adsorption in mesopore and macropores, and is contrary to the phenomenon of methane adsorption in micropore. It indicates that the mesopores and macropores in YW coal sample finally determine the temperature effect on methane adsorption.

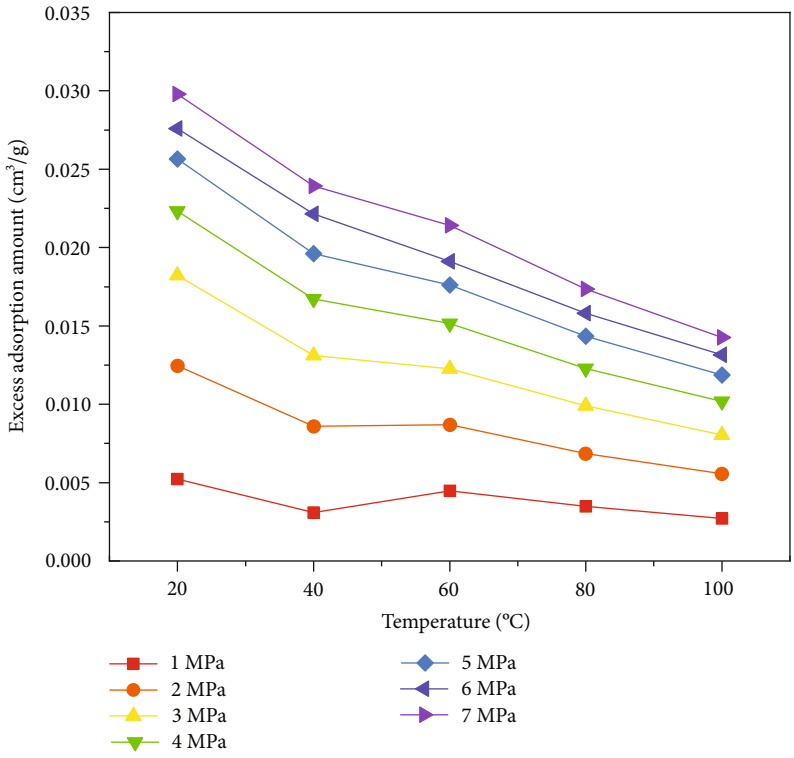

Figure 11: The effect of temperature on methane adsorption amount in mesopores (simulation data).

5. Conclusions

(1) Based on the ^{13}C NMR data and FT-IR data, the carbon skeleton of YW coal sample is mainly composed by aromatic carbon structure (72%), followed by aliphatic carbon structure (14.2%). Carbons connected to the oxygen atoms contribute 13.7% of the total carbons in coal molecule, and the oxygen atoms mainly exit in the form of carbonyl

(2) The average chemical formula of the coal molecule is $C_{200}H_{133}O_{21}N_3$ and the nitrogen atoms are in the form of pyrrole rings. By combining 14 coal molecules, the 3D macromolecular model was built and the size of the 3D macromolecular model is 3.345 nm × 3.345 nm × 3.345 nm

(3) The experimental methane adsorption isothermal data of the YW coal sample under different temperatures show that with increasing the temperature, the methane adsorption amount decreased obviously. At 7 MPa, the methane adsorption amount of the YW coal sample is 28.5 cm^3/g under 20°C. Comparably, less than 100°C and 2 MPa, the methane adsorption amount is only 15.9 cm^3/g, and decreases by 44%. Besides, the experimental data show that in YW coal sample, the temperature has larger effects on methane adsorption methane adsorption at higher pressure stage

(4) In mesopores and macropores, temperature has larger effects on methane adsorption at higher pressure than that at lower pressure. On the contrary, in micropores, temperature has weaker effects on methane adsorption at higher pressure than that at lower pressure

Data Availability

The data used to support the findings of this study are included within the article.

Conflicts of Interest

The authors declare that there are no conflicts of interest.

Acknowledgments

The authors would like to thank Mining Branch of Huaneng Yunnan Diandong Energy Co., Ltd. for their help to offer the cores. This research was funded by China Huaneng Group High-Level Talents Programme (Research on Spatial Distribution and Control Technology of Methane in Yunnan Diandong Mining Area), China Huaneng Group Science and Technology Projects (No. HNKJ21-H51, HNKJ21-H67, HNKJ22-H10), Beijing Science and Technology Plan (No. Z201100004520028), National Natural Science Foundations of China (No. 41972123), and National Key Research and Development Program (Project No. 2019YFE0100100). The authors are also very grateful to Postdoc Zhang Yu in Department of Energy and Power Engineering, Tsinghua University, for accessing the simulation software.

References

[1] M. H. Plumlee, J. F. Debroux, T. Dawn et al., "Coalbed methane produced water screening tool for treatment technology and beneficial use," *Journal of Unconventional Oil and Gas Resources*, vol. 5, pp. 22–34, 2014.

[2] Y. Li, C. Zhang, D. Tang, Q. Gan, X. Niu, and R. Shen, "Coal pore size distributions controlled by the coalification process: an experimental study of coals from the Junggar, Ordos and Qinshui basins in China," *Fuel*, vol. 206, pp. 352–363, 2017.

[3] Y. Li, S. Pan, S. Ning, L. Shao, Z. Jing, and Z. Wang, "Coal measure metallogeny: metallogenic system and implication for resource and environment," *Science China Earth Sciences*, vol. 65, no. 7, pp. 1211–1228, 2022.

[4] S. D. Chen, S. Tao, W. G. Tian, D. Z. Tang, B. Zhang, and P. C. Liu, "Hydrogeological control on the accumulation and production of coalbed methane in the Anze block, southern Qinshui basin, China," *Journal of Petroleum Science and Engineering*, vol. 198, p. 108138, 2021.

[5] S. Tamamura, T. Murakami, A. Ueno et al., "Formation of coalbed methane and water-dissolved gas in Kushiro Coal Mine, Japan, based on isotopic compositions of gas, groundwater, and calcite," *International Journal of Coal Geology*, vol. 229, p. 103577, 2020.

[6] P. J. Crosdale, B. B. Beamish, and M. Valix, "Coalbed methane sorption related to coal composition," *International Journal of Coal Geology*, vol. 35, no. 1–4, pp. 147–158, 1998.

[7] Y. Li, J. Yang, Z. Pan, S. Meng, K. Wang, and X. Niu, "Unconventional natural gas accumulations in stacked deposits: a discussion of upper Paleozoic coal-bearing strata in the east margin of the Ordos Basin, China," *Acta Geologica Sinica (English Edition)*, vol. 93, no. 1, pp. 111–129, 2019.

[8] Y. Li, J. Yang, Z. Pan, and W. Tong, "Nanoscale pore structure and mechanical property analysis of coal: an insight combining AFM and SEM images," *Fuel*, vol. 260, p. 116352, 2020.

[9] K. Jian, X. Fu, Y. Ding, H. Wang, and T. Li, "Characteristics of pores and methane adsorption of low-rank coal in China," *Journal of Natural Gas Science and Engineering*, vol. 27, pp. 207–218, 2015.

[10] H. H. Hou, L. Y. Shao, Y. H. Li et al., "Influence of coal petrology on methane adsorption capacity of the Middle Jurassic coal in the Yuqia coalfield, northern Qaidam Basin, China," *Journal of Petroleum Science and Engineering*, vol. 149, pp. 218–227, 2017.

[11] Z. Pan and D. A. Wood, "Coalbed methane (CBM) exploration, reservoir characterisation, production, and modelling: a collection of published research (2009-2015)," *Journal of Natural Gas Science and Engineering*, vol. 26, pp. 1472–1484, 2015.

[12] Y. Li, Z. Wang, S. Tang, and D. Elsworth, "Re-evaluating adsorbed and free methane content in coal and its ad- and desorption processes analysis," *Chemical Engineering Journal*, vol. 428, article 131946, 2022.

[13] K. Mosher, J. He, Y. Liu, E. Rupp, and J. Wilcox, "Molecular simulation of methane adsorption in micro- and mesoporous carbons with applications to coal and gas shale systems," *International Journal of Coal Geology*, vol. 109-110, pp. 36–44, 2013.

[14] H. Y. Hu, T. W. Zhang, J. D. Wiggins-Camacho, G. S. Ellis, M. D. Lewan, and X. L. Zhang, "Experimental investigation of changes in methane adsorption of bitumen-free Woodford shale with thermal maturation induced by hydrous pyrolysis," *Marine and Petroleum Geology*, vol. 59, pp. 114–128, 2015.

[15] J. H. Levy, S. J. Day, and J. S. Killingley, "Methane capacities of Bowen Basin coals related to coal properties," *Fuel*, vol. 76, no. 9, pp. 813–819, 1997.

[16] B. Ryan and T. Gentzis, "Controls on methane adsorption capacity of lower cretaceous coals from northeastern British Columbia, Canada: part 2-effect of temperature, pressure," *Maceral Composition, and Mineral Matter on Adsorption*, vol. 25, no. 12, pp. 1155–1170, 2003.

[17] L. W. Zhong and X. M. Zhang, "The relationship between methane adsorption capacity and the rank and composition of coal," *Coal Geology & Exploration*, no. 4, p. 29–36+71–74, 1990.

[18] D. Zhao, Y. S. Zhao, Z. C. Feng, Z. X. Liu, and T. Liu, "Experiments of methane adsorption on raw coal at 30-270°C," *Energy Sources, Part A: Recovery, Utilization, and Environmental Effects*, vol. 34, no. 4, pp. 324–331, 2011.

[19] Y. Zhao, Y. Sun, S. Liu, K. Wang, and Y. Jiang, "Pore structure characterization of coal by NMR cryoporometry," *Fuel*, vol. 190, pp. 359–369, 2017.

[20] X. X. He, Y. P. Cheng, B. Hu et al., "Effects of coal pore structure on methane–coal sorption hysteresis: an experimental investigation based on fractal analysis and hysteresis evaluation," *Fuel*, vol. 269, p. 117438, 2020.

[21] B. Hu, Y. P. Cheng, X. X. He, Z. Y. Wang, Z. N. Jiang et al., "New insights into the CH4 adsorption capacity of coal based on microscopic pore properties," *Fuel*, vol. 262, article 116675, 2020.

[22] F. An, Y. Cheng, D. Wu, and L. Wang, "The effect of small micropores on methane adsorption of coals from northern China," *Adsorption*, vol. 19, no. 1, pp. 83–90, 2013.

[23] S. Wu, D. Tang, S. Li, H. Chen, and H. Wu, "Coalbed methane adsorption behavior and its energy variation features under supercritical pressure and temperature conditions," *Journal of Petroleum Science and Engineering*, vol. 146, pp. 726–734, 2016.

[24] C. J. Liu, S. X. Sang, X. F. Fan et al., "Influences of pressures and temperatures on pore structures of different rank coals during CO_2 geological storage process," *Fuel*, vol. 259, p. 116273, 2020.

[25] M. S. A. Perera, P. G. Ranjith, S. K. Choi, D. Airey, and P. Weniger, "Estimation of gas adsorption capacity in coal: a review and an analytical study," *Estimation of Gas Adsorption Capacity in Coal: A Review and an Analytical Study. International Journal of Coal Preparation and Utilization*, vol. 32, no. 1, pp. 25–55, 2012.

[26] G. Yue, Z. Wang, X. Tang, H. Li, and C. Xie, "Physical simulation of temperature influence on methane sorption and kinetics in coal (II): temperature evolvement during methane adsorption in coal measurement and modeling," *Energy & Fuels*, vol. 29, no. 10, pp. 6355–6362, 2015.

[27] L. Zhong, "Adsorptive capacity of coals and its af fecting factors," *Earth Science*, vol. 29, no. 3, p. 327-332+368, 2004.

[28] J. Shen, Y. Qin, X. H. Fu, G. Wang, R. Chen, and L. J. Zhao, "Study of high-pressure sorption of methane on Chinese coals of different rank," *Arabian Journal of Geosciences*, vol. 8, no. 6, pp. 3451–3460, 2015.

[29] Y. Qin, T. A. Moore, J. Shen, Z. B. Yang, Y. L. Shen, and G. Wang, "Resources and geology of coalbed methane in China: a review," *International Geology Review*, vol. 60, no. 5–6, pp. 777–812, 2018.

[30] J. You, L. Tian, C. Zhang et al., "Adsorption behavior of carbon dioxide and methane in bituminous coal: a molecular simulation study," *Chinese Journal of Chemical Engineering*, vol. 24, no. 9, pp. 1275–1282, 2016.

[31] K. Dong, F. Zeng, J. Jia, C. Chen, and Z. Gong, "Molecular simulation of the preferential adsorption of CH4and CO2in middle-rank coal," *Molecular Simulation*, vol. 45, no. 1, pp. 15–25, 2019.

[32] S. Yu, Z. Yan-ming, and L. Wu, "Macromolecule simulation and CH4 adsorption mechanism of coal vitrinite," *Applied Surface Science*, vol. 396, pp. 291–302, 2017.

[33] J. Xiang, F. Zeng, H. Liang, B. Li, and X. Song, "Molecular simulation of the CH4/CO2/H2O adsorption onto the molecular structure of coal," *Science China Earth Sciences*, vol. 57, no. 8, pp. 1749–1759, 2014.

[34] J. Zhang, K. Liu, M. B. Clennell, D. N. Dewhurst, and M. Pervukhina, "Molecular simulation of CO_2-CH_4 competitive adsorption and induced coal swelling," *Fuel*, vol. 160, pp. 309–317, 2015.

[35] A. Marzec, "Towards an understanding of the coal structure: a review," *Fuel Processing Technology*, vol. 77-78, pp. 25–32, 2002.

[36] Y. Liu, S. Liu, R. Zhang, and Y. Zhang, "The molecular model of Marcellus shale kerogen: experimental characterization and structure reconstruction," *International Journal of Coal Geology*, vol. 246, p. 103833, 2021.

[37] P. C. Painter, R. W. Snyder, M. Starsinic, M. M. Coleman, D. W. Kuehn, and A. Davis, "Concerning the application of FT-IR to the study of coal: a critical assessment of band assignments and the application of spectral analysis programs," *Applied Spectroscopy*, vol. 35, no. 5, pp. 475–485, 1981.

[38] J. H. Xiang, F. Zeng, B. Li, and L. Zhang, "Construction of macromolecular structural model of anthracite from Chengzhuang coal mine and its molecular simulation," *Journal of Fuel Chemistry and Technology*, vol. 41, no. 4, pp. 391–400, 2013.

[39] Y. Liu, Y. Zhu, W. Li, C. Zhang, and Y. Wang, "Ultra micropores in macromolecular structure of subbituminous coal vitrinite," *Fuel*, vol. 210, pp. 298–306, 2017.

[40] B. Erdenetsogt, I. Lee, S. K. Lee, Y. Ko, and D. Bat-Erdene, "Solid-state C-13 CP/MAS NMR study of Baganuur coal, Mongolia: oxygen-loss during coalification from lignite to subbituminous rank," *International Journal of Coal Geology*, vol. 82, no. 1–2, pp. 37–44, 2010.

[41] S. Wang, Y. Tang, H. H. Schobert, Y. N. Guo, and Y. Su, "FTIR and13C NMR investigation of coal component of late Permian coals from southern China," *Energy & Fuels*, vol. 25, no. 12, pp. 5672–5677, 2011.

Hindawi
Geofluids
Volume 2022, Article ID 3311827, 13 pages
https://doi.org/10.1155/2022/3311827

Research Article

Optimal Injection Parameters for Enhancing Coalbed Methane Recovery: A Simulation Study from the Shizhuang Block, Qinshui Basin, China

Du Liu,[1,2] **Longyong Shu**,[2] **Yanbin Wang**,[3] **Zhonggang Huo**,[2] **Shihu Zhao**,[3] **and Xing Xiong**[3]

[1]*China Coal Research Institute, Beijing 100013, China*
[2]*Mine Safety Technology Branch, China Coal Research Institute, Beijing 100013, China*
[3]*College of Geoscience and Surveying Engineering, China University of Mining and Technology, Beijing 100083, China*

Correspondence should be addressed to Longyong Shu; slyccri@163.com

Received 3 February 2022; Revised 25 May 2022; Accepted 29 September 2022; Published 11 October 2022

Academic Editor: Chao-Zhong Qin

The injection of N_2 into coal reservoir has great potential in improving recovery of coalbed methane (CBM). In this study, a numerical model was established based on the GEM component model to evaluate the influences of different N_2 injection parameters (production injection well spacing, gas injection timing, gas injection duration, gas injection rate, and the bottom-hole injection pressure) on the production of CBM in the Shizhuang Block of Qinshui Basin, China. Based on the economic benefit of CBM production, the production increasing rate and nitrogen replacement ratio were established to optimize the N_2 injection parameters. The results show that (1) the production injection well spacing had the greatest influence on CBM production, followed by injection duration and the bottom-hole injection pressure, and injection timing and injection rate had a relatively small influence. (2) With increasing gas injection duration, injection rate, and the bottom-hole injection pressure, the rate of production increased and the nitrogen replacement ratio decreased. (3) The optimal N_2 injection scheme was revealed with the production injection well spacing of 180 m, the injection timing of a second year after gas production, an injection duration of 7 years, an injection rate of 5000 m^3/d, and a bottom-hole injection pressure of 10 MPa. Under these conditions, the rate of production increasing rate, the nitrogen displacement ratio, and the regional recovery of the four production wells were 18.14%, 0.5, and 48.96%, respectively, some 8.88% higher than that without nitrogen displacement, showing good effect in terms of CBM production.

1. Introduction

Coalbed methane (CBM) is an important unconventional natural gas resource, and it is abundant in China. According to the fourth round of CBM resource assessment, the geological resources of shallow CBM at a burial depth of 2 km are 29.82×10^{12} m^3 in China [1–5]. There are about 20,000 CBM wells at the end of 2020, and the CBM production is about 57.67×10^8 m^3. The average gas production per well is generally low. It is not only affected by the complex geological conditions but also depends on the adaptability of CBM development technology. By the end of the 13th Five-Year Plan, the production of CBM has gradually increased, but the increase is small. The CBM production still has not exceeded 10 billion cubic meters. At present, China's CBM industry is characterized by the low exploration and development, low adaptability of agent technology, low return on investment, small development scale, etc. [6–9]. Under the background of "peak carbon and carbon neutralization," clean energy is in high demand. CBM industry needs to be closely linked around the value chain in terms of "how to improve the single CBM well production and the overall CBM recovery." Therefore, CBM development needs to conduct the refine exploitation geology research and the

development of more targeted engineering technology research. This strengthens the geological and engineering technology integration evaluation and implements technology industrialization, which can achieve the goal of improving the development benefit of CBM and promote the development of China's CBM industry. Therefore, efficient techniques are needed to improve CBM recovery [10].

Exploitation of CBM mainly depends on drainage and pressure reduction, which promotes desorption of methane [11, 12]. Injecting N_2 can reduce the partial pressure of methane in a coal reservoir [13] and improve the permeability of coal reservoir [14], thus significantly improving the CBM production. Based thereon, a gas-injection technique is proposed, which is called "enhancing CBM recovery by injecting N_2 (N_2-ECBM)" [15, 16]. Many laboratory and field tests have been conducted [17–23]. The adsorption of N_2 will cause the shrinkage of coal matrix when the N_2 is injected into coal, which mainly changes the mechanical properties and permeability of coal. After N_2 injection, the permeability of coal increases, and it can promote the diffusion and migration of CBM. Meanwhile, the mechanical strength of coal changes readily, which is conducive to improving CBM recovery. Additionally, some scholars explored and compared the results of N_2 injection and the mixture of N_2 and CO_2 injection [24]. The process is nonpiston displacement when N_2 displaces CH_4. The breakthrough of N_2 occurs rapidly, and the two-element transition zone is narrow. The CH_4 and N_2 are produced for a long time after breakthrough. The ratio of N_2 injection is higher when the mixture of N_2 and CO_2 is injected into the coal, which can increase the permeability of the coal and is beneficial to CBM recovery. Most of the previous studies focused on the mechanism analysis of N_2 injection to enhance CBM recovery, however, less work on the effect of N_2 injection parameters on CBM recovery and the optimization of N_2 injection scheme has been undertaken.

The Shizhuang Block has realized the industrial development of CBM which shows considerable production volumes in the Qinshui Basin [25–27]. However, with the development of CBM, many CBM wells have been found to have low efficiency and low rates and amounts of overall productivity [28, 29]. To promote the long-term stable production of CBM in the area, it is necessary to enhance the recovery based on an N_2-ECBM technique.

Therefore, in the present research, the production variations under different N_2 injection parameters (including the production injection well spacing, gas injection timing, gas injection duration, gas injection rate, and the bottom-hole injection pressure) in coal reservoir were studied using numerical simulation, to optimize the N_2 injection parameters and enhance CBM recovery. The results may provide theoretical guidance for an optimal N_2-ECBM scheme in the study area.

2. Model Establishment

2.1. Geological Model. The Cartesian coordinate system was adopted for the reservoir grid model. The grid distribution is $51 \times 51 \times 1$. The length, width, and height of a single grid are $10\,\text{m} \times 10\,\text{m} \times 6\,\text{m}$, and the model measures $510\,\text{m} \times 510\,\text{m} \times 6\,\text{m}$. Based on the five point well pattern, an N_2 injection well is located in the middle of the model, four production wells are located around the injection well, and the well spacing between the injection well and the four production wells is equal (Figure 1).

The Shizhuang Block is located in the south of Qinshui Basin (Figure 2). The target layer is the no. 3 coal seam. Previous studies have shown that its burial depth is 500-1300 m, the coal thickness is 4-10 m, and the gas content is 8-28 m^3/t [30, 31]. Based on the above, basic parameters of the basic model are described as follows: the depth of the coal seam is 1000 m, the thickness of the coal seam is 6 m, and the gas content is 24 m^3/t. Thus, the geological reserves of CBM in this area amount to $57.8 \times 10^6\,m^3$; other basic parameters are listed in Table 1.

2.2. Numerical Model. A coal reservoir is the dual porosity system composed of matrix pores and fracture [32]. Matrix pores are the main gas storage area where CBM is present as an adsorption phase, and fracture controls the permeability of coal reservoir [33]. Therefore, the Gliman and Kazemi dual porosity model was adopted, which assumes that the matrix does not consider flow, and the fractures does [34].

In addition, the GEM component model was used to simulate the multicomponent fluid flow state in the process of N_2-ECBM. According to the occurrence conditions of coal reservoir, the assumptions proposed by our predecessors were employed to set some basic settings of simplified operation in the model, namely: (1) there are two-phase flows of water and gas in the coal reservoir [35]. (2) The free gas in coal reservoir is an ideal gas [36]. (3) CBM experiences desorption, diffusion, and seepage processes, in which the desorption process conforms to the Langmuir model, the diffusion process is Fickian, and seepage in fractures conforms to Darcy's law [37, 38].

According to the conservation of mass and continuity equation the balance equation of gas-water two-phase flow in fractured systems can be expressed as

$$\frac{\partial(\varnothing S_w/B_w)_f}{\partial t} = \nabla\bullet\left(\frac{kk_{rw}}{\mu_w B_w}(\nabla p_w - \rho_w g \nabla d\right)_f - q_{fw} + q_{cwmf}, \tag{1}$$

$$\frac{\partial\left(\varnothing S_g/B_g\right)_f}{\partial t} = \nabla\bullet\left(\frac{kk_{rg}}{\mu_g B_g}\left(\nabla p_g - \rho_g g \nabla d\right)_f - q_{fg} + q_{cgmf}.\right. \tag{2}$$

The equilibrium equation of gas-water two-phase flow in the matrix system can be expressed as

$$\frac{\partial(\varnothing \rho_w S_w/B_w)_m}{\partial t} = -q_{cwmf}, \tag{3}$$

$$\frac{\partial\left(\varnothing \rho_g S_g/B_g\right)_m}{\partial t} = -q_{cgmf} + q_{md}, \tag{4}$$

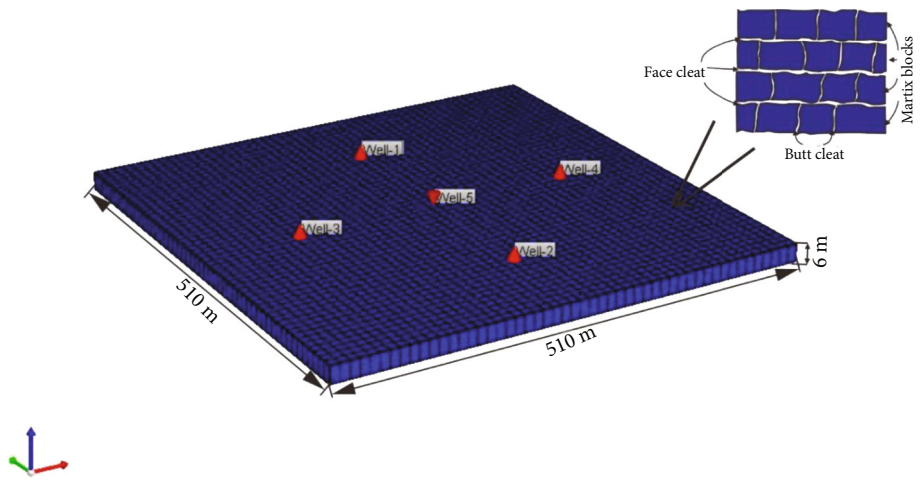

Figure 1: Geological model of coal reservoir in this study.

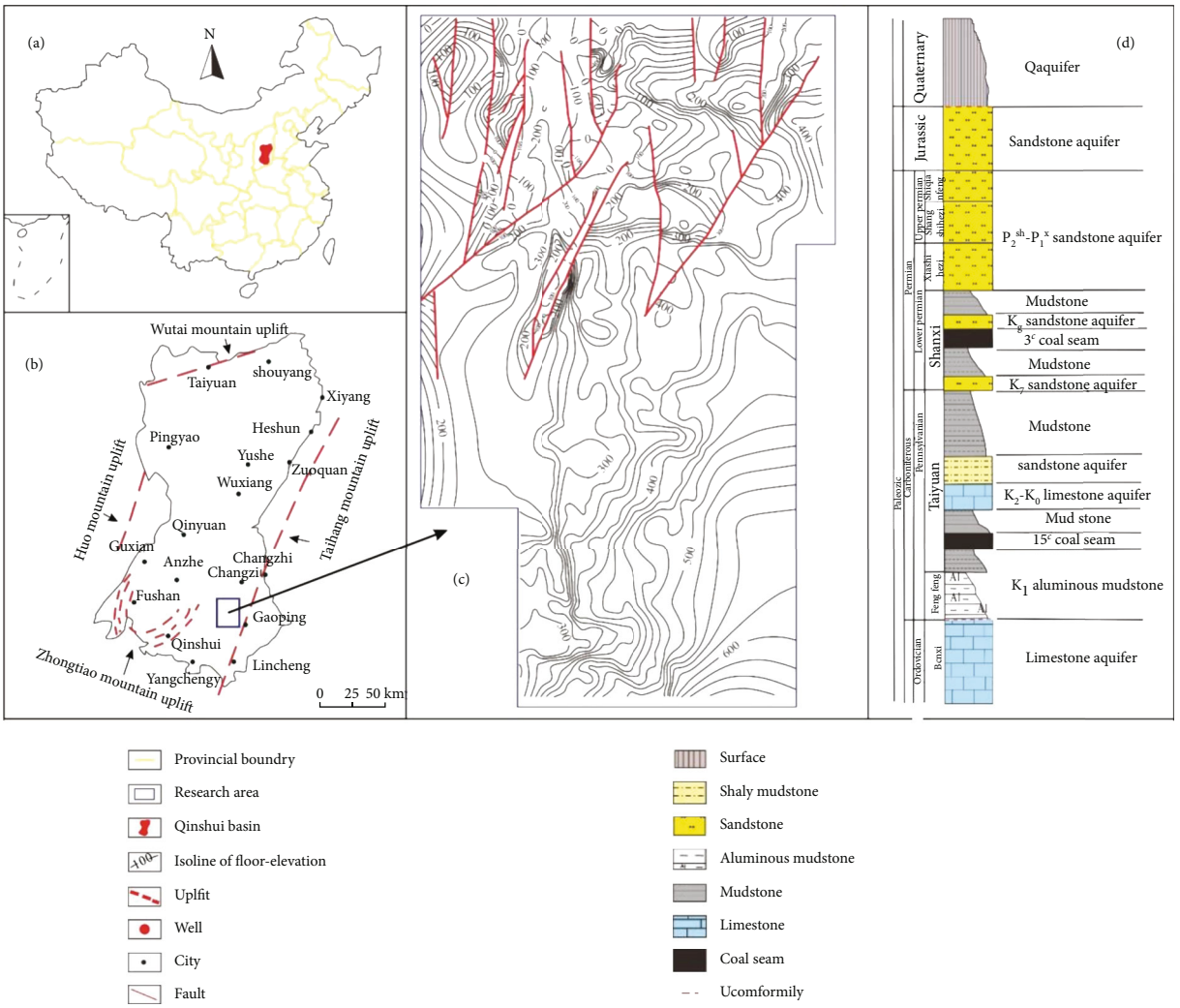

Figure 2: Locations of the study area and wells. (a) Location of the study area in China. (b) Location of the Shizhuang Block in the southern Qinshui Basin. (c) Topography of the study area. (d) Stratigraphic column of the coal-bearing strata [31].

Table 1: Basic parameters used in the numerical simulation.

Parameter	Value	Unit	Remark	Parameter	Value	Unit	Remark
Gas content	24	m^3/t	Measurement	Reservoir temperature	25	°C	Well testing
Reservoir pressure	10	MPa	Well testing	Water viscosity	0.7	Cp	Empirical value
Buried depth of coal	1000	m	Measurement	Density of coal	1435	kg/m^3	Experiment
Coal seam thickness	6	m	Average value	Compressibility of coal	2×10^{-5}	MPa^{-1}	Empirical value
Langmuir volume of CH_4	34.24	m^3/t	Experiment	Matrix porosity	6	%	Experiment
Langmuir volume of N_2	21.72	m^3/t	Experiment	Fracture porosity	1	%	Empirical value
Langmuir pressure of CH_4	3500	kPa	Experiment	Matrix permeability	0.01	mD	Experiment
Langmuir pressure of N_2	3520	kPa	Experiment	Fracture permeability	1.0	mD	Well testing
Diffusion coefficient of CH_4	4×10^{-6}	cm^2/s	Empirical value	Matrix water saturation	1	%	Empirical value
Diffusion coefficient of N_2	1.5×10^{-6}	cm^2/s	Empirical value	Fracture water saturation	99	%	Empirical value

$$q_{md} = -\rho_{ga}\rho_c \frac{dV}{dt}, \tag{5}$$

where ϕ represents the porosity, ρ_w is the density of water, ρ_g is the density of gas, S_w is the saturation of water, S_g is the saturation of gas, μ_w is kinematic viscosity of water, μ_g is kinematic viscosity of gas, g is gravity acceleration, d is the coal burial depth, q_w is the production of water, q_g is the production of gas, q_{cwmf} is the water exchange capacity between the matrix and fracture, q_{cgmf} is the gas exchange capacity between the matrix and fracture, B_w is the water volume factor, B_g is the gas formation volume factor, ρ_{ga} is the gas density at standard conditions, ρ_c is the coal density, V is the average residual gas content in coal matrix, and subscripts f and m denote fracture and matrix.

Based on the studies of Redlich and Kwong [39] and Soave [40], the equations of state for gases are

$$P = \frac{RT}{V-b} - \frac{a(T)}{V(V+b)}, \tag{6}$$

$$a(T) = 0.42748\frac{RT_c^2}{P_c}\left[1 + m\left(1 - \left(\frac{T}{T_c}\right)^{0.5}\right)\right]^2, \tag{7}$$

$$b = 0.086640\frac{RT_c}{P_c}, \tag{8}$$

$$m = 0.48508 + 1.55171\omega - 0.15613\omega^2, \tag{9}$$

where R denotes the universal gas constant of 8.314 J/(mol •K), T_c is the critical temperature in K, P_c is the critical pressure in Pa, and ω is the acentric factor.

Binary mixed gas migrates in coal reservoir in the process of N_2 displacement [36]. Here, the subscript 1 and the subscript 2 represent CBM and injected nitrogen, respectively. The gas in coal reservoir is stored in adsorbed state and free state, and the content of adsorbed component can be expressed by the generalized Langmuir equation [41]:

$$C_1 = \frac{V_{L1}p_1b_1}{1 + p_1b_1 + p_2b_2}, \tag{10}$$

$$C_2 = \frac{V_{L2}p_2b_2}{1 + p_1b_1 + p_2b_2}, \tag{11}$$

where C is adsorption gas volume, V_L denotes the Langmuir volume constant, p represents gas pressure in matrix, and b is the Langmuir constant for gas component 1 and 2 which is equal to the reciprocal of the Langmuir volume, V_L.

Palmer and Mansoori [42] established a model to predict the change in coal permeability caused by coal shrinkage, which is applicable to the mixed gas adsorption/desorption equation:

$$\frac{\phi}{\phi_0} = 1 + c_f(p - p_0) + \frac{1}{\phi_0}\left(\frac{K}{M} - 1\right)\left(\frac{\varepsilon_{L1}p(y_1/p_{L1}) + \varepsilon_{L2}p(y_2/p_{L2})}{1 + p((y_1/p_{L1}) + (y_2/p_{L2}))} - \frac{\varepsilon_{L1}p_0(y_{0,1}/p_{L1}) + \varepsilon_{L2}p_0(y_{0,2}/p_{L2})}{1 + p_0((y_{0,1}/p_{L1}) + (y_{0,2}/p_{L2}))}\right), \tag{12}$$

where ϕ represents the porosity, subscript 0 is the initial conditions, p_L is the Langmuir pressure, ε_L is the strains at infinite pressure, subscripts 1 and 2 denote CBM and injected nitrogen, c_f represents the fracture pore volume compressibility, M represents the constrained axial modulus, K is the bulk modulus, p is the pressure, $y_{0,1}$ and $y_{0,2}$ stand for the composition of components 1 and 2 at the initial or reference conditions, and y_1 and y_2 refer to the composition of components 1 and 2 with pressure p.

2.3. Simulation Scheme. Previous studies have shown that the factors affecting the production increase of N_2 injection

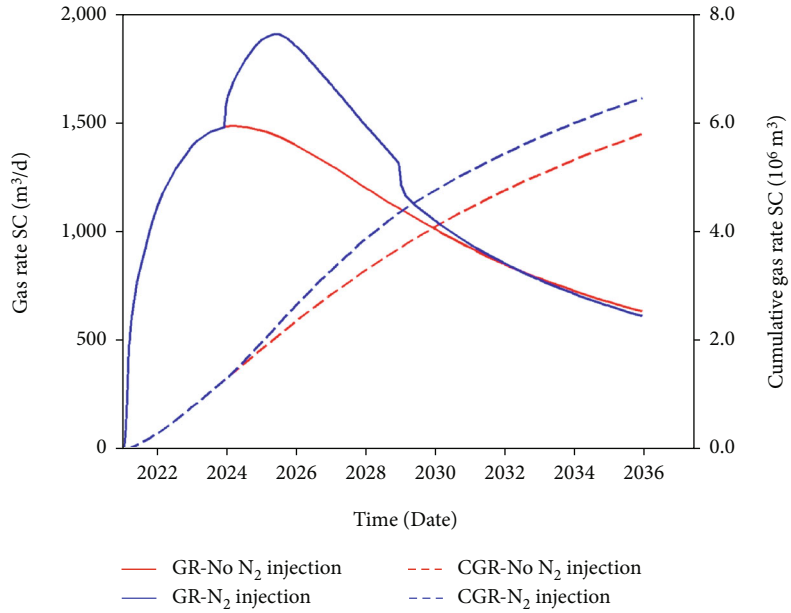

Figure 3: CBM production curves of N_2 injection displacement and no N_2 injection displacement in Well-1. GR denotes daily gas production, and CGR represents cumulative gas production. SC denotes surface condition.

in coal reservoirs are mainly limited by the spacing between production wells and injection wells, the timing of N_2 injection, the duration of gas injection, the rate of gas injection, and the bottom hole pressure of gas injection [13]. Therefore, the productivity of coal reservoir under different nitrogen injection production parameters was simulated based on the above factors.

According to the geological conditions of the Shizhuang Block, the basic nitrogen injection parameters were set as follows: the production injection well spacing is 150 m, the injection timing is the third year after gas production, the gas injection duration is 5 years, the gas injection rate is 4000 m^3/d, and the bottom-hole injection pressure is 10 MPa. Compared with these, the influences of various nitrogen injection production parameters on CBM Recovery were analyzed to optimize the N_2-ECBM production scheme.

To select the optimal parameters of N_2 injection for increasing production, the coefficient of production increasing rate (I) was established, and the increasing production effect of CBM under the influences of different factors was expounded, which provides a favorable basis for optimizing productivity.

$$I = \frac{C_i - C_0}{C_i}, \tag{13}$$

where C_i represents the total cumulative gas rate of parameter i, and C_0 is the total cumulative gas rate of coal reservoir without N_2 injection. The larger the value of I, the greater the effect of N_2 injection on increased production, the higher the recovery.

The value of I can characterize the stimulation effect of N_2 injection in coal reservoir, however, the economic benefit of coal reservoir should be considered, that is, the total amount of nitrogen needed to be consumed. Therefore, the establishment of the coefficient replacement ratio (R) reflects the volume of methane that can be replaced by 1 m^3 of N_2, to study N_2 injection into coal reservoir and consider the ensuing economic benefits.

$$R = \frac{C_i - C_0}{N_i}, \tag{14}$$

where N_i represents the total amount of N_2 injection with parameter i. The larger the value of R, the better the displacement effect of CH_4 by N_2, and the higher the economic benefit.

3. Results

First, the real productivity of coal reservoir without N_2 displacement was simulated, and then the productivity of coal reservoir with basic N_2 injection parameters was taken as the control group for simulation, to provide the basis for analyzing different N_2 injection conditions when aiming to enhance CBM recovery. Based on the application of the above reservoir parameters and nitrogen injection production parameters, the bottom-hole injection pressure was controlled by the pressure drop rate of 0.1 MPa/d. When the bottom-hole injection pressure dropped to 0.2 MPa, the bottom-hole injection pressure was kept unchanged and CBM production continues [43]. The model simulated the production capacity of four production wells in 15 years, and the gas-production time ranged from 2021 to 2036. Since the parameters of the four production wells were the same, Well-1 was taken as an example (Figure 3).

When the coal reservoir was not stimulated by N_2 injection, the cumulative gas flow per single well in 15 years was 5.79×10^6 m^3, the peak gas rate was 1486.8 m^3/d, and the

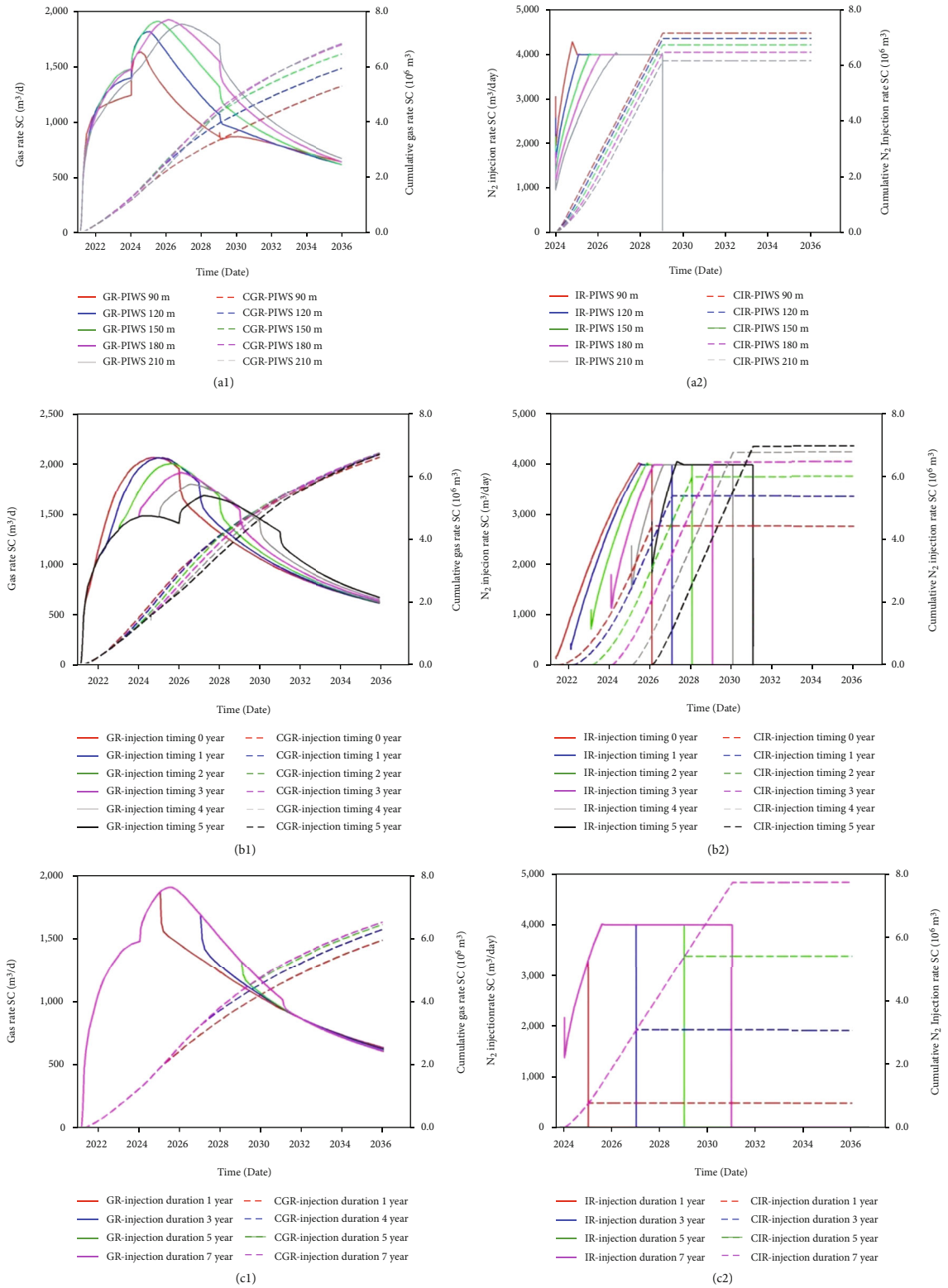

Figure 4: CBM production curves and N_2 injection curves under different N_2 injection production conditions: (a, c, and e) are CBM production curves of production injection well spacing, gas injection timing, and gas injection duration, respectively; (b, d, and f) are the N_2 injection curves of production injection well spacing, gas injection timing, and gas injection duration, respectively. PIWS stands for production injection well spacing, GR denotes daily gas production, CGR represents cumulative gas production, IR denotes daily gas injection, and CIR denotes cumulative gas injection. SC refers to surface condition.

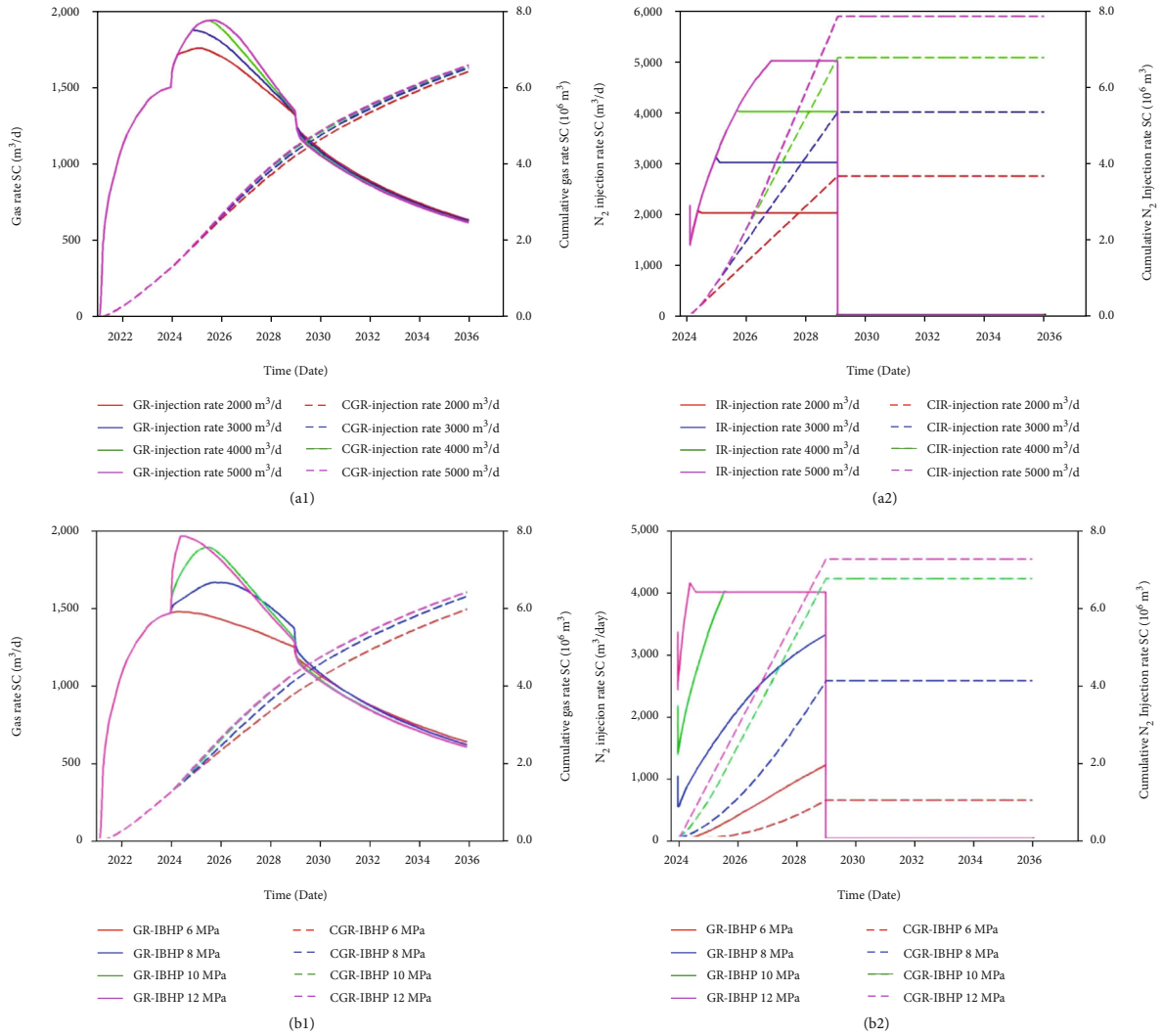

Figure 5: CBM production curves and N_2 injection curves under different N_2 injection production conditions: (a and c) are CBM production curves of gas injection rate and the bottom-hole injection pressure, respectively; (b and d) are N_2 injection curves of gas injection rate and the bottom-hole injection pressure, respectively. IBHP denotes the bottom-hole injection pressure, GR refers to daily gas production, CGR denotes cumulative gas production, IR represents daily gas injection, and CIR denotes cumulative gas injection. SC denotes surface condition.

average gas production amounted to 1057.65 m^3/d. The cumulative gas rate of the four wells was 23.18×10^6 m^3, and the recovery factor was 40.08%. When the control group was subject to N_2 injection displacement production, the cumulative gas flow from a single well in 15 years increased to 6.46×10^6 m^3, the peak gas rate was 1909.43 m^3/d, and the average gas rate was 1178.61 m^3/d. The cumulative gas rate of the four wells was 25.83×10^6 m^3, the value of I was 10.26%, the value of R was 0.39, the recovery factor was 44.68%, the cumulative gas rate net increase was 2.65×10^6 m^3, and the recovery factor was increased by 3.88%.

3.1. Production Injection Well Spacing. The simulation conditions are the same as the other parameters. On this basis, the productivity of production wells and N_2 injection wells with a spacing of 90 m, 120 m, 150 m, 180 m, and 210 m could be simulated, respectively. The simulation results indicated that the longer the interval between production wells and injection wells, the longer the time to reach the peak gas rate. When the production injection well spacing was greater than 180 m to 210 m, the peak gas rate tended to decrease from 1922.42 m^3/d to 1884.44 m^3/d. The increase in cumulative gas rate was also small. The total cumulative gas rate of four wells was only increased by 19.08×10^6 m^3 (Figure 4(a)). Meanwhile, the smaller the production injection well spacing, the shorter the time for N_2 to reach the maximum N_2 injection rate, but the higher the total amount of N_2 injection (Figure 4(b)). The CBM recovery factor was then 36.62%, 41.03%, 44.68%, 46.98%, and 47.31% according to the respective well spacing.

3.2. Gas Injection Timing. To analyze the influences of different injection timings on N_2-ECBM, the N_2 injection productivity of injection wells in 0, 1, 2, 3, 4, and 5 years after gas

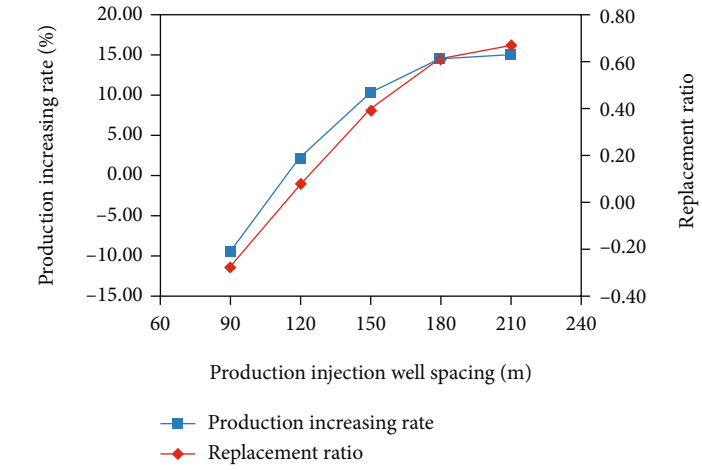

(a)

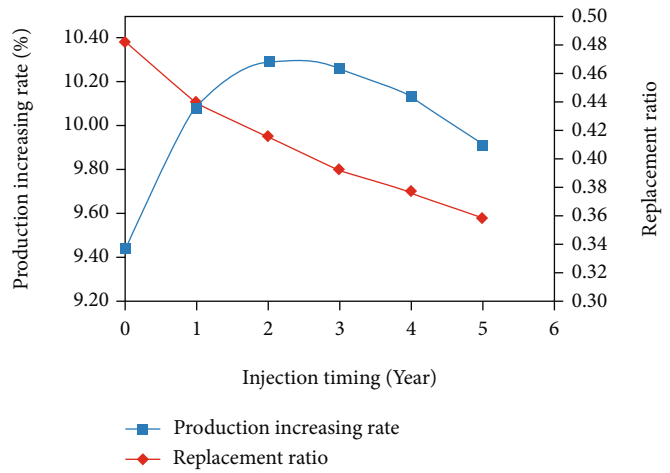

(b)

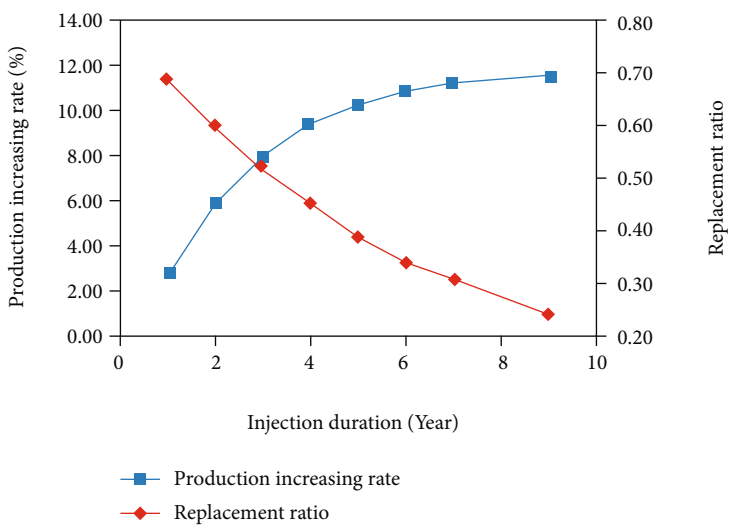

(c)

Figure 6: Continued.

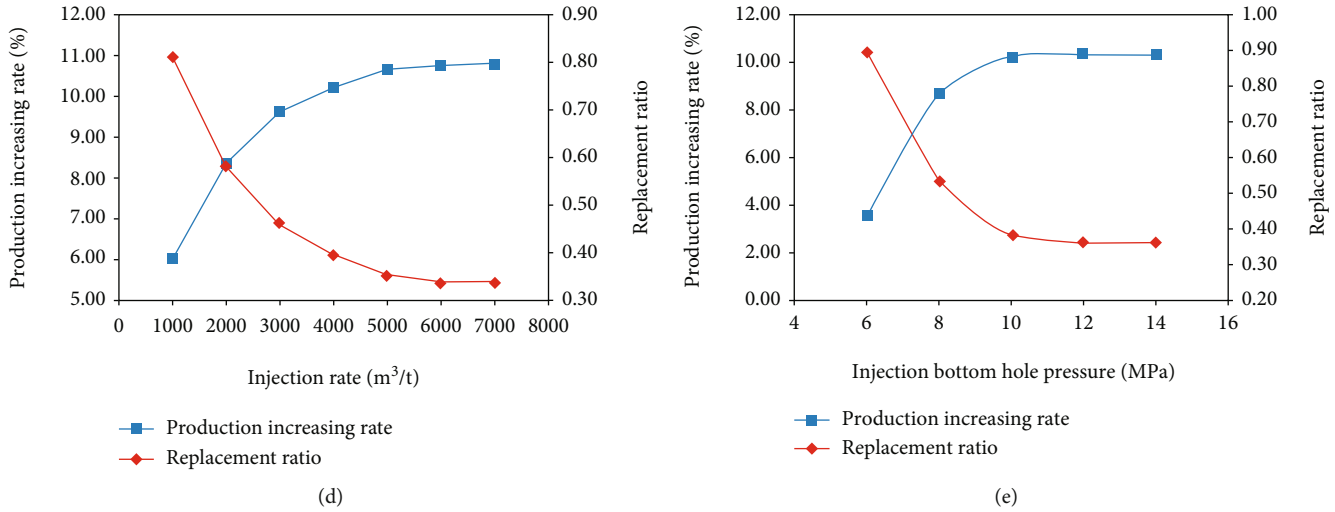

FIGURE 6: (a–e), respectively, describe the production increasing rate and replacement ratio of production injection well spacing, gas injection timing, gas injection duration, gas injection rate, and the bottom-hole injection pressure.

production was simulated, respectively. According to the simulation results (Figures 4(c) and 4(d)), when the gas injection timing was one year after gas production, the gas rate peak value was the largest, reaching 2003.92 m^3/d, but, in general, the influence of gas injection timing on cumulative gas rate was small. Meanwhile, the total amount of N_2 injection was 501.46×10^6 m^3, 591.35×10^6 m^3, 640.5×10^6 m^3, 675.48×10^6 m^3, 692.26×10^6 m^3, and 711.02×10^6 m^3, which increased with the delay of injection timing. The recovery factors of CBM were 44.28%, 44.59%, 44.70%, 44.68%, 44.61%, and 44.51%, respectively. The trend was that the recovery factor first increased, then decreased, reaching a maximum in the second year.

3.3. Gas Injection Duration. The productivity of injection wells with an N_2 injection duration of 1 year, 3 years, 5 years, and 7 years was simulated, respectively. According to the simulation results (Figures 4(e) and 4(f)), when the injection duration exceeded 3 years, the gas rate peak value increased to 1909.43 m^3/d and then did not increase. With the increase of the injection duration, the cumulative gas rate increased, but the growth rate decreased. The total cumulative gas rates of the four wells were 2383.84×10^6 m^3, 2516.92×10^6 m^3, 2582.56×10^6 m^3, and 2611.36×10^6 m^3, and the total amount of N_2 injection also increased. The recovery factors of CBM were 41.24%, 43.55%, 44.685%, and 45.18%, respectively.

3.4. Gas Injection Rate. The simulation conditions were set to match the other parameters. On this basis, the productivity of injection wells with N_2 injection rates of 2000 m^3/d, 3000 m^3/d, 4000 m^3/d, and 5000 m^3/d could be simulated. According to the simulation results (Figures 5(a) and 5(b)), the effect of injection rate on cumulative gas rate was relatively small, and the peak gas rate was 1729.56 m^3/d, 1843.24 m^3/d, 1909.43 m^3/d, and 1909.89 m^3/d, respectively. The total amount of nitrogen injection was 364.07×10^6 m^3, 532.66×10^6 m^3, 675.48×10^6 m^3, and 784.05×10^6 m^3, which increased with the increase in N_2 injection rate but also decreased in the later period. The recovery factors of CBM were 43.76%, 44.36%, 44.68%, and 44.89%, respectively.

3.5. The Bottom-Hole Injection Pressure. The bottom-hole injection pressure could push the injected gas into the pore and fracture space of coal reservoir, compete with methane for adsorption, reduce the partial pressure of CBM, and then promote methane desorption. To study the influence of the bottom-hole injection pressure on N_2-ECBM, the productivity of 6 MPa, 8 MPa, 10 MPa, and 12 MPa injection pressure was simulated by increasing the injection pressure of 2 MPa. Through comprehensive analysis of the gas rate (Figures 5(c) and 5(d)), the higher the bottom-hole injection pressure, the larger the peak gas production, the maximum value was 1976.9 m^3/d, and the shorter the time to reach the gas rate peak value. At the same time, the cumulative gas rate and the total amount of N_2 injection were larger, but the increase was smaller, which indicated that higher injection pressure was not an ideal parameter for optimization of the technique. The CBM recovery factors were then 41.65%, 43.92%, 44.68%, and 44.72%, respectively.

4. Discussion

The results show that the production parameters of N_2 injection, such as production injection well spacing, gas injection timing, gas injection duration, gas injection rate, and the bottom-hole injection pressure, have a significant impact on N_2-ECBM. Therefore, it is necessary to use the values of I and R to analyze the stimulation and economic applicability of various control factors for N_2 injection in a coal reservoir in more depth.

4.1. Production Injection Well Spacing. Both N_2 injection and CBM drainage were realized by reducing the pressure of coal reservoir through drainage. When the well spacing was less

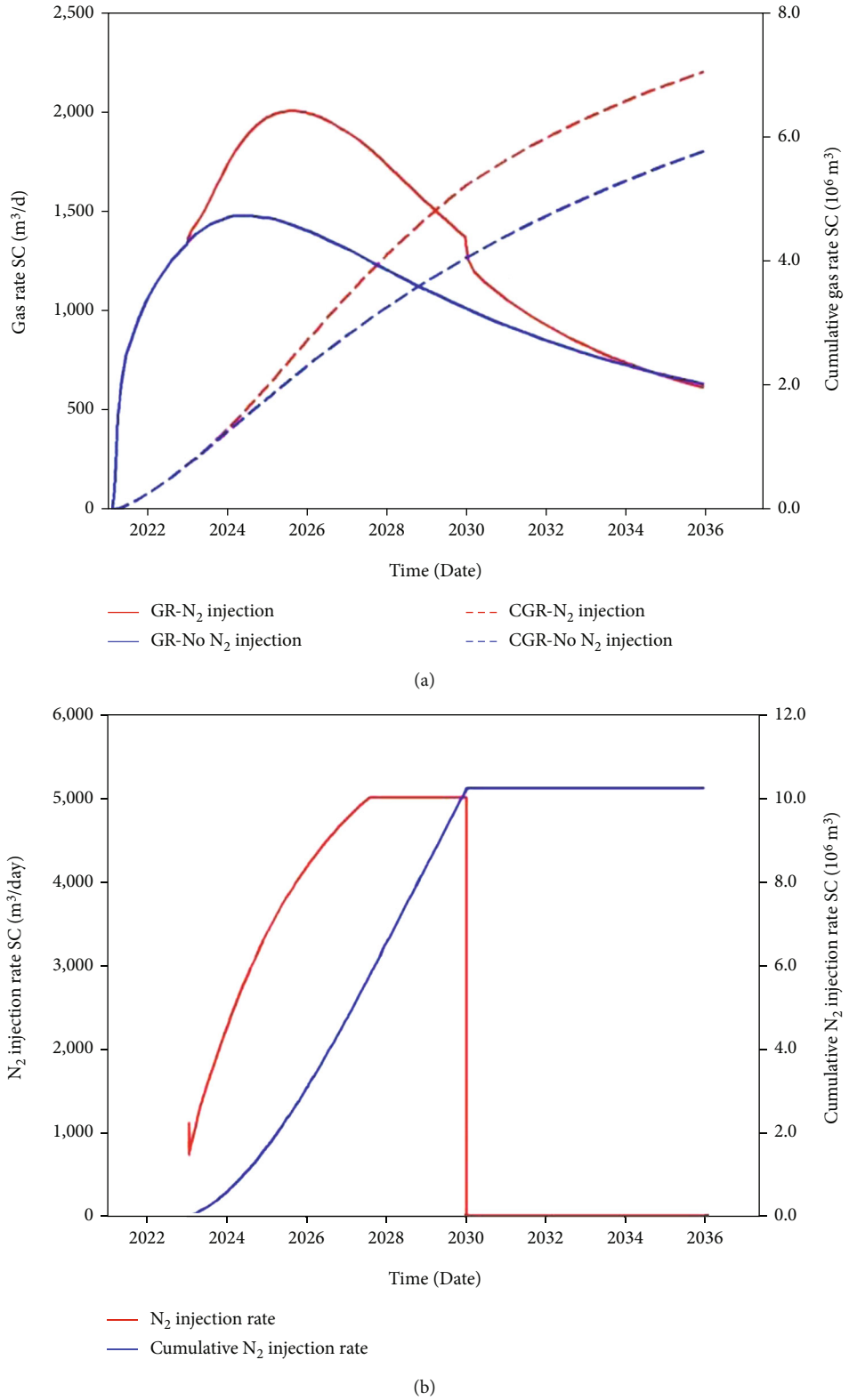

Figure 7: The CBM production curves and N_2 injection curves of N_2 injection optimized displacement and no N_2 injection displacement. GR denotes daily gas production, and CGR denotes cumulative gas production. SC denotes surface condition.

than the radius of influence of each well, the depression funnels formed in the drainage process of production wells would overlap, resulting in inter-well interference, which would increase the corresponding development cost and worsen the economic effect. However, if the well spacing was too large, the drainage and depressurization effect would be affected, and the N_2 injectability would be reduced [44]. Therefore, choosing the right spacing between production

wells and injection wells was conducive to obtaining the best N_2-ECBM effect. Based on numerical simulations of productivity, the production increasing rate I and the replacement ratio R of different production injection well spacings were calculated (Figure 6(a)), and the production increase and replacement efficiency under five spacings were revealed. The results indicate that I and R increased with the increase of production injection well spacing, which indicated that the increase of well spacing was beneficial to the increase of production and economy of coalfield. However, when the well spacing exceeded 180 m, I tended to remain unchanged and R increased greatly. Considering the boundary problem of geological model, the optimal production injection well spacing should be 180 m.

4.2. Gas Injection Timing. By changing the timing of gas injection, its influences on the production increasing rate of coal reservoir N_2 injection and its economics could be studied (Figure 6(b)). The results show that the later the gas injection timing was, the smaller the R was, and the less economical it was, but I first increased, then decreased, reaching its peak in the second year after gas production. It showed that the best time for gas injection was the second year after gas production, but the economic benefit was general. Considering that the main benefit of coal field was the increase of production, the best time of gas injection was the second year after gas production.

4.3. Gas Injection Duration. Through the numerical simulation of the production capacity under different injection durations, the control of the injection duration on the production increasing of N_2 injection and the economy of the total amount of N_2 injection were obtained. The results (Figure 6(c)) showed that, with the increase of injection duration, I increased and R decreased, indicating with the increase of N_2 injection amount, the production increasing rate of coal reservoir increased, but the efficiency of use of N_2 decreased, and the amount of waste increased. Moreover, the longer the gas injection duration, the rate of production increase tended to be flat. Considered comprehensively, the production capacity with a gas injection duration of 7 years should be selected.

4.4. Gas Injection Rate. By changing the gas injection rate, the productivity simulation results (Figure 6(d)) imply that when the injection rate was less than 4000 m^3/d, with the increase of the injection rate, I increased rapidly, R decreased sharply, and finally tended to slow down. The finding showed that increasing the gas injection rate was beneficial to the increase of coalfield production, but it would reduce the rate of utilization of N_2 and weaken the economic effect of coalfield production. Considered comprehensively, a rate of injection of 5000 m^3/d was optimal.

4.5. The Bottom-Hole Injection Pressure. By changing the bottom-hole injection pressure, the increases in production benefit and economic benefit of N_2 injection in the coal field were analyzed. The results (Figure 6(e)) show that the influences of the bottom-hole injection pressure, injection rate, and injection timing on N_2 injection in coalfield had a similar trend. With the increase of the bottom-hole injection pressure, I increased and R decreased, and when the pressure exceeded 10 MPa, the rate of production increase and replacement ratio tended to be constant. On the one hand, the higher N_2 injection pressure in the fracture would increase the N_2 diffusion from the fracture system to the coal matrix system and lead to the earlier breakthrough of N_2, which would increase the industrial cost of N_2 and CH_4 separation in the N_2-ECBM process. On the other hand, if the N_2 injection pressure was too low, it was not conducive to gas injection and migration. Considered comprehensively, it was more appropriate to choose a bottom-hole injection pressure of 10 MPa.

4.6. Scheme Optimization. As mentioned above, the injection of N_2 reduced the partial pressure and concentration of methane in the fracture system, caused desorption of methane on the coal surface and contraction of the coal matrix [45, 46], promoted the exploitation of methane, and improved the recovery of CBM. Therefore, according to the above summary, the production parameters of N_2 injection optimization scheme were designed as follows: the production injection well spacing was 180 m, the injection timing was two years after gas production, the injection duration was 7 years, the injection rate was 5000 m^3/d, and the bottom-hole injection pressure was 10 MPa. The simulation results are shown in Figure 7.

Figure 7 demonstrates that, compared with the case of no nitrogen displacement production, the average gas rate, daily gas peak value, and cumulative gas rate increased significantly when nitrogen injection displacement production was implemented under the proposed scheme. The cumulative gas rate per single well in 15 years was 7.07×10^6 m^3, increasing by 22.1%, the peak gas rate was 2011.44 m^3/d, increasing by 35.3%, and the average gas rate was 1291.27 m^3/d, increasing by 9.6%. The cumulative gas rate of the four production wells was 28.29×10^6 m^3, I was 18.34%, R was 0.5, and recovery factor was 48.95%. Compared with the case with no displacement, the cumulative gas rate net was increased by 5.11×10^6 m^3, and the recovery factor was increased by 8.88%. The simulation results were well verified in the physical experiment [47].

5. Conclusion

In this study, an N_2-ECBM numerical model was established to study the effects of various N_2 injection parameters on the production of CBM, and the values of I and of R were established to optimize the N_2 injection parameters. The following conclusions were drawn:

(1) The stimulation effect of N_2 displacement is related to the production injection well spacing, injection timing, injection duration, injection rate, and the bottom-hole injection pressure. Among them, the production injection well spacing has the greatest influence on methane cumulative gas rate, followed by injection duration and the bottom-hole injection

pressure, while injection timing and injection rate have relatively little effect

(2) In the process of displacement, N_2 injection can significantly improve the gas production of CBM. The gas production of production wells increases rapidly in the early stage, reaches its peak value, and then decreases. At the end of N_2 injection, the gas rate decreases greatly and then decreases steadily in the later stage

(3) With the increase of the production injection well spacing, the production increasing rate and nitrogen replacement ratio of coal reservoir increase. However, with a delay to the timing of the gas injection, the replacement ratio of nitrogen injection in a coal reservoir decreases, and the rate of production first increases and then decreases. Injection duration, injection rate, and the bottom-hole injection pressure have similar controlling effects on N_2-ECBM, manifest as an increased rate of production and a decrease in the nitrogen replacement ratio

(4) The best nitrogen injection scheme is as follows: the production injection well spacing should be 180 m, the injection should occur in the second year after gas production, the injection duration should be 7 years, the injection rate should be 5000 m^3/d, and the bottom-hole injection pressure should be 10 MPa. Under these conditions, the cumulative gas rate of four production wells is 28.29×10^6 m^3, which is 5.11×10^6 m^3 greater than that without nitrogen displacement, the recovery rate is 48.96%, and the net increase therein is 8.88%.

Data Availability

The data used to support the findings of this study are included within the article.

Conflicts of Interest

The authors declare no conflicts of interest.

Acknowledgments

This study was supported by the National Science and Technology Major Project of China (no. 2016ZX05066001–002) and the National Science and Technology Major Project of China (no. 2017ZX05064–003–001). We thank China United Coalbed Methane Co. Ltd. for providing details of the geological conditions in the study area and our colleagues for their beneficial suggestions.

References

[1] L. H. Xu and C. L. Jiang, "Initial desorption characterization of methane and carbon dioxide in coal and its influence on coal and gas outburst risk," *Fuel*, vol. 203, pp. 700–706, 2017.

[2] Y. Qin, T. A. Moore, J. Shen, Z. Yang, Y. Shen, and G. Wang, "Resources and geology of coalbed methane in China: a review," *International Geology Review*, vol. 60, no. 5-6, pp. 777–812, 2018.

[3] C. Ö. Karacan, F. A. Ruiz, M. Cotè, and S. Phipps, "Coal mine methane: a review of capture and utilization practices with benefits to mining safety and to greenhouse gas reduction," *International Journal of Coal Geology*, vol. 86, no. 2-3, pp. 121–156, 2011.

[4] F. H. An, Y. P. Cheng, L. Wang, and W. Li, "A numerical model for outburst including the effect of adsorbed gas on coal deformation and mechanical properties," *Computers and Geotechnics*, vol. 54, no. 10, pp. 222–231, 2013.

[5] T. A. Moore, "Coalbed methane: a review," *International Journal of Coal Geology*, vol. 101, no. 11, pp. 36–81, 2012.

[6] J. Chengzao, M. Zheng, and Y. Zhang, "Unconventional hydrocarbon resources in China and the prospect of exploration and development," *Petroleum Exploration and Development*, vol. 39, no. 2, pp. 139–146, 2012.

[7] A. Busch and Y. Gensterblum, "CBM and CO_2-ECBM related sorption processes in coal: a review," *International Journal of Coal Geology*, vol. 87, no. 2, pp. 49–71, 2011.

[8] M. Sayyafzadeh, A. Keshavarz, A. R. M. Alias, K. A. Dong, and M. Manser, "Investigation of varying-composition gas injection for coalbed methane recovery enhancement: a simulation-based study," *Journal of Natural Gas Science and Engineering*, vol. 27, no. 11, pp. 1205–1212, 2015.

[9] Y. Li, S. Pan, S. Ning, L. Shao, Z. Jing, and Z. Wang, "Coal measure metallogeny: metallogenic system and implication for resource and environment," *Science China Earth Sciences*, vol. 65, no. 7, pp. 1211–1228, 2022.

[10] X. Cui, R. M. Bustin, and G. Dipple, "Selective transport of CO_2, CH_4, and N_2 in coals: insights from modeling of experimental gas adsorption data," *Fuel*, vol. 83, no. 3, pp. 293–303, 2004.

[11] Q. H. Niu, Q. H. Wang, W. Wang et al., "Responses of multiscale microstructures, physical-mechanical and hydraulic characteristics of roof rocks caused by the supercritical CO_2-water-rock reaction," *Energy*, vol. 238, article 121727, 2022.

[12] K. Baris, C. Keles, N. Ripepi, K. Luxbacher, S. Gurpinar, and M. Karmis, "The first commercial coal bed methane project in Turkey-reservoir simulation and prefeasibility study for the Amasra coalfield," *International Journal of Oil Gas and Coal*, vol. 13, no. 2, pp. 170–199, 2016.

[13] F. D. Zhou, W. W. Hou, G. Allinson, J. Wu, J. Wang, and Y. Cinar, "A feasibility study of ECBM recovery and CO_2 storage for a producing CBM field in southeast Qinshui Basin, China," *International Journal of Greenhouse Gas Control*, vol. 19, no. 11, pp. 26–40, 2013.

[14] C. J. Fan, L. Yang, G. Wang, Q. Huang, X. Fu, and H. Wen, "Investigation on coal skeleton deformation in CO_2 injection enhanced CH_4 drainage from underground coal seam," *Frontiers in Earth Science*, vol. 9, pp. 1–11, 2021.

[15] J. Lin, T. Ren, G. D. Wang, and J. Nemcik, "Simulation investigation of N_2-injection enhanced gas drainage: model development and identification of critical parameters," *Journal of Natural Gas Science and Engineering*, vol. 55, no. 6, pp. 30–41, 2018.

[16] S. Durucan and J. Q. Shi, "Improving the CO_2 well injectivity and enhanced coalbed methane production performance in coal seams," *International Journal of Coal Geology*, vol. 77, no. 1-2, pp. 214–221, 2009.

[17] K. Jessen, G. Q. Tang, and A. R. Kovscek, "Laboratory and simulation investigation of enhanced coalbed methane recovery

by gas injection," *Transport in Porous Media*, vol. 73, no. 2, pp. 141–159, 2008.

[18] R. Packham, L. Connell, Y. Cinar, and R. Moreby, "Observations from an enhanced gas recovery field trial for coal mine gas management," *International Journal of Coal Geology*, vol. 100, no. 10, pp. 82–92, 2012.

[19] H. Seomoon, M. Lee, and W. Sung, "Analysis of methane recovery through CO2–N2mixed gas injection considering gas diffusion phenomenon in coal seam," *Energy Exploration & Exploitation*, vol. 34, no. 5, pp. 661–675, 2016.

[20] H. C. Wang, X. H. Fu, K. Jian, T. Li, and P. Luo, "Changes in coal pore structure and permeability during N_2 injection," *Journal of Natural Gas Science and Engineering*, vol. 27, no. 11, pp. 1234–1241, 2015.

[21] J. Lin, T. Ren, Y. P. Cheng, J. Nemcik, and G. Wang, "Cyclic N_2 injection for enhanced coal seam gas recovery: a laboratory study," *Energy*, vol. 188, no. 12, article 116115, 2019.

[22] Z. L. Fan, G. W. Fan, D. S. Zhang et al., "Optimal injection timing and gas mixture proportion for enhancing coalbed methane recovery," *Energy*, vol. 222, no. 5, article 119880, 2021.

[23] L. G. Wang, Z. F. Wang, K. Z. Li, and H. Chen, "Comparison of enhanced coalbed methane recovery by pure N_2 and CO_2 injection: experimental observations and numerical simulation," *Journal of Natural Gas Science and Engineering*, vol. 23, no. 5, pp. 363–372, 2015.

[24] L. Zhou, X. Zhou, C. Fan, and G. Bai, "Coal permeability evolution triggered by variable injection parameters during gas mixture enhanced methane recovery," *Energy*, vol. 252, article 124065, 2022.

[25] S. H. Zhao, Y. Li, Y. B. Wang, Z. Ma, and X. Huang, "Quantitative study on coal and shale pore structure and surface roughness based on atomic force microscopy and image processing," *Fuel*, vol. 244, no. 5, pp. 78–90, 2019.

[26] Y. Li, C. Zhang, D. Z. Tang et al., "Coal pore size distributions controlled by the coalification process: an experimental study of coals from the Junggar, Ordos and Qinshui basins in China," *Fuel*, vol. 206, no. 10, pp. 352–363, 2017.

[27] X. M. Ni, C. Yang, Y. B. Wang, and Z. Li, "Prediction of spatial distribution of coal seam permeability based on key interpolation points: a case study from the southern Shizhuang area of the Qinshui Basin," *Natural Resources Research*, vol. 30, no. 2, pp. 1547–1559, 2021.

[28] C. Li-wei, Y. Tian-hong, Y. Hong-min, and W. Li-guo, "Time characteristics of the influence radius by injecting N_2 to displace coalbed methane: a case study," *Geofluids*, vol. 2019, Article ID 4176535, 11 pages, 2019.

[29] J. Lin, T. Ren, G. D. Wang, P. Booth, and J. Nemcik, "Experimental investigation of N_2 injection to enhance gas drainage in CO_2-rich low permeable seam," *Fuel*, vol. 215, no. 3, pp. 665–674, 2018.

[30] X. B. Su, X. Y. Lin, M. J. Zhao, Y. Song, and S. Liu, "The upper Paleozoic coalbed methane system in the Qinshui Basin, China," *AAPG Bulletin*, vol. 89, no. 1, pp. 81–100, 2005.

[31] D. Liu, Y. B. Wang, X. M. Ni et al., "Classification of coal structure combinations and their influence on hydraulic fracturing: a case study from the Qinshui Basin, China," *Energies*, vol. 13, no. 17, p. 4559, 2020.

[32] C. R. Clarkson and R. M. Bustin, "The effect of pore structure and gas pressure upon the transport properties of coal: a laboratory and modeling study. 1. Isotherms and pore volume distributions," *Fuel*, vol. 78, no. 11, pp. 1333–1344, 1999.

[33] X. D. Gao, Y. B. Wang, X. Wu, Y. Li, X. M. Ni, and S. H. Zhao, "Nanoscale pore structure characteristics of deep coalbed methane reservoirs and its influence on CH4Adsorption in the Linxing area, eastern Ordos Basin, China," *Journal of Nanoscience and Nanotechnology*, vol. 21, no. 1, pp. 43–56, 2021.

[34] Z. J. Pan and L. D. Connell, "Modelling permeability for coal reservoirs: a review of analytical models and testing data," *International Journal of Coal Geology*, vol. 92, no. 3, pp. 1–44, 2012.

[35] X. F. Sun, Y. Y. Zhang, K. Li, and Z. Gai, "A new mathematical simulation model for gas injection enhanced coalbed methane recovery," *Fuel*, vol. 183, no. 11, pp. 478–488, 2016.

[36] C. J. Fan, D. Elsworth, S. Li et al., "Modelling and optimization of enhanced coalbed methane recovery using CO_2/N_2 mixtures," *Fuel*, vol. 253, no. 10, pp. 1114–1129, 2019.

[37] F. Shi, *Study on N_2 Displacement of CBM Well in Luan Mining Area*, Henan Polytechnic University, 2018.

[38] Z. J. Pan and L. D. Connell, "A theoretical model for gas adsorption-induced coal swelling," *International Journal of Coal Geology*, vol. 69, no. 4, pp. 243–252, 2007.

[39] O. Redlich and J. N. S. Kwong, "On the thermodynamics of solutions. V: an equation of state. Fugacities of gaseous solutions," *Chemical Reviews*, vol. 44, no. 1, pp. 233–244, 1949.

[40] G. Soave, "Equilibrium constants from a modified Redlich-Kwong equation of state," *Chemical Engineering Science*, vol. 27, no. 6, pp. 1197–1203, 1972.

[41] F. Zhou, F. Hussain, and Y. Cinar, "Injecting pure N_2 and CO_2 to coal for enhanced coalbed methane: experimental observations and numerical simulation," *International Journal of Coal Geology*, vol. 116-117, no. 9, pp. 53–62, 2013.

[42] I. Palmer and J. Mansoori, "How permeability depends on stress and pore pressure in coalbeds: a new model," *SPE Reservoir Evaluation & Engineering*, vol. 1, no. 6, pp. 539–544, 1998.

[43] S. H. Zhao, Y. B. Wang, Y. Li et al., "Co-production of tight gas and coalbed methane from single wellbore: a simulation study from northeastern Ordos Basin, China," *Natural Resources Research*, vol. 30, no. 2, pp. 1597–1612, 2021.

[44] J. J. Fan, *Research on the Influence Factors of CO_2 Sequestration in Coal Seams and Numerical Simulation of CO_2 Sequestration Process*, China University of Mining & Technology, Beijing, 2018.

[45] X. R. Wei, P. Massarotto, G. Wang, V. Rudolph, and S. D. Golding, "CO_2 sequestration in coals and enhanced coalbed methane recovery: new numerical approach," *Fuel*, vol. 89, no. 5, pp. 1110–1118, 2010.

[46] A. Saghafi, M. Faiz, and D. Roberts, "CO_2 storage and gas diffusivity properties of coals from Sydney Basin, Australia," *International Journal of Coal Geology*, vol. 70, no. 1-3, pp. 240–254, 2007.

[47] S. H. Tang, C. X. Ma, J. P. Ye et al., "A modeling experiment of enhancing coalbed methane recovery by carbon dioxide injection," *Journal of China University of Mining & Technology*, vol. 35, no. 5, pp. 607–616, 2006.

Hindawi
Geofluids
Volume 2022, Article ID 8753217, 17 pages
https://doi.org/10.1155/2022/8753217

Research Article

Spatial and Temporal Distribution of Groundwater in Open-Pit Coal Mining: A Case Study from Baorixile Coal Mine, Hailaer Basin, China

Wenfeng Du,[1] **Lei Chen**,[1,2] **Yunlan He**,[1] **Qiangmin Wang**,[3] **Peiqiang Gao**,[1,2] **and Quansheng Li**[4,5]

[1]*State Key Laboratory of Coal Resources and Safe Mining, China University of Mining & Technology (Beijing), Beijing 100083, China*
[2]*College of Geoscience and Surveying Engineering, China University of Mining & Technology (Beijing), Beijing 100083, China*
[3]*Xi'an Research Institute of China Coal Technology and Engineering Group Corp, Xi'an 710054, China*
[4]*State Key Laboratory of Water Resource Protection and Utilization in Coal Mining, Beijing 102209, China*
[5]*National Energy Group Co., Ltd., Beijing 100011, China*

Correspondence should be addressed to Wenfeng Du; duwf66@126.com and Lei Chen; chenlei_8971@163.com

Received 1 March 2022; Accepted 30 May 2022; Published 29 June 2022

Academic Editor: Haijiao Fu

Groundwater distribution influenced by mining activities is hard to be tracked due to the lack of accurate and real-time monitoring data. To address the groundwater dynamic change data under the mining conditions of open-pit coal mines, a three-dimensional automatic observation network of groundwater was constructed, and this observation network takes open-pit as the center, showing a radioactive distribution, based on hydrogeological conditions, and observes different aquifers. The data was analyzed by integrating hydrology, mining activity, and meteorological data. Analytic hierarchy process was adopted to reveal the underground disturbance influencing factors, and suggestions for groundwater protection were given. The results show that the dynamic variations of the groundwater with time can be divided into 3 types (precipitation affected, unaffected type, and mining affected types). The drainage operation during the open-pit mining triggered the drop of groundwater level, resulting in a cone of depression. The maximum drawdown of the central groundwater level was 60 m. And the disturbance mainly occurred in the mining area where the maximum groundwater disturbance radius was 8 km. Artificial drainage was the main disturbance factor of groundwater, and the range of groundwater level drop within the disturbance radius was closely related to the distance from the open-pit coal mine and the drainage volume. The closer the distance to the mines and the higher the drainage volume led to the deeper the groundwater level drop. This study shows the importance of the three-dimensional observation network of groundwater and provides a good reference for groundwater resources protection and ecological restoration in open-pit coal mines.

1. Introduction

China is highly rely on the coal, and the proportion of coal in the energy structure will be continuously high [1]. For effective coal production, open-pit coal mining is adopted for their high recovery rate and high safety coefficient [2]. Open-pit coal mining can bring great economic benefits to the mining area; however, it may also induce ecological environment issues, especially in arid and semiarid mining areas [3–9]. Hailaer Basin is an arid and semiarid area, which contains rich coal resources. It is an important base for the integrated development of coal and electricity in China [10]. The carrying capacity of groundwater resources is extremely limited, and the contradiction between groundwater protection and coal development is particularly prominent, especially in opencast coal mines located in grassland areas. Therefore, it is of great significance to study the impact of mining activities on groundwater in arid and semiarid regions.

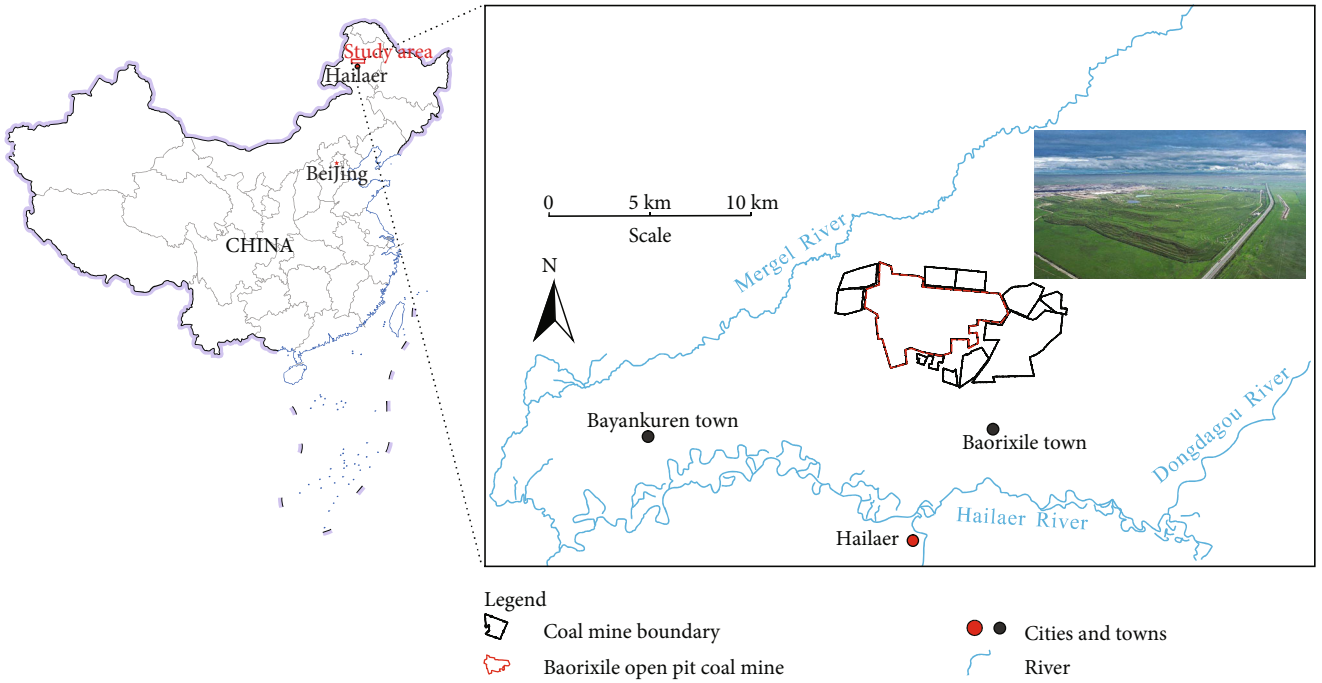

Figure 1: Location of the study area.

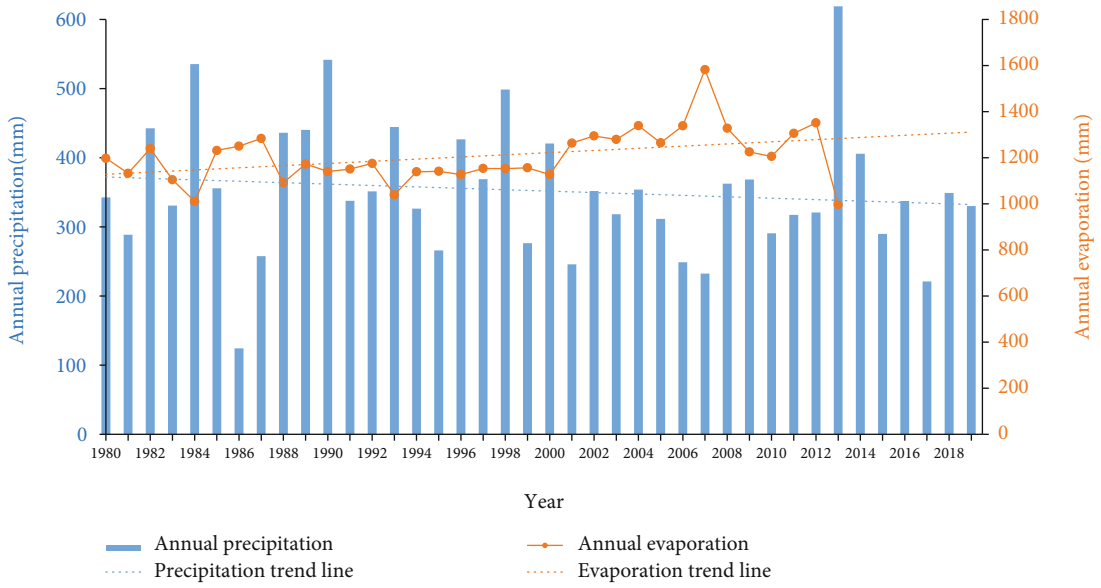

Figure 2: Variation curves of precipitation and evaporation in the study area.

Open-pit coal mining groundwater drainage can cause groundwater disturbance [9, 11–14], and the existing articles on groundwater in open-pit mines mainly focus on the prediction of groundwater inflow [2, 14–17], groundwater as a disaster-causing factor for the safety evaluation of open-pit mine slopes [18–22], groundwater chemistry [5, 6, 23], and ecological evaluation [3, 4, 23, 24]. There are many articles on the change and prediction of groundwater inflow caused by open-pit mining from the perspective of numerical simulation, such as Soni and Manwatkar [16] used the modflow model to simulate and predict the groundwater inflow and groundwater flow field changes in an open-pit coal mine in India under different mining conditions. Xue et al. [17] used a mining geological model to calculate the groundwater impact under different precipitation levels in the Zhuanlongwan mining area, Inner Mongolia. Zhao et al. [2] used the surfact model to assess the groundwater impact of an opencast coal mine in New South Wales and predicted the inflow of groundwater into the mining area during the entire project mining cycle. Ró˙zkowski et al. [14] used numerical calculation and simulation of groundwater inflow in open-pit mines to formulate a reasonable drainage scheme. Haque et al. [9]

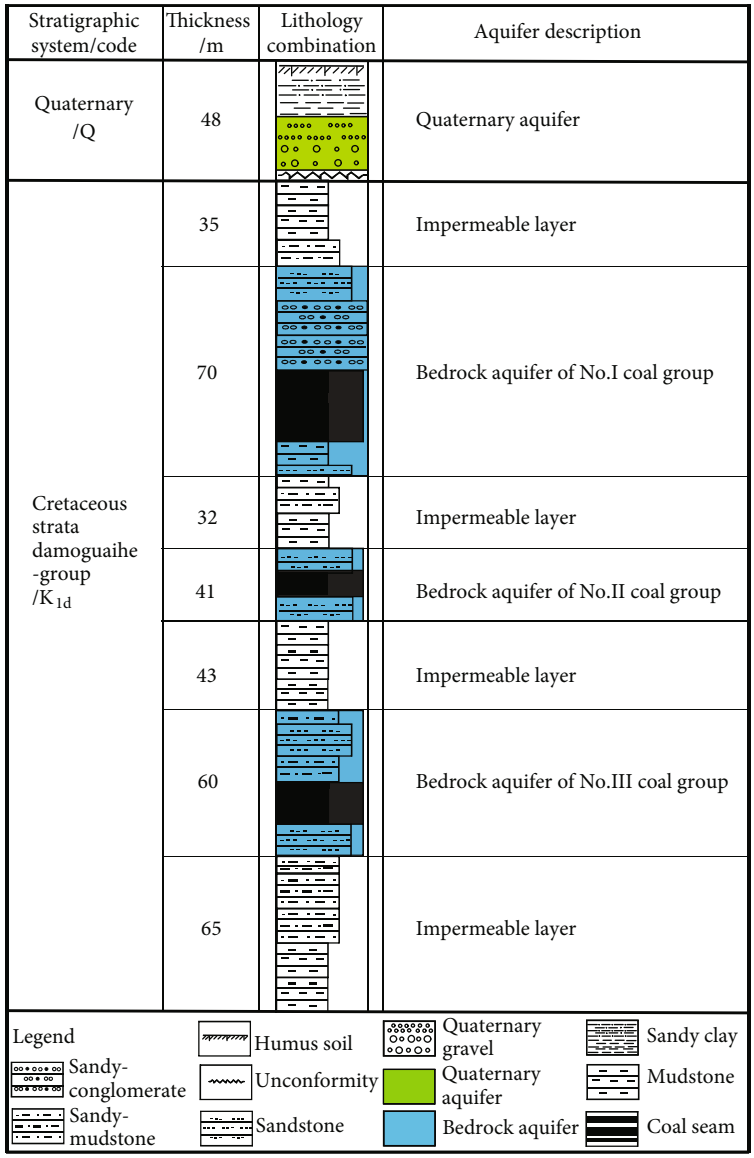

Figure 3: The schematic diagram of stratum and aquifer profile in the study area.

assess the vulnerability of groundwater due to open-pit coal mining using a drastic model. In terms of slope safety, Islam et al. [22] used the fem model to study the stress redistribution caused by mining and the impact of groundwater influx on slope safety. In the chemical change of groundwater in open-pit coal mines, Dong et al. [23] through the groundwater system evolutions in mining area before and after the mining actions of Yimin open-pit coal mine, the interactions between groundwater chemical and its environment was investigated. In the field of groundwater monitoring in open-pit coal mining areas, through long-term monitoring and analysis of the mining area in Riyadh, Saudi Arabia, Yihdego and Drury [15] found that open-pit mining activities in arid areas resulted in a significant drop in groundwater level. Existing articles on groundwater dynamic observation and data analysis mainly focus on urban groundwater source areas [11, 12, 25–28] and underground coal mining area [29–36], there are few articles about the spatial and temporal distribution characteristics of groundwater, disturbance range, and factors under the condition of high-intensity mining in open-pit coal mines, and the distribution of the diving ecological groundwater level needs to be further studied.

Long-term drainage of groundwater in open-pit coal mining will lead to changes in groundwater flow near the stope [18, 23] and formed groundwater drawdown funnels in the mining pits [13, 15, 29, 37]. Through long-term observation of groundwater, the influence of open-pit coal mining on groundwater can be studied [11], which is helpful for groundwater management and protection [11, 12, 38–45]. Long-term observation of open-pit groundwater in arid areas generally shows a downward trend in groundwater level [15, 46]. At present, the observation of groundwater in an open-pit coal mine is mainly based on manual observation, which is time-consuming, labor-consuming, and error-prone [47]. In the cold and arid area, it is difficult to monitor groundwater due to low temperature in the autumn

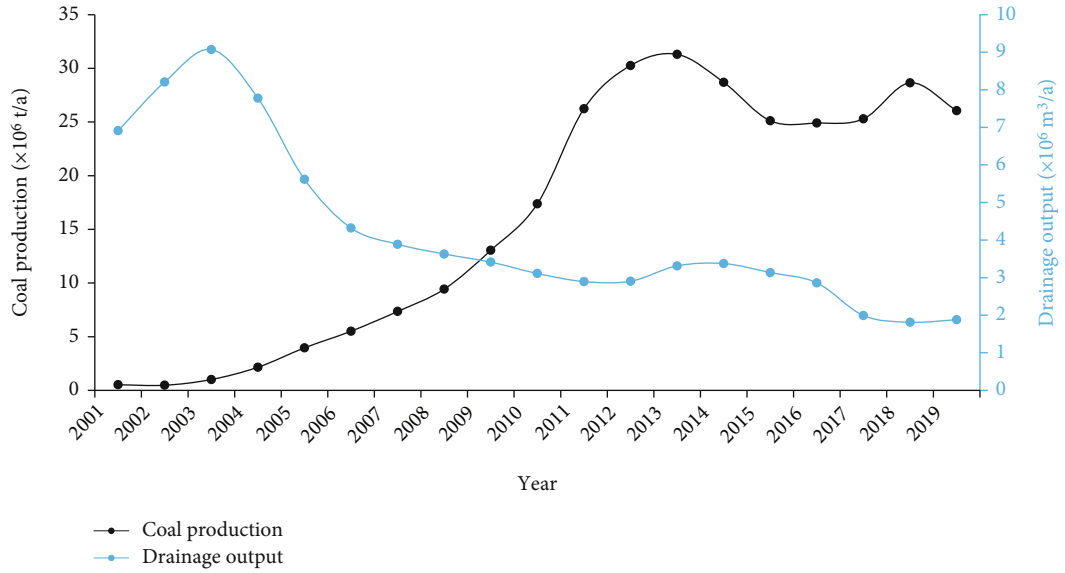

Figure 4: The variation of coal production and drainage output.

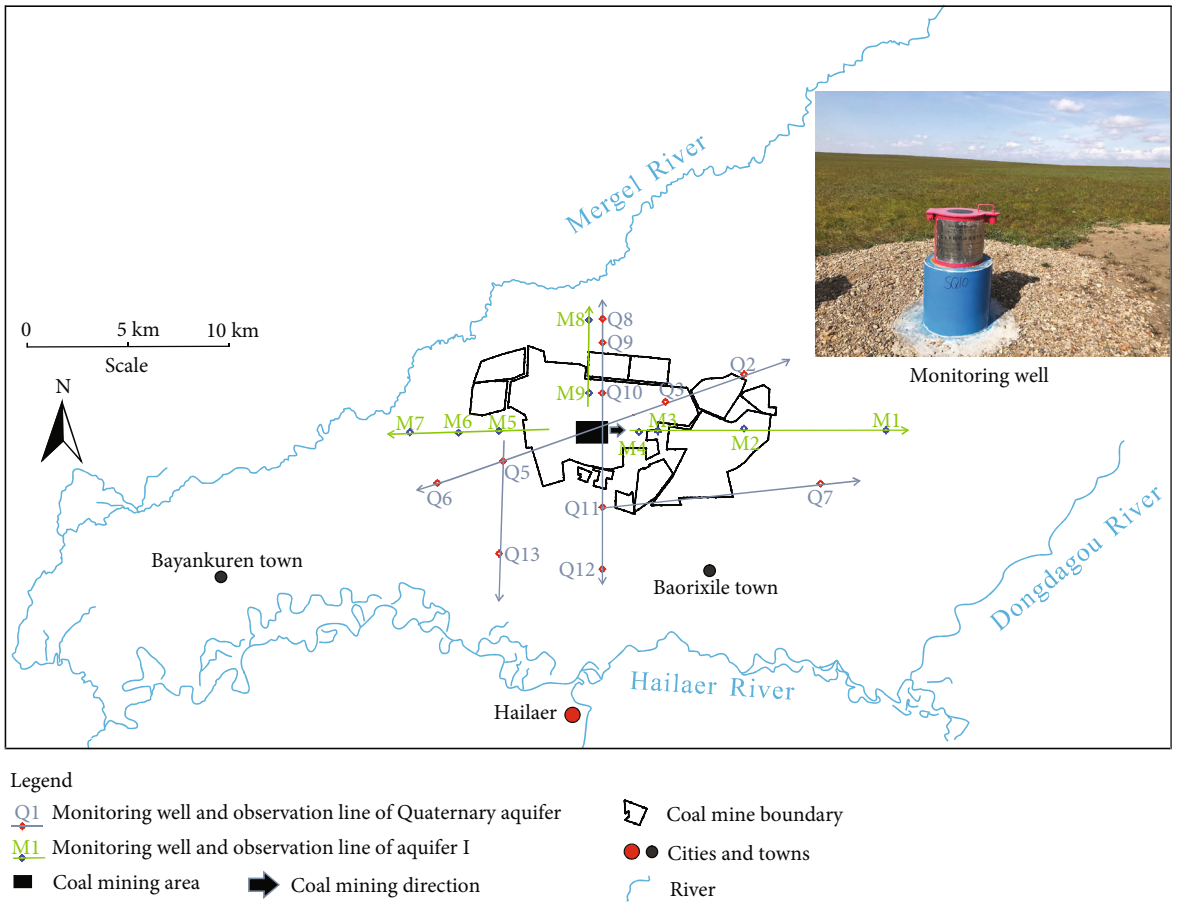

Figure 5: Drilling distribution map of the three-dimensional automatic observation network of groundwater.

and winter. The research on the spatial and temporal distribution characteristics of groundwater under high-intensity mining conditions in cold areas has not been systematically studied. In this paper, through the establishment of a remote three-dimensional observation network of groundwater, the automatic monitoring of groundwater level and temperature and the spatial and temporal distribution of groundwater under high-intensity mining are revealed in Inner Mongolia.

Table 1: Layout parameters of groundwater automatic observation network.

Aquifer	Well	Equipment depth (m)	Distance from open-pit mine (m)
Quaternary groundwater aquifer	Q2	38.67	11000
	Q3	32.28	7000
	Q5	48.39	4000
	Q6	30.42	9000
	Q7	22.43	13000
	Q8	32.28	8000
	Q9	29.62	6000
	Q10	46.94	4000
	Q11	59.96	4000
	Q12	48.49	7000
	Q13	35.51	8000
Coal groundwater aquifer	M1	30.47	14000
	M2	50.80	10000
	M3	120.00	4000
	M4	140.00	3000
	M5	60.02	5000
	M6	59.68	8000
	M7	30.23	11000
	M8	28.74	8000
	M9	108.00	3000

The groundwater disturbance factors are discussed, and the targeted groundwater protection measures are proposed. The result can be of significance for groundwater resources protection and ecological restoration of open-pit coal mines in cold regions.

2. Geological Setting and Coal Mining Activities

The Baorixile open-pit mine (annual output of 35 million tons raw coal) is located in Baorixile town (Figure 1) where it is cold in winter, with the lowest temperature at -47°C and the annual average temperature at -1.9°C. The mining area contains 30 km longitudinally and 10 km latitudinally with a 300 km^2 mining area. The hydrogeological unit thereby covers about 80 km long from east to west, about 25 km wide from north to south, with an area of about 2000 km^2.

The topography of the study area is high in the east and low in the west, with an altitude ranging between 600 and 750 m. The Hailar River in the south is the main river in this area, and the Dongdagou River in the east flows into the Hailar River from north to south. The Mergel River runs from north to west and flows into the Hailar River in the west.

The mining area belongs to an arid and semiarid climate with less precipitation and large evaporation. The annual precipitation from 1980 to 2018 is 124.5–619.1 mm (Figure 2), and the average precipitation is 352.3 mm. The precipitation mainly occur in July and August. With global warming and gradual drought, the precipitation in the area is decreasing year by year. From 1980 to 2018, the evaporation range was 996.9–1582.7 mm, and the average evaporation was 1205.9 mm, showing an increasing trend year by year. Evaporation is greater than precipitation, which will reduce surface water to some extent.

The main strata of the mining area are Cretaceous (K) and Quaternary (Q), and the coal-bearing strata are the Cretaceous Damoguaihe formation (K_1d). There are three main mineable coal layers, which are named no. I, no. II, and no. III coal seams from top to bottom. At present, the main coal seam of the Baorixile open-pit coal mine is no. I. The aquifers are mainly Quaternary phreatic aquifer and Cretaceous coal bearing rock confined aquifer (Figure 3). The lithology of the Quaternary phreatic aquifer is mainly gravels, and the lithology of the Cretaceous confined aquifer is mainly composed of coal seam with developed fractures, roof, and floor conglomerate and sandstone, which are named coal-bearing aquifer no. I, coal-bearing aquifer no. II, and coal-bearing aquifer no. III from top to bottom. The lithology of the impermeable layer is mainly mudstone and siltstone.

Since the commissioning of the Baorixile mining area in 2001, at first, due to the high groundwater abundance of coal bearing formation, the initial value of artificial drainage of groundwater is relatively large, and the coal production is low. With the continuous groundwater drainage operation, the drainage amount increases first and then decreases. After the completion of the drainage of the static groundwater reserves, the drainage is mainly dynamic reserves, and the drainage amount reaches relatively stable. The coal production gradually increases and then tends to be relatively stable. Raw coal production was inversely proportional to drainage volume (Figure 4).

3. Methodology

3.1. Groundwater Data Acquisition Method. Groundwater data collection is divided into automatic acquisition and manual acquisition. The groundwater level acquisition method in the study area has been used for irregular artificial observation of groundwater before the construction of an automatic observation network. The error is large, and the observation well is few. The cold weather in winter brings difficulties to the artificial long-term observation of groundwater. In order to realize the automatic collection of groundwater data, the three-dimensional automatic observation network of groundwater is designed firstly. This observation network takes the open-pit stope as the center, showing a radioactive distribution, based on hydrogeological conditions, and observes different aquifers. The confined groundwater in the Quaternary phreatic layer and the aquifer layer of coal no. I is observed hierarchically, and the long-term monitoring of groundwater in different directions and aquifers is realized.

Groundwater observation network in the Baorixile open-pit mine is shown in Figure 5. The observation network is centered on an open-pit mine, and 20 hydrological boreholes are arranged on the plane (Table 1), including 11 Quaternary aquifer observation wells and 9 coal no. I bearing aquifer observation wells. After the completion of each hydrological observation hole, the construction of a

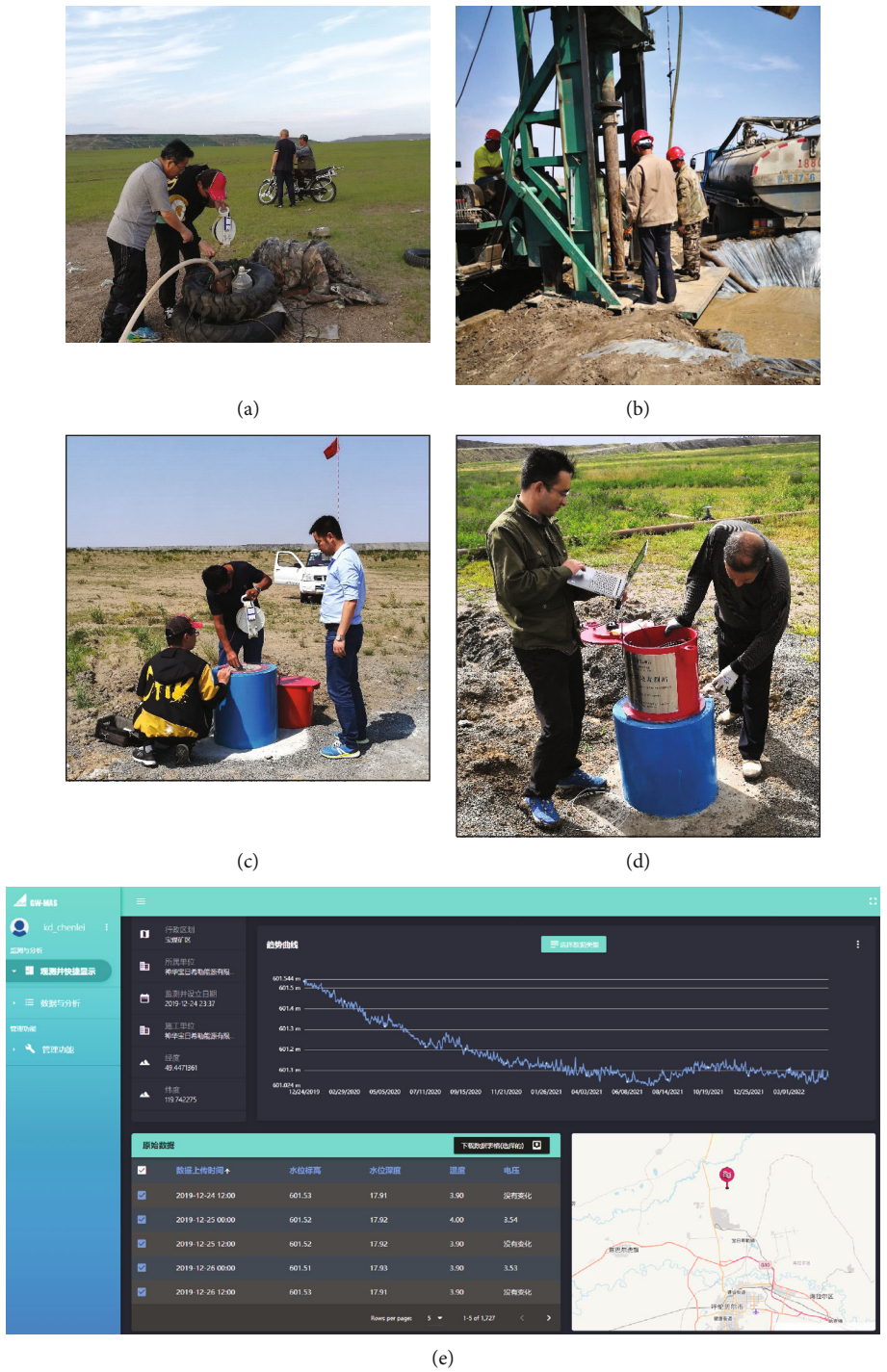

Figure 6: Groundwater automatic observation network construction process pictures. (a) Workers are observing the groundwater level of herdsmen's wells. (b) Workers are drilling hydrogeological boreholes. (c) Workers are installing automatic groundwater level observation equipment. (d) Workers are calibrating parameters of automatic groundwater level observation equipment. (e) This is the client interface of the automatic groundwater observation system.

groundwater automatic monitoring well is carried out. The automatic monitoring equipment for groundwater cold resistance (Figure 6) is installed in each observation well. The acquisition and transmission time of groundwater parameters (groundwater level and groundwater temperature double parameters) is set. The groundwater data is collected every 12 hours and transmitted to the Aliyun server through the internet of things wireless network. The groundwater level data is viewed and downloaded online through the remote monitoring system. This project has been completed in November 2019. The automatic acquisition, wireless transmission, and online remote monitoring of

Table 2: Judgement matrix scale and its meaning.

Scale	Implication
1	Comparing the two factors, they have the same importance.
3	Comparing two factors, the former is slightly more important than the latter.
5	Comparing the two factors, the former is more important than the latter.
7	Comparing two factors, the former is more important than the latter.
9	Comparing two factors, the former is more important than the latter.
2, 4, 6, 8	Represents the intermediate value of the above judgment
Reciprocal	The scale of factor i versus j is the reciprocal of the scale of factor j versus i

Table 3: Random indicators RI.

n	1	2	3	4	5	6	7	8
RI	0	0	0.58	0.90	1.12	1.24	1.32	1.41

groundwater data (groundwater level and groundwater temperature) under high-intensity mining conditions of open-pit coal mines in cold regions are accomplished.

3.2. Weight Analysis Method of Groundwater Disturbance Factors. Determining the weight of groundwater disturbance factors can help to develop targeted groundwater protection measures [48], this paper uses the analytic hierarchy process (AHP) [49, 50] qualitatively and quantitatively evaluated the index weight [51]. The target was divided into several levels, the factors in each level were compared in pairs to obtain the relative comparison value of any two factors, and then the judgment matrix at each level was constructed. The maximum eigenvalues and corresponding eigenvectors of the judgment matrix at each level are calculated, and the rationality of the element value of the judgment matrix is verified by the consistency test results of the judgment matrix. Finally, the weight value of each factor in the judgment matrix relative to all factors in the corresponding level is obtained after normalization.

3.2.1. Construction of Judgment Matrix. When using AHP analysis, it is necessary to establish a judgment matrix for the same level of indicators by pairwise comparison. The level W contains events $W_1, W_2, \cdots, W_n$. The expression of judgment matrix is

$$W = [W_1, W_2, \cdots, W_n], \tag{1}$$

$$W_i = \left[W_{i1}, W_{i2}, \cdots, W_{ij}, \cdots, W_{\text{in}}\right]. \tag{2}$$

Among them, W_{ij} is the relative importance of W_i to W_j, which is usually expressed by the natural number 1–9 and its reciprocal. The larger the value, the higher the importance of W_i to W_j. The scale and meaning of the judgment matrix are shown in Table 2.

3.2.2. Calculate the Sum of Feature Vectors and the Corresponding Feature Roots. According to the constructed judgment matrix, the feature vector and feature root are obtained, and the judgment matrix is normalized:

$$\overline{W_{ij}} = \frac{W_{ij}}{\sum_{k=1}^{m} W_{ij}} (i, j = 1, 2, 3, \cdots, m). \tag{3}$$

The normalized judgment matrix is added by rows to obtain $\overline{U_{ij}}$:

$$\overline{U_{ij}} = \sum_{j=1}^{m} W_{ij} (i, j = 1, 2, 3, \cdots, m). \tag{4}$$

Calculating the maximum eigenvalue of judgment matrix $\lambda_{\max}$:

$$\lambda_{\max} = \frac{1}{m} \sum_{j=1}^{m} \frac{\sum_{j=1}^{m} W_{ij} U_j}{U_j}. \tag{5}$$

3.2.3. Consistency Testing. Consistency test for constructed judgment matrix. Consistency indicators:

$$\text{CI} = \frac{\lambda - n}{n - 1}. \tag{6}$$

The random indicators RI are shown in Table 3.
Define consistency ratios:

$$\text{CR} = \frac{\text{CI}}{\text{RI}}. \tag{7}$$

Usually, CR < 0.1 passes the consistency test.

4. Results

4.1. Distribution of Groundwater Flow Field under Mining Conditions. In order to study the spatial distribution characteristics of groundwater, we draw the groundwater flow field diagram according to the monitoring data of groundwater level in 2020. It can be seen from the groundwater contour map (Figure 7) of the Quaternary phreatic aquifer that the flow direction of groundwater in the Quaternary aquifer is generally northeast to southwest. In the mining area, the contour density increases, the hydraulic gradient increases, and the groundwater level decreases significantly, forming a groundwater drawdown funnel, and the central groundwater level is 570 m. It can be seen from the groundwater

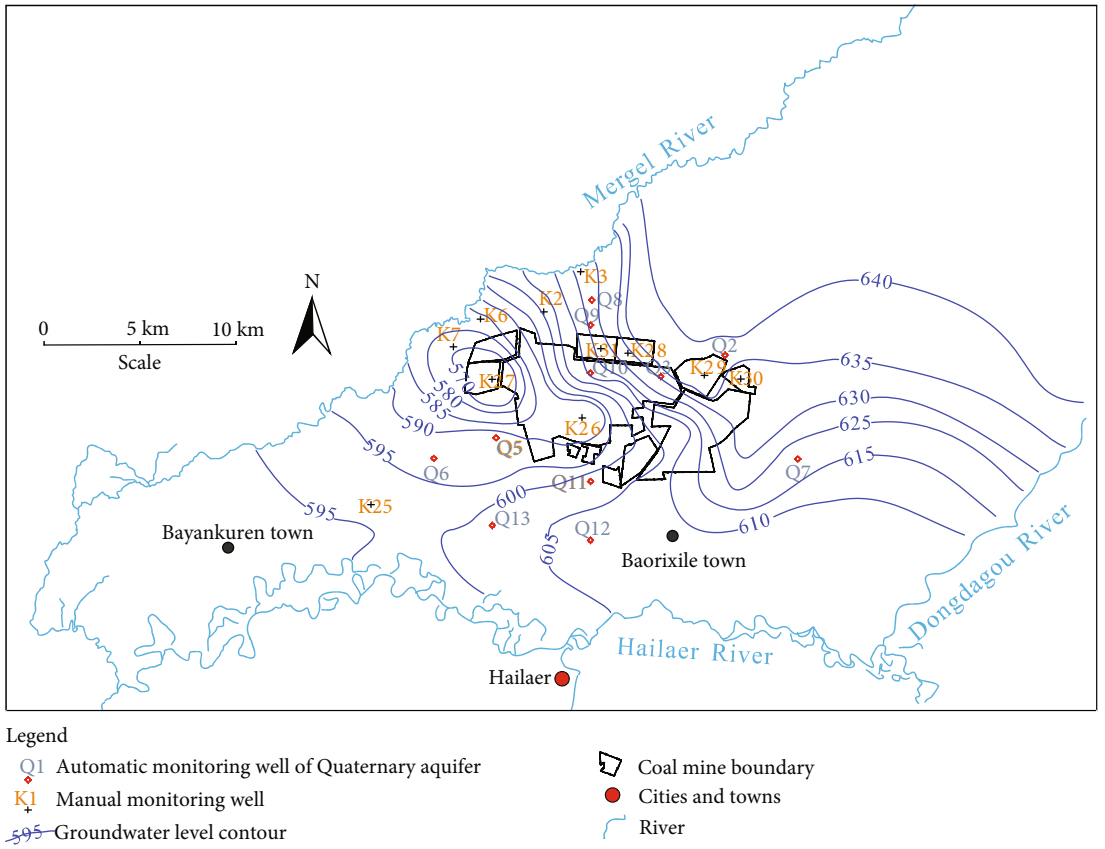

Figure 7: Groundwater contour map of Quaternary aquifer under open-pit coal mining conditions in 2020.

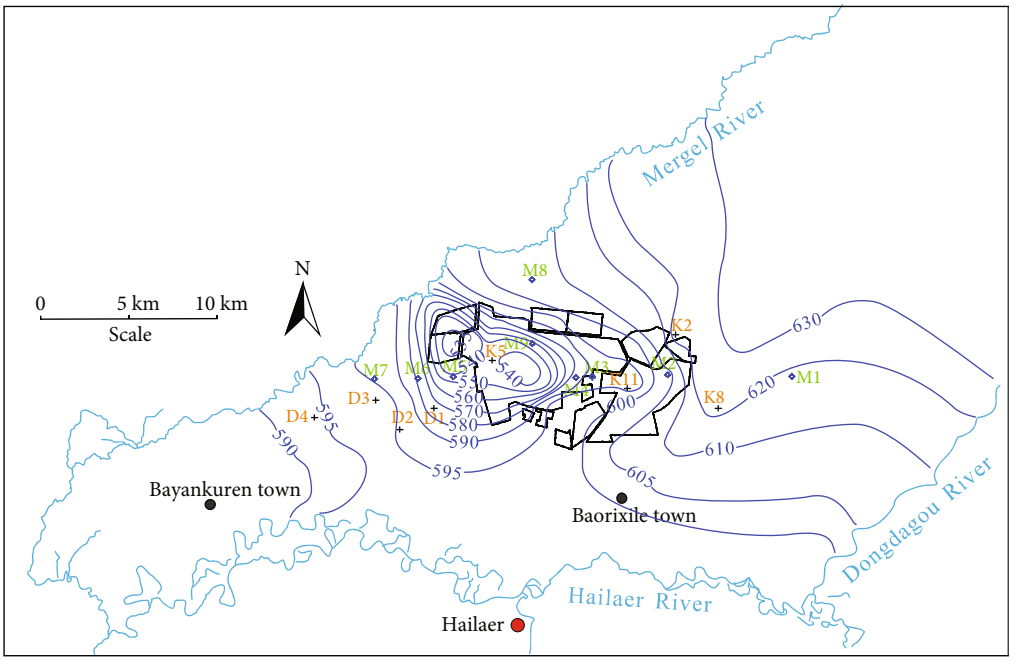

Figure 8: Groundwater contour map of coal I aquifer after open pit mining in 2020.

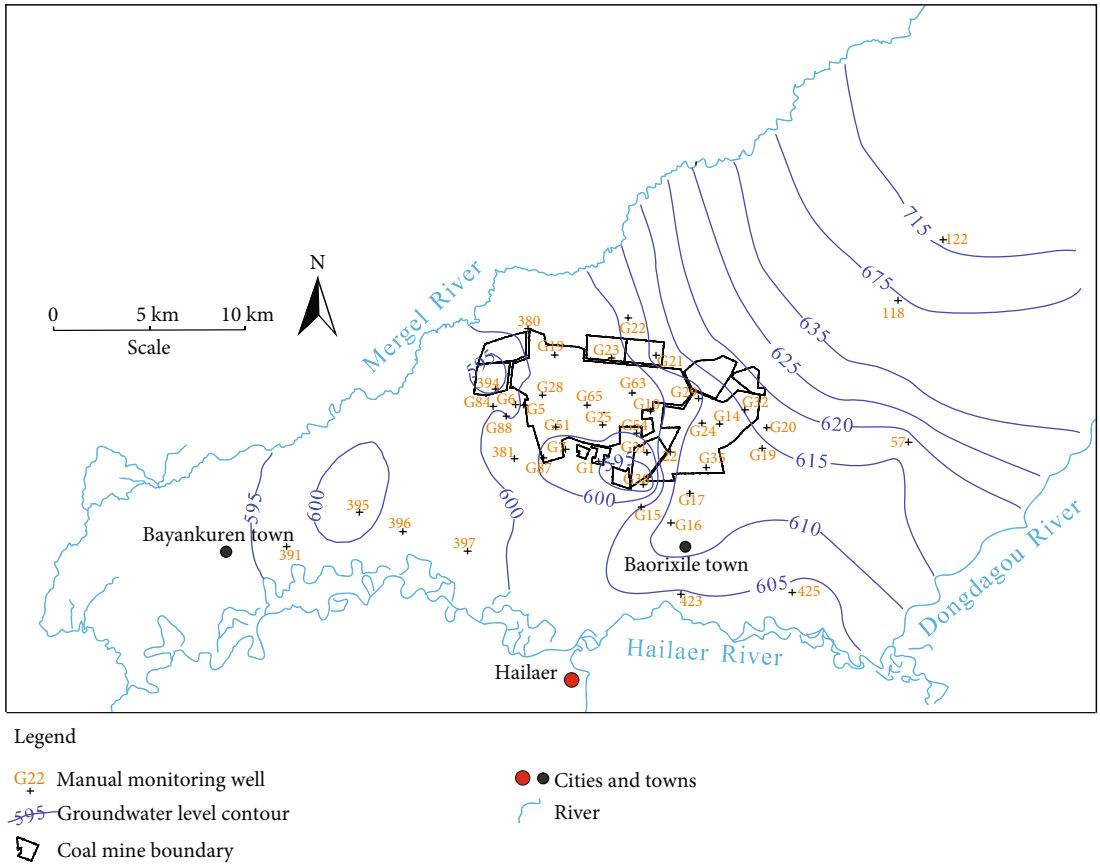

Figure 9: Contour map of groundwater in coal seam confined aquifer before open-pit mining in 1985.

contour map of aquifer I (Figure 8) that the flow direction of groundwater is generally similar to that of the Quaternary phreatic aquifer, and runoff flows from northeast to southwest. In the mining area, the closer to the pit, the greater the contour density, forming a groundwater drawdown funnel, the central groundwater level is 535 m.

4.2. Variation of Groundwater Flow Field before and after Mining. In order to study the characteristics of groundwater disturbance after coal mining, the groundwater level data of the coal-bearing seam before coal mining in 1985 were collected. At that time, the coal mine had not been developed, and the flow field was mainly controlled by topography. The groundwater level data can be used as the initial value of the groundwater level. From the contour map of the groundwater flow field before coal mining (Figure 9), the groundwater flow east to west as a whole, and the groundwater elevation in the mining area is 595–620 m.

After interpolation of groundwater level data in Figures 8 and 9, the contour map of drawdown (Figure 10) can be obtained. From the diagram, it can be seen that the maximum drawdown of groundwater level in the mining area is about 60 m. Through measurement, the influence radius and range of groundwater disturbance in open-pit coal mining can be obtained (Table 4). The maximum influence radius is about 8 km, and the maximum influence area is about 200 km^2. The mining affected type mainly occurs in the mining area, and the maximum influence area accounts for about 66.7% of the mining area and 10% of the research area.

4.3. Temporal Variation of Groundwater Level. According to the groundwater level data of groundwater automatic monitoring network in 2020, the variation curve is plotted. Combined with the fluctuation of the groundwater level curve and the variation of precipitation and drainage, the variation curve of the groundwater level can be divided into precipitation affected type, unaffected type, and mining affected type.

4.3.1. Precipitation Affected Type. This type is revealed by the observation wells of Q11, Q13, and M2. The fluctuation of the groundwater level curve of observation wells changes with the change of precipitation (Figure 11). The groundwater level increases after the increase of precipitation and decreases after the decrease of precipitation. The peak value of groundwater level lags slightly behind the peak value of precipitation and is less affected by drainage. It is mainly distributed in the area far from the open pit coal mining pit, deep aquifer burial, and good precipitation infiltration conditions.

4.3.2. Unaffected Type. This type is revealed by the observation wells of Q2, Q8, Q9, Q12, and M7. The fluctuation of groundwater level curve of observation wells is gentle

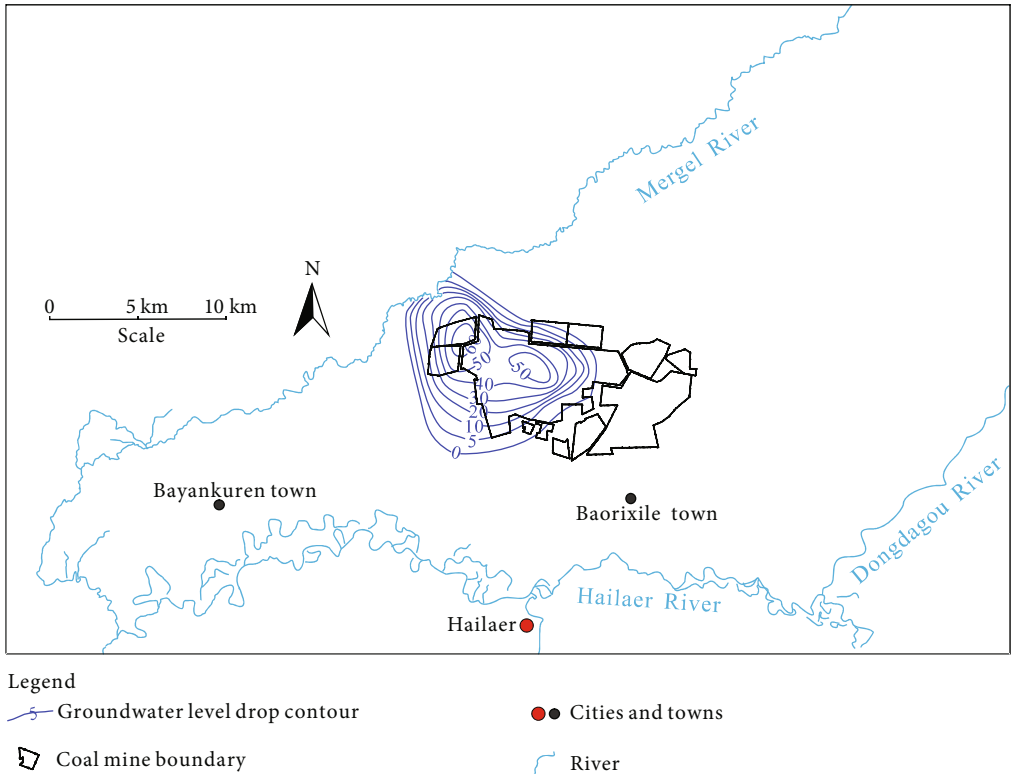

Figure 10: Contour map of groundwater in coal seam confined aquifer after open pit mining in 2020.

Table 4: Radius and range of groundwater disturbance after open pit mining.

Groundwater drawdown (m)	Influence radius (km)	Influence area (km^2)
5	4.0-8.0	50-200
10	3.5-7.5	38-176
20	3.5-7.0	38-153
30	3.0-6.0	28-113
40	2.5-3.5	20-39
50	2.0-2.5	12-20
60	1.5-2.0	7-12

(Figure 12), which is basically not affected by drainage and precipitation changes. It is mainly distributed in areas far from open pit coal mining, good groundwater runoff conditions, and deep aquifer burial.

4.3.3. Mining Affected Type. This type is revealed by the observation wells of Q3, Q5, Q6, Q7, Q10, M1, M3, M4, M5, M6, M8, and M9. The fluctuation of groundwater level curve of observation wells is greatly affected by drainage (Figure 13). When the precipitation increases, the groundwater level does not increase but decreases. When the drainage amount is greater than the supply amount, the groundwater level shows a gradual downward trend, and the groundwater level dynamic shows a typical consumption type, which is mainly distributed in the area near the open-pit coal mining area.

4.4. Spatial Variation of Groundwater before and after Coal Mining. Before open-pit coal mining, the groundwater flow field was mainly controlled by topography. The distribution of groundwater was basically consistent with the topography, and the groundwater flow field generally flowed from northeast to southwest.

After the open-pit coal mining, the overburden and rock layers on the coal seam were completely stripped, resulting in the destruction of the aquifer above the coal measure strata, which changed the running state of the groundwater. And under the action of gravity, the mining pits became the new groundwater catchment center, and the open-pit coal mine drainage became the main factor controlling the groundwater flow field. The drainage of open-pit coal mines is a dynamic and continuous process. With the continuous drainage of aquifers, the groundwater level continues to drop, forming a groundwater depression cone with the mining pit as the center. In the groundwater cone area, the flows of groundwater are changed from the horizontal direction to the vertical, increasing both the hydraulic gradient and the groundwater velocity. The groundwater disturbance factor is mainly the influence of artificial drainage, followed by precipitation evaporation. When the drainage groundwater and precipitation evaporation are consistent, the groundwater disturbance at different locations is also affected by the distance between observation wells and mining pits, recharge

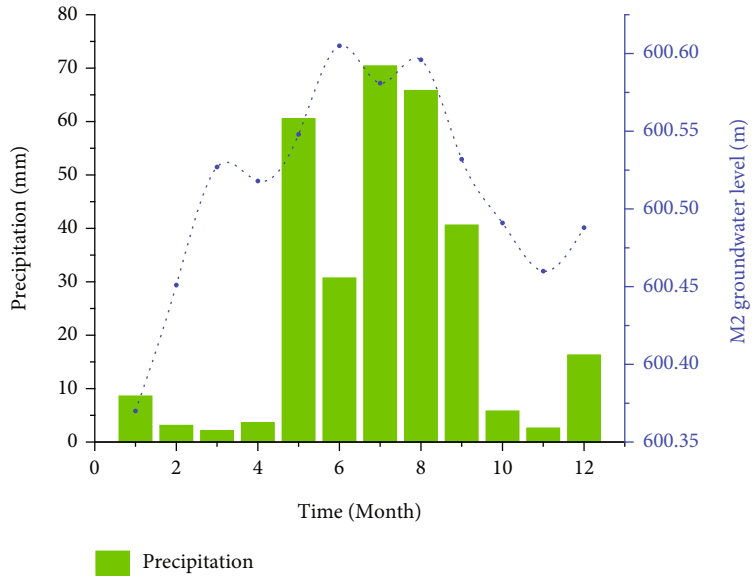

Figure 11: Characteristics of temporal dynamic change curve of precipitation-affected groundwater level (M2).

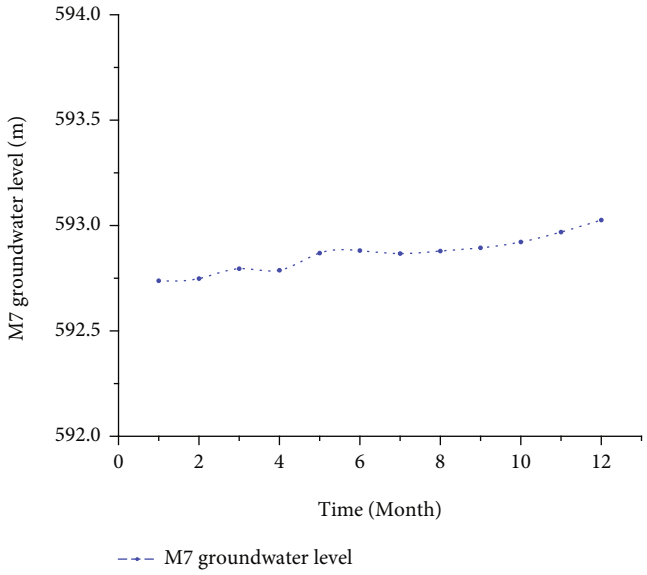

Figure 12: Characteristics of time series dynamic change curve of unaffected groundwater level (M7).

runoff conditions, aquifer buried depth, and landform factors. With the expansion in the scale of open-pit coal mining and the nonstop advancement of the stope, the outflow of groundwater increases continuously, the groundwater level drops, and the cone of depression becomes larger. When the static reserves of groundwater in the open-pit coal mining area are drained to reach the dynamic reserves, the groundwater depression cone also reaches a dynamic equilibrium, and the groundwater flow field is mainly determined by the topography and the open-pit coal mine drainage combined, instead of being determined solely by the topography.

5. Discussion

5.1. Groundwater Disturbance Influencing Factors after Coal Mining. In the process of open-pit mining, the load above the coal seam in the mining area will be completely stripped, the aquifer above the coal series will be drained, and an open funnel area will be formed. The groundwater discharge of the aquifer in the mining area changes from the original natural runoff discharge along the dip direction of the strata to the drainage mode dominated by drainage and artificial discharge. Due to the destruction of the natural recharge, runoff, and discharge conditions of the groundwater in the region, the groundwater recharge in the downstream area is reduced, and the groundwater resources are reduced. The destruction of groundwater resources during open-pit mining is mainly caused by the drainage of groundwater caused by coal mining, which leads to the loss of regional groundwater resources. Drainage volume and precipitation are the direct factors that cause groundwater level fluctuation.

5.1.1. Drainage Volume. In order to study the relationship between drainage volume and groundwater level, taking M5 observation station as an example, the plot of average groundwater level from January to December 2020 and the corresponding monthly drainage volume are drawn. The correlation diagram between the two was established (Figure 14). It can be seen from the diagram that with the increase of drainage, the groundwater level decreases, the decline is large, and the trend is obvious. There is a negative correlation between the two, and R^2 value is 0.9316. It indicates that a large amount of groundwater drainage is an important reason for groundwater level decline.

5.1.2. Precipitation. Precipitation is an important source of groundwater recharge, and its seasonal and interannual variations have important driving significance for the dynamic

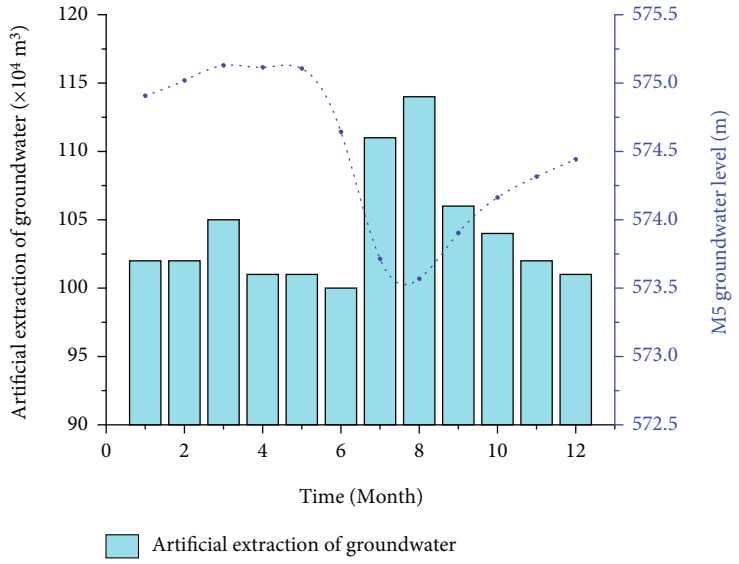

Figure 13: Time series dynamic curve characteristics of mining-affected groundwater level (M5).

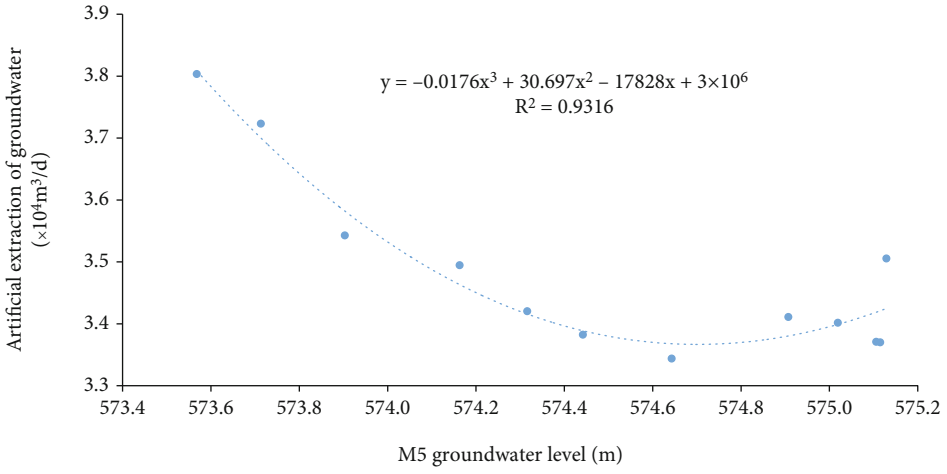

Figure 14: Correlation curve between groundwater level of M5 observation well and drainage volume of coal mine (January–December 2020).

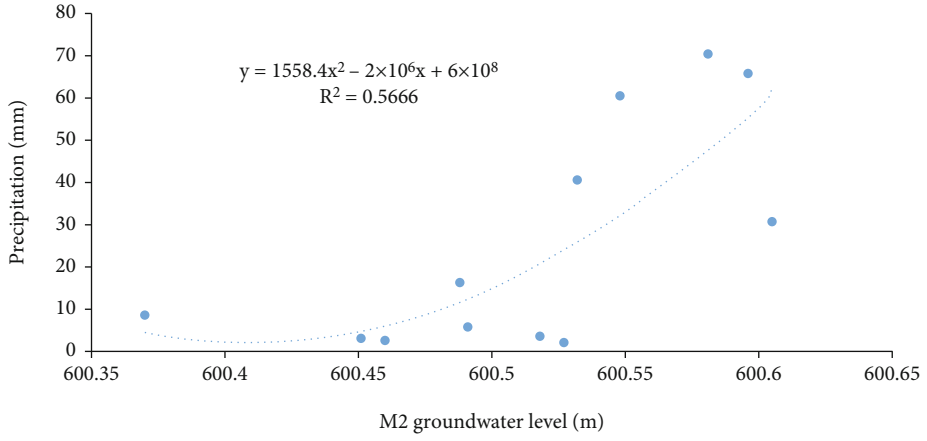

Figure 15: Correlation curve between groundwater level and precipitation in M2 observation well (January–December 2020).

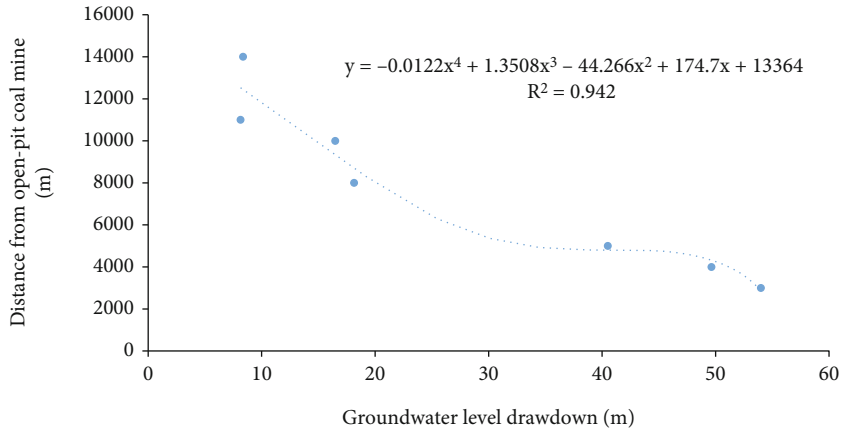

Figure 16: Correlation curve between groundwater level drop of observation well and open-pit mine distance.

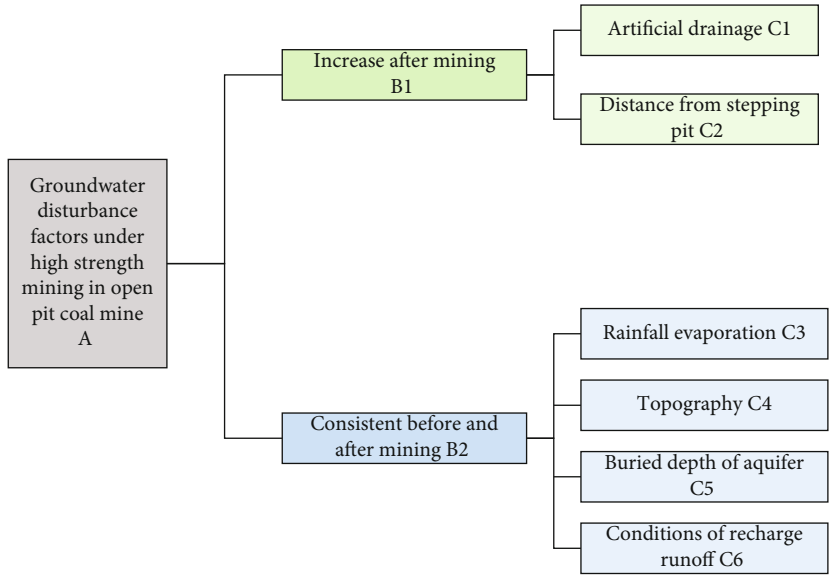

Figure 17: Structural model of groundwater disturbance factors.

change of groundwater in the region. Groundwater recharge is directly related to the amount of local precipitation. Precipitation in open-pit mining area is directly converted into water accumulation in mining area. In order to further analyze the variation of groundwater level with precipitation, the groundwater level from January to December in 2020 was used as the abscissa, and the corresponding monthly precipitation was used as the ordinate. The correlation diagram between the two was established (Figure 15), from the diagram, it can be seen that with the increase of precipitation, the groundwater level increased, and the groundwater level decreased after the decrease of precipitation, they were shown to be positively correlated, and the R^2 value reached 0.5666.

5.1.3. Other Influencing Factors. In a certain period of drainage and precipitation, the groundwater level at different locations is disturbed differently. In order to study the relationship between groundwater drawdown and pit distance, the groundwater level drawdown of M1, M2, M3, M4, M5, M6, and M7 observation wells is used as the abscissa, and the distance from the pit is used as the ordinate. The correlation diagram between the two is established (Figure 16). It can be seen from the figure that the closer to the open-pit coal mine, the greater the decline of groundwater level in the observation well. The decline of groundwater level is negatively correlated with the distance to the open-pit mine, and the R^2 value reaches 0.942. It indicates that drainage is an important factor affecting groundwater resources. The closer to the mining pit, the greater the amount of artificial drainage is, and the greater the disturbance is. The drainage effect of mining pit has different degrees of influence on groundwater resources in different distribution areas, and the magnitude of this influence is inversely proportional to

Table 5: Pair-wise comparison judgment matrix A-$B_{1\text{-}2}$.

A	B1	B2	Weight
B1	1	3	0.75
B2	1/3	1	0.25

Table 6: Pair-wise comparison judgment matrix B_1-$C_{1\text{-}2}$.

B1	C1	C2	Weight
C1	1	3	0.75
C2	1/3	1	0.25

Table 7: Pair-wise comparison judgment matrix B_2-$C_{3\text{-}6}$.

B2	C3	C4	C5	C6	Weight
C3	1	5	5	5/3	0. 5
C4	1/5	1	1	1/3	0.1
C5	1/5	1	1	1/3	0.1
C6	3/5	3	3	1	0.3

Table 8: Standard weight of all factors.

Goal A	Weight B	Weight C	Weight
A	B1	C1	0.5625
		C2	0.1875
	B2	C3	0.1250
		C4	0.0250
		C5	0.0250
		C6	0.0750

the distance from the coal mining area, that is, the closer to the open-pit coal mine, the greater the influence of coal mining on groundwater resources.

In addition to drainage volume, precipitation, and observation well location, groundwater disturbance is also affected by other secondary factors such as topography, aquifer depth, and recharge runoff conditions: The lower the terrain is, the more groundwater will be collected, and the more groundwater will be lost after dredging. The shallower the aquifer is, the more easily it will be disturbed. The location with more groundwater recharge and less discharge will be more likely to be disturbed after dredging and drainage. The discharge volume increases, and the groundwater disturbance degree increases.

5.2. Quantitative Analysis of Groundwater Disturbance Factors

5.2.1. Different Influencing Factors Classification. Combined with mining conditions, six factors, namely, artificial drainage (A), precipitation (B), landform (C), distance from mining pit (D), aquifer burial depth (E), and recharge-runoff condition (F), were determined to classify the target layer hierarchically (Figure 17).

5.2.2. Different Influencing Factors Weight. Random consistency ratio CR = 0 < 0.1 (Tables 5, 6, and 7). It shows that the judgment matrix is consistent and does not need to adjust the element value of the judgment matrix.

The analytic hierarchy process (AHP) was used to analyze the influencing factors of each disturbance, and the weight value of each influencing factor in different mining periods (Table 8) was determined. The calculation results show that the artificial drainage weight is 0.5625, which is the main factor, followed by the distance from the mining pit, the weight is 0.1875, the influence weight of precipitation, recharge runoff conditions, aquifer depth, and topography are 0.125, 0.075, 0.025, and 0.025.

5.3. Suggestions on Groundwater Protection in High-Strength Mining Area. According to the characteristics of groundwater disturbance factors and the results of influence weight analysis, artificial drainage is the main factor. Precipitation-evaporation, topography, distance from mining pit, and recharge runoff conditions are secondary factors and objective natural factors. With the climate drought, the decrease of precipitation, and the increase of evaporation, the groundwater level decreased to some extent. By reducing the drainage capacity of groundwater and improving the utilization rate of drainage are the main measure to reduce the disturbance of groundwater in mining area. The excessive drainage of groundwater in mining area can be reduced by stopping drainage vertical wells. After the groundwater gushing from the mining pit is treated as the production and living water for recycling, the abundant water is stored in the underground reservoir constructed under the dump and the ground reservoir after the ecological restoration of the waste land on the dump for standby. These water saving measures have important practical significance for the protection of groundwater in the high-intensity mining of open-pit coal mines and are beneficial to the coordinated development of green mining of open-pit coal mines and the sustainable utilization of groundwater.

6. Conclusions

To address the groundwater dynamic change data under the mining conditions of open-pit coal mines, a three-dimensional automatic observation network of groundwater was constructed to obtain long-term dynamics, with the variation of groundwater flow field under the mining conditions can be compared and analysed, the conclusions obtained are as follows:

(1) The maximum drawdown in the study area was about 60 m and the maximum influence radius of about 8 km. The maximum influence range accounted for about 66.7% of the mining area and about 10% of the hydrological unit area

(2) Apart from mining influenced groundwater variation curves, the precipitation influenced and unaffected groundwater were also recognized. Both of which are distributed in the mining area and beyond, accounting for 33.3% of the mining area. The

precipitation affected type was mainly distributed upstream of the mining area, and the precipitation infiltration conditions were good. The unaffected type was mainly distributed in the north and south of the mining area, far from the mining pit, and the aquifer is deeply buried

(3) The groundwater was influenced by topography and precipitation before coal mining, of which topography was the most important. After mining, artificial drainage and precipitation were the key factors. Thus, groundwater recycling and protection should be conducted during mining activities

Data Availability

The data used to support the findings of this study are available from the corresponding author upon request.

Disclosure

Part of the manuscript has been published in the preprint, the link to the preprint is doi:10.20944/preprints202202.0016.v1, although the preprint has been successfully withdrawn.

Conflicts of Interest

The authors declare that they have no conflicts of interest.

Authors' Contributions

Funding acquisition and methodology were done by Wenfeng Du; conceptualization, data curation, and writing—original draft were done by Lei Chen; investigation was done by Yunlan He; investigation and methodology were done by Qiangmin Wang; investigation was done by Peiqiang Gao; project administration was done by Quansheng Li.

Acknowledgments

The Baorixile Open-pit Coal Mine is thanked for providing coal production data, coal mine drainage data, precipitation-evaporation data, initial groundwater level data, and hydrogeological data. Senior engineers Wei Zhao and Zhiguo Cao are thanked for their helpful construction of the groundwater automatic observation network. This research was funded by China's National Key Research and Development Program (no. 2016YFC0501102) and Green, Intelligent and Safe Mining for Coal Resources (Grant number: 52121003).

References

[1] H. P. Xie, L. X. Wu, and D. Z. Zheng, "Prediction on the energy consumption and coal demand of China in 2025," *Journal of China Coal Society*, vol. 44, no. 7, pp. 1949–1960, 2019.

[2] L. Zhao, T. Ren, and N. Wang, "Groundwater impact of open cut coal mine and an assessment methodology: a case study in NSW," *International Journal of Mining Science and Technology*, vol. 27, no. 5, pp. 861–866, 2017.

[3] H. B. Feng, J. W. Zhou, A. G. Zhou et al., "Grassland ecological restoration based on the relationship between vegetation and its below-ground habitat analysis in steppe coal mine area," *Science of the Total Environment*, vol. 778, no. 2021, article 146221, 2021.

[4] H. Q. Lian, H. Y. Yi, Y. Yang, B. Wu, and R. Wang, "Impact of coal mining on the moisture movement in a vadose zone in open-pit mine areas," *Sustainability*, vol. 13, no. 8, p. 4125, 2021.

[5] J. Liu, D. W. Jin, T. T. Wang, M. Gao, J. Yang, and Q. Wang, "Hydrogeochemical processes and quality assessment of shallow groundwater in Chenqi coalfield, Inner Mongolia, China," *Environmental Earth Sciences*, vol. 78, no. 12, p. 347, 2019.

[6] H. L. Liu, Q. Wu, M. J. Wang, and M. Zhang, "Multivariate analysis of water quality of the Chenqi Basin, Inner Mongolia, China," *Mine Water and the Environment*, vol. 37, no. 2, pp. 249–262, 2018.

[7] M. H. Xia, S. G. Dong, Y. Chen, and H. Liu, "Study on evolution of groundwater-lake system in typical prairie open-pit coal mine area," *Environmental Geochemistry and Health*, vol. 43, no. 10, pp. 4075–4087, 2021.

[8] J. Park, E. Kwon, E. Chung, H. Kim, B. Battogtokh, and N. C. Woo, "Environmental sustainability of open-pit coal mining practices at Baganuur, Mongolia," *Sustainability*, vol. 12, no. 1, p. 248, 2020.

[9] E. Haque, S. Reza, and R. Ahmed, "Assessing the vulnerability of groundwater due to open pit coal mining using DRASTIC model: a case study of Phulbari coal mine, Bangladesh," *Geosciences Journal*, vol. 22, no. 2, pp. 359–371, 2018.

[10] Q. Li, "Progress of ecological restoration and comprehensive remediation technology in large-scale coal-fired power base in the eastern grassland area of China," *Journal of China Coal Society*, vol. 44, no. 12, pp. 3625–3635, 2019.

[11] M. Islam, M. Van Camp, D. Hossain et al., "Impacts of large-scale groundwater exploitation based on long-term evolution of hydraulic heads in Dhaka City, Bangladesh," *Water*, vol. 13, no. 10, p. 1357, 2021.

[12] Y. Zhou, D. Dong, J. Liu, and W. Li, "Upgrading a regional groundwater level monitoring network for Beijing Plain, China," *Geoscience Frontiers*, vol. 4, no. 1, pp. 127–138, 2013.

[13] Q. W. Chunhu Zhao, H. Wang, J. Yang, J. Liu, and Y. Zhan, "Analysis of influence of open-pit coal mining on groundwater system and curtain wall protection in grassland area of Northeastern China," *Journal of China Coal Society*, vol. 44, no. 12, pp. 3685–3692, 2019.

[14] K. Różkowski, R. Zdechlik, and W. Chudzik, "Open-pit mine dewatering based on water recirculation—case study with numerical modelling," *Energies*, vol. 14, no. 15, p. 4576, 2021.

[15] Y. Yihdego and L. Drury, "Mine dewatering and impact assessment in an arid area: case of gulf region," *Environmental Monitoring and Assessment*, vol. 188, no. 11, p. 634, 2016.

[16] A. K. Soni and B. Manwatkar, "Seepage modeling for a large open pit coal mine in India," *Geotechnical and Geological Engineering*, vol. 33, no. 4, pp. 997–1007, 2015.

[17] S. Xue, Y. Liu, S. Liu, W. Li, Y. Wu, and Y. Pei, "Numerical simulation for groundwater distribution after mining in Zhuanlongwan mining area based on visual MODFLOW," *Environmental Earth Sciences*, vol. 77, no. 11, p. 400, 2018.

[18] S. Jiang, X. Kong, H. Ye, and N. Zhou, "Groundwater dewatering optimization in the Shengli no. 1 open-pit coalmine, Inner Mongolia, China," *Environmental Earth Sciences*, vol. 69, no. 1, pp. 187–196, 2013.

[19] A. I. Theocharis, I. E. Zevgolis, A. V. Deliveris, R. Karametou, and N. C. Koukouzas, "From climate conditions to the numerical slope stability analysis of surface coal mines," *Applied Sciences*, vol. 12, no. 3, p. 1538, 2022.

[20] Y. Hong, Z. Shao, G. Shi, Y. Dou, W. Wang, and W. Zhang, "Freeze-thaw effects on stability of open pit slope in high-altitude and cold regions," *Geofluids*, vol. 2021, Article ID 8409621, 10 pages, 2021.

[21] T. Guo, W. Zhou, Z. Li et al., "Optimization of land saving and loss reducing and slope stability variation patterns in open-pit mine," *Geofluids*, vol. 2021, Article ID 6620235, 10 pages, 2021.

[22] M. R. Islam, R. Shinjo, M. O. Faruque, H. Shimada, and M. F. Howladar, "Finite element method (FEM) groundwater inflow modeling associated with an unconfined aquifer into the open-pit coalmine of the Phulbari area, NW Bangladesh," *Arabian Journal of Geosciences*, vol. 9, no. 5, 2016.

[23] S. Dong, H. Feng, M. Xia, Y. Li, C. Wang, and L. Wang, "Spatial–temporal evolutions of groundwater environment in prairie opencast coal mine area: a case study of Yimin coal mine, China," *Environmental Geochemistry and Health*, vol. 42, no. 10, pp. 3101–3118, 2020.

[24] Z. Q. Hu, Q. Zhu, X. R. Liu, and Y. Li, "Preparation of topsoil alternatives for open-pit coal mines in the Hulunbuir grassland area, China," *Applied Soil Ecology*, vol. 147, article 103431, 2020.

[25] Y. M. Liu, H. Wang, Y. G. Wu, Y. Zhao, and X. Ren, "Aquifer response to stream-stage fluctuations: field tests and analytical solution for a case study of the Yangtze River in Wuhan, China," *Water*, vol. 13, no. 17, p. 2388, 2021.

[26] L. Lin and H. Lin, "Determination of groundwater sustainable yield using a numerical modelling approach for the Table Mountain group sandstone aquifer, Rawsonville, South Africa," *Hydrogeology Journal*, vol. 27, no. 3, pp. 841–855, 2019.

[27] H. E. Júnez-Ferreira, G. S. Herrera, E. Saucedo, and A. Pacheco-Guerrero, "Influence of available data on the geostatistical-based design of optimal spatiotemporal groundwater-level-monitoring networks," *Hydrogeology Journal*, vol. 27, no. 4, pp. 1207–1227, 2019.

[28] J. Alkhatib, I. Engelhardt, L. Ribbe, and M. Sauter, "An integrated approach for choosing suitable pumping strategies for a semi-arid region in Jordan using a groundwater model coupled with analytical hierarchy techniques," *Hydrogeology Journal*, vol. 27, no. 4, pp. 1143–1157, 2019.

[29] Z. Chunhu, J. Dewu, W. Qiangmin et al., "Water inflow characteristics of coal seam mining aquifer in Yushen mining area, China," *Arabian Journal of Geosciences*, vol. 14, no. 4, p. 278, 2021.

[30] S. Liu, S. Dai, W. Zhang et al., "Impacts of underground coal mining on phreatic water level variation in arid and semiarid mining areas: a case study from the Yushenfu mining area, China," *Environmental Earth Sciences*, vol. 81, no. 9, p. 269, 2022.

[31] Z. Wang, W. Li, Q. Wang, Y. Hu, and J. du, "Monitoring the dynamic response of the overlying rock–soil composite structure to underground mining using BOTDR and FBG sensing technologies," *Rock Mechanics and Rock Engineering*, vol. 54, no. 9, pp. 5095–5116, 2021.

[32] W. J. Sun, Q. Wu, H. L. Liu, and J. Jiao, "Prediction and assessment of the disturbances of the coal mining in Kailuan to karst groundwater system," *Physics and Chemistry of the Earth*, vol. 89-90, no. 2015, pp. 136–144, 2015.

[33] Q. Wang, S. Dong, H. Wang et al., "Effects of groundwater table decline on vegetation transpiration in an arid mining area: a case study of the Yushen mining area, Shaanxi Province, China," *Mine Water and the Environment*, vol. 39, no. 4, pp. 839–850, 2020.

[34] Q. Wu, Y. Liu, X. Wu, S. Liu, W. Sun, and Y. Zeng, "Assessment of groundwater inrush from underlying aquifers in Tunbai coal mine, Shanxi province, China," *Environmental Earth Sciences*, vol. 75, no. 9, p. 737, 2016.

[35] M. Chi, Z. Cao, Q. Li et al., "Water supply and regulation of underground reservoir in coal mine considering coal-water occurrence relationship," *Geofluids*, vol. 2022, Article ID 2892694, 22 pages, 2022.

[36] Z. Wu, T. Xia, J. Nie, and F. Cui, "The shallow strata structure and soil water content in a coal mining subsidence area detected by GPR and borehole data," *Environmental Earth Sciences*, vol. 79, no. 22, 2020.

[37] B. Pepliński and W. Czubak, "The influence of opencast lignite mining dehydration on plant production—a methodological study," *Energies*, vol. 14, no. 7, p. 1917, 2021.

[38] M. T. Bhatti, A. A. Anwar, and M. Aslam, "Groundwater monitoring and management: status and options in Pakistan," *Computers and Electronics in Agriculture*, vol. 135, no. 2017, pp. 143–153, 2017.

[39] H. H. Zhu, Y. A. Dong, L. T. Xing, X. Lan, L. Yang, and Z. Liu, "Protection of the Liuzheng water source: a karst water system in Dawu, Zibo, China," *Water*, vol. 11, no. 4, p. 698, 2019.

[40] Y. Li, F. Zhang, Z. Han, P. Wang, H. Chen, and Z. Zhang, "Evolution characteristics and influence factors of deep groundwater depression cone in North China Plain, China—a case study in Cangzhou region," *Journal of Earth Science*, vol. 25, no. 6, pp. 1051–1058, 2014.

[41] Z. P. Xu, X. Zhou, R. G. Chen, Y. Shen, Z. Shang, and K. Hai, "Numerical simulation of deep thermal groundwater exploitation in the Beijing plain area," *Water*, vol. 11, no. 7, p. 1494, 2019.

[42] K. Martens, M. Van Camp, and K. Walraevens, "Quantification of water table dynamics as a reference for impact assessment of ecohydrological enhancement measures in a dune area in Belgium," *Environmental Earth Sciences*, vol. 73, no. 5, pp. 2223–2240, 2014.

[43] H. H. Li, Y. D. Lu, C. Zheng, X. Zhang, B. Zhou, and J. Wu, "Seasonal and inter-annual variability of groundwater and their responses to climate change and human activities in arid and desert areas: a case study in Yaoba oasis, Northwest China," *Water*, vol. 12, no. 1, p. 303, 2020.

[44] M. Kavusi, A. K. Siuki, and M. Dastourani, "Optimal design of groundwater monitoring network using the combined election-kriging method," *Water Resources Management*, vol. 34, no. 8, pp. 2503–2516, 2020.

[45] L.-M. Fan, T. Li, M. Xiang et al., "Effect of coal mining on springs in the Yushenfu mining area of China," *Geofluids*, vol. 2018, no. 2018, Article ID 3564360, p. 16, 2018.

[46] M. Hosseini and R. Kerachian, "Improving the reliability of groundwater monitoring networks using combined numerical, geostatistical and neural network-based simulation models," *Hydrological Sciences Journal*, vol. 64, no. 15, pp. 1803–1823, 2019.

[47] S. Q. Wang, X. F. Song, Q. X. Wang, G. Xiao, C. Liu, and J. Liu, "Shallow groundwater dynamics in North China plain," *Journal of Geographical Sciences*, vol. 19, no. 2, pp. 175–188, 2009.

[48] Y. Xu, L. Ma, and Y. Yu, "Water preservation and conservation above coal mines using an innovative approach: a case study," *Energies*, vol. 13, no. 11, p. 2818, 2020.

[49] T. L. Saaty, *The Analytic Hierarchy Process: Planning, Priority Setting, Resource Allocatio*, Mcgraw-Hill, 1980.

[50] M. Uyan, "GIS-based solar farms site selection using analytic hierarchy process (AHP) in Karapinar region, Konya/Turkey," *Renewable & Sustainable Energy Reviews*, vol. 28, pp. 11–17, 2013.

[51] Q. Li and W. Sui, "Risk evaluation of mine-water inrush based on principal component logistic regression analysis and an improved analytic hierarchy process," *Hydrogeology Journal*, vol. 29, no. 3, pp. 1299–1311, 2021.

Hindawi
Geofluids
Volume 2022, Article ID 3078233, 10 pages
https://doi.org/10.1155/2022/3078233

Research Article

Extension Limit of a Straight-Swirling Mixed Jet Bit and Its Influential Factors in Radial Jet Drilling

Peng Du, Weikang Xia, and Chaoxiong Yu

School of Mechanical Engineering, Anhui University of Science and Technology, Huainan 232001, China

Correspondence should be addressed to Peng Du; dpeng@aust.edu.cn

Received 3 April 2022; Revised 9 May 2022; Accepted 11 May 2022; Published 23 May 2022

Academic Editor: Yong Li

Radial jet drilling (RJD) is applied to low-permeability and unconventional natural gas. A self-propelled bit chiefly affects the borehole length and drilling efficiency. Herein, for a straight-swirling mixed jet (SSMJ) bit, a prediction model of the drilling extension limit L_{EL} was established by analysing the forces and pressure loss of RJD system. L_{EL} of a specific project was calculated and the pressure loss and forces distribution were obtained. Additionally, the influence laws of the main factors on L_{EL} were studied using the established model. The results indicated that the high-pressure hose contributes the main system pressure loss, and the recoil force of backward nozzles is the sole driving force of RJD. The recoil force of forward nozzle and friction between the hose and borehole constitute the main resistances. Increasing the pump pressure p_b, backward nozzle diameter d_b, and jet diffusion angle θ_x and reducing forward nozzle diameter d_f, impeller central hole diameter d_m, and backward nozzle inclination angle θ_b are conducive to improving L_{EL}. However, larger p_b and d_b increase the hydraulic consumption, besides larger θ_x or smaller d_f, and d_m will reduce the rock-breaking capability. From a sensitivity analysis, p_b and d_m have the maximum and minimum influence on L_{EL}, respectively. Finally, prediction value L_{EL} of an oil well in Eastern Sichuan can be up to 63.7 m. The results provide a guidance for the hydraulic parameters and key component selection, additionally bit structure optimization of RJD.

1. Introduction

China is rich in unconventional natural gas resources of coalbed methane (CBM) and shale gas, etc. [1]. Of these, the total CBM resources in China that are within 2000 m from the ground are estimated to be 36.81 trillion cubic meters [2, 3]. Most of the production wells are located in the southern Qinshui Basin and eastern Ordos Basin [4, 5]. Radial jet drilling (RJD) technology was imposed in the 1980s [6]. The use of RJD to exploit low-permeability oil-gas reservoirs, CBM, and shale gas is a hot topic and an important direction for the development of oil-gas resource drilling [7–10]. A RJD technique utilizes hydraulic energy to create several lateral holes in different directions and levels with several different lengths. These lateral holes are made by milling the casing with a small bit and then extending these holes laterally using high-pressure hydraulic jetting, which can improve the recovery of oil and gas with lower cost [11]. In 2011, Petrobel Company drilled five 50 m radial wells and one 90 m well at two stratums at No.1 well in Belayin Oil Field [12]. The successful application of RJD in the world reflects its promising future.

Predicting the extension limit of the RJD can optimize the layout of boreholes, and it is significant to improve their output. To date, some authors researched the main factors influencing the extension limit, such as the self-propelled force of the bit and system pressure loss. Buset et al. researched the self-propelled force of multiple nozzle jet bits of a RJD system [13]; Ma et al. established a calculation model of pressure loss for RJD system by analysing the pressure loss of a coiled tube and high-pressure hose [14]; Zhang et al. designed a jet radial horizontal drilling simulation experiment system of the casing windowing and evaluated the self-propelled force of a multiorifice nozzle [15].

A self-propelled bit, the "core" of RJD, chiefly affects the borehole length and drilling efficiency. RJD technology changes the direction from a vertical to horizontal direction using a diverter [15]. The turning radius of the interior trail

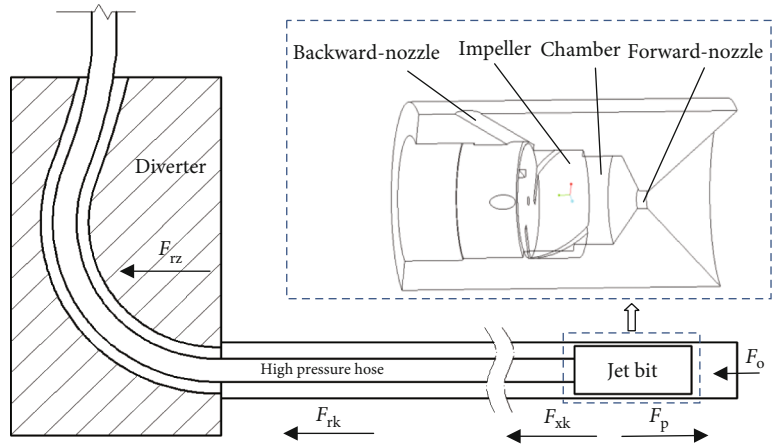

Figure 1: Force model of the RJD system.

within the diverter is small, which limits the dimension of the bit. Therefore, only a simple structure can be selected in the design of bit. Research [16–19] indicated that the jets used for drilling can be divided into three main types: straight, swirling, and a combination thereof. Li et al. researched sandstone-breaking characteristics by experiment and studied the influence of working conditions of lithology, axis length, jet pressure, and standoff distance [20]. Liu et al. adopted the FLUENT combined with RNG turbulence model to analyze the multinozzle jet flow field and study the effects of inclination angle of forward nozzles and standoff distance [21]. Du et al. researched the damage characteristics of straight jet, swirling jet, and SSMJ and then obtained the velocity fields of the three jets by 3DPIV [22]. Overall, a straight jet can drill a deep hole, yet the diameter is smaller because the energy of the jet is more centralized. A swirling jet can be used to drill a larger diameter hole, but it has a boss at the centre owing to the central low-velocity zone of the jet. A combination of a dual-jet nozzle or an SSMJ nozzle can combine the advantages of both a straight jet and swirling jet [23–25]. Few articles have been published on the research on predicting the extension limit of an SSMJ and its influential factors.

With an SSMJ as the research objective, this study established a model to predict the extension limit of a RJD system by analysing the distributions of force and pressure loss. Thereafter, the drilling extension limit of a specific project was calculated and the pressure loss and forces were obtained. Finally, the influence laws of the main parameters (pump pressure, diameter of the forward nozzle and backward nozzles, diffusion angle of the jet, inclination angle of the backward nozzle, etc.) on the extension limit were studied using the established prediction model; additionally, the influence degree of parameters was investigated. We conducted these studies in an attempt to provide a guidance for the construction parameter selection of the RJD.

2. Mathematical Model

During drilling, the horizontal section of the RJD system has a self-propelled force of the bit (F_p), the pressure of an external fluid on the bit (F_o), friction between the diverter and high-pressure hose (F_{rz}), friction between the borehole and high-pressure hose (F_{rk}), and friction between the borehole and bit (F_{xk}), as shown in Figure 1. Owing to the lower flow rate of the system and the use of a pure water jet during operation, the viscosity is low, and the viscous resistance of the fluid in the borehole to the hose is also small, which can be ignored. The resultant force F on the RJD system is expressed as

$$F = F_p - F_o - F_{rz} - F_{rk} - F_{xk}. \quad (1)$$

2.1. Self-Propelled Force of the Bit. An SSMJ bit composes of a body and an impeller with a central hole and several slots (Figure 1). Its basic operating principle is as follows: the fluid flows into the mixing chamber through the central hole and slots of the impeller, generating a low-speed, straight-swirling flow. An SSMJ with a high axial velocity and peripheral rotational intensity is then created successively under the pressurization of the nozzle outlet, and the extended section ensures a specific target distance when breaking rock. In addition, the jets created by the backward nozzles can push the bit and high-pressure hose forward. A straight jet has only a one-dimensional velocity; however, for a swirling jet, the trajectory is approximately a helix, and the velocity of any particle is a space vector, its axial velocity u is parallel to the jet axis, and its radial and tangential velocities v and w are perpendicular to the jet axis [26, 27]. When the system is operating, the forces of the bit include the recoil force of the backward nozzles (F_b) and recoil force of the forward nozzle (F_f). Naturally, the self-propelled force of the bit F_p is F_b minus F_f.

2.1.1. Recoil Force of the Forward Nozzle. The recoil force of the SSMJ forward nozzle was produced from two parts: straight jet and swirling jet. If the forward nozzle and the impeller central hole diameter are d_f and d_m, respectively, the flow area of the swirling jet is the difference between the forward nozzle area and the central hole area, and the equivalent diameter of the swirling jet can be obtained:

$$d_x = \sqrt{d_f^2 - d_m^2}. \quad (2)$$

(a) Recoil Force of the Straight Jet. The equation to calculate the recoil force of the straight jet acting on the bit is [27]

$$F_m = 1.56\mu_f d_m^2 p_i, \quad (3)$$

where p_i is the nozzle inlet pressure (MPa) and μ_f is the flow coefficient of the forward nozzle

(b) Recoil Force of the Swirling Jet. Swirling jet is a three-dimensional flow different from the straight one. The axial velocity u of any particle of the swirling jet is perpendicular to v and w; thus, v and w do not produce an axial recoil force. According to the law of mass conservation, the total flow rate q_x is the sum of the axial flow rate q_u, radial flow rate q_v, and tangential flow rate q_w. The recoil force of the swirling jet acting on the jet bit is only related to q_u and can be expressed as

$$F_x = 0.745 q_u \sqrt{p_i} \quad (4)$$

The axial velocity distribution along the radial of the swirling jet is approximately shaped as "M"; therefore, for ease of calculation, we can assume that all fluid particles of the swirling jet are distributed on the cone with a diffusion angle of θ_x. Moreover, the approximate relationship between the axial velocity flow rate (q_u) and total flow rate (q_x) can be obtained:

$$q_u = q_x \cos\frac{\theta_x}{2}. \quad (5)$$

Additionally, q_x is

$$q_x = 2.1\mu_f d_x^2 \sqrt{p_i}. \quad (6)$$

Combining Equations (4), (5), and (6), we obtain

$$F_x = 1.56\mu_f \left(d_f^2 - d_m^2\right) p_i \cos\frac{\theta_x}{2}. \quad (7)$$

Finally, the forward nozzle recoil force is

$$F_f = F_m + F_x = 1.56\mu_f p_i \left[d_m^2 + \left(d_f^2 - d_m^2\right)\cos\frac{\theta_x}{2}\right]. \quad (8)$$

2.1.2. Recoil Force of Backward Nozzles. Referring to the analysis method in the previous section, the equation for the backward nozzle recoil force can be written as

$$F_b = \sum_{b=1}^{n_b} 1.56\mu_b d_b^2 p_i \cos\theta_b, \quad (9)$$

where n_b is the number of backward nozzles and d_b, θ_b, and μ_b are the diameter, inclination angle, and flow coefficient of a backward nozzle, separately.

Combining Equations (8) and (9), the self-propelled force of the SSMJ bit can be obtained:

$$F_p = 1.56 p_i \left[\sum_{b=1}^{n_b} \mu_b d_b^2 \cos\theta_b - \mu_f d_m^2 - \mu_f\left(d_f^2 - d_m^2\right)\cos\frac{\theta_x}{2}\right]. \quad (10)$$

2.2. Pressure of the External Fluid on the Bit. In the axial direction, the drill bit is subjected to the pressure of the fluid in the hole on the front end face. The following equation of this pressure F_o is obtained:

$$F_o = \frac{\pi}{4} p_o \left(d_o^2 - d_f^2\right), \quad (11)$$

where d_o is the outer diameter of the bit (mm) and p_o is the pressure of the external fluid on the front end face of the bit (MPa). To be specific, p_o is the sum of the annulus pressure loss and ground pressure, and the ground pressure is 0; thus, the value of p_o is the annulus pressure loss, which can be calculated according to the relevant research [14].

2.3. Friction Resistance of the System. The friction resistance (F') of the RJD system primarily includes the friction between the diverter and hose (F_{rz}), the friction between the borehole and the hose (F_{rk}), and the friction between the borehole and the bit (F_{xk}). Of these, F_{rz} can be obtained through a laboratory test, while

$$F_{rk} = \mu_{rk} G_r l_{rk}, \; F_{xk} = \mu_{xk} G_x, \quad (12)$$

where μ_{rk} is the friction coefficient between the hose and borehole, G_r is the submerged weight of a unit length of the hose (N/m), l_{rk} is the friction section length of the hose (m), μ_{xk} is the friction coefficient between the bit and borehole, and G_x is the submerged weight of the jet bit (N).

Substituting Equations (10), (11), and (12) into (1), the force model of the RJD system can be obtained:

$$F = 1.56 p_i \left[\sum_{b=1}^{n_b} \mu_b d_b^2 \cos\theta_b - \mu_f d_m^2 - \mu_f\left(d_f^2 - d_m^2\right)\cos\frac{\theta_x}{2}\right] - \frac{\pi}{4} p_o \left(d_o^2 - d_f^2\right) - F_{rz} - \mu_{rk} G_r l_{rk} - \mu_{xk} G_x. \quad (13)$$

2.4. Pressure Loss of the System. We need to calculate the pressure loss of the RJD system to obtain the inlet pressure of the bit (p_i). Ignoring the leakage at the joint and the local pressure loss such as hose diameter variation and bending, the system pressure loss is primarily generated by the coiled tubing (Δp_{cti}) and the high-pressure hose (Δp_r):

$$p_i = p_b - \Delta p_{cti} - \Delta p_r, \quad (14)$$

where p_b is the pump pressure (MPa).

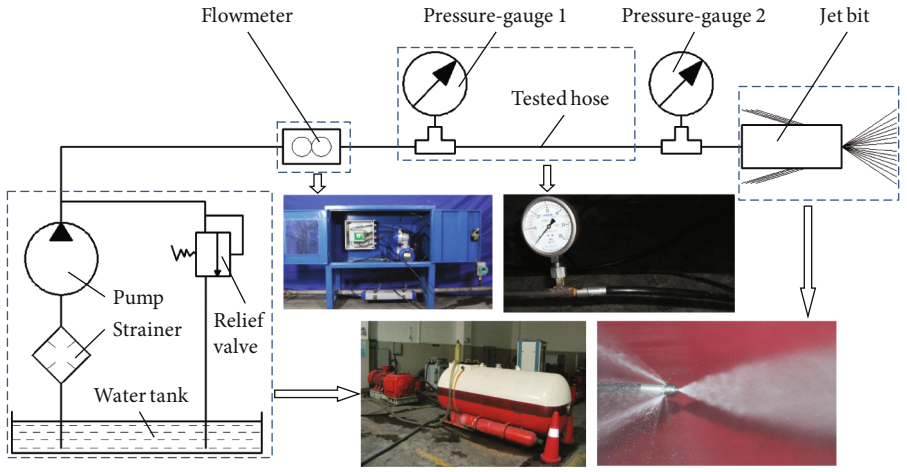

Figure 2: Schematic of the test system.

2.4.1. Theoretical Pressure Loss. The pressure loss along the coiled tubing Δp_{cti} includes the spiral section loss Δp_{cti1} and straight section loss Δp_{cti2}, i.e., $\Delta p_{cti} = \Delta p_{cti1} + \Delta p_{cti2}$, which can be obtained from the previous studies [14].

The theoretical pressure loss of the hose can be obtained using the following equation [28]:

$$\Delta p_r = K_r \times \frac{59.7 q^2 l_r}{d_{ri}^5 \, \mathrm{Re}^{0.25}}, \tag{15}$$

where $K_r = 1$, d_{ri} is the hose inner diameter (mm), q is the volume flow rate (L/min), l_r is the total length of the hose (m), and Re is the Reynolds number, which should be written as $\lambda q / d_{ri}$, and the coefficient λ is 1.12×10^4 under turbulent condition. According to the previous studies [14], the theoretical value of hose pressure loss is quite deviation from the actual, and then, it will greatly affect the judgment of the inlet pressure value of the bit. The correction of Equation (15) is necessary to be performed through an experimental test.

2.4.2. Experimental Test. In this study, several groups of tests were executed under different factors of the flow rate, hose inner diameter, and length; then, the measured pressure loss values under different factors were obtained; moreover, the parameters under each factor were substituted into Equation (15) to obtain the calculated value. By comparing the measured and calculated values, the correction factor K_r is introduced to Equation (15), and the deviation of K_r is analyzed to evaluate the effectiveness of the test. Eventually, K_r is taken as an average value.

The following apparatuses were used (Figure 2): a high-pressure pump, an SSMJ bit, high-pressure hoses of 1/4" (inner diameter of 6.35 mm) and 3/8" (inner diameter of 8 mm), a flowmeter, and two pressure gauges. The two gauges were, respectively, allocated at the inlet and outlet of the tested hose; therefore, the difference reading between pressure gauges No.1 and No.2 was the pressure loss value of the hose when the system operated steadily. The test results are listed in Table 1. K_r is introduced to correct Equation (15). The values of K_r under different conditions range from 0.23 to 0.27, with the relative standard deviation of 1.3%. A small deviation rate proves the effectiveness of the test; then, the final correction factor is taken as an average value, i.e., $K_r = 0.25$.

2.5. Mathematical Model of the Extension Limit. When the resultant force $F > 0$, the RJD system can continuously drill forward. As the drilled radial borehole length increases, the friction increases and F decreases gradually until $F = 0$. Herein, the system is in an equilibrium condition of forces and the bit will not continue to drill forward with the hose; eventually, the value l_{rk} under this condition is exactly the extension limit of the RJD system. Substituting $F = 0$ into Equation (13), we can obtain the prediction model of the extension limit L_{EL}:

$$L_{EL} = \frac{1.56 p_i \left[\sum_{b=1}^{n_b} \mu_b d_b^2 \cos\theta_b - \mu_f \left(d_m^2 + \left(d_f^2 - d_m^2\right) \cos\left(\theta_x/2\right)\right)\right] - (\pi/4) p_o \left(d_o^2 - d_f^2\right) - F_{rz} - \mu_{xk} G_x}{\mu_{rk} G_r}. \tag{16}$$

3. Results and Discussion

3.1. Project Setting. A field construction condition of an oil well in Eastern Sichuan, China, with a radial well depth of 1500 m and casing model of 7" (inner diameter of 168.6 mm) was selected as the analyzed case of this study, and the working pressure of the field pump is 60 MPa. A pure water jet, with a temperature of approximately 90°C

Table 1: Test data of the high-pressure hoses.

Hose length (m)	Hose inner diameter (mm)	Flow rate (L/min)	Tested Δp_r (MPa)	Calculated Δp_r (MPa)	Correction factor Kr
10	6.35	117	10.8	41.68	0.26
10	6.35	55	2.8	11.18	0.25
20	6.35	117	20.0	83.35	0.24
20	6.35	55	5.6	22.35	0.25
10	8	117	3.4	13.13	0.26
10	8	55	0.8	3.52	0.24
20	8	117	7.1	26.26	0.27
20	8	55	1.6	7.04	0.23

Table 2: Main parameters of the project.

l_{ct} (m)	d_{cto} (mm)	d_{cti} (mm)	l_r (m)	d_{ro} (mm)	d_{ri} (mm)	G_r (N/m)	ρ_z (g/cm^3)	l_z (mm)	d_o (mm)	d_i (mm)	d_f (mm)	d_m (mm)	θ_x (°)	n_b	d_b (mm)	θ_b (°)
2000	38.1	31.75	120	14.3	8	2.3	15	30	18	8	1.8	1	60	3	1.3	30

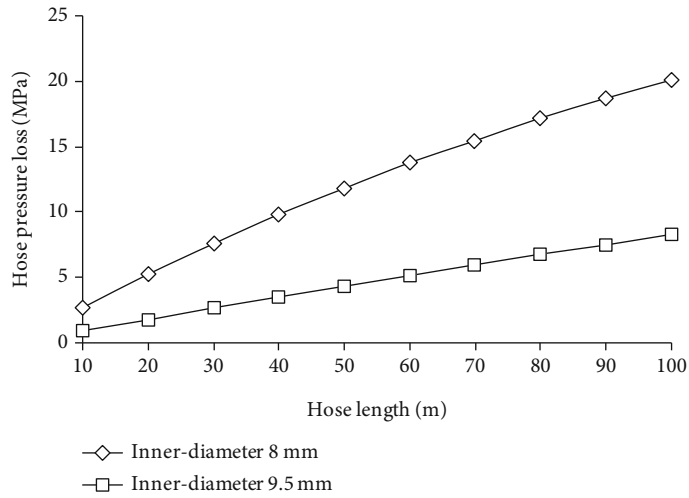

Figure 3: Hose pressure loss influenced by the hose length.

under this operating condition, a density of 965.4 kg/m^3, and a viscosity of 0.315×10^{-3} Pa·s, was used. A drilling experiment using an SSMJ bit has been executed previously; then, a borehole with a diameter of 25 mm was obtained, and μ_{rk} and μ_{zk} are both 0.3. According to experience and the previous laboratory tests, the flow coefficients of the forward and backward nozzles μ_f and μ_b are both set as 0.83; furthermore, the friction between the hose and diverter F_{rz} was obtained as 20 N through a ground test.

A coiled tubing with a model of 1.5" was used, and its main parameters of length l_{ct} and outer and inner diameter d_{cto} and d_{cti} are shown in Table 2; additionally, Table 2 shows the length l_r and outer and inner diameter d_{ro} and d_{ri} and submerged weight G_r of high-pressure hose with a model of 5/16"; the self-propelled bit was made by cemented carbide, and its specific dimensions are also shown in Table 2, such as density ρ_z, length l_z, outer diameter d_o, inner diameter d_i, forward nozzle diameter d_f, impeller central hole diameter d_m, jet diffusion angle θ_x, number of backward nozzles n_b, diameter of backward nozzle d_b, and inclination angle of backward nozzle θ_b.

3.2. Pressure Loss Analysis. The construction parameters were substituted into Ma et al.'s study [14] and Equation (15) to obtain the pressure loss distribution along the coiled tubing and high-pressure hose, separately. The main pressure loss of the system was observed to emanate from the high-pressure hose, which was 20.1 MPa, accounting for 92.6% of the total.

The hose parameters (inner diameter d_{ri} and length l_r) have a significant impact on the pressure loss (Figure 3). The pressure loss increases as a quadratic function with the increase in l_r, which will reduce the extension limit. Therefore, the length of the hose should be as short as possible. During engineering construction, l_r must be chosen according to the designed radial borehole length, and a little longer than the designed borehole length should be most suitable. The pressure loss is highly sensitive to the variation in d_{ri}; therefore,

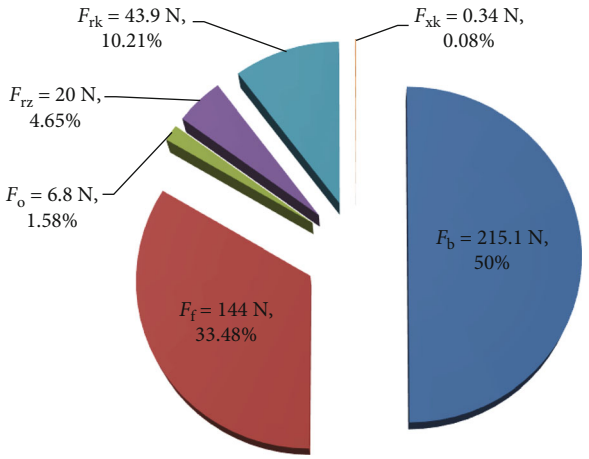

Figure 4: Force distribution of the RJD system.

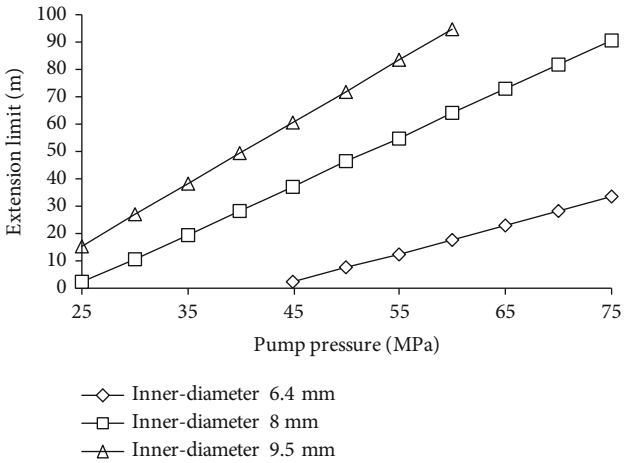

Figure 5: Extension limit influenced by the pump pressure.

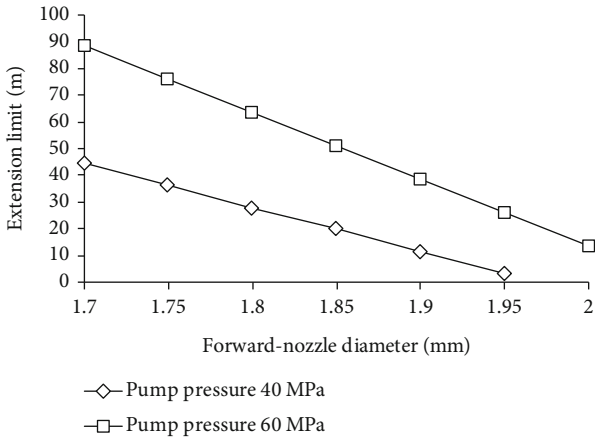

Figure 6: Extension limit influenced by the forward nozzle diameter.

d_{ri} should be as large as possible, provided that the high-pressure hose can smoothly pass through the diverter.

3.3. Extension Limit Results and Analysis. The construction parameters of an oil well in Eastern Sichuan were placed into Equation (16), and the extension limit of the RJD system L_{EL} was calculated as 63.7 m. The force distribution in the horizontal section of RJD is shown in Figure 4. We observe that the recoil force (F_b) of the backward nozzle is the sole driving force for the system to drill forward; thus, increasing the equivalent diameter of the backward nozzles (any nozzle diameter or number) is the most effective method of increasing the drilling depth. The recoil force (F_f) of the forward nozzle is the main resistance of the system, accounting for 66.96% of the total resistance. Therefore, the diameter of the forward nozzle should be appropriately reduced, provided that its rock-breaking performance satisfies the design requirements. The friction between the hose and borehole (F_{rk}) increases with the increase in drilling depth. When the axial force of the system is balanced, F_{rk} also reaches the maximum. Herein, F_{rk} accounts for 20.42% of the total resistance. A hose with a light weight and smooth outer surface should be selected to reduce F_{rk}. In the bit structure design, the roundness of the drilled hole is used as an evaluation index. The friction between the hose and diverter (F_{rz}) accounts for 9.3% of the total resistance. A hose with a small turning radius should be selected in a RJD system to reduce F_{rz}. In the design of diverter, the hose and bit should be investigated on whether they can pass through the diverter smoothly.

3.4. Influential Factor Analysis for Extension Limit

3.4.1. Pump Pressure. We changed the pump pressure p_b and maintained other parameters in the engineering example to obtain the variation law of extension limit L_{EL} with p_b under different inner diameters of the hose (Figure 5). We observed that the extension limit increases approximately linearly with the increase in p_b. Besides, the inner diameter of the high-pressure hose has a significant influence on L_{EL}. When the inner diameter is 6.4 mm, the drill bit can drag the high-pressure hose forward after p_b reaches 45 MPa, whereas when the diameter is 8 mm, the drill bit can drag the high-pressure hose forward when p_b reaches 25 MPa. The larger the inner diameter, the greater the slope, additionally the higher the rise rate of L_{EL}, which indicates that the increase in the inner diameter of the hose can effectively reduce the pressure loss and improve the inlet pressure of the bit.

3.4.2. Forward Nozzle Diameter. We changed the forward nozzle diameter (d_f) and maintained other parameters in the engineering example to obtain the variation law of L_{EL} (Figure 6). We observed that when the pump pressure is 60 MPa, the decline rate of L_{EL} is greater than that when 40 MPa. This is because when the pump pressure is relatively high, the flow rate of the system is relatively large. As d_f increases, the increase rate of the system pressure loss is also faster, which increases the decline rate of the nozzle inlet pressure compared with when the pump pressure is relatively low, and finally increases the decline rate of the drilling extension limit. Under the same pump pressure, L_{EL} decreases approximately linearly with the increase in d_f;

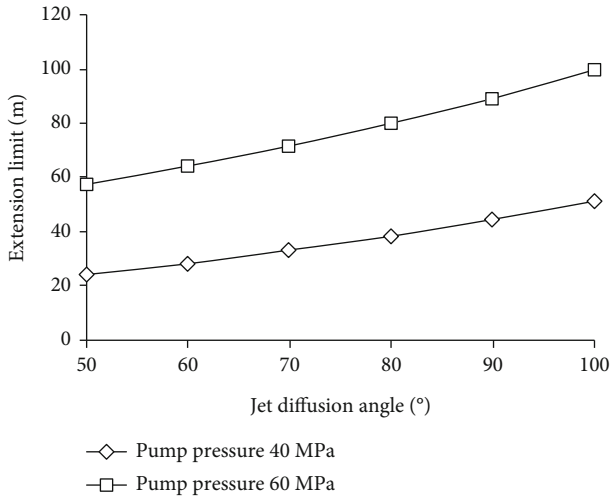

Figure 7: Extension limit influenced by the diffusion angle.

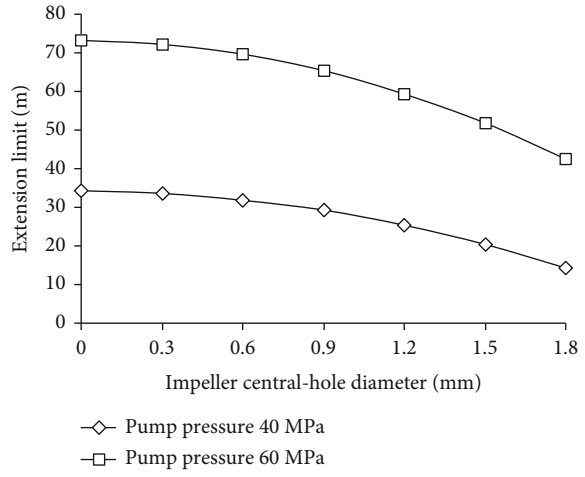

Figure 8: Extension limit influenced by the impeller central hole.

therefore, reducing the diameter of the forward nozzle is conducive to increasing L_{EL}. However, the main function of the forward nozzle is to generate an SSMJ for rock-breaking to enable the system to continuously drill forward. The smaller diameter of the forward nozzle weakens the energy of the jet and the rock-breaking performance of the bit becomes worse. Therefore, when selecting d_f, we should also combine with rock-breaking research and appropriately reduce d_f under the premise that the rock-breaking efficiency satisfies the operating requirements.

3.4.3. Jet Diffusion Angle. We changed the jet diffusion angle (θ_x) by adjusting the slot dip angle of the impeller and maintained other parameters in the engineering example to obtain the variation law of L_{EL} (Figure 7). We observed that under the same pump pressure, L_{EL} increases as a cosine curve with the increase in θ_x. By increasing θ_x, the axial velocity of the swirling jet decreases, and then, the recoil force of the forward nozzle decreases. The decrease in the system resistance can improve L_{EL} of the system, but an excessively large diffusion angle will also weaken the rock-breaking efficiency of the SSMJ. Therefore, the flow field and erosion performance analysis must be combined to obtain the optimal θ_x.

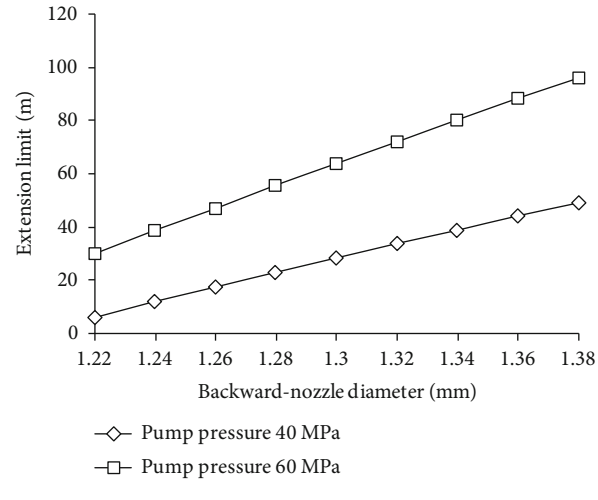

Figure 9: Extension limit influenced by the backward nozzle diameter.

3.4.4. Impeller Central Hole Diameter. The variation law of L_{EL} was obtained by changing the diameter of the impeller central hole d_m (Figure 8). Under the same pump pressure, L_{EL} decreases in a quadratic function with the increase in d_m. Therefore, the diameter can be appropriately reduced to increase L_{EL}. However, according to the previous research, when d_m is small, the central boss easily appears in the borehole bottom, which hinders the advancement of the bit and reduces the drilling speed. Therefore, the size of the central hole should satisfy the larger L_{EL} and drilling speed. When d_m is greater than 1.5 mm, L_{EL} decreases to a lower value, and the decline rate reaches 40% under the pump pressure of 60 MPa. Thus, d_m less than 1.5 mm is more appropriate; additionally, the specific results can be further investigated combining the drilling efficiency test.

3.4.5. Backward Nozzle Diameter. We changed the backward nozzle diameter (d_b) and maintained other parameters in the engineering example to obtain the variation law of L_{EL} (Figure 9). Under the same pump pressure, L_{EL} increases approximately linearly with the increase in d_b. According to the data, the increase rate of L_{EL} decreases with the increase in d_b. For example, under the condition of a pump pressure of 60 MPa, when d_b changes from 1.22 to 1.24 mm, L_{EL} increases by 8.55 m, whereas for a d_b changes from 1.36 to 1.38 mm, L_{EL} increases by 7.85 m. Increasing d_b is the most effective method of increasing the drilling depth. However, at the same pump pressure, the increase in d_b increases the flow rate, additionally increases the water consumption and pressure loss of the system, and reduces the increase rate of L_{EL}. Therefore, considering the system loss and economy, d_b cannot increase indefinitely and should be determined according to the drilling extension limit required by the construction design.

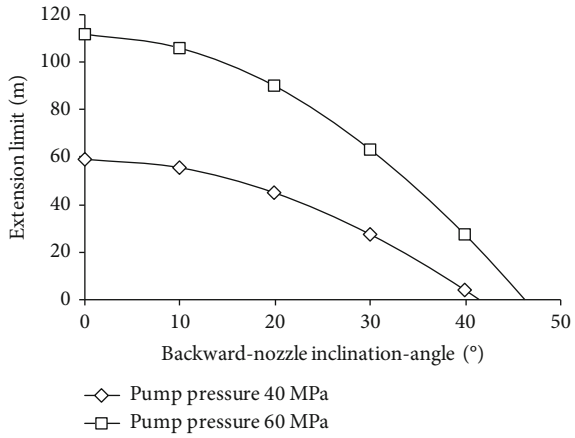

Figure 10: Extension limit influenced by the backward nozzle inclination angle.

3.4.6. Backward Nozzle Inclination Angle. We changed the inclination angle of the backward nozzle (θ_b) to obtain the variation law of L_{EL} (Figure 10). Under the same pump pressure, L_{EL} decreases as a cosine function with an increase in θ_b. Except for providing the SSMJ a driving force, the backward nozzle also has the function of reaming. Reducing θ_b is conducive to increasing L_{EL}, but its reaming capacity decreases, and too small θ_b will cause the fluid to erode the high-pressure hose. According to the prediction model of L_{EL}, when the pump pressure is 60 MPa and θ_b is 0, L_{EL} is 111.91 m. When θ_b increases to 20°, 30°, and 40°, L_{EL} decreases to 90.20, 63.68, and 27.69 m, respectively. When θ_b reaches 48.4°, L_{EL} is 0. Overall, L_{EL} decreases relatively rapidly when θ_b exceeds 30°. Therefore, it is reasonable to select θ_b of 30° to ensure both a large L_{EL} and borehole diameter.

3.5. Parameter Sensitivity Analysis. In this study, the method of grey relational analysis (GRA) was used to investigate the influence degree of six factors above on the extension limit, such as pump pressure p_b, forward nozzle diameter d_f, jet diffusion angle θ_x, impeller central hole diameter d_m, backward nozzle diameter d_b, and backward nozzle inclination angle θ_b. GRA refers to the uncertain correlation between objects or between subsystems and between factors and main behavior. Its basic assignment is to analyze and determine the influence degree between factors or the contribution degree of factors to main behavior, based on the micro or macro geometric proximity of behavior factor sequences. The detailed calculation process is as follows:

(1) Determine the reference and comparison sequences: taking the reference sequence reflecting the characteristics of system behavior as y, and the comparison sequence affecting system behavior as x_i, the corresponding equation is as follows:

$$\begin{cases} y = \{y(k) | k = 1, 2, \cdots, n\}, \\ x_i = \{x_i(k) | k = 1, 2, \cdots, n\}, \end{cases} \tag{17}$$

where k and i are the group k and column i of a specific quantity value in the matrix composed of sequences, $y(k)$ is the reference sequence value of the data group k and its unit is related to the chosen physical quantity, and $x_i(k)$ is the value of the i'th influential factor of data group k and its unit is also related to the selected physical quantity

(2) Dimensional normalization processing of the data: it is necessary to unify the unit for different parameters, usually the dimensional normalization methods including mean value, initial value, maximization, and minimization. The initial value method was adopted, since it is suitable for the data with a tendency and regularity and is often used in comprehensive evaluation, such as GRA

(3) Calculation of relation coefficient: the equation is as follows:

$$\xi_i(k) = \frac{\min\limits_i \min\limits_k |x_0(k) - x_i(k)| + \rho \bullet \max\limits_i \max\limits_k |x_0(k) - x_i(k)|}{|x_0(k) - x_i(k)| + \rho \bullet \max\limits_i \max\limits_k |x_0(k) - x_i(k)|}, \tag{18}$$

where ρ is the resolution coefficient and has a value range between 0 and 1, usually as 0.5. The smaller ρ, the greater the difference between relation coefficients, and the stronger the discrimination ability. After calculating the relation coefficient, take the average value of each coefficient as the grey relation coefficient of the factor, and the calculation equation is

$$r_i = \frac{1}{n} \sum_{k=1}^{n} \xi_i(k), \tag{19}$$

where r_i is the relation degree of the i'th influential factor

Take the extension limit L_{EL} of the jet bit under different parameters as the reference sequence, which is y_o, and take p_b, d_f, θ_x, d_m, d_b, and θ_b as the comparison sequence, which are x_1 to x_6, respectively. It is found that taking L_{EL} as the

Table 3: Calculation results.

Comparison sequence	Relation coefficient	Sensitivity order
p_b	0.52963	1
θ_x	0.51874	2
d_f	0.51867	3
d_b	0.51856	4
θ_b	0.51852	5
d_m	0.51842	6

evaluation index, the order of parameter sensitivity from large to small is p_b, θ_x, d_f, d_b, θ_b, and d_m (Table 3).

4. Conclusions

Through analysing the force and pressure loss of the RJD system, a model to predict the drilling extension limit L_{EL} was established. The L_{EL} value of a specific project was calculated and the pressure loss and forces were obtained. The influence laws of the main parameters on L_{EL} were studied using the established prediction model. The conclusions are summarized as follows:

(1) The sensitivity of pressure loss to the variation in the inner diameter is higher, because the diameter of high-pressure hose is significantly lower than that of the coiled tubing, and the main pressure loss of the system results from the high-pressure hose. The backward nozzle recoil force is the only driving force of the system, and the forward nozzle recoil force and friction between the hose and borehole contain the main resistance of the system. The drilling extension limit prediction value of the project in this article can reach up to 63.7 m

(2) Under the same pump pressure, L_{EL} of the system increases approximately linearly with the increase in backward nozzle diameter, yet this will significantly increase hydraulic consumption and pressure loss; it decreases linearly with the increase in the forward nozzle diameter. Therefore, the design of the rear nozzle should not blindly pursue the large L_{EL} but also consider that the hydraulic consumption and pressure loss are within a reasonable range; the forward nozzle diameter can be as small as possible on the premise of ensuring rock-breaking efficiency. L_{EL} increases with the increase in the swirling jet diffusion angle; the diffusion angle can also be reduced to ensure the capability of rock-breaking rock. L_{EL} decreases as a quadratic function with the increase in the backward nozzle installation angle; when the angle is larger than 30°, the decrease in L_{EL} rate is high. From parameter sensitivity analysis, the factors that have the greatest and least influence on L_{EL} are p_b and d_m, respectively. Hence, increasing p_b is the most direct and effective way to raise L_{EL}, while the design of d_m does not depend on the requirements of L_{EL}, but on its rock-breaking capacity

(3) This research provides a theoretical guideline for predicting the extension limit of RJD under a specific working condition, optimizing the bit structure, and choosing high-pressure hose and hydraulic parameters. The specific bit structure parameters should be further obtained through rock-breaking performance tests combined with this study. In addition, laboratory simulation of RJD experiment and field test will be performed in the future

Data Availability

All data generated or used during the study appearing in the submitted article are available from the corresponding author upon request.

Conflicts of Interest

The authors declared no potential conflicts of interest with respect to the research, authorship, and/or publication of this article.

Acknowledgments

This study was financially supported by the National Natural Science Foundation of China (NSFC) under Grant No. 51804007.

References

[1] Y. Li, Z. S. Wang, S. H. Tang, and D. Elsworth, "Re-evaluating adsorbed and free methane content in coal and its ad- and desorption processes analysis," *Chemical Engineering Journal*, vol. 428, article 131946, 2022.

[2] Y. Qin, T. A. Moore, J. Shen, Z. Yang, Y. Shen, and G. Wang, "Resources and geology of coalbed methane in China: a review," *International Geology Review*, vol. 60, no. 5-6, pp. 777–812, 2018.

[3] R. M. Flores, *Coal and Coalbed Gas: Fueling the Future*, Elsevier Science Publishing Co Inc, United States, 2014.

[4] Y. Li, J. Yang, Z. Pan, S. Meng, K. Wang, and X. Niu, "Unconventional natural gas accumulations in stacked deposits: a discussion of Upper Paleozoic coal-bearing strata in the east margin of the Ordos Basin, China," *Acta Geologica Sinica-English Edition*, vol. 93, no. 1, pp. 111–129, 2019.

[5] Y. Li, Z. Wang, Z. Pan, X. Niu, Y. Yu, and S. Meng, "Pore structure and its fractal dimensions of transitional shale: a cross-section from east margin of the Ordos Basin, China," *Fuel*, vol. 241, pp. 417–431, 2019.

[6] W. Dickinson and R. W. Dickinson, "Horizontal radial drilling system," in *Presented at the SPE California Regional Meeting*, pp. 27–29, Bakersfifield, California, 1985.

[7] Y. Li and T. Zhang, "Investigation of the factors affecting the self-propelled force in a multi-orifice nozzle using a novel simulation method," *Energy Science and Engineering*, vol. 8, no. 9, pp. 3136–3147, 2020.

[8] Y. Y. Lu, Z. Zhou, Z. L. Ge, X. W. Zhang, and Q. Li, "Research on and design of a self-propelled nozzle for the tree-type drilling technique in underground coal mines," *Energies*, vol. 8, no. 12, pp. 14260–14271, 2015.

[9] X. L. Li, S. J. Chen, S. Wang, M. Zhao, and H. Liu, "Study on in situ stress distribution law of the deep mine: taking Linyi mining area as an example," *Advances in Materials Science and Engineering*, vol. 2021, Article ID 5594181, 11 pages, 2021.

[10] D. Z. Dong, C. N. Zhou, J. Z. Li, S. J. Wang, X. Li, and J. L. Huang, "Resource potential, exploration and development prospect of shale gas in the whole world," *Geological Bulletin of China*, vol. 30, no. 2, pp. 324–336, 2011.

[11] A. Kochnev, S. Galkin, S. Krivoshchekov, N. Kozyrev, and P. Chalova, "Application of machine learning algorithms to

predict the effectiveness of radial jet drilling technology in various geological conditions," *Applied Sciences*, vol. 11, no. 10, p. 4487, 2021.

[12] A. M. Ragab and A. M. Kamel, "Radial drilling technique for improving well productivity in petrobel-Egypt," in *Proceedings of the North Africa Technical Conference and Exhibition*, Held in Cairo, Egypt, 2013.

[13] P. Buset, M. Riiber, and A. Eek, "Jet drilling tool: cost-effffective lateral drilling technology for enhanced oil recovery," in *Paper SPE 68504 Presented at the SPE/ICoTA Coiled Tubing Round table*, Houston, Texas, USA, 2001.

[14] D. J. Ma, G. S. Li, and Z. W. Huang, "A model of calculating the circulating pressure loss in coiled tubing ultra-short radius radial drilling," *Petroleum Exploration and Development*, vol. 39, no. 4, pp. 528–533, 2012.

[15] T. Zhang, Y. Li, H. Lu, and J. Jiang, "Simulation and experimental study on characteristics of multiorifice nozzle in radial jet drilling," *Geofluids*, vol. 2022, Article ID 2531181, 8 pages, 2022.

[16] Y. Y. Lu, Y. Liu, X. H. Li, and Y. Kang, "A new method of drilling long boreholes in low permeability coal by improving its permeability," *International Journal of Coal Geology*, vol. 84, no. 2, pp. 94–102, 2010.

[17] D. J. Ma, G. S. Li, J. L. Niu, H. L. Liao, and Z. W. Huang, "Experimental study on rock breaking and drilling laws by multi-hole jet bit," *Fluid Mach*, vol. 43, no. 3, pp. 1–5, 2015.

[18] Y. Tang, P. Sun, G. R. Wang, B. W. Fu, and J. X. Yao, "Rock-breaking mechanism and efficiency of straight-swirling mixed nozzle for the nondiagenetic natural gas hydrate in deep-sea shallow," *Energy Science & Engineering*, vol. 8, no. 10, pp. 3740–3752, 2020.

[19] J. B. Li, G. S. Li, Z. W. Huang, X. Z. Song, R. R. Yang, and K. W. Peng, "The self-propelled force model of a multi-orifice nozzle for radial jet drilling," *Journal of Natural Gas Science and Engineering*, vol. 24, pp. 441–448, 2015.

[20] J. B. Li, J. C. Dai, Z. W. Huang, G. Zhang, X. Liu, and H. Li, "Rock breaking characteristics of the self-rotating multi-orifice nozzle for sandstone radial jet drilling," *Rock Mechanics and Rock Engineering*, vol. 54, no. 11, pp. 5603–5615, 2021.

[21] Y. B. Liu, Q. B. Ba, L. P. He, K. Shen, and W. Xiong, "Study on the rock-breaking effect of water jets generated by self-rotatory multinozzle drilling bit," *Energy Science & Engineering*, vol. 8, no. 7, pp. 2457–2470, 2020.

[22] P. Du, Y. Y. Lu, J. R. Tang, H. Zhou, and W. F. Zhang, "Characteristics and mechanism of rock breaking for new type straight-swirling integrated jet," *Journal of Xi'an Jiaotong University*, vol. 50, no. 3, pp. 81–89, 2016.

[23] W. G. Buckman, *Method and Apparatus for Jet Drilling Drainholes from Wells*, U.S. Patent 6, 263, 984 B1, 2001.

[24] D. J. Ma, G. S. Li, X. N. Zhang, and Z. W. Huang, "Experimental study on rock breaking by a combined round straight jet with a swirling jet nozzle," *Atomization and Sprays*, vol. 21, no. 8, pp. 645–653, 2011.

[25] H. L. Liao, G. S. Li, J. L. Niu, and Z. W. Huang, "Integrating straight & swirling jets bit design and its rock breaking characteristics for radial horizontal hole drilling," *Journal of China Coal Society*, vol. 38, no. 3, pp. 424–429, 2013.

[26] I. Toh, D. Honnery, and J. Soria, "Velocity and scalar measurements of a low swirl jet," in *Fourth Australian Conference on Laser Diagnostics in Fluid Mechanics and Combustion, The University of Adelaide*, pp. 129–132, South Australia, Australia, 2005.

[27] Z. H. Shen, *Water Jet Theory and Technology*, Petroleum University Publishing House, Dongying, Shandong, China, 1998.

[28] T. J. Labus, *Fluid Jet Technology: Fundamentals and Application*, Water Jet Technology Association, St. Louis, MO, USA, 1995.

Hindawi
Geofluids
Volume 2022, Article ID 5055273, 9 pages
https://doi.org/10.1155/2022/5055273

Research Article

Study on the Effect of Salinity and Water Content on CBM Adsorption/Desorption Characteristics of Coal Reservoir in Baode Block

Wei Zhang,[1,2] Yanxiang He,[1,2] Qingfeng Zhang,[1,2] Yanjun Meng,[3,4] Tuo Liu,[1,2] Wenhui Meng,[1,2] Yun Zuo,[1,2] and Hongbo Fan[1,2]

[1]*School of Resources and Geoscience, China University of Mining and Technology, Xuzhou 221006, China*
[2]*China United Coalbed Methane Co. Ltd., Beijing 100016, China*
[3]*College of Mining Engineering, Taiyuan University of Technology, Taiyuan 030024, China*
[4]*Shanxi Key Laboratory of Coal and Coal Measure Gas Geology, Taiyuan 030024, China*

Correspondence should be addressed to Yanjun Meng; mengyanjun15@126.com

Received 18 March 2022; Accepted 6 May 2022; Published 21 May 2022

Academic Editor: Dan Ma

The adsorption/desorption characteristics of a coal reservoir play an important role in coalbed methane (CBM) development. The proximate analysis, maceral analysis and methane isothermal adsorption/desorption experiment are carried out based on coal samples from no. 4+5 coal seam in Baode block. Combing with coal experimental data and the CBM well-produced water salinity data in the Baode block, the effect of salinity and water content on CBM adsorption/desorption characteristics of the coal reservoir and its influencing mechanism is discussed. The results show that the CBM adsorption and desorption capacity decreases with the increase of water salinity and the decrease value shows a decreasing trend. The increase of water salinity reduces the solubility of methane in coal seam water and then reduces the adsorption capacity of methane. With the increase of water content, the adsorption and desorption capacities of CBM decrease gradually. The CBM adsorption and desorption capacities decrease with the increase of water content in coal samples. The adsorption/desorption capacities of coal samples change rapidly in the low-water content stage and slowly in the high-water content stage. The competitive adsorption effect and water blocking effect between water and methane molecules are the main influencing mechanisms of water content on CBM adsorption/desorption. It can be seen that the salinity and water content will have a certain adverse impact on the adsorption and desorption capacity of CBM in the Baode block. The influence of the difference in water content and salinity in the coal seam cannot be ignored in reserve evaluation and productivity prediction of CBM. The continuous, stable, and effective drainage is one of the key factors to ensure the efficient development of CBM wells in the Baode block.

1. Introduction

China is rich in CBM resources, and the amount of CBM resources buried at a depth of 2000 m or shallower is 30.05×10^{12} m^3, accounting for 11.6% of the total global CBM resources, with huge development potential [1]. According to incomplete statistics, by the end of 2020, 19540 vertical CBM wells and 1677 horizontal CBM wells had been drilled in China, in which 12880 had been put into production [2]. The accumulative proven CBM geological reserves are 9302×10^8 m^3, and the national production of CBM in 2020 was 58.2×10^8 m^3 [2]. Committing to achieving peak carbon dioxide emissions before 2030 and achieving carbon neutrality before 2060, promoting the efficient development and utilization of CBM is of great significance to "carbon neutrality;" however, the unconventional characteristics of CBM mainly in the adsorbed state have always been one of the difficult issues in the CBM development field.

Adsorption/desorption characteristics are the basis for revealing the occurrence mechanism and efficient development of CBM. The adsorption/desorption property has a significant impact on the gas content in a coal reservoir

and the productivity of a CBM well and is an important parameter for evaluating the development potential of a coal reservoir [3–5]. The adsorption/desorption characteristics of a coal reservoir are usually characterized by methane isothermal adsorption/desorption experiment and the Langmuir equation, but the curves and parameters measured by the national standard method are unable to fully reflect the influence of high-salinity water on the adsorption/desorption characteristics in the in-situ state of a coal reservoir.

Previous studies revealed that salinity inhibits the adsorption capacity of coal seams [6–9]. Liu et al. carried out simulation experiments on the adsorption capacity of lignite to CBM under different salinity conditions and found that the increase of salinity could lead to the decrease of adsorption capacity in a coal reservoir [6]. Wang et al. studied the adsorption capacity of a coal core under different salinity conditions and believed that high salinity will reduce the adsorption capacity [7]. Yi et al. studied the methane desorption rate of granular anthracite coal samples under the condition of water injection with different salinity and found that the salinity reduced the methane desorption rate in coal [8]. Wei et al. found that there was a limit value for the influence of water salinity on the coal adsorption capacity and the limit was about 10000 mg/L for long-flame coal from the southern margin of the Junggar Basin [9].

Compared with the salinity, the influence of water on the adsorption/desorption characteristics of CBM was more widely studied. Joubert et al. first studied American bituminous coal samples and found that the adsorption of methane by moisture is closely related to the properties of coal. Under the condition of saturated moisture, water will not further affect the adsorption of methane in coal [10]. Krooss et al. carried out the adsorption experiments of methane and CO_2 on multiple coal samples under dry and wet conditions and found that the adsorption capacity of methane will decrease by 25% when the water content increases by 1% [11]. Other researchers in China successively carried out isothermal adsorption experiments on coal samples under the condition of equilibrium water. They believe that the molecular force between water and coal is stronger than methane, which reduces the adsorption performance of coal [12–14]. In addition, in the process of CBM development, when the water-based fracturing fluid invades the nanopore structure of coal, it will inevitably affect the adsorption/desorption characteristics of the coal reservoir and then affect the production of CBM wells.

Although predecessors have recognized that salinity and water will affect the adsorption/desorption capacity of coal reservoirs, no relevant research has been carried out on the Baode block, which is a hot spot area of medium-low-rank CBM development in China. Due to the low degree of thermal evolution of coal in the Baode block, the adsorption capacity of a coal reservoir is weak and the gas content is low. Therefore, compared with medium- and high0-rank coal blocks, the influence of salinity and water content on the adsorption/desorption capacity of coal reservoirs is particularly significant in this block. It has a great impact on the accuracy of CBM reserve calculation and coal reservoir adsorption/desorption capacity evaluation. In view of the abovementioned problems, relying on the major national science and technology project of CBM, this study studies the influence of salinity and water content on the adsorption/desorption characteristics of coal reservoirs in the Baode block, in order to provide basic support for the deployment and optimization of efficient exploration and development scheme of CBM in this block.

2. Sampling Background and Experimental Methods

2.1. Geological Setting. In the administrative division, the Baode block is located in the northwest of Shanxi province, covering an area of 476.46 km^2. Structurally, it is located in the northern part on the eastern edge of the Ordos Basin (Figure 1). It is generally characterized by a monoclinal structure inclined to the west, with a stratigraphic dip angle of 5°~10°, and the fault structure is not very developed. Groundwater in the block mainly comes from atmospheric precipitation and lateral recharge of Ordovician limestone. It is generally runoff from east to west, and the hydrological environment is in the runoff weak runoff area.

The main coal-bearing strata in the Baode block are the Taiyuan Formation and Shanxi Formation. The no. 4+5 coal seam in the Shanxi Formation and the no. 8+9 coal seam in the Taiyuan Formation are the main coal seams for CBM development [15]. The single-layer thickness of the no. 4+5 coal seam is between 5 and 14.6 m, with an average of 7.6 m. The single-layer thickness of no. 8+9 is between 5 and 14.2 m, with an average of 10.2 m. The vitrinite reflectance of the coal in the Baode block ranges from 0.71% to 1.22%, belonging to highly volatile bituminous coal [16].

2.2. Sample Collection. The coal samples used in this study were collected from no. 4+5 coal samples of Wangjialing coal mine in the Baode block (Figure 1). The sampling was carried out in accordance with the methods for coal seam sampling (following Chinese National Standards GB/T482-2008). The macrolithotypes and heterogeneity of coal seams were fully considered in the sample collection, and the samples were highly representative. The samples were collected from the fresh coal face of the mine and then immediately put into the sampling bag and fasten to prevent pollution and oxidation.

2.3. Experimental Methods. The maximum vitrinite reflectance ($R_{o,max}$, %) measurements and maceral analysis were performed on the same polished section of coal samples, following Chinese National Standards GB/T6948-1998 and GB/T8899-1998. Proximate analysis was performed following Chinese National Standard GB/T212-2001 for samples to obtain the ash yield, moisture, and volatile contents of the coals.

The isothermal adsorption experiment is the main technical method to characterize the ability of a coal reservoir to adsorb CBM. In order to study the influence of salinity and water content on adsorption/desorption characteristics of coal reservoirs, methane isothermal adsorption desorption tests of coal samples from the Baode block under different

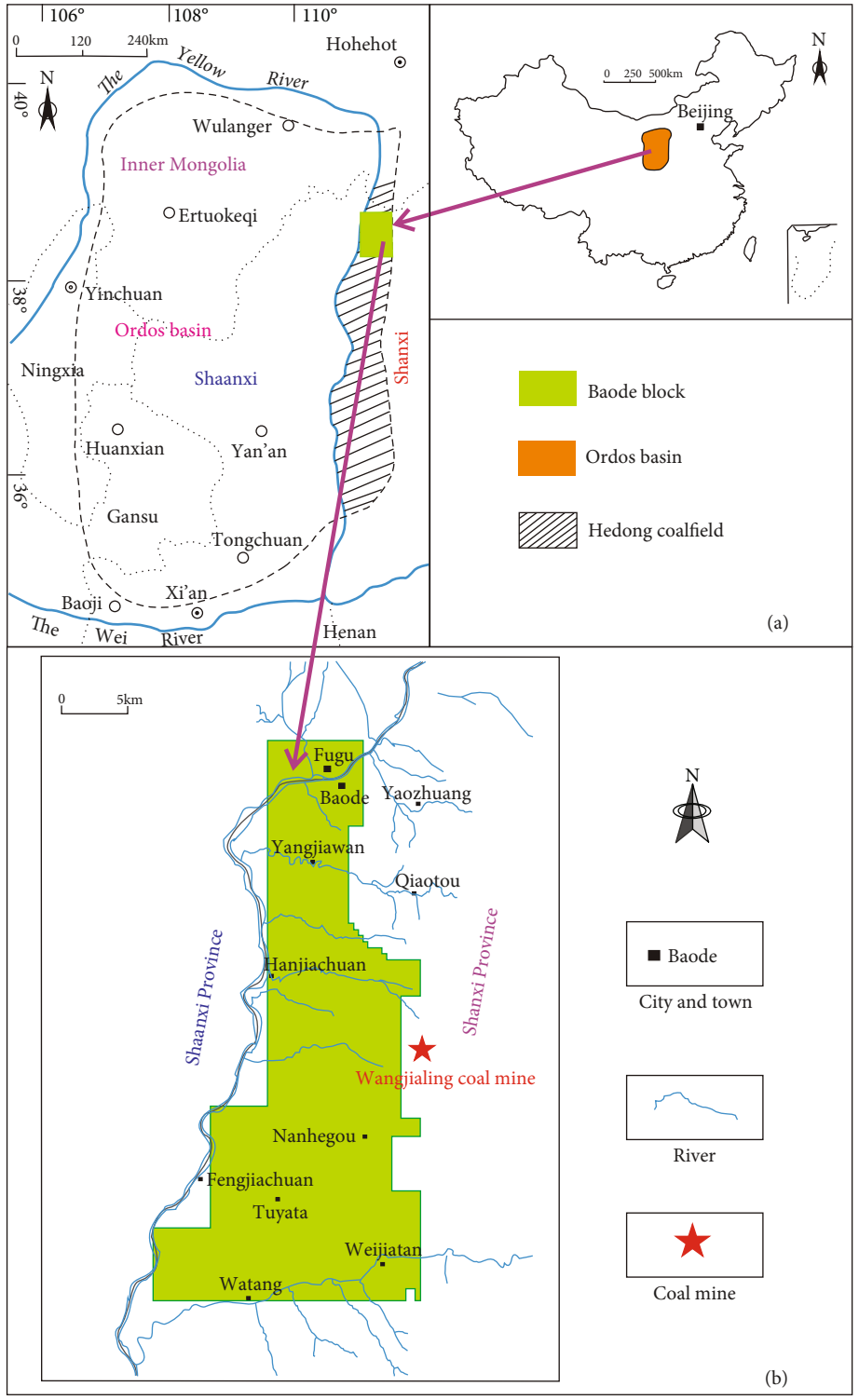

Figure 1: (a) Location of the Ordos Basin and Baode block. (b) Location of Wangjialing coal mine and the scope of the Baode block.

salinity and water contents were carried out. The experimental instrument adopts the automatic isothermal adsorption instrument, which is implemented in accordance with the high-pressure isothermal adsorption test method of coal (GB/T 19560-2008). It should be noted that all adsorption capacity data and Langmuir isothermal adsorption parameter data in this study are based on air drying basis. The experimental tests were carried out in the Shanxi Key Laboratory of Coal and Coal-Measure Gas Geology.

3. Results and Discussions

3.1. Coal Petrology and Quality Characteristics. The results of vitrinite reflectance, proximate analysis, and maceral

Table 1: Coal vitrinite reflectance, proximate analysis, and maceral composition in the Baode block.

Sample no.	$R_{o,max}$ (%)	Proximate analysis (%)			Maceral composition (%)			
		M_{ad}	A_d	V_{daf}	V	I	E	MM
BD-WJL-04	0.81	2.16	14.44	35.62	48.7	32.1	5.8	13.6

$R_{o,max}$: maximum vitrinite reflectance; V: vitrinite; I: inertinite; E: liptinite; MM: mineral matter; M_{ad}: moisture (air dry basis (ad)); A_d: ash yield (air dry basis (ad)); V_{daf}: volatiles (dry and ash free (daf)).

composition of the coal samples are shown in Table 1. The maximum vitrinite reflectance of the experimental coal sample is 0.81%, belonging to highly volatile bituminous coal. The organic maceral composition of the experimental coal sample is dominated by vitrinite (48.7%), followed by inertinite (32.1%) and liptinite(5.8%). Besides, the proximate analysis result shows that moisture, ash yield, and volatiles are 2.16%, 14.44%, and 35.62%, respectively.

3.2. Effects of Salinity on Adsorption/Desorption CBM Characteristics. This study carried out the experimental analysis of methane isothermal adsorption and desorption of coal samples under different salinity conditions for no. 4 +5 coal samples of Wangjialing coal mine. Since the coal seam water salinity measured by the chemical analysis of the produced water of no. 4+5 CBM well in the Shanxi Formation of the Baode block ranges from 902 to 2026 mg/L (Table 2) [17], the salinity gradients of the simulated formation water used in the isothermal adsorption/desorption experiment were set as 1000, 1400, 1800, and 2200 mg/L in this study.

3.2.1. Effects of Salinity on CBM Adsorption/Desorption Capacity. By comparing the adsorption and desorption curves of coal samples from the Baode block soaked in water with different salinity gradients (1000, 1400, 1800, and 2200 mg/L), it can be found that the adsorption and desorption capacities of CBM generally decrease with the increase of coalbed water salinity and the decline value of adsorption and desorption capacities generally decrease with the increase of coalbed water salinity (Figure 2).

The isothermal adsorption constants of the coal samples with different salinity gradients (1000, 1400, 1800, and 2200 mg/L) were calculated by the Langmuir equation (Table 3). The Langmuir volumes of the coal samples were 18.75, 15.68, 13.86, and 12.43 m^3/t, and the Langmuir pressure values are 3.86, 3.18, 3.08, and 2.79 MPa, respectively. The adsorption capacity with a salinity of 1000 mg/L is the largest. The higher the salinity, the smaller the Langmuir volume characterizing the adsorption capacity, indicating that the salinity of coalbed water will have an adverse impact on the adsorption of CBM.

3.2.2. Effects of Different Salinity on CBM Desorption Lag Characteristics. The isothermal adsorption/desorption curves of no. 4+5 coal samples from the Baode block under different salinity conditions are shown in Figure 2. It can be found that for each salinity gradient, there is always a desorption lag in the desorption curve, reflecting that the adsorption capacity of CBM is greater than the desorption capacity under the same differential pressure. From the comparison of curve characteristics under different salinity, it is evident that the desorption lag phenomenon has no obvious relationship with the salinity gradients (Figure 2). Because the equivalent adsorption heat of CBM desorption is greater than that of adsorption, the desorption process needs to absorb heat from the outside system. The energy difference between the adsorption process and the desorption process may be the key factor of the CBM desorption lag [18]. Ma et al. analyzed from the perspective of the pore structure and believed that the main reason for the desorption lag was the stronger binding ability of micropores and small pores to methane molecules [19].

3.2.3. Effect Mechanism of Salinity on CBM Adsorption/Desorption Characteristics. Wei et al. studied the massive coal samples of the Jurassic Xishanyao Formation in the Manas mining area on the southern edge of the Junggar Basin; they found that with the increase of inorganic salt concentration in the solution, the surface tension of the solution increased and the capillary phenomenon became more obvious, which further reduced the adsorption site on the surface of the coal matrix, thus reducing the Langmuir volume and adsorption capacity of coal samples to methane. However, there is also a limit value. If the salinity is greater than 20000 mg/L, the salinity can no longer significantly reduce the Langmuir volume of coal samples [9].

In recent years, with the successful application of nanopore analysis and molecular simulation technology in the field of unconventional oil and gas, some scholars have verified and explained the characteristics of methane adsorption/desorption from the perspective of numerical simulation. Zhou et al. confirmed through the research of molecular simulation technology that salinity has a negative impact on the methane adsorption capacity of kerogen [20]. In a certain salinity range, the higher the salinity, the greater the impact on methane adsorption, and when the salinity was 6 mol/L and the temperature was 338.15 K, the methane adsorption capacity decreased by about 6.0% [20] (Figure 3). The existence of NaCl reduces the solubility of methane in brine and then reduces the adsorption capacity of methane. These research results can also explain the reason why the methane adsorption capacity and desorption capacity of the coal reservoir in the Baode block decrease with the increase of coalbed water salinity in this study from aspects of experiment and numerical simulation. Meanwhile, it also indicates that the influence of salinity should not be ignored in the evaluation of the CBM reservoir.

3.3. Effects of Water Content on CBM Adsorption/Desorption Characteristics. This study carried out the experimental analysis of methane isothermal adsorption and desorption

Table 2: The ion composition and water type of produced water in no. 4+5 coal in the Baode block. [17].

Well no.	Cationic concentration (mg/L)			Anion concentration (mg/L)			Salinity (mg/L)	Water type
	$Na^+ + K^+$	Mg^{2+}	Ca^{2+}	SO_4^{2-}	Cl^-	HCO_{3-}		
B-1	283	44	29	7	336	471	1175	$NaHCO_3$
B-2	398	69	59	21	558	474	1580	$NaHCO_3$
B-3	305	43	51	7	319	465	1190	$NaHCO_3$
B-8	432	50	75	1	591	460	1610	$NaHCO_3$
B-11	577	57	64	8	607	715	2026	$NaHCO_3$
B-12	252	24	36	4	236	781	1333	$NaHCO_3$
B-23	128	45	25	82	114	311	707	$NaHCO_3$
B-22	105	22	30	2	130	432	721	$NaHCO_3$
B-24	314	63	64	23	425	413	1301	$NaHCO_3$
B-25	287	41	22	42	282	393	1067	$NaHCO_3$
B-26	167	73	50	189	243	180	902	Na_2SO_4
B-27	459	16	24	10	460	567	1538	$NaHCO_3$
B-29	174	51	91	98	198	432	1045	Na_2SO_4
B-17	574.6	54.7	125	1	725	485	1969	$NaHCO_3$
B-19	604	53.4	25	3	733	522	1943	$NaHCO_3$

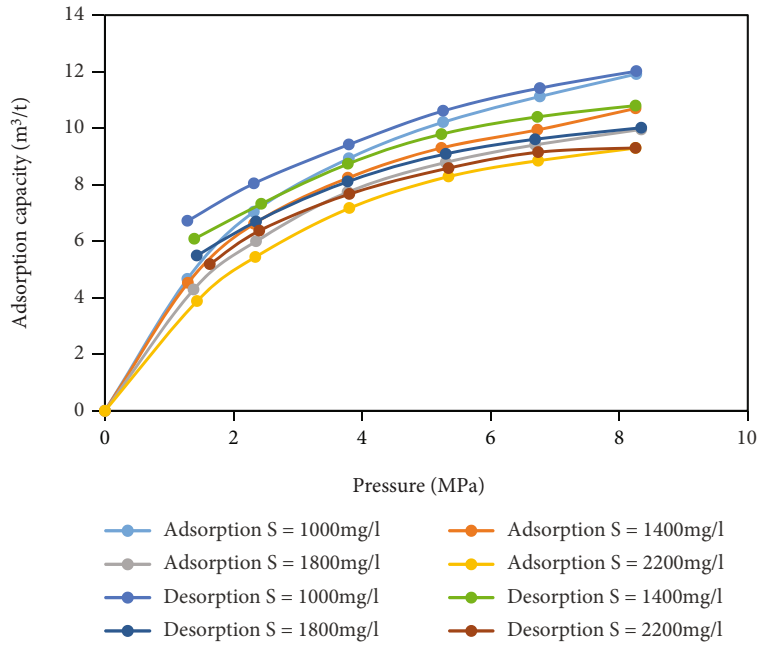

Figure 2: Methane isothermal adsorption/desorption curves of coal samples with different salinity.

Table 3: Langmuir isothermal adsorption parameters of Baode coal samples with different salinity.

Salinity gradients	V_L (m^3/t)	P_L (MPa)
1000 mg/L	18.75	3.86
1400 mg/L	15.68	3.18
1800 mg/L	13.86	3.08
2200 mg/L	12.43	2.79

of coal samples under different water content gradients for no. 4+5 coal samples of Wangjialing coal mine. The water content gradient values are set according to the equilibrium water content value of the no. 4+5 coal seam in the Baode block. The preliminary exploration well coal core experiment shows that the equilibrium water saturation obtained from the isothermal adsorption experiment of lump coal samples in Baode district is about 5%. Therefore, in this study, the water content gradients of experimental coal samples are set as 2%, 3%, 4%, and 5%.

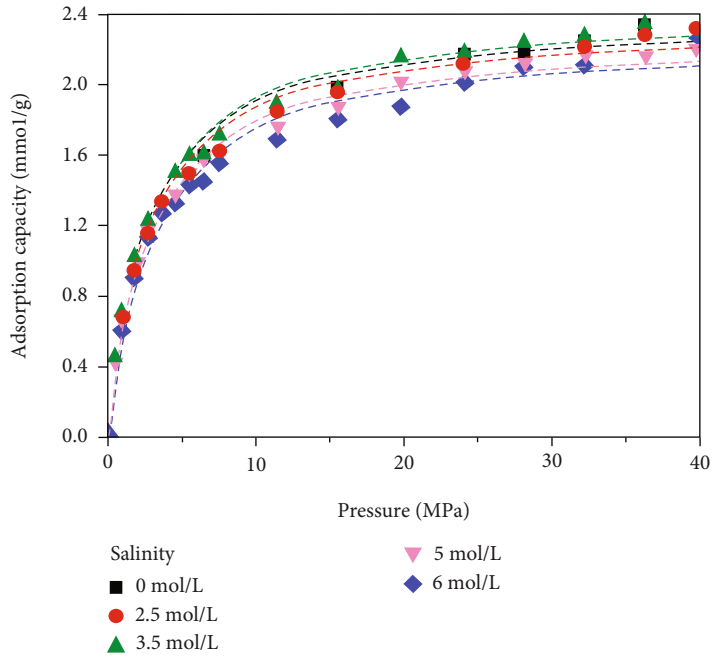

Figure 3: Methane adsorption isotherms of different salinities with the water content of 3 wt % at 338.15 K. Points are results of simulation, and lines are results of Langmuir fitting [20].

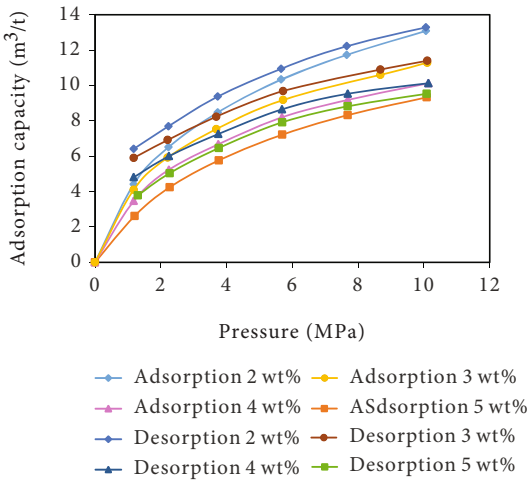

Figure 4: Methane isothermal adsorption/desorption curves of coal with different water contents.

3.3.1. Effects of Water Content on CBM Adsorption/Desorption Capacity. By comparing the adsorption and desorption curves of coal samples with different water contents of coal 4+5 in the Baode block, it can be found that the CBM adsorption and desorption capacities generally decrease with the increase of water content in coal samples (Figure 4). The CBM adsorption and desorption in coal samples will decrease with the increase of water content. In the stage of low water content, the adsorption/desorption of methane changes rapidly, and in the stage of high water content, the change is slow. It can be seen that the high water content of coal seams will have an adverse impact on the rapid and efficient desorption of CBM in the Baode block.

Table 4: Langmuir isothermal adsorption parameters of Baode coal samples with different water content.

Coal samples with different water content	V_L (m^3/t)	P_L (MPa)
2%	16.78	3.52
3%	14.09	3.05
4%	13.05	3.35
5%	13.03	4.71

The isothermal adsorption constants of the samples were calculated by the Langmuir equation (Table 4). The Langmuir volumes of the samples were 16.78, 14.09, 13.05, and 13.03 m^3/t, and the Langmuir pressure values are 3.52, 3.05, 3.35, and 4.71 MPa, respectively. The adsorption capacity with a water content of 2% is the largest. The higher the water content, the smaller the Langmuir volume characterizing the adsorption capacity, indicating that the water in the coal seam will have an adverse impact on the desorption/adsorption of the CBM.

3.3.2. Effects of Water Content on CBM Desorption Lag Characteristics. The isothermal adsorption/desorption curve of no.4+5 coal samples of the Shanxi Formation in the Baode block under different water content conditions is shown in Figure 5. It can be seen that there is always a desorption lag in coal samples under different water content conditions but there is no obvious correlation with the water content (Figure 4). Previous studies have shown that the lag mechanism of coal samples is mainly reflected in two aspects, i.e.,

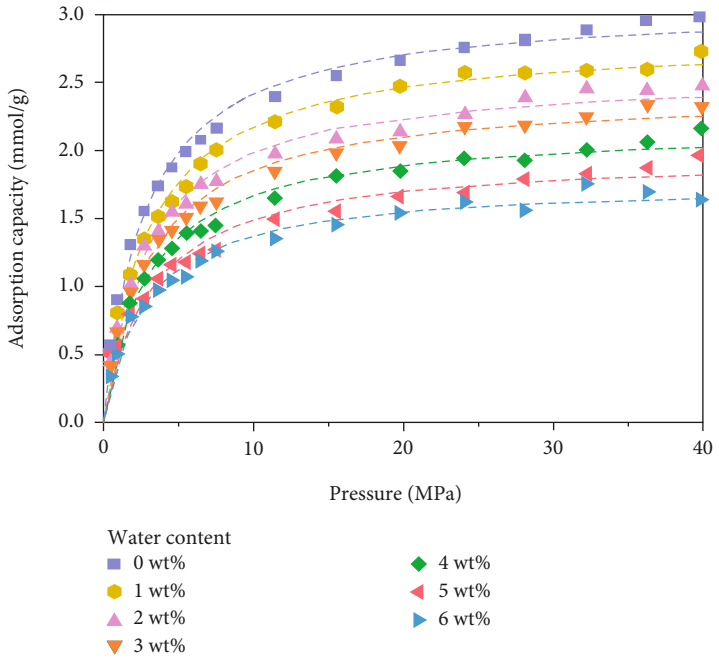

Figure 5: CH_4 adsorption isotherms under different water contents at 338.15 K. Points are results of simulation, and lines are results of Langmuir fitting [20].

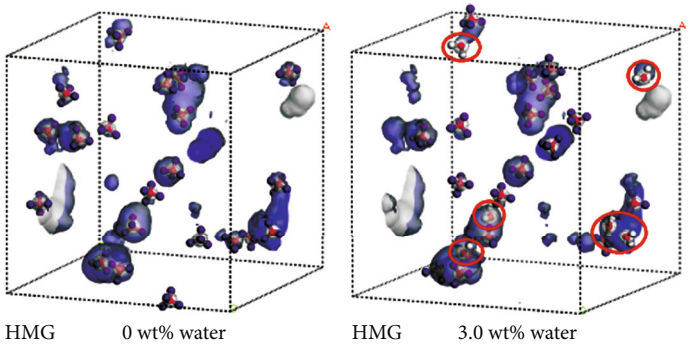

Figure 6: Simulation of adsorption of CH_4 on coal macromolecules with different water content [25] (red elliptic circles represent water competitive adsorption sites).

desorption obstruction and gas migration obstruction. The moisture is one of the main factors affecting the desorption lag of CBM. The lag degree of the water-bearing coal sample is significantly higher than that of the dry coal sample, but it has no obvious relationship with water content [21, 22], which is confirmed by the results of this study.

3.3.3. Effect Mechanism of Water Content on CBM Adsorption/Desorption Characteristics. Previous studies have shown that water has a significant impact on the adsorption/desorption characteristics of the CBM [12–14, 21, 22]. The influence mechanism of water content on methane adsorption/desorption characteristics of coal samples is mainly reflected in two aspects, i.e., the competitive adsorption effect between water and methane molecules and the water lock effect.

Because the interaction force between coal and water molecules is much greater than that of coal and methane molecules, in the case of three-phase medium coexistence, water and methane molecules produce competitive adsorption on the coal surface and water molecules will be replaced to partially adsorb methane, resulting in the reduction of methane adsorption capacity of the coal reservoir. Zhou et al. confirmed through molecular simulation technology that the increase of water content will reduce the adsorption capacity of the kerogen to methane (Figure 5). The density distribution changes of methane and water molecules show that water molecules occupy some adsorption sites in the kerogen matrix to prevent methane from entering the nanopores, which leads to the decline of methane adsorption capacity of the kerogen [20].

The water content of coal is closely related to the coal wettability, which can indirectly affect the adsorption/desorption characteristics of CBM [23, 24]. Water molecules are easy to combine with the broken chemical bonds on the surface of the coal matrix and the hydrophilic functional

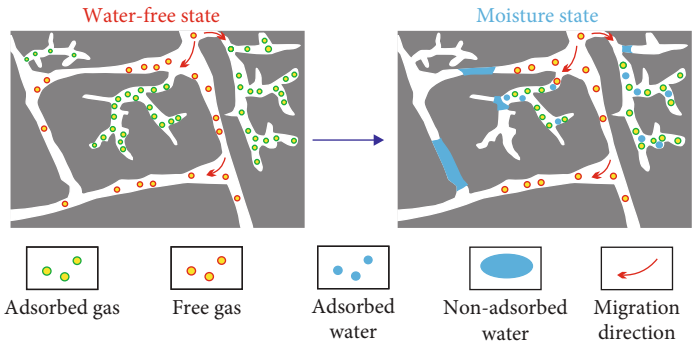

Figure 7: Influence of water locking effect on adsorption/desorption characteristics of methane in coal (modified from literature [26]).

groups inside the coal matrix, resulting in the enhancement of hydrophilicity of the coal. The surface free energy of coal is reduced to a certain extent, and the heat released by reaching the methane-coal adsorption system equilibrium state is decreasing. The molecular force between water and coal is stronger than that of methane, which can occupy effective adsorption sites on the coal surface and weaken the methane adsorption capacity of coal (Figure 6) [25].

In addition, the continuous accumulation of adsorption of water molecules on the surface of micropores and fissures in coal will lead to water molecules occupying some pore and throat channels in coal, leading to a water lock effect [26]. The higher the water content of the coal is, the stronger the water locking effect is. The existence of the water lock effect leads to the blockage of some pore channels and the obstruction of methane movement channels, which leads to the decrease of methane adsorption and desorption capacity in coal (Figure 7). In this study, the experimental results of methane adsorption and desorption capacities of coal reservoir in the Baode block decrease with the increase of coal water content, which is consistent with the understanding of previous theoretical studies and also indicates that the influence of coal water content cannot be ignored in the reserve evaluation and development effect prediction of CBM in a high water-bearing coal seam.

4. Conclusion

(1) Desorption lag phenomenon exists, under any condition of salinity and water content, in coal of the Baode block, but there are differences in desorption lag degree with different salinity and water content. The moisture content is the main factor affecting the desorption lag. The CBM desorption lag mechanism is mainly reflected in blocked desorption and blocked gas migration. The energy difference between the adsorption and desorption processes is the key internal factor of the desorption lag. The influence of water content and the strong binding effect of micropores on methane are also important factors of the CBM desorption lag

(2) With the increase of salinity, the adsorption and desorption capacities of coal in the Baode block show a decreasing trend in general and the decrease value of adsorption and desorption capacities shows a decreasing trend. The increase of coal seam water salinity reduces the solubility of methane in brine and then reduces the adsorption capacity of methane. The influence of coalbed water salinity cannot be ignored in the reserve evaluation of CBM resources

(3) The adsorption and desorption capacities of CBM decrease gradually with the increase of water content. The adsorption and desorption capacities decrease rapidly in the stage of low water content, while slowly in the stage of high water content. The competitive adsorption effect and water locking effect between water and methane molecules are the main influencing mechanisms of water content on methane adsorption/desorption. The influence of water content in the coal seam cannot be ignored in CBM reserve evaluation and productivity prediction in a high water-bearing coal seam

(4) The salinity and water content in the coal reservoir will have a certain adverse effect on the adsorption and desorption capacities of CBM in the Baode block. Continuous, stable, and effective water production is one of the key factors to ensure the efficient development of CBM in this block

Data Availability

All data are from our team's coal sample experimental test data and references, which have been described in detail in this paper.

Conflicts of Interest

The authors declare that they have no conflicts of interest.

Acknowledgments

This work was funded by the Natural Science Foundation of Shanxi Province, China (20210302123165), and the National Major Science and Technology Project (2016ZX05042). We would like to thank engineers Sun Xiaoguang and Shang Yanjie from China United Coalbed Methane Co. Ltd. for helping in the coal sample collection.

References

[1] X. Y. Men, Z. Han, B. S. Gao, J. H. Ren, and B. L. Cui, "Present situation and development suggestion of CBM exploration and development in China," *China Mining Magazine*, vol. 26, no. S2, pp. 1–4, 2017.

[2] F. Y. Xu, B. Wang, X. Zhao et al., "Thoughts and suggestions on promoting high quality development of China's CBM business under the goal of double carbon," *China Petroleum Exploration*, vol. 26, no. 3, pp. 9–18, 2021.

[3] Y. J. Meng, D. Z. Tang, H. Xu, Y. J. Qu, Y. Li, and W. Z. Zhang, "Division of coalbed methane desorption stages and its significance," *Petroleum Exploration and Development*, vol. 41, no. 5, pp. 671–677, 2014.

[4] S. Tao, S. D. Chen, D. Z. Tang, X. Zhao, H. Xu, and S. Li, "Material composition, pore structure and adsorption capacity of low-rank coals around the first coalification jump: a case of eastern Junggar Basin, China," *Fuel*, vol. 211, pp. 804–815, 2018.

[5] J. C. Ye, S. Tao, S. P. Zhao, S. Li, S. D. Chen, and Y. Cui, "Characteristics of methane adsorption/desorption heat and energy with respect to coal rank," *Journal of Natural Gas Science and Engineering*, vol. 99, p. 104445, 2022.

[6] H. L. Liu, J. M. Li, H. Y. Wang, and Q. B. Zhao, "The difference of hydrodynamics on coalbed methane reservoir formation," *Natural Gas Industry*, vol. 26, no. 3, pp. 35–37, 2006.

[7] B. Wang, J. Li, and M. Zhang, "Study on chemical characteristics of coalbed methane reservoir formation water," *Journal of Oil and Gas Technology*, vol. 29, no. 5, pp. 66–68, 2007.

[8] X. Y. Yi, H. J. Wu, Y. Lu, X. L. Qiu, H. Zhang, and C. Y. Li, "Experimental study on the effect of salinity on coalbed methane desorption-diffusion," *Coal Geology & Exploration*, vol. 41, no. 5, pp. 33–35, 2013.

[9] Y. C. Wei, X. X. Xiang, A. M. Wang, Q. Zang, and C. D. Yong, "Influence of water with different salinity on the adsorption performance of coal reservoir," *Journal of China Coal Society*, vol. 44, no. 9, pp. 2833–2839, 2019.

[10] J. I. Joubert, C. T. Grein, and D. Bienstock, "Effect of moisture on the methane capacity of American coals," *Fuel*, vol. 53, no. 3, pp. 186–191, 1974.

[11] B. M. Krooss, F. van Bergen, Y. Gensterblum, N. Siemons, H. J. M. Pagnier, and P. David, "High-pressure methane and carbon dioxide adsorption on dry and moisture- equilibrated Pennsylvanian coals," *International Journal of Coal Geology*, vol. 51, no. 2, pp. 69–92, 2002.

[12] S. Y. Zhang, S. Y. Sang, and Z. G. Yang, "Mechanism analysis on the effect of liquid water on coal adsorbing methane," *Journal of China University of Mining&Technology*, vol. 5, pp. 105–110, 2009.

[13] L. W. Zhong, "Adsorptive capacity of coals an its affecting factors," *Earth Science*, vol. 29, no. 3, pp. 327–332, 2004.

[14] W. B. Tian, A. F. Li, and W. C. Han, "Effect of water content on adsorption /desorption of coalbed methane," *Journal of China Coal Society*, vol. 42, no. 12, pp. 3196–3202, 2017.

[15] W. G. Tian, D. Z. Tang, Z. L. Wang, and B. Sun, "Origin of coalbed methane in Baode, northeastern Ordos basin," *Geological Journal of China Universities*, vol. 18, no. 3, pp. 479–484, 2012.

[16] X. C. Yang, J. S. Mao, W. J. Lin et al., "Explorationhistory and enlightenment of coalbed methane in Baode block," *Xinjiang Petroleum Geology*, vol. 42, no. 3, pp. 381–388, 2021.

[17] J. Li, B. Wang, L. Y. Shao et al., "Hydrogeological zoning and gas control-a case study of Baode block in eastern Hubei Gas Field," *Journal of China University of Mining&Technology*, vol. 46, no. 4, pp. 869–876, 2017.

[18] Z. Gao, D. M. Ma, and Y. Chen, "Law and quantitative evaluation of methane desorption hysteresis of coal seam in Huanglong coalfield," *Journal of Henan Polytechnic University(Natural Science)*, vol. 40, no. 5, pp. 22–79, 2021.

[19] D. M. Ma, W. Ma, and Y. B. Lin, "Desorption hysteresis characteristics of CBM," *Journal of China Coal Society*, vol. 37, no. 11, pp. 1885–1889, 2012.

[20] J. Zhou, Q. Mao, and K. H. Luo, "Effects of moisture and salinity on methane adsorption in kerogen: a molecular simulation study," *Energy & Fuels*, vol. 33, no. 6, pp. 5368–5376, 2019.

[21] G. X. Dang, C. F. Wu, and B. Wang, "Quantitative analysis of methane adsorption/desorption hysteresis effect on coal sample," *Coal Science and Technology*, vol. 45, no. 5, pp. 191–222, 2017.

[22] Z. Gao, D. M. Ma, Y. Chen, H. Zhang, and L. Zhang, "Effect of water content on adsorption /desorption of methane of different macroscopic lithotypes," *Coal Science and Technology*, vol. 48, no. 8, pp. 97–105, 2020.

[23] P. Li, D. M. Ma, H. Zhang, W. B. Li, and F. Du, "Influence of high and low rank coal wettability and methane adsorption/desorption characteristics," *Coal Geology & Exploration*, vol. 44, no. 5, pp. 80–85, 2016.

[24] Y. Chen, D. M. Ma, Y. C. Xia, C. Guo, F. Yang, and K. Shao, "Study on wettability and influencing factors of different macroscopic components in low rank coal," *Coal Science and Technology*, vol. 9, pp. 97–104, 2019.

[25] P. F. Li, *Pore Structural Characterization and Adsorption Properties of Deep Coal Reservoir Based on Molecular Smulation: A Case Study from Daning-Jixian District Coalbed [M.S. Thesis]*, Taiyuan University of Technology, 2019.

[26] F. Wang, Y. B. Yao, W. Zhang, Q. P. Sun, and X. H. Yuan, "Effect of water occurrences on methane adsorption capacity of coal: a comparison between bituminous coal and anthracite coal," *Fuel*, vol. 266, p. 117102, 2020.

Hindawi
Geofluids
Volume 2022, Article ID 8336315, 10 pages
https://doi.org/10.1155/2022/8336315

Review Article

Coalbed Methane Industry Development Framework and Its Limiting Factors in China

Rui Li[1,2] **and Guofu Li**[1]

[1]*State Key Laboratory of Coal and Coalbed Methane Co-mining, Shanxi Jinneng Holding Group Co. Lt, Jincheng 048000, China*
[2]*State Key Laboratory of Coal Mine Disaster Dynamics and Control, Chongqing University, Chongqing 400044, China*

Correspondence should be addressed to Rui Li; ruilicug@hotmail.com

Received 6 February 2022; Revised 24 March 2022; Accepted 25 April 2022; Published 14 May 2022

Academic Editor: Yong Li

The current average daily gas production of single coalbed methane (CBM) wells in China is less than 1,300 m^3. The low production rate of CBM wells dramatically limits the sustainable development of the CBM industry in China. To promote CBM industry development, three universal geological factors, i.e., gas sources, channels, and driving force of the low production wells are analyzed, considering the various and complicated geological conditions of CBM reservoirs in China. Additionally, we find that the growth in proven CBM reserves should be greatly promoted as the CBM proven rate is only less than 3% by the end of 2020. The widespread CBM extraction mode based on depressurization via dewatering generates very limited effects in coal seams with notable deformation, high in situ stress, or little water. Therefore, a specific design of CBM development modes is proposed, according to the applicable geological conditions of different CBM development modes. It covers depressurization via dewatering, depressurization via stress release, and coal and CBM comining. Moreover, the regional governments play a key role in the development of the regional CBM industry, and favorable policies should be formulated to promote the multipoint development conditions across China. This study is concluded to provide a recommended development framework involving sustainable CBM production in China and its development processes.

1. Introduction

Coalbed methane (CBM), generated and mainly adsorbed in coal seams, is a form of unconventional natural gas [1, 2]. Given the actual energy structure in China, the dominant position of coal in energy consumption over other energy forms would persist for a long time in the future [3]. The extraction of CBM resources can increase the energy supply and reduce mining hazards. Moreover, acknowledged as a type of greenhouse gas, the development of CBM in the process of coal mining is beneficial for reducing greenhouse gas emissions and protecting the environment. Therefore, CBM development is of significance in both economic and environmental respects.

In the past 30 years, China has made great achievements in CBM exploration and development, with the production volume of CBM wells exceeding 100×10^8 m^3 since 2020 [4]. Two CBM industrialization bases including Qinshui Basin and the eastern margin of Ordos Basin have been built. Unfortunately, the average daily gas production of single CBM wells in China is currently lower than 1,300 m^3, and the low production rate of CBM wells greatly restricts the development of CBM in China. The limiting factors concerning low CBM production are thought to include geological conditions, engineering technologies, and management policies [5]. Admittedly, under multistage tectonism, the geological conditions of coal-bearing basins in China are extremely variable and complicated. Hence, the preservation conditions of CBM are definitely poorer than those other countries developing CBM [6]. The various and complicated geological conditions of CBM reservoir in China make the development technology meet great bottleneck. In addition, the management policies of the government and enterprises

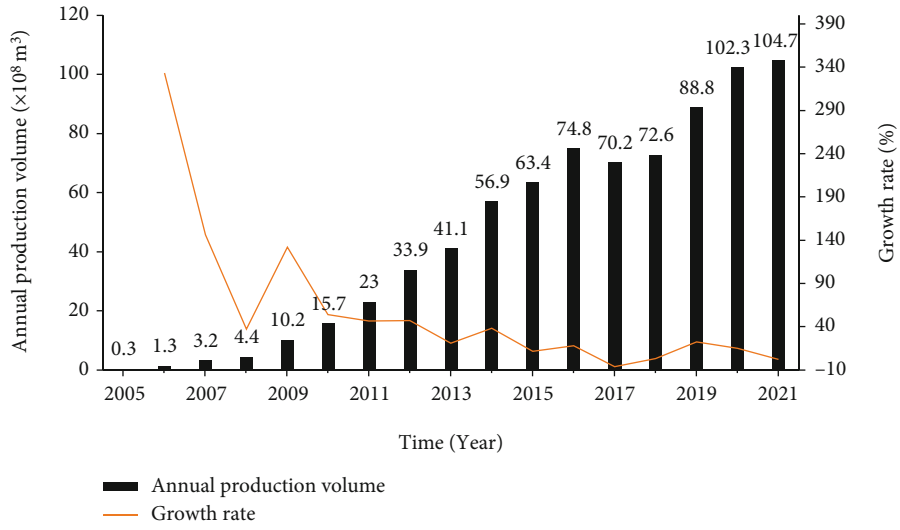

Figure 1: Annual production volume and growth rate of CBM wells in China (2005-2021).

cannot effectively stimulate investment enthusiasm in present hard stage of CBM industry [7]. Therefore, it is urgent to determine the universal limitations based on the movement process of CBM in coal seams. In this way, a recommended framework should be established to achieve a significant increase in CBM production throughout China.

The objective of this study is to reveal the limiting factors of CBM development and provide a fundamental framework for CBM industry development in China. The universal geological reasons for the low production rate of CBM wells are first analyzed. A recommended framework including ensuring the growth of proven CBM reserves, specific design of CBM development modes, and the role of regional governments is developed. This work is intended to promote CBM industry development across China.

2. CBM Industry Progress in China

China's CBM development over the past 30 years, especially the large-scale development of CBM resources since 2006, has been provided notable policy support by the state. Consequently, the CBM industry in China has attained remarkable achievements. From 2005 to 2020, the number of gas accidents in coal mines decreased from 414 to 7, at a reduction rate of 98.3%, with the number of deaths decreasing from 2171 to 30 [8, 9]. The annual production volume of CBM wells has dramatically increased from less than 1×10^8 m^3 in 2005 to 104.7×10^8 m^3 in 2021 [4], as shown in Figure 1. However, CBM production in China still lags far behind that in major countries developing CBM, such as the USA, Canada, and Australia. Moreover, China has failed to meet the annual production target during two consecutive five-year plans, and the implementation of the fourteenth five-year plan barely realized the annual production target [10]. Figure 1 shows that in recent years, the growth rate of CBM production has continuously decreased, even exhibiting a negative growth in 2017, which has resulted in the current CBM industry in China experiencing a rather unfortunate situation, and the confidence of investors and practitioners in the CBM industry is low.

The initial CBM drainage mode is coal mine gas extraction of coal seams or the adjacent layers in the subsurface coal mines. The aim is to reduce gas content and gas pressure, ensuring mining safety. At the end of the last century, drawing lessons from the surface CBM development of depressurization via dewatering in the United States [11], China has developed the development technology systems involving drilling, fracturing, and drainage processes. At present, this is still the main mode of CBM surface development. With the progress of CBM development technologies, the coal and CBM comining in the mining areas gradually formed between 2010 and 2015 [12]. By coordinating the relationship between CBM development and coal mining in time and space dimensions, CBM resources are extracted in coordination with coal mining process to achieve rapid release of reservoir pressure [13, 14]. The coal and CBM comining have achieved an excellent adaptability to CBM reservoirs in coal mine areas [15]. However, successful commercial development of CBM in a few areas is inadequate to support the development of CBM industry in China [16, 17]. A specific design of CBM development modes suitable for the specific geological conditions in China has not been established yet [18]. There is still a great need to innovate development technologies that can cover complicated geological conditions and extract CBM resources efficiently.

Additionally, in the past, due to the urgent demand for CBM production, field trials and error correction became a common means to assess the effect of development methods. This has caused substantial financial and time losses. The relatively extensive technical development and management have hindered the sustainable development of CBM industry in China. Therefore, to overcome the abovementioned bottlenecks of CBM development, improve the production rate of single CBM wells, and complete the long-term planning

Table 1: Universal geological reasons for the low production rate of single CBM wells in China.

Reasons	Gas sources	Channels	Driving force	Applicability of development technologies
Characteristics	(1) Methane occurs the adsorption state (2) The gas saturation is low	(1) Low mechanical strength and high stress sensitivity (2) Easy to produce coal fines (3) Tectonically deformed coal is widely distributed where fracture connectivity is poor [25]	(1) Low reservoir pressure (2) High capillary pressure [26] (3) High water saturation	(1) In the process of drilling, horizontal wellbores easily collapse (2) In the process of fracturing, it is difficult to create effective propped fractures (3) In the process of drainage, it is difficult to ensure the smooth output of CBM
Consequences	(1) The output of CBM wells hardly peaks within a short time (2) CBM production involves a slow process	(1) Gas migration channels are easily blocked (2) It is difficult to construct diversion channel in tectonically deformed coal [27]	(1) This factor influences the development cycle of CBM wells (2) Pressure release within the coal matrix is difficult to obtain [7]	(1) The extraction methods of CBM wells are not fully adapted to the geological conditions of CBM reservoirs (2) The stimulation effect of development methods is poor [28]

target of the CBM industry, relevant development processes must be updated.

3. Geological Factors concerning Low Production of CBM Wells

Studies have analyzed the different geological factors of CBM reservoirs in China and other countries, which probably cause the low production rate of CBM wells, such as the permeability, buried depth, thickness, gas content, gas saturation, coal structure, and coal rank [19–24]. Admittedly, due to repeated plate movements and tectonic activities during historical periods, the geological conditions of coal-bearing basins in China are extremely variable and complicated. However, under the various and complicated geological conditions, investigations of geological factors among different areas are inadequate to guide CBM exploitation. Moreover, CBM development in only limited areas has been promoted. Hence, in China, it is necessary to analyze the universal geological reasons for the low production rate of CBM wells. This could be helpful to optimize development methods that adapted to the various geological conditions and improve the production of single CBM wells.

Generally, the necessary conditions for CBM movement include gas sources, channels, and driving force. From this perspective, the universal geological reasons for the low single CBM well production in China, based on the gas movement process, are listed in Table 1. The objective limiting factors determine that the production rate of single CBM wells cannot reach a peak within a short time as other kinds of natural gas wells, such as wells in tight sandstone gas and shale gas reservoirs. Nevertheless, this table does not indicate that the CBM production rate cannot be greatly improved, on condition that the expected stimulation methods must overcome these three constraints. Furthermore, the current development methods of CBM extraction are not fully adapted to the various and complicated geological conditions of CBM reservoirs, which significantly restricts CBM development. Therefore, if the production rate of CBM wells is expected to distinctly increase across China, a CBM development framework is urgently needed.

4. Recommended Development Frameworks

4.1. Ensuring the Growth in Proven CBM Reserves. Abundant coal reserves provide a basic condition for CBM development. The CBM resources in China are highly abundant, and at a buried depth of 2,000 m, the CBM resources in China total are approximately $30.05 \times 10^{12}\ m^3$, with the recoverable resources reaching approximately $12.5 \times 10^{12}\ m^3$ [29]. CBM development areas with the large-scale CBM exploitation activities in China include the Qinshui Basin in Shanxi Province, the eastern margin of Ordos Basin in Shanxi and Shaanxi Provinces, the Qianxi-Diandong area in Guizhou and Yunnan Provinces, the Junggar Basin in Xinjiang Autonomous Region, and the Erlian Basin in Inner Mongolia Autonomous Region (Figure 2), due to their advantageous geological resources.

At present, the CBM resource evaluation area in China covers $37.5 \times 10^4\ km^2$, and the registered mining right area reaches $4.83 \times 10^4\ km^2$, which only accounts for 12.87% of the total CBM resource evaluation area [31]. After more than 30 years of development, China has successively established two major CBM industrialization bases, namely, the Qinshui Basin and the eastern Ordos Basin. Most high-quality blocks in these areas have been put into development. However, by the end of 2020, China's total proven CBM reserves reached $7857.54 \times 10^8\ m^3$ (Figure 3), with a proven rate lower than 3% [32], mainly distributed in the Qinshui Basin and eastern Ordos Basin, North China. The annual increased proven CBM reserves lacked sustained growth, exhibiting a very low and highly unstable pattern (Figure 3). Furthermore, only Shanxi Province accounted for approximately 88% of the proven CBM reserves in China [33]. Therefore, it is necessary to further conduct geological exploration of CBM-bearing basins and to increase the proven gas reserves, which is an effective way to sustainably develop the CBM industry in China.

4.2. CBM Development Modes. A shale gas revolution swept the USA in the early 2000s. The development mode of horizontal drilling associated with fracturing created a surge in shale gas production in the United States, transforming it from an energy importer into a net energy exporter. Moreover, this surge altered the landscape of energy markets globally. The applicable modes of CBM development have not been determined, which represents the development bottleneck of the CBM industry in China. In the process of CBM exploitation, the extraction mode based on depressurization via dewatering has been increasingly questioned to determine whether this mode is suitable for all the geological conditions in China [34, 35]. Depressurization via dewatering performs well in CBM exploitation of shallow and weakly deformed coal seams in China. However, hydraulic fracturing applied to achieve dewatering generates very limited effects in coal seams with notable deformation, wherein hydraulic fractures rarely propagate (Li et al., 2020; [27, 36]). Moreover, the buried depth of CBM reservoirs increases in the process of CBM development. The basic geological conditions and fluid production characteristics of deep CBM reservoirs distinctly differ from those of shallow reservoirs [37, 38]. Under the high in situ stress conditions of deep coal seams, the damage exerted by stress on the fracture system during dewatering distinctly increases, which greatly limits the flow and output of gas and deformation water [39–41]. Therefore, depressurization involving only dewatering hardly extracts deep CBM resources [42]. The limitation of the depressurization mode via dewatering should be overcome to account for the geological conditions of deep CBM reservoirs.

Depressurization of deep coal seams and strongly deformed coal seams has been suggested to be enhanced via stress release. An increasing number of recent studies have indicated that cavity establishment is a feasible approach for stress release, and directional drilling and hydraulic jetting technologies can create many cavities within coal seams for stress release [43–46]. In terms of gas sources, depressurization via stress release can enhance the desorption rate of coalbed methane. Furthermore, the change of stress condition induces the movement and deformation of coal seams, which can

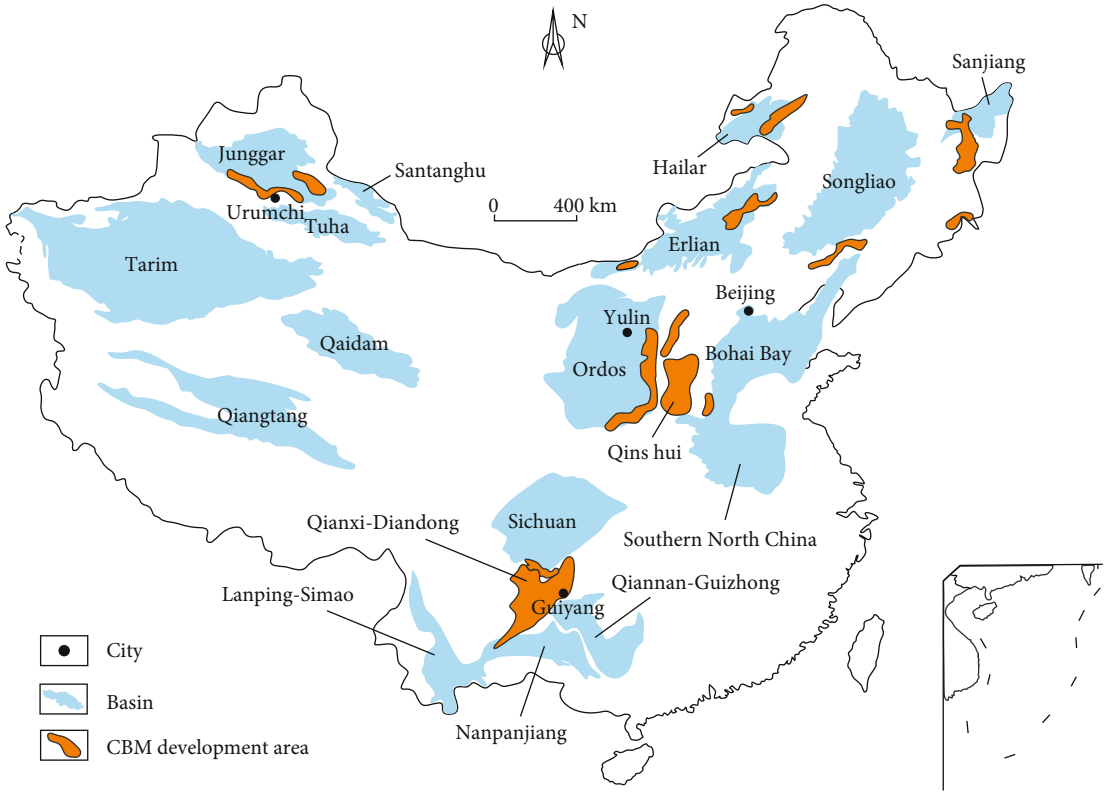

Figure 2: Distribution of the main CBM development areas in China (revised from [30]).

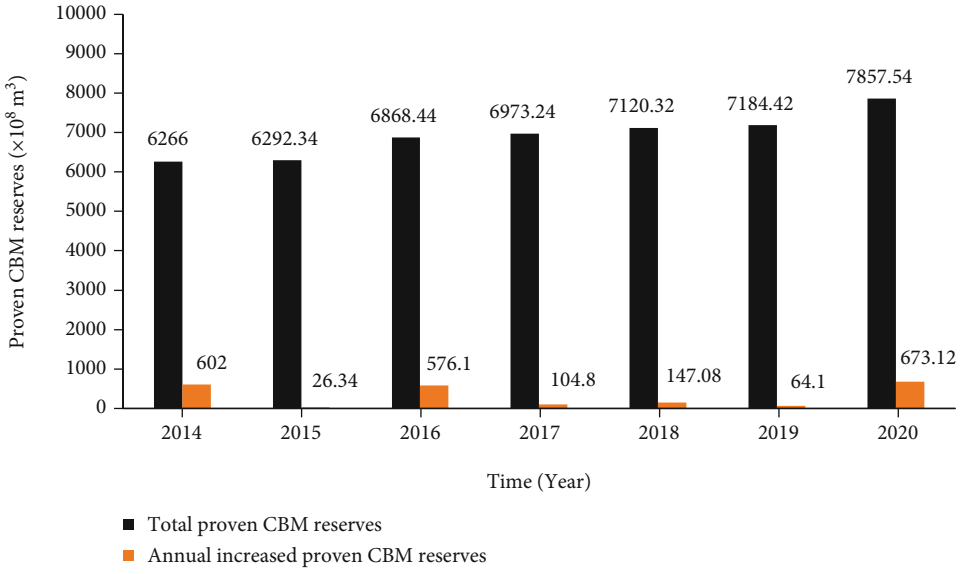

Figure 3: Annual proven CBM reserves in China (2014-2020).

improve reservoir permeability. In addition, the expansion deformation of coal seams enlarges the volume of pores and fractures, which can reduce the capillary resistance of gas migration in flow channels [16]. Therefore, this development mode should be further researched and applied in CBM industry. In addition, in coal mining areas, employing the advantages of rapidly releasing the reservoir pressure through mining, CBM extraction can be significantly enhanced. Hence, the development mode of coal and CBM comining has been demonstrated as a suitable way to develop CBM resources in practice [47, 48]. In China, the maximum depth of coal mining reaches approximately 1500 m. Hence, the coal and CBM comining mode can be employed to develop CBM in mining areas.

According to different CBM development modes and their applicable geological conditions, a certain design of CBM development modes is proposed, as summarized in Table 2.

Table 2: Design of CBM development modes.

Area categories	Buried depth (m)	Stress	Special geological conditions	Suggested development mode
In situ coal seams	Shallow	Low in situ stress	Weakly deformed coal; water-bearing coal	Depressurization via dewatering
			Strongly deformed coal; water-free coal	Depressurization via stress release
	Deep	High in situ stress	Low permeability and high effective stress	Depressurization via stress release
Coal mining areas	<1500	Reservoir pressure release through mining	Continuous coal seams with large thickness	Coal and CBM comining

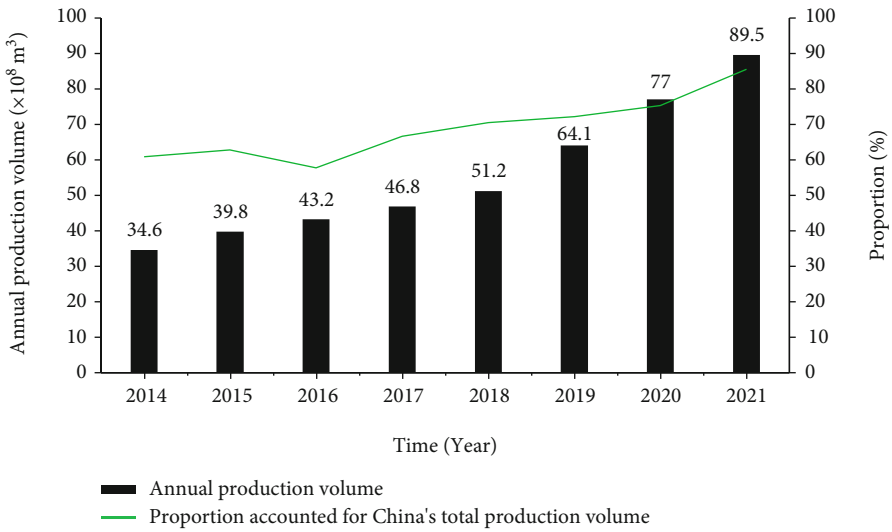

Figure 4: Annual CBM production volume in Shanxi Province (2014-2021).

In shallow weakly deformed coal seams or water-bearing coal seams, the development mode of depressurization via dewatering can be optimized and innovated to further improve the CBM extraction effect, because this development mode exhibits a high geological adaptability. In coal mining areas, coal and CBM comining mode should be continuously developed and popularized. In deep coal seams, strongly deformed coal seams, or water-free coal seams, the development mode of depressurization via stress release should be vigorously developed, as current development modes are inefficient in terms of extraction in these areas. The geological conditions described in Table 2 can cover most CBM development areas in China. Hence, this design achieves a universal geological adaptability. It should be noted that Table 2 does not provide detailed values of the buried depth in in situ coal seams, as there exists no absolute critical conversion value between deep and shallow coal seams.

4.3. Recommended Policies and Managements. Since 2008, China has implemented several National Science and Technology Major Projects for the development of CBM resources from 2006 to 2020 [49, 50]. Nevertheless, considering the low production rate of single CBM wells, it is also difficult to establish a high gas production capacity to satisfy the energy demand in China. Therefore, the support and overall management provided by the central government alone is far from sufficient. CBM resources in China are widely distributed [51]. If the regional governments could strengthen the development of local CBM resources and prioritize fulfillment of the demand of local users, this probably facilitates the formation of multipoint development conditions across China.

In 2010, the Government of Shanxi Province proposed the gasification of Shanxi strategy and issued pump priming policies in investment, fiscal taxation, finance, land, and other areas of the CBM industry [52]. In 2017, the Science and Technology Department of Shanxi Province issued a major project on key and core technologies to realize an energy revolution in this province, explicitly supporting breakthroughs in CBM exploration, development, and utilization [53]. These policies have led to and driven the sustainable and rapid development of the Shanxi CBM industry. In April 2020, Shanxi Province issued the Administration Measures of CBM Exploration and Exploitation in Shanxi Province to further standardize the CBM exploration and development market and ensure ecological protection in this province [54]. Prior policies and effective management measures have

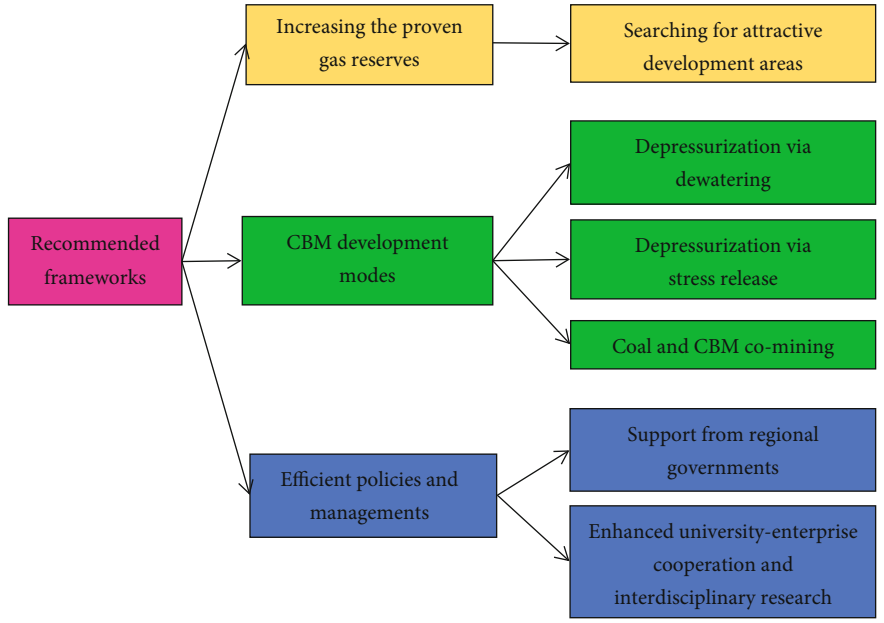

Figure 5: Recommended framework for CBM development.

driven the CBM industry in Shanxi Province to progress rapidly. In recent years, the production volume of CBM in Shanxi Province has always accounted for more than 60% of China's total CBM production volume, as shown in Figure 4 [55]. Particularly, in 2021, the surface CBM production in Shanxi Province reached 89.5×10^8 m^3, and the CBM well production capacity of Shanxi Province alone accounted for 85.5% of the national total well production capacity.

Additionally, more than 100 wells have been constructed in the abandoned mines in Shanxi Province, and approximately 1.28×10^8 m^3 of CBM resources have been extracted and utilized by the end of 2021 [56]. This terrific amount is equivalent to reducing 1.92×10^6 tons of carbon dioxide (CO_2) emissions, with a great significance for the local atmospheric environment.

The abovementioned demonstrate that regional governments play a key role in the development of the regional CBM industry. Therefore, we argue that regional governments should formulate more favorable policies, such as tax relief policies, gas production subsidies, and scientific research projects, to promote the engagement of CBM production enterprises.

In addition, current CBM production management remains extensive, and the extraction methods of CBM wells are excessively uniform across different areas, lacking professional design of CBM development modes as mentioned in Section 4. 2. In this way, the sameness of CBM extraction method in China must be disrupted in the future. Enterprises must strengthen the cooperation between enterprises and universities and establish professional construction teams. The focus of CBM development is to improve the fundamental theories and solve the key technical problems. Based on these aspects, it is also suggested that interdisciplinary collaboration should give full play to breakthroughs in key CBM development technologies. For example, research and development of fracturing fluids and proppant materials should fully utilize the advances of materials science. A breakthrough in reservoir stimulation and permeability enhancement depends on the integration of basic science theories such as physics, chemistry, and biology. In addition, research and development of major CBM extraction equipment require the application of mechanical and electronic sciences, combined with artificial intelligence. Therefore, cooperation and interdisciplinary research are expected to break through the technical restricts in CBM development.

Based on the above discussion, a recommended framework for CBM development in China is proposed, as shown in Figure 5. Increasing the proven gas reserves can ensure a sufficient number of attractive areas for CBM development. The design of CBM development modes can be employed to provide guidance for the development direction of CBM extraction technologies. Support by regional governments and cooperation between enterprises and universities are important for the CBM industry across China.

5. Conclusions

The low production rate of CBM wells limits the development of the CBM industry in China. In this study, the limiting factors of CBM development in China are analyzed involving the geological reasons for the low gas production, proven CBM reserves, CBM development modes, and managements. On the basis, a recommended framework of CBM development is established to promote the CBM industry in China. In this study, the following conclusions are obtained:

(1) There are three objective limiting factors restricting gas movement and production in CBM reservoirs, including gas sources, channels, and driving force.

CBM stimulation methods must overcome these three constraints

(2) The proven rate of CBM resources in China is much less than 3%, and the annual increase in proven CBM reserves in recent years exhibits a very low and highly unstable pattern. It is suggested to greatly increase the proven CBM reserves

(3) Depending on the applicable geological conditions of different CBM development modes, a specific design of CBM development modes is proposed, including depressurization via dewatering, depressurization via stress release, and coal and CBM comining

(4) Regional governments can play a key role in the development of the CBM industry and should formulate more favorable policies to promote the multipoint development conditions across China. Cooperation and interdisciplinary research are expected to break through the technical restricts in CBM development

The limitation of this study is that the favorable policies are not elaborated, as the development status of CBM in different regions is variable across the country. Further works are needed to survey the market and formulate detailed policies that can be implemented by different regional governments.

Conflicts of Interest

The authors declare that they have no conflict of interest.

Acknowledgments

This work is sponsored by the National Natural Science Foundation of China (No. U19B2009), National Science and Technology Major Project of China (No. 2016ZX05067001-007), Natural Science Foundation of Chongqing (cstc2020jcyj-bshX0035), and Shanxi Science and Technology Major Project (No. 20181101013). In additional, special thanks are due to Prof. YiYu Lu from Chongqing University. These supports are gratefully acknowledged.

References

[1] Y. Li, J. H. Yang, Z. J. Pan, S. Z. Meng, K. Wang, and X. L. Niu, "Unconventional natural gas accumulations in stacked deposits: a discussion of upper paleozoic coal-bearing strata in the east margin of the Ordos Basin, China," *Acta Geologica Sinica-English Edition*, vol. 93, no. 1, pp. 111–129, 2019.

[2] Y. Li, D. Z. Tang, P. Wu et al., "Continuous unconventional natural gas accumulations of Carboniferous-Permian coal-bearing strata in the Linxing area, northeastern Ordos basin, China," *Journal of Natural Gas Science and Engineering*, vol. 36, pp. 314–327, 2016.

[3] National Energy Administration of China, *The 13th Five-Year Plan for Coal Industry Development*, 2016, December 2016, http://www.nea.gov.cn/2016-12/30/c_135944439.htm.

[4] National Bureau of Statistics of China, *Annual Cumulative Production Volumes of CBM Wells*, 2022, January 2022, https://data.stats.gov.cn/easyquery.htm?cn=A01.

[5] H. C. Lau, H. Y. Li, and S. Huang, "Challenges and opportunities of coalbed methane development in China," *Energy & Fuels*, vol. 31, no. 5, pp. 4588–4602, 2017.

[6] C. P. Jack, "Geology of north American coalbed methane reservoirs," in *Coal Bed Methane (Second Edition)*, T. Pramod, S. J. Schatzel, K. Aminian, G. Rodvelt, M. H. Mosser, and J. S. D'Amico, Eds., pp. 35–64, Elsevier, 2020.

[7] S. Tao, S. D. Chen, and Z. J. Pan, "Current status, challenges, and policy suggestions for coalbed methane industry development in China: a review," *Energy Science & Engineering*, vol. 7, no. 4, pp. 1059–1074, 2019.

[8] National Coal Mine Safety Administration of China, *There Are no Major Gas Accidents in China's Coal Mines in 2020*, 2021, January 2021, https://www.chinamine-safety.gov.cn/xw/mkaqjcxw/202101/t20210108_376767.shtml.

[9] National Energy Administration of China, *Analysis of Coal Mine Gas Accidents in 2005*, 2006, March 2006, http://www.nea.gov.cn/2006-03/05/c_131111733.htm.

[10] National Energy Administration of China, *The 13th Five-Year Plan for the Development and Utilization of Coalbed Methane (Coal Mine gas)*, 2016, November 2016, http://zfxxgk.nea.gov.cn/auto85/201612/t20161202_2326.htm?keywords.

[11] I. Karakurt, G. Aydin, and K. Aydiner, "Sources and mitigation of methane emissions by sectors: a critical review," *Renewable Energy*, vol. 39, no. 1, pp. 40–48, 2012.

[12] T. C. He, B. Y. Wang, and Y. D. Tian, "Development and issues with coal and coal-bed methane simultaneous exploitation in Jincheng mining area," *Journal of China Coal Society*, vol. 39, pp. 1779–1785, 2014.

[13] M. Ji, Z. G. Sun, and W. Sun, "A case study on the gas drainage optimization based on the effective borehole spacing in Sima coal mine," *Geofluids*, vol. 2021, Article ID 5510566, 9 pages, 2021.

[14] C. Zhang, S. H. Tu, Q. S. Bai, G. Y. Yang, and L. Zhang, "Evaluating pressure-relief mining performances based on surface gas venthole extraction data in longwall coal mines," *Journal of Natural Gas Science and Engineering*, vol. 24, pp. 431–440, 2015.

[15] P. Liu, J. Y. Fan, D. Y. Jiang, and J. J. Li, "Evaluation of underground coal gas drainage performance: mine site measurements and parametric sensitivity analysis," *Process Safety and Environment Protection*, vol. 148, pp. 711–723, 2021.

[16] Y. Y. Lu, R. Li, X. F. Xian, Z. L. Ge, and B. W. Xian, "Discussion on the efficient exploitation method of deep coalbed methane with pressure relief by ground directional well + hydraulic slotting," *Journal of China Coal Society*, vol. 46, pp. 876–884, 2021.

[17] Y. Qin, T. A. Moore, J. Shen, Z. B. Yang, Y. L. Shen, and G. Wang, "Resources and geology of coalbed methane in China: a review," *International Geology Review*, vol. 60, no. 5-6, pp. 777–812, 2018.

[18] Y. J. Meng, D. Z. Tang, H. Xu, C. Li, L. Li, and S. Z. Meng, "Geological controls and coalbed methane production potential evaluation: a case study in Liulin area, eastern Ordos Basin, China," *Journal of Natural Gas Science and Engineering*, vol. 21, pp. 95–111, 2014.

[19] Y. D. Cai, D. M. Liu, Y. B. Yao, J. Q. Li, and Y. K. Qiu, "Geological controls on prediction of coalbed methane of No. 3 coal seam in Southern Qinshui Basin, North China," *International Journal of Coal Geology*, vol. 88, no. 2-3, pp. 101–112, 2011.

[20] Y. Li, Z. S. Wang, S. H. Tang, and D. Elsworth, "Re-evaluating adsorbed and free methane content in coal and its ad- and

desorption processes analysis," *Chemical Engineering Journal*, vol. 428, article 131946, 2022.

[21] Y. Li, C. Zhang, D. Z. Tang et al., "Coal pore size distributions controlled by the coalification process: an experimental study of coals from the Junggar, Ordos, and Qinshui basins in China," *Fuel*, vol. 206, pp. 352–363, 2017.

[22] X. B. Su, X. Y. Lin, S. B. Liu, M. Zhao, and J. Y. Song, "Geology of coalbed methane reservoirs in the southeast Qinshui Basin of China," *International Journal of Coal Geology*, vol. 62, no. 4, pp. 197–210, 2005.

[23] B. Wang, J. M. Li, Y. Zhang et al., "Geological characteristics of low rank coalbed methane, China," *Petroleum Exploration and Development*, vol. 36, no. 1, pp. 30–34, 2009.

[24] Q. Wei, B. L. Hu, X. Q. Li et al., "Implications of geological conditions on gas content and geochemistry of deep coalbed methane reservoirs from the Panji Deep Area in the Huainan Coalfield, China," *Journal of Natural Gas Science and Engineering*, vol. 85, article 103712, 2021.

[25] Z. G. Zhang, Y. Qin, G. Wang et al., "Evaluation of coal body structures and their distributions by geophysical logging methods: case study in the Laochang block, eastern Yunnan, China," *Natural Resources Research*, vol. 30, no. 3, pp. 2225–2239, 2021.

[26] Z. W. Wang, S. M. Liu, and Y. Qin, "Coal wettability in coalbed methane production: a critical review," *Fuel*, vol. 303, 2021.

[27] R. Li, S. W. Wang, S. F. Lyu, W. Lu, G. F. Li, and J. C. Wang, "Geometry and filling features of hydraulic fractures in coalbed methane reservoirs based on subsurface observations," *Rock Mechanics and Rock Engineering*, vol. 53, no. 5, pp. 2485–2492, 2020.

[28] H. R. Gu and E. Siebrits, "Effect of formation modulus contrast on hydraulic fracture height containment," *SPE Production & Operations*, vol. 23, no. 2, pp. 170–176, 2008.

[29] Ministry of Natural Resources of China, *China Mineral Resources*, Geological Publishing House, Beijing, 2016, November 2016, http://www.mnr.gov.cn/sj/sjfw/kc_19263/zgkczybg/201611/t20161115_1997929.html.

[30] C. N. Zou, Z. Yang, S. P. Huang et al., "Resource types, formation, distribution and prospects of coal-measure gas," *Petroleum Exploration and Development*, vol. 46, no. 3, pp. 451–462, 2019.

[31] M. Y. Sun, *The Development of Coal-Bed Methane Industry Enters the Key "Window Period"*, China Energy News, 2019.

[32] Ministry of Natural Resources of China, *China Mineral Report*, Geological Publishing House, Beijing, 2021, October 2019, http://www.mnr.gov.cn/sj/sjfw/kc_19263/zgkczybg/202111/t20211105_2701985.html.

[33] Natural Resources Department of Shanxi Province, *Overview of Mineral Resources in Shanxi Province*, 2017, June 2017, http://zrzyt.shanxi.gov.cn/zwgk/zwgkjbml/kjgl/kxpj/201706/t20170613_108701.shtml.

[34] A. Salih and E. Müller, "Determination of adsorptive and diffusive properties of carbon dioxide - methane - water in coal-like structures using molecular simulations," *Nature Precedings*, pp. 1–13, 2008.

[35] J. T. Shi, X. F. Li, B. X. Xu et al., "Review on desorption-diffusion-flow model of coal-bed methane," *Scientia Sinica*, vol. 43, no. 12, pp. 1548–1557, 2013.

[36] Y. P. Cheng and Z. J. Pan, "Reservoir properties of Chinese tectonic coal: a review," *Fuel*, vol. 260, article 116350, 2020.

[37] S. Li, D. Z. Tang, Z. J. Pan et al., "Geological conditions of deep coalbed methane in the eastern margin of the Ordos Basin, China: implications for coalbed methane development," *Journal of Natural Gas Science and Engineering*, vol. 53, pp. 394–402, 2018.

[38] L. Wang, S. M. Liu, Y. P. Cheng, G. Z. Yin, D. M. Zhang, and P. K. Guo, "Reservoir reconstruction technologies for coalbed methane recovery in deep and multiple seams," *International Journal of Mining Science and Technology*, vol. 27, no. 2, pp. 277–284, 2017.

[39] Y. G. Geng, D. Z. Tang, H. Xu et al., "Experimental study on permeability stress sensitivity of reconstituted granular coal with different lithotypes," *Fuel*, vol. 202, pp. 12–22, 2017.

[40] Y. Li, Y. B. Wang, J. Wang, and Z. J. Pan, "Variation in permeability during CO2–CH4 displacement in coal seams: part 1 – experimental insights," *Fuel*, vol. 263, article 116666, 2020.

[41] X. Zhou, S. M. Liu, and Y. D. Zhang, "Permeability evolution of fractured sorptive geomaterials: a theoretical study on coalbed methane reservoir," *Rock Mechanics and Rock Engineering*, vol. 54, no. 7, pp. 3507–3525, 2021.

[42] Y. J. Lu, Z. Z. Yang, X. G. Li, J. X. Han, and G. F. Ji, "Problems and methods for optimization of hydraulic fracturing of deep coal beds in China," *Chemistry and Technology of Fuels and Oils*, vol. 51, no. 1, pp. 41–48, 2015.

[43] L. Cheng, Z. L. Ge, B. W. Xia et al., "Research on hydraulic technology for seam permeability enhancement in underground coal mines in China," *Energies*, vol. 11, no. 2, p. 427, 2018.

[44] R. Gao, B. Yu, H. C. Xia, and H. F. Duan, "Reduction of stress acting on a thick, deep coal seam by protective-seam mining," *Energies*, vol. 10, no. 8, p. 1209, 2017.

[45] G. M. Wei, H. Wen, J. Deng et al., "Enhanced coalbed permeability and methane recovery via hydraulic slotting combined with liquid CO_2 injection," *Process Safety and Environment Protection*, vol. 147, pp. 234–244, 2021.

[46] Q. Ye, Z. Jia, and C. Zheng, "Study on hydraulic-controlled blasting technology for pressure relief and permeability improvement in a deep hole," *Journal of Petroleum Science and Engineering*, vol. 159, pp. 433–442, 2017.

[47] Y. Q. Liu, C. Zhao, G. F. Li et al., "Optimized decision method of coordinated development mode of coal and coalbed methane in Jincheng mining area," *Journal of China Coal Society*, vol. 45, pp. 2575–2589, 2020.

[48] C. S. Zheng, B. Y. Jiang, S. Xue, Z. W. Chen, and H. Li, "Coalbed methane emissions and drainage methods in underground mining for mining safety and environmental benefits: a review," *Process Safety and Environment Protection*, vol. 127, pp. 103–124, 2019.

[49] National Energy Administration of China, *11th Five-Year Plan for the Development and Utilization of Coalbed Methane (Coal Mine gas)*, 2006, June 2006, http://www.nea.gov.cn/2006-06/28/c_131215308.htm.

[50] National Energy Administration of China, *Notice of the National Development and Reform Commission on Printing and Distributing the 12th Five-Year Plan for the Development and Utilization of Coalbed Methane (Coal Mine gas)*, 2011, December 2011, http://www.nea.gov.cn/2011-12/31/c_131337364.htm.

[51] D. Y. Lin, J. P. Ye, Y. Qin, and S. Tang, "Characteristics of coalbed methane resources of China," in *31st International Geological Congress*, pp. 706–710, Rio Janeiro, Brazil, 2000.

[52] The People's Government of Shanxi Province, *Some Opinions on Accelerating the Integrated Development of "Four Gases" Industry in Shanxi province*, 2010, September 2010, http://www.shanxi.gov.cn/zw/zfcbw/zfgb/2010nzfgb/d1718q/szfbgtwj_5097/201009/t20100930_101300.shtml.

[53] Science and Technology Department of Shanxi Province, *Notice on the Issuance of Guidelines for Application of Major Special Projects of Key Core Technologies of Shanxi Energy Revolution*, 2017, September 2017, https://kjt.shanxi.gov.cn/.

[54] Natural Resources Department of Shanxi Province, *Administration Measures of CBM Exploration and Exploitation in Shanxi Province*, 2020, April 2020, http://zrzyt.shanxi.gov.cn/zwgk/zwgkjbml/zcfg/yqgll/flfg/202004/t20200409_171970.shtml.

[55] National Bureau of Statistics of China, *Annual Cumulative Production Volumes of CBM Wells for Different Provinces*, 2022, January 2020, https://data.stats.gov.cn/easyquery.htm?cn=E0101.

[56] L. N. Yan, *Let Abandoned Mine Coalbed Methane Become Valuable*, China Coal News, 2021.

Hindawi
Geofluids
Volume 2022, Article ID 3028969, 8 pages
https://doi.org/10.1155/2022/3028969

Research Article

Imbibition Retention in the Process of Fluid Replacement in Tight Sandstone Reservoir

Xiong Liu,[1,2] Yang Zhang,[1] Desheng Zhou,[1,2] Le Yan,[1] Hai Huang,[1,2] and Xinru Li[1,2]

[1]*College of Petroleum Engineering, Xi'an Shiyou University, Xi'an, Shaanxi 710065, China*
[2]*Shaanxi Key Laboratory of Advanced Stimulation Technology for Oil & Gas Reservoirs, Xi'an, Shaanxi 710065, China*

Correspondence should be addressed to Le Yan; 2233128087@qq.com

Received 30 January 2022; Revised 10 March 2022; Accepted 31 March 2022; Published 10 May 2022

Academic Editor: Yong Li

"Fracture network stimulation and oil-water infiltration and replacement" are recent attempts to effectively produce oil from tight reservoirs. On the one hand, the formation can be fractured by the fracturing fluid, which can carry proppant into fractures. On the other hand, the fracturing fluid can spontaneously infiltrate into the pores under the action of capillary pressure to displace the oil phase, thereby enhancing the oil recovery. To distinguish imbibition and displacement processes during fluid replacement in tight reservoirs is difficult, and the effect of these two processes is also vaguely defined. In this study, an experimental method that can visualize the imbibition and displacement process is proposed by combining the core slice displacement experiment. Based on this method, the process of imbibition and displacement can be effectively distinguished, and imbibition retention rate can be quantitatively characterized. The effectiveness of this method is proved by taking the core of Chang 7 tight sandstone reservoir in the Ordos Basin as the research object. The results show that the force direction of the fluid under imbibition is related to the wettability, and it is always from the wetting phase to the nonwetting phase, while the force direction of fluid under displacement is mainly related to the directivity of displacement pressure difference. Based on the difference of force action, imbibition and displacement can be quantitatively characterized, respectively. During the imbibition process, the peak value of the NMR curve corresponding to the small pore throat shifts to the left, and the signal amplitude increases. During the displacement process, the peak value of the NMR curve corresponding to the small pore throat has no obvious shift, nor signal amplitude change, but the peak value of the curve corresponding to the large pore throat shifts to the right. The results also indicate that there is an exponential negative correlation between imbibition retention rate and gas permeability. The greater the gas permeability is, the smaller the imbibition retention rate is.

1. Introduction

Imbibition refers to the process that the wetting fluid spontaneously sucks into the pores and displaces the nonwetting fluid under the action of capillary force [1–3]. The concept of displacement can be divided into broad sense and narrow sense. In a broad sense, displacement refers to the process of one fluid driving and replacing another fluid; that is to say, all fluid replacement can be called displacement (including imbibition process). In a narrow sense, displacement refers to the process of fluid replacement under the action of production pressure difference. The displacement described in this study refers to the displacement in a narrow sense [4, 5].

At present, the study of fluid replacement in tight oil reservoirs mainly depends on laboratory experimental. Arab et al. and Mai and Kantzas conducted core displacement experiments in the hydrophilic system and showed that the injection rate has different effects on the recovery under different oil-water viscosity [6, 7]. Li et al. conducted core imbibition experiments to show that chemical solutions can turn more remaining oil into movable oil to improve oil recovery [8]. Bertoncello et al. used NMR technology to study the influence factors on the imbibition [9–14]. Mason et al. and Li et al. showed that the fluid replacement in imbibition and displacement during the process of shut-in can improve the fracturing stimulation effect of tight oil reservoirs via the

imbibition experiment under pressure [15, 16]. Wang et al. studied the contribution of displacement and imbibition to the oil displacement rate via mathematical models [17–20]. Wang et al. carried out NMR tests, which showed that microfractures have little effect on improving spontaneous imbibition efficiency [21–24]. Wang Z. et al. and Gao et al. directly observed fluid replacement in the process of imbibition via the microfluidic pump, indicating that the chips with a larger average pore throat radius had a higher degree of imbibition recovery [25, 26]. Yao et al. and Li et al. studied the imbibition-displacement law in different reservoirs via capillary models [27, 28].

The existing researches have the following problems: (1) it is difficult to distinguish the processes of imbibition and displacement. During the process of fracturing or postfracturing production in tight reservoirs, the reservoir fluids are affected by many factors, such as pressure difference, capillary force, and gravity. The processes of displacement and imbibition are carried out at the same time and interact with each other. Especially for small pores (25 nm < pore diameter ≤100 nm), whose capillary force and displacement pressure difference are relatively balanced, so it is difficult to distinguish the effects of imbibition and displacement [29–31]. (2) There is a big deviation in the definition of capillary force effect. Self-imbibition experiments are often used to study the effect of imbibition replacement in recent years. Many scholars have concluded that "the greater the permeability, the higher the imbibition replacement efficiency" and "the smaller the interfacial tension, the higher the imbibition replacement efficiency." However, these conclusions are contrary to the effect of capillary force. The smaller the core permeability and the pore throat radius, the greater the capillary force and the more obvious the corresponding imbibition effect in general. Similarly, the smaller the interfacial tension, the smaller the capillary force effect and the worse the imbibition effect [32–34]. The reason why some contrary conclusions are drawn is that self-imbibition process is not only affected by capillary force, and the effect of which has not been clearly defined.

Based on the core slice displacement experiment, this study effectively distinguishes the imbibition and displacement effects, quantitatively characterizes the imbibition retention rate, and realizes the visual observation of imbibition and displacement processes.

2. Methodology

2.1. The Principle of Experiment. The force direction of the fluid under imbibition is related to wettability, and it is always from the wetting phase to the nonwetting phase. When the nonwetting phase is replaced with the wetting phase under the action of capillary force, the fluid replacement occurs spontaneously. When the wetting phase is replaced with the nonwetting phase, a larger external force is required to achieve fluid replacement. Different from capillary force, the direction of fluid flow under displacement is mainly related to the directivity of displacement pressure difference and has nothing to do with wettability. In a word, when the nonwetting phase is replaced with the wetting phase, the direction of the force is from the wetting phase to the nonwetting phase. When the wetting phase is replaced with the nonwetting phase, the direction of the force is from the nonwetting phase to the wetting phase.

Assuming that the wettability of the core tends to be hydrophilic, the process of wetting phase displacing nonwetting phase is shown in Figure 1(a), where the blue area represents water phase, red area represents oil phase, and black area represents rock skeleton. Under the action of the production pressure difference, most of the water phase flows through the large pore throat to displace the oil phase. At the same time, spontaneous imbibition occurs in the small pore throat under the action of capillary force, the water phase is sucked into the small pore throats to displace the oil phase, and the water phase fills the affected pore throat areas.

After the wetting phase displaces the nonwetting phase to reach the displacement limit, the nonwetting phase is used to reversely displace the wetting phase (oil reverse displacement water), as shown in Figure 1(b). The water phase in the large pore throat is displaced by the oil phase under the action of the production pressure difference. Since the production pressure difference is much smaller than the capillary force of the small pore throat, the water phase in the small pore throat is retained. Comparing the two processes of the wetting phase displacing the nonwetting phase and the nonwetting phase displacing the wetting phase, we can effectively distinguish the imbibition and displacement in the process of fluid replacement in the tight reservoir.

2.2. The Process of Experiment. The six cores used in the experiment are from the tight sandstone reservoir of the Chang 7 Formation in the Ordos Basin. The basic physical parameters are shown in Table 1. The porosity distribution is 8.06%~10.86%, with an average of 9.33%. The permeability distribution is 0.144 mD~0.387 mD, with an average of 0.251 mD. The clay content is 3.28%~4.92%, with an average of 3.96%. In addition, the contents of illite, chlorite, and illite/montmorillonite in each core are similar. Since these cores come from the same block, there is little difference in physical properties between the cores. Core slices made from six cores are shown in Figure 2.

The detailed experimental procedures are as follows:

(1) The core is made into a core slice sample with a length of 2 cm, a width of 2 cm, and a thickness of about 0.5 mm, which is sealed with glass. The experimental device is shown in Figure 3

(2) Turn on the vacuum pump and evacuate the core slices for at least 5 hours. Turn off the evacuation pump to saturate the core with water, and end when there is no significant change in the color of the core (methyl blue is added to the water phase for easy identification). This process simulates the process of water filling the rock pores first under the original geological conditions

(3) Displace the saturated simulated oil, which is added with oil red solution for easy identification. The ratio

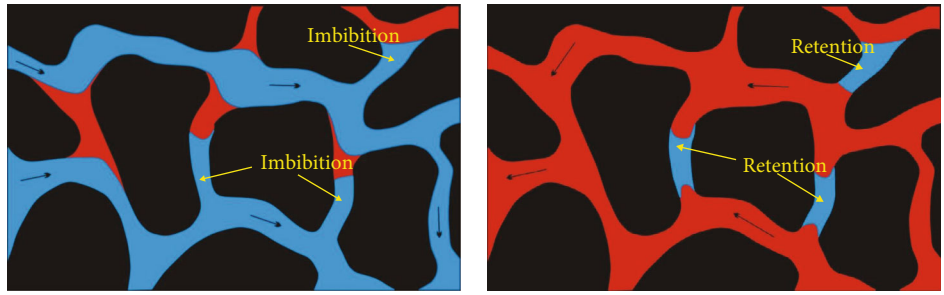

(a) The process of water displacing oil (b) The process of oil reversely displacing water

Figure 1: Schematic diagram of fluid displacing and reversely displacing (the blue area represents water phase, the red area represents oil phase, and the black area represents the rock skeleton).

Table 1: Basic physical parameters of cores.

Number	Length (cm)	Diameter (cm)	Dry weight (g)	Porosity (%)	Average of gas permeability ($10^{-3}\mu m^2$)	Clay content (%)	Mineral types and relative content (%)		
							Illite	Chlorite	Illite/montmorillonite
A12	4.342	2.51	49.49	10.86	0.387	3.57	15.42	5.11	13.47
B17	4.328	2.52	51.63	8.06	0.181	3.28	16.18	5.09	15.73
B30	4.358	2.51	52.83	9.61	0.313	4.92	13.06	4.83	14.11
B33	4.364	2.52	52.23	8.48	0.144	3.71	13.27	6.65	15.08
C35	4.306	2.52	50.24	8.69	0.199	4.41	15.99	6.57	15.85
C37	4.406	2.52	50.54	10.28	0.284	3.86	15.26	6.27	14.47

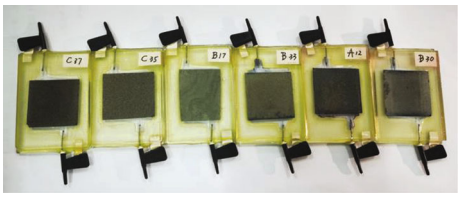

Figure 2: Core slices.

of crude oil and kerosene in the target reservoir is 1 : 2, and the viscosity of the simulated oil phase is 1.87 mPa·s. This process simulates the accumulation process of the reservoir, and the first NMR scan is performed after displacement until no water phase is produced at the output end

(4) In the process of water displacing oil, the core slices are observed in real time by a microscope. When there is no oil phase produced at the production end, stand still for a period of time to allow the water phase to be fully imbibed. Then, record the oil-water distribution at the moment, and conduct the second NMR scan

(5) In the process of oil reversely displacing water, the core slices are observed in real time by a microscope. When there is no water phase produced at the production end, stand still for a period of time. Then, record the oil-water distribution at the moment, and conduct the third NMR scan

(6) Analyze the experimental data. Compare the processes of displacing saturation simulation oil, water displacing oil, and oil reverse displacing water. The Nikon NIS-Elements Documentation software was used to identify and quantify the displacement range of water and oil phases, and the measuring cylinder was used to calculate the water phase imbibition retention rate of core slices

The specific measurement process is as follows: when measured using conventional measuring cylinder, the injection and production flow rates of the core slices can be measured after the oil and water collected in the measuring cylinder are separated, and the physical parameters of the core slices can be used to calculate the volume of each fluid in the core slices. When calculated using microscopic image recognition software, the water phase containing methyl blue and the oil phase containing oil red solution were mixed, and the corresponding mixed colors under different water saturation were calibrated. During the experiment, a microscope was used to observe the core slices in real time, and the images of the fluid color in the core slices observed by the microscope corresponded to the calibrated saturation values. Then, the control ranges of different saturation were calculated to obtain the fluid volumes in the core slices at different times. The formula for calculating the imbibition retention rate is

$$\eta = \frac{V_r}{V_\Phi}, \tag{1}$$

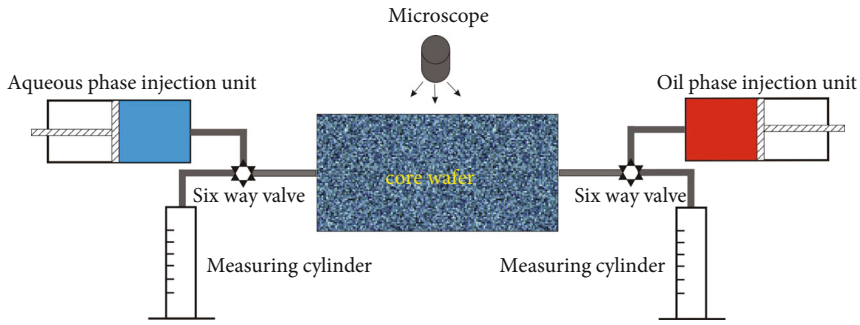

Figure 3: The experimental device.

where η is the imbibition retention rate, %; V_r is the imbibition retention volume of water phase, m^3; and V_Φ is the total pore volume of core slices, m^3.

Compared with the core self-imbibition experiment and the core displacement imbibition experiment, the experimental method provided in this study can effectively define the imbibition and displacement effects, quantitatively characterize the imbibition retention rate, and realize the visual observation of the imbibition and displacement process. However, this method also has certain limitations. When using microscopic images to identify fluids, only one surface of the core slice can be observed, and the measurement accuracy will be affected by the thickness of the core slice and the accuracy of color calibration. At the same time, due to the total displacement volume flow is small, the error of flow measurement increases. Compared with the calculation of displacement flow rate method, the average relative error of the six cores calculated by the microscopic image recognition method is about 6.8%. The average value of the two methods is taken in this experiment.

3. Results and Discussion

Based on the experimental principle, most of the pore throat areas in the core slices will be filled with simulated oil after the process of saturating simulated oil, which makes the core slices dyed red. After the process of water displacing oil, whether in the displacement area or the imbibition area, the water phase will replace the oil phase under the action of displacement or imbibition, which makes the core slices dyed blue. After the process of oil reversely displacing water, the water phase in the displacement area will be displaced by the oil phase under the action of pressure difference, which makes this area dyed red. In the imbibition area, the displacement pressure difference is less than the capillary force, resulting in the water phase being retained. This area appears as a blue area. This study takes B17 and C37 core slices as examples to illustrate.

3.1. The Displacement Experiment of the B17 Core Slice. The observation image of the B17 core slice saturated with simulated oil is shown in Figure 4(a), the observation image of the B17 core slice after water displacing oil is shown in Figure 4(b), and the observation image of the B17 core slice after the process of oil reversely displacing water is shown in Figure 4(c).

Comparing the core slice images of the three stages of the B17 core, three small areas were selected, which are enclosed by the dotted circle in Figures 4(a)–4(c). The area 1 and area 2 appear red after the process of saturating simulated oil, blue after the process of water displacing oil, and remain blue after the process of oil reversely displacing water. This phenomenon indicates that these areas are mainly controlled by imbibition. The blue area after oil reversely displacing water is the water phase left by imbibition. The area 3 appears red after the process of saturating simulated oil, blue after the process of water displacing oil, and red after the process of oil reversely displacing water. This phenomenon indicates that this area is mainly controlled by the effect of displacement. The experiment results indirectly verify the correctness of the experimental principle.

The NMR curve of the B17 core slice after positive and negative displacement is shown in Figure 5. The abscissa is the relaxation time, which corresponds to the pore throat size. The larger the relaxation time is, the larger the pore throat diameter is. The ordinate is the amplitude of NMR signal. Through the experimental calibration, the NMR signal of the water phase is much stronger than that of the oil phase, so the signal amplitude of the NMR curve mainly reflects the amount of the water phase. By comparing the changes of the curves, it can be seen that after the process of saturating simulated oil, the NMR curve of the core slice shows a double hump shape. The peak signal intensity of the curve corresponding to the small pore throat is higher than that corresponding to the large pore throat, indicating that the small pore throat accounts for a large proportion of the core. After the process of water displacing oil, the peak of the curve corresponding to the small pore throat has a slight left deviation, and the NMR signal amplitude has little change. The peak of the curve corresponding to the large pore throat deviates significantly to the left, and the signal amplitude decreases. The range of the hump across the pore throat increases. This is due to fluid displacement; the water phase is more likely to enter from larger pore throat and invade into smaller pore throat under the action of pressure difference and capillary force, which affects the area that was not affected by the process of saturating simulated oil. After the process of oil reversely displacing water, the peak value

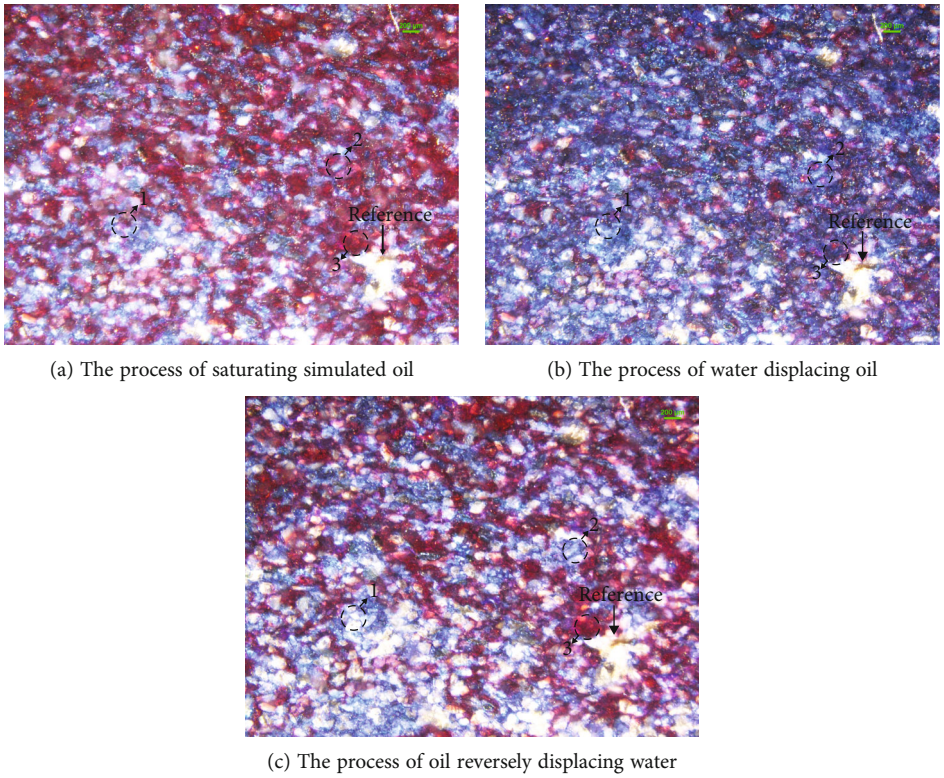

(a) The process of saturating simulated oil

(b) The process of water displacing oil

(c) The process of oil reversely displacing water

Figure 4: Observation images of B17 core slices at different displacement stages.

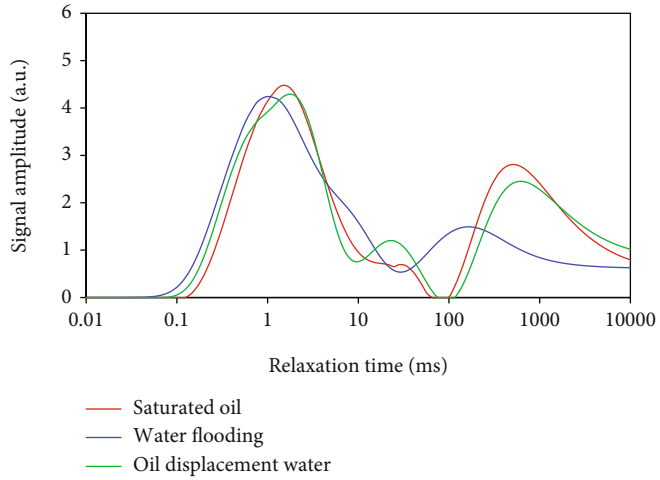

Figure 5: The NMR curve of B17 core slice after positive and negative displacement.

of the curve corresponding to the small pore throat has no obvious lateral shift, and the signal amplitude has little change. This is because the water phase in the small pore throat is retained by the capillary force. The peak value of the curve corresponding to the large pore throat deviates significantly to the right, and the peak signal amplitude increases greatly. We can conclude that the displacement process makes more fluid flow in the larger pore throat, and the fluid flow direction is the migration from the larger pore throat to the largest pore throat.

3.2. The Displacement Experiment of the C37 Core Slice. The observation image of the C37 core slice after the oil simulation saturating process is shown in Figure 6(a), the observation image of the C37 core slice after the water displacing oil process is shown in Figure 6(b), and the observation image of the C37 core slice after the oil reversely displacing water process is shown in Figure 6(c).

Comparing the core slice images of the three stages of the C37 core, three small areas were selected, which are enclosed by the dotted circle in Figures 6(a)–6(c). The area

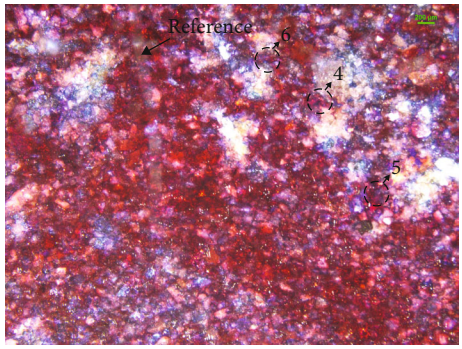

(a) The process of saturating simulated oil

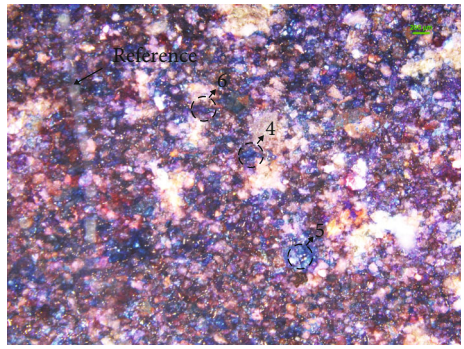

(b) The process of water displacing oil

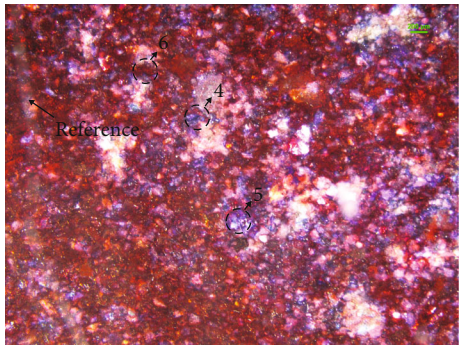

(c) The process of oil reversely displacing water

Figure 6: Observation images of C37 core slices at different displacement stages.

4 and area 5 appear red after the process of saturating simulated oil, blue after the process of water displacing oil, and remain blue after the process of oil reversely displacing water. This phenomenon indicates that these areas are mainly controlled by imbibition, and the blue area is the water phase left behind by imbibition retention. The area 6 will be dyed red after the process of saturating simulated oil, blue after the process of water displacing oil, and red after the process of oil reversely displacing water, which indicates that the pore throat in this area is larger and is mainly controlled by the action of displacement.

The NMR curve of the C37 core slice after positive and negative displacement is shown in Figure 7. By comparing the changes of the curves, it can be seen that after the process of saturating simulated oil, the NMR curve of the core slice is in the shape of a double hump. The peak value of the curve corresponding to the large pore throat is higher than the peak value of the curve corresponding to the small pore throat, which indicates that the core has a high proportion of large pore throats. After the process of water displacing oil, the peak value of the curve corresponding to the small pore throat shifted significantly to the left, and the amplitude of NMR signal increased. This is due to the imbibition of the small pore throat; the water phase enters into the small pore throat under the action of capillary force, which affects the area not affected by the simulated oil. At the same time, the NMR signal is enhanced because of a large amount of water phase imbibition. The peak value of the curve corresponding to the large pore throat has no obvious shift from left to right. However, the signal amplitude decreases and the range of the hump across the pore throat increases, indicating that the fluid flows to the larger pore throat under the joint action of displacement and imbibition. After the process of oil reversely displacing water, the peak value of the curve corresponding to the small pore throat has no obvious lateral shift, and the signal amplitude changes little, which is because the water phase in the small pore throat is bound and retained by the capillary force. The peak value of the curve corresponding to the large pore throat deviates significantly to the right. This illustrates that the displacement process makes more fluid flow in the larger pore throat, and the flow direction of the fluid is the migration from the larger pore throat to the larger pore throat.

3.3. Relationship between Imbibition Retention Rate and Permeability. On the basis of the displacement experiments of six core slices, combined with the recognition software of microscope images and the calculation of displacement flow rate, the amount of fluid controlled by displacement and imbibition can be effectively quantified, and the rate of imbibition retained also can be measured.

The statistical data after the displacement experiment is shown in Figure 8. It is not difficult to see from the curve shape that the imbibition retention rate decreases exponentially with the increase of permeability, and the fitting relationship is as follows:

$$\eta = 5.2047 \times K^{-1.176}, \tag{2}$$

where K is the gas permeability, $10^{-3}\mu m^2$.

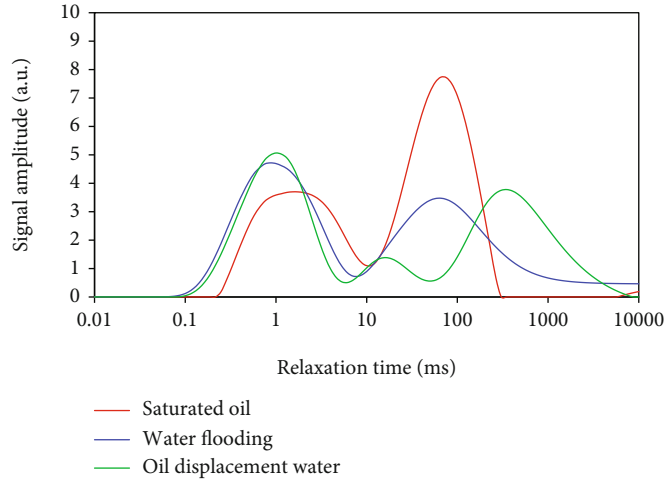

Figure 7: The NMR curve of C37 core slice after positive and negative displacement.

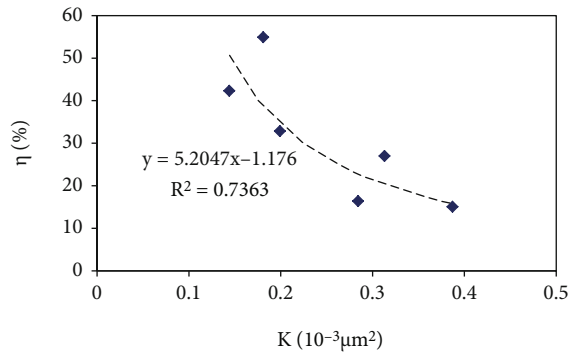

Figure 8: The relationship between the imbibition retention rate and the permeability.

4. Conclusions

(1) According to the difference between imbibition and displacement, an experimental method that can visualize the imbibition and displacement process is proposed by combining the core slice displacement experiment. Based on this method, the process of imbibition and displacement can be effectively distinguished, and imbibition retention rate can be quantitatively characterized

(2) During the imbibition process, the peak value of the NMR curve corresponding to the small pore throat shifted to the left, and the signal amplitude increased. During the displacement process, the peak value of the NMR curve corresponding to the small pore throat has no obvious shift and signal amplitude change, but the peak value of the curve corresponding to the large pore throat is shifted to the right

(3) There is an exponential negative correlation between imbibition retention rate and gas permeability. The larger the gas permeability is, the smaller the imbibition retention rate is

Data Availability

Raw data and derived data supporting the findings of this study are available from the author Xiong Liu (email: liuxiong2016@xsyu.edu.cn) on request.

Conflicts of Interest

The authors declare no competing interest.

Acknowledgments

We would like to express appreciation to the following financial support: the National Natural Science Foundation of China (Nos. 51934005, 52174028, and 52174029) and the Innovation and Practice Training Program for Graduate Students (YCS21211006).

References

[1] G. Mason and N. R. Morrow, "Developments in spontaneous imbibition and possibilities for future work," *Journal of Petroleum Science and Engineering*, vol. 110, pp. 268–293, 2013.

[2] M. Meng, H. Ge, Y. Shen, Q. Li, and J. Yu, "The study of tight gas reservoirs imbibition by nuclear magnetic resonance," in *ARMA-CUPB 199407, ARMA-CUPB Geothermal International Conference*, Beijing, China, 2019.

[3] C. Wang, W. Cui, H. Zhang, X. Qiu, and Y. Liu, "High efficient imbibition fracturing for tight oil reservoir," in *SPE 191274, SPE Trinidad and Tobago Section Energy Resources Conference*, Port of Spain, Trinidad and Tobago, 2018.

[4] Z. Wu, C. Cui, Y. Ye, X. Cheng, and J. Trivedi, "A fractal model for quantitative evaluating the effects of spontaneous imbibition and displacement on the recovery of tight reservoirs," *Journal of Petroleum Science and Engineering*, vol. 198, pp. 108120–108120, 2021.

[5] J. O. Alvarez and D. S. Schechter, "Wettability, oil and rock characterization of the most important unconventional liquid reservoirs in the United States and the impact on oil recovery," in *URTEC 2461651, SPE/AAPG/SEG Unconventional Resources Technology Conference*, San Antonio, Texas, USA, 2016.

[6] D. Arab, A. Kantzas, and S. L. Bryant, "Effects of oil viscosity and injection velocity on imbibition displacement in sandstones," in *SPE 199909, SPE Canada Heavy Oil Conference*, Virtual, 2020.

[7] A. Mai and A. Kantzas, "Heavy oil waterflooding: effects of flow rate and oil viscosity," in *PETSOC 2007144, Canadian International Petroleum Conference*, Calgary, Alberta, 2007.

[8] S. K. Li, W. D. Liu, H. Q. Zhang et al., "Experimental study on spontaneous imbibition oil displacement in low permeability reservoirs," *Journal of Petroleum*, vol. 2, pp. 109–112, 2007.

[9] A. Bertoncello, J. Wallace, C. Blyton, M. Honarpour, and C. S. Kabir, "Imbibition and water blockage in unconventional reservoirs: well-management implications during flowback and early production," in *SPE 167698, SPE/EAGE European Unconventional Conference*, Vienna, Austria, 2014.

[10] A. Habibi, H. Dehghanpour, M. Binazadeh, D. Bryan, and G. Uswak, "Advances in understanding wettability of tight oil formations: a montney case study," *SPE Reservoir Evaluation & Engineering*, vol. 19, no. 4, pp. 583–603, 2016.

[11] W. Jialu, L. Yuzhang, C. Maoqian, L. Li, and G. Jian, "Experimental study on fracture dynamic imbibition mechanism in low permeability reservoir," *Journal of Petroleum Exploration and Development*, vol. 36, no. 1, pp. 86–90, 2009.

[12] Y. B. Su, G. Y. Lin, and Y. Han, "Effects of surfactants on spontaneous imbibition oil displacement in tight sandstone reservoirs," *Journal of Fault-Block Oil and Gas Fields*, vol. 24, no. 5, pp. 691–694, 2017.

[13] M. S. Ju, X. Y. Wang, W. S. Yu, S. L. Yang, W. Z. Ye, and T. Q. Zhang, "Static imbibition law of tight reservoirs based on NMR technology," *Journal of Xinjiang Petroleum Geology*, vol. 40, no. 3, pp. 334–339, 2019.

[14] Y. Li, J. Yang, Z. Pan, and W. Tong, "Nanoscale pore structure and mechanical property analysis of coal: an insight combining AFM and SEM images," *Fuel*, vol. 260, article 116352, 2020.

[15] G. Mason, H. Fischer, N. R. Morrow, and D. W. Ruth, "Correlation for the effect of fluid viscosities on counter-current spontaneous imbibition," *Journal of Petroleum Science and Engineering*, vol. 72, no. 1-2, pp. 195–205, 2010.

[16] S. Li, Y. H. Ding, D. Meng, LU. Yongjun, and XU. Jiangwen, "Experiments and multiscale simulations of volume stimulation in tight reservoirs considering imbibition and displacement," *Journal of Oil Drilling and Production Technology*, vol. 38, no. 5, pp. 678–683, 2016.

[17] F. Y. Wang, F. C. Zeng, and J. Y. Zhao, "Mathematical model of displacement imbibition in low permeability / tight reservoir and its application," *Journal of Petroleum*, vol. 41, no. 11, pp. 1396–1405, 2020.

[18] Q. Feng, S. Xu, X. Xing, W. Zhang, and S. Wang, "Advances and challenges in shale oil development: a critical review," *Advances in Geo-Energy Research*, vol. 4, no. 4, pp. 406–418, 2020.

[19] X. Y. Wang, A. G. He, M. S. Ju, Y. P. Xu, Y. Zhang, and C. M. Xu, "Improving tight oil imbibition and recovery degree based on microfluidic method," *Journal of Science Technology and Engineering*, vol. 21, no. 15, pp. 6272–6277, 2021.

[20] S. Du, S. Lee, X. H. Wen, and Y. Efendiev, "A similarity solution for imbibition process and its adaptation in finite difference simulation of fractured reservoirs," in *SPE 203959, SPE Reservoir Simulation Conference*, On-Demand, 2021.

[21] X. Z. Wang, X. S. Zhao, H. L. Dang et al., "Study on the characteristics of spontaneous imbibition and displacement in tight oil reservoirs based on NMR," *Journal of Progress in geophysics*, vol. 35, no. 5, pp. 1870–1877, 2020.

[22] Z. N. Shen, X. Z. Wang, X. Y. Kang, C. J. Wang, and Z. Jin, "Quantitative analysis of imbibition and displacement oil recovery mechanism in typical tight oil reservoirs in Yan-Chang oilfield," *Journal of Petroleum Geology and Recovery Efficiency*, vol. 25, no. 5, pp. 99–103, 2018.

[23] X. W. Li, J. Liu, G. Guo, K. Li, and X. Liu, "Mathematical model and application of imbibition in tight sandstone reservoirs," *Journal of Special Oil and Gas Reservoirs*, vol. 24, no. 6, pp. 79–83, 2017.

[24] Z. M. Yang, X. W. Liu, H. B. Li, Q. Lei, and X. Wang, "Analysis on the influencing factors of imbibition and the effect evaluation of imbibition in tight reservoirs," *Journal of Petroleum Exploration and Development*, vol. 26, no. 4, pp. 779–785, 2019.

[25] Z. Wang, H. Li, X. Lan, K. Wang, Y. Yang, and V. Lisitsa, "Formation damage mechanism of a sandstone reservoir based on micro-computed tomography," *Advances in Geo-Energy Research*, vol. 5, no. 1, pp. 25–38, 2021.

[26] K. X. Gao, Y. Q. Fan, Z. M. Jin, S. C. Liu, and Y. J. Zhang, "Application of microfluidic chip in enhanced oil recovery technology," *Journal of Fault-Block Oil and Gas Fields*, vol. 25, no. 2, pp. 269–272, 2018.

[27] C. J. Yao, J. Zhao, G. X. Zhan et al., "Design of simulation device for capillary imbibition displacement in ultra-low permeability tight reservoir," *Journal of Laboratory Research and Exploration*, vol. 40, no. 3, pp. 67–70, 2021.

[28] Y. Li, D. Tang, P. Wu et al., "Continuous unconventional natural gas accumulations of Carboniferous-Permian coal-bearing strata in the Linxing area, northeastern Ordos basin, China," *Journal of Natural Gas Science and Engineering*, vol. 36, pp. 314–327, 2016.

[29] R. Dutta, "Laboratory study of fracturing fluid migration due to spontaneous imbibition in fractured tight formations," in *SPE 160915, SPE Annual Technical Conference and Exhibition*, San Antonio, Texas, USA, 2012.

[30] M. K. Valluri, J. O. Alvarez, and D. S. Schechter, "Study of the rock/fluid interactions of sodium and calcium brines with ultra-tight rock surfaces and their impact on improving oil recovery by spontaneous imbibition," in *SPE 180274, SPE Low Perm Symposium*, Denver, Colorado, USA, 2016.

[31] Y. Li, Z. Wang, Z. Pan, X. Niu, Y. Yu, and S. Meng, "Pore structure and its fractal dimensions of transitional shale: a cross-section from east margin of the Ordos basin, China," *Fuel*, vol. 241, pp. 417–431, 2019.

[32] B. Goudarzi, P. Mohammadmoradi, and A. Kantzas, "Pore-level simulation of heavy oil reservoirs; competition of capillary, viscous, and gravity forces," in *SPE 181188, SPE Latin America and Caribbean Heavy and Extra Heavy Oil Conference*, Lima, Peru, 2016.

[33] P. Mohammadmoradi and A. Kantzas, "Wettability and capillary imbibition in shales; analytical and data-driven analysis," in *SPE 189806, SPE Canada Unconventional Resources Conference*, Calgary, Alberta, Canada, 2018.

[34] Y. Li, X. Gao, S. Meng et al., "Diagenetic sequences of continuously deposited tight sandstones in various environments: a case study from upper Paleozoic sandstones in the Linxing area, eastern Ordos basin, China," *AAPG Bulletin*, vol. 103, no. 11, pp. 2757–2783, 2019.

Hindawi
Geofluids
Volume 2022, Article ID 8130349, 15 pages
https://doi.org/10.1155/2022/8130349

Research Article

Main Factors of Mesozoic Tectonic Deformation in the Erlian Basin, Inner Mongolia, China: Insights from Physical Modelling

Yue Zhao,[1] Qiang Xu,[1] Yongchen Li,[2] Xiujia Bai,[1] Rong Ding,[2] Jianxin Wang,[3] and Tao Hou[4]

[1]*General Prospecting Institute of China National Administration of Coal Geology, Beijing 100039, China*
[2]*PetroChina Coalbed Methane Company Limited 100028, China*
[3]*China National Offshore Oil Corporation Research Institute, Beijing 100028, China*
[4]*Petrochina Huabei Oilfield Company, Renqiu 062550, China*

Correspondence should be addressed to Qiang Xu; 454123526@qq.com

Received 14 February 2022; Accepted 7 April 2022; Published 4 May 2022

Academic Editor: Yanjun Meng

Erlian Basin is a Mesozoic oil and gas-bearing basin in northeast of China. The extension rate, extension direction, and stratum thickness of this rift basin have a clear control on its shape and extension. In this study, we design three sandbox models of the Erlian Basin to represent the effects of changing these three factors. The extension rate controls the timing of secondary fault formation inside the rift basin; a high extension rate promotes faster deformation inside the rift. The extension direction controls the strike of the fault inside the rift; a greater angle between the extension direction and the normal direction of the strike of the rift favors rapid evolution of internal secondary faults. The stratum thickness represents the control of sedimentation on the rift basin; the thinner the brittle layer, the wider the rift. The simulation results also show that the extension direction is the major factor controlling tectonic deformation in the basin. Stratum thickness and extension rate are secondary controlling factors. Additionally, according to geometric and kinematic similarities between typical Mesozoic rift basins in eastern and adjacent areas of China, we suggest that southeastward extension is a possible kinematic mechanism for basin formation.

1. Introduction

Erlian Basin is a Mesozoic oil- and gas-bearing basin in northeast China (Figure 1). There are significant geometric and kinematic similarities between Erlian Basin and other Mesozoic rift basins in eastern China [1–8]. For example, the structural style of fault depression in both Erlian Basin and peripheral Mesozoic rift basins such as Hailar Basin and Yin'e Basin predominantly includes a long, narrow half graben, a graben, and a composite structure combining the two [1]. The evolutionary features of the study area can be divided into two stages of tectonic deformation: Mesozoic early continental and late depression [9, 10]. Previous research has involved long-term oil and gas exploration of the basin ([11]) and indicates that tectonic deformation plays an important role in controlling the distribution of oil and gas resources [5]. Consequently, there is an in-depth understanding of the distribution of early Cretaceous oil-bearing strata and the structural characteristics formed by continental rifting in this basin. According to previous research on the factors controlling basin deformation, four different models have been proposed: (1) The formation and distribution of rifting in the Erlian Basin were controlled by the pre-Mesozoic basement structure ([12, 13]). (2) The preexisting basal fault network, the tectonic stress field during the rifting period, and other factors at depth all controlled the formation and distribution of the rift basin [1]. (3) Five large-scale, long-active, and deep faults oriented EWW and NE in the basin basement controlled the tectonic evolution of the basin in different periods [14]. (4) The basement properties and preexisting structure of the basin controlled the structural pattern of the basin [5, 15, 16]. Thus,

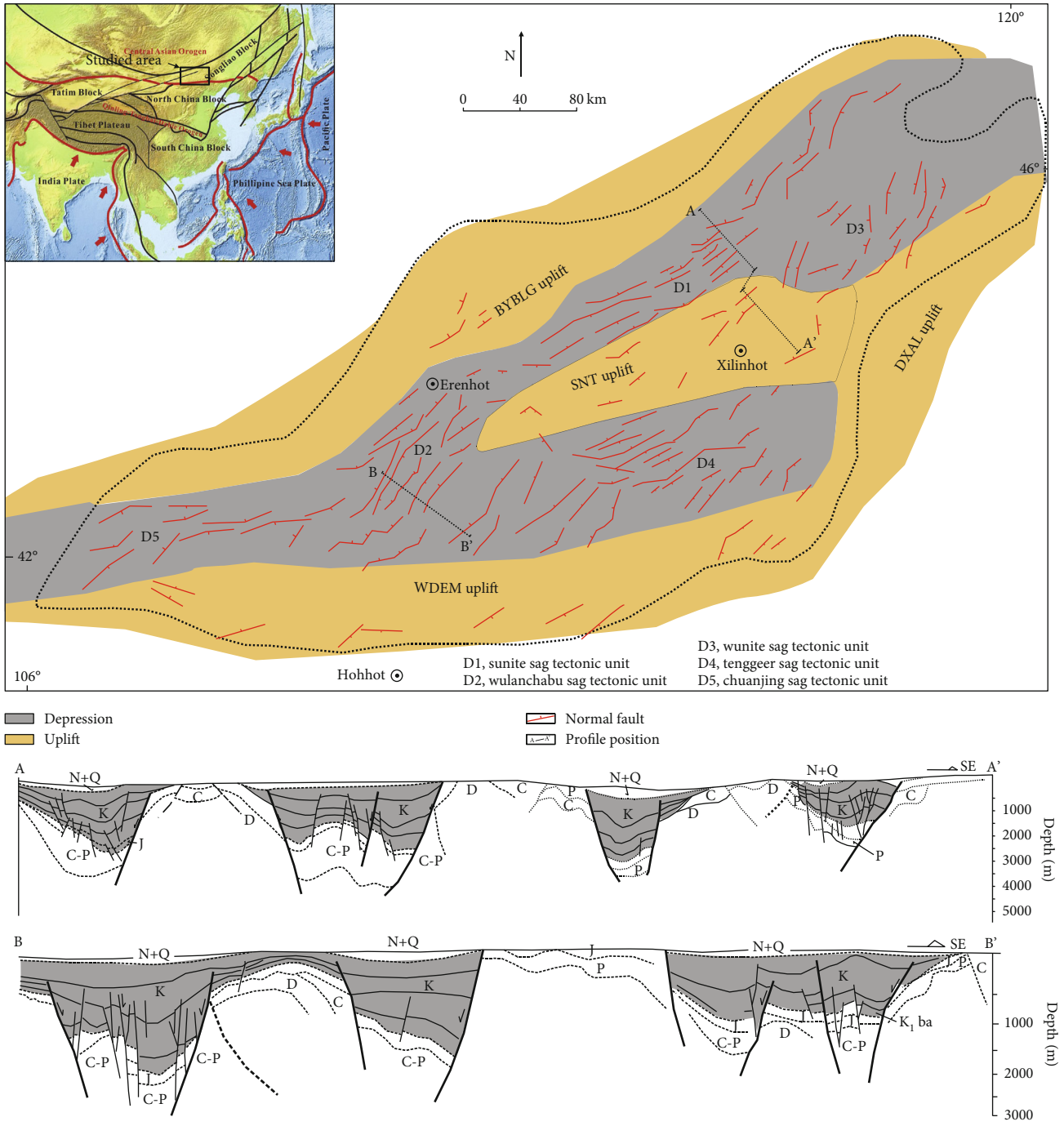

Figure 1: Distribution of tectonic units, major faults, and typical sections of faulted-sag basins in Erlian Basin interpreted from seismic data (revised after [16]).

the factors controlling Mesozoic tectonic deformation in the Erlian Basin remain controversial. Specifically, there is a lack of physical models that simulate deformation mechanisms, particularly the influence and control of pre-Mesozoic basement properties on deformation.

Deformation analysis of rifting and extension in basins has shown that physical simulations are an effective way to explore the mechanisms of tectonic formation; they can replicate the tectonic deformation and effectively verify the relevant formation mechanisms and evolution processes. Physical modelling has been widely used for rift and extensional structures and provides many new insights for understanding the tectonic deformation mechanism of rift basins [17, 18]; for example, experiments have shown that rift basin fault strike and combination is related to the extension direction [19–23], boundary geometry [24–26], preexisting structure [27–29], and basement properties [28].

According to the structural characteristics of a seismic section and the distribution characteristics of the planar fault system in the study area, combined with previous geological

analyses, we designed an experimental sandbox model that could control the extension rate, stratum thickness, and extension direction of the basin. The model was used to determine the major factors controlling tectonic deformation in the Erlian Basin, and our experimental results were compared with the present structural features. We then proposed a kinematic mechanism for formation of Erlian Basin and other basins with similar tectonic properties in northeast China.

2. Geological Background

Erlian Basin is generally oriented NNE; it has a wide central area, is narrow in the NE and NW, and has an elliptical shape. The tectonic units consist of five depressions: Sunite Sag, Wulanchabu Sag, Wunite Sag, Tenggeer Sag, and Chuanjing Sag, and three areas of uplift: the BYBLG uplift, SNT uplift, and WDEM uplift (Figure 1). The structural pattern is complex and exhibits different fault strikes. There are a series of three-level structural units inside the depressions and uplifted areas known as sunken areas and bulges. The master fault strike of Sunite Sag and Wulanchabu Sag in the central basin is NE50°–70°. The internal secondary fault depression of the central rift zone in Sunite-Wulanchabu is dominated in tandem and oblique structures and is characterized by a deep and narrow graben and a half graben. Multiple faulted depressions form a narrow, long, and positive fault depression zone, whose strike is essentially consistent with the extension direction of the depression. The strike of the master fault between Chuanjing Sag in the west and Tenggeer Sag in the south is EN50°–70°, whereas that of Wunite Sag in the east is NE15°–451. The internal secondary fault depressions in the rift zone around basin are dominated by oblique structures and are characterized by a shallow and wide graben and a half graben. Multiple fault depression oblique rows form a short, wide, and oblique fault depression zone, whose strike is oblique to the extension direction of the depression [16, 30]. This type of fault depression in the Erlian Basin is widespread in the rift basins of northeastern China, such as Hailar Basin and Yin'e Basin in the west of the Greater Khingan Mountains, which have a similar distribution direction and shape and combine to form the Mongolian fault basin system [10, 31].

The Erlian Basin is divided into three sets of construction. Internally, the pre-Mesozoic basement includes the Atrial crystalline metamorphic rock, Proterozoic era, and Paleozoic sedimentary rocks. Mesozoic Strata is the main body of the basins, including the Jurassic, the Lower Cretaceous, and a small amount of Upper Cretaceous, missing Triassic. Among them, the whole basin of the Jurassic is widely distributed, mainly in volcanic debris, volcanic rock, etc., and the thickness of the formation is relatively stable. The Lower Cretaceous is mainly filled with a series of debris rock layers, and the formation thickness is obviously subject to fault control. The Upper Cretaceous is only sporadic in partial depression; the Neogene and Quaternary are mainly distributed in the depression zone.

The basement of the Erlian Basin belongs to the Mongolian orogenic belt and has undergone multiple stages of tectonic evolution, including the Caledonian, Hercynian, Indosinian, and early Yanshanian periods. The basement structure is characterized by nonuniformity and composed of three anticlinorium and two synclinorium [32], which constitute a positive and negative tectonic pattern, as well as a number of large-scale faults oriented NNE and NE. Among them, the NE-NEE Erlian-Hegenshan fault and deep, near EW Ondor Sum-Xar Moron fault form two important structural boundaries. They divide the basement into three regions with significantly different tectonic directions and crustal structure properties, revealing the complex structural features of the strong deformation zone surrounding the weakly deformed block body. The anticlinorium uplift zone belongs to the weak deformation zone of the basement and forms the uplift zones of the basin. The synclinorium or fault zone belongs to the strong deformation zone of the basement, which mainly controls the development of basin depressions. Sunite Sag and Wulanchabu Sag in the middle of the basin are superimposed on the Dong Ujimqin-Erlian curved fold belt, which strikes from NE to NEE and protrudes southward. The strike of the master fault in the rift is essentially the same as that of the basement structure. Sunite Sag in the eastern margin of the basin is superimposed on the NEE-striking Erlian-Hegenshan Deep Fault Zone, whereas Chuanjing-Tenggeer Sag is superimposed on the EW-striking Ondor Sum-Xar Moron Deep Fault Zone, and on both sides of the fold belt, the strike of the master fault in the rift is oblique to the strike of the basement structure [16].

Some seismic sections in the Erlian Basin exhibit deformation characteristics of rapid Mesozoic rifting and slow late settlement (Figure 1), as well as strongly continuous fault activity. Early Cretaceous fault activity was strong, and fault displacement was large before weakening in the late stage. The structure pattern of the central positive rift zone is half-graben in tandem and codirectional composite structure. The master fault has a steep dip angle, and the resulting fault depression is narrow and long. The structural pattern of the peripheral oblique rift zone is half-graben in tandem and oblique arrangement. In the shallow layer, the fault is mainly characterized as a high-angle normal fault, with a dip angle up to 80°, a large fault displacement, a deep part that gradually becomes shovel type, and a resulting fault depression that is shallow and wide (Figure 1 A-A' and B-B').

3. Model Design

All the models in this study used a 60 cm × 45 cm sandbox (Figure 2). The models are driven by a motor to pull one side of the movable baffle; as the rubber at the bottom is stretched, the upper sand layer gradually produces normal faults and different types of rift. The model surface was photographed regularly using a computer-controlled camera. All experiments were repeated, revealing reproducible results. After each experiment, a layer of white quartz sand was spread evenly on the surface of the model to prevent deformation of the model surface. After spraying with water mist, the model was sliced at equidistant intervals to observe the internal deformation. Only one variable was changed in

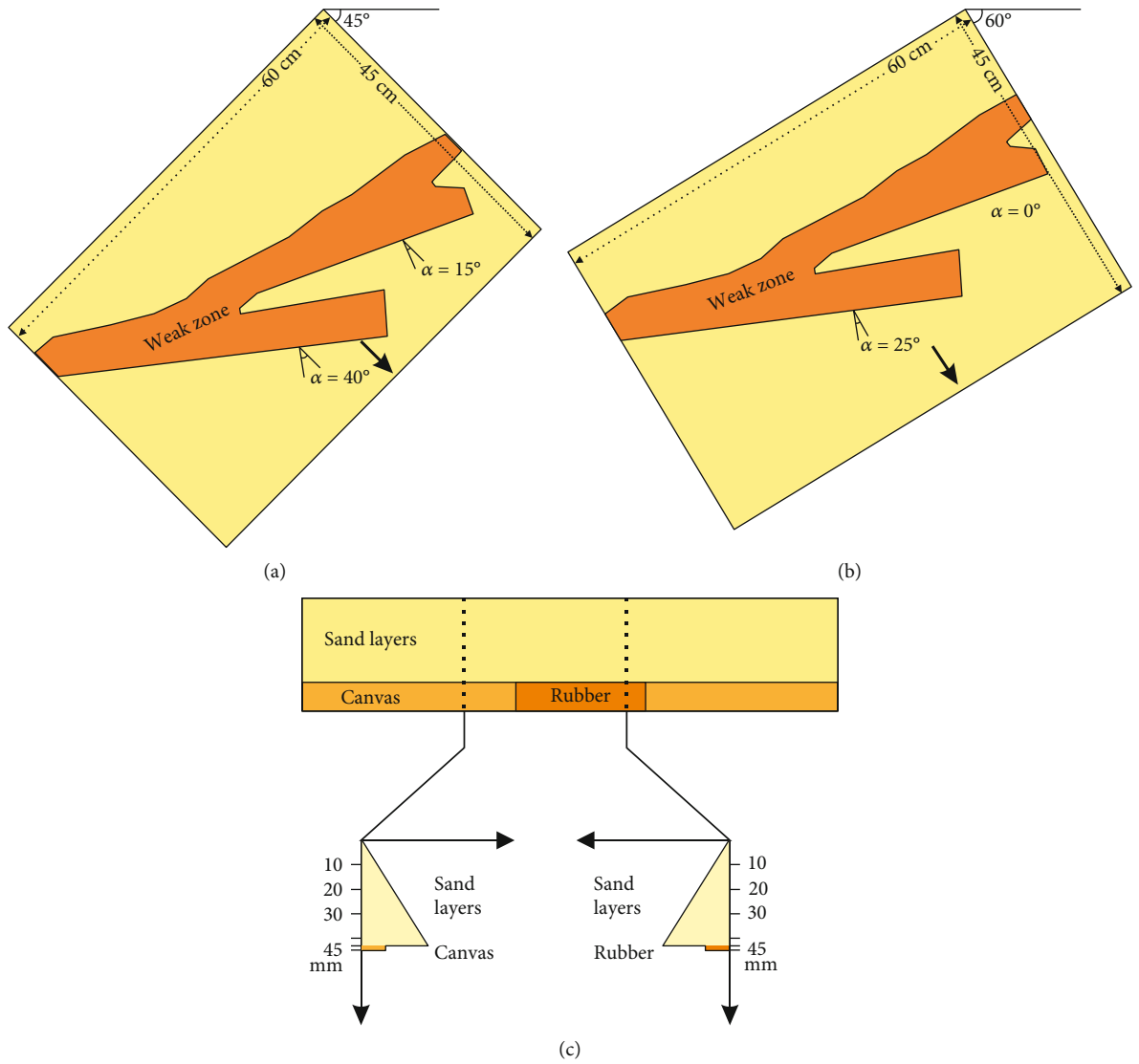

Figure 2: Schematic diagram of the experimental model. (a) Plan view of the extension direction oriented N315°E–N135°E, (b) plan view of the extension direction oriented N330°E–N150°E, and (c) cross-sectional view.

each model to examine the effect of different factors on tectonic deformation. The experimental design was simplified to reduce the impacts of minor factors. The sandbox experiments were carried out in the State Key Laboratory of Oil and Gas Resources and Exploration, China University of Petroleum (Beijing).

3.1. Experimental Setup. All models were 60 cm long and 45 mm wide. The shape of the base retractable eraser was similar to "Y"(Figure 2(a)); this design not only considers the actual Paleozoic basement shape of the Erlian Basin, but also the influence of different oblique rifting directions on tectonic deformation. Except for model 3, all models were 42 mm thick, in which the overlying sand layer was 40 mm and the base retractable rubber and nonstretchable canvas were 2 mm (Figure 2). The initial thickness of the overlying sand layer on model 3 was 25 mm, and a 5 mm sand layer was added for extensions of 20 mm, 40 mm, and 60 mm. The final thickness of the sand layer was therefore 40 mm, like the other models. In order to study the influence of syn-deposition and the thickness of the brittle layer (equivalent to changing the strength of the brittle layer) on tectonic deformation (similar to [33]) (Figure 2(c)), the final extension of all models was 80 mm (Table 1).

This series of models was designed to investigate the effect of stratum thickness, extension rate, and extension direction. Changing the extension direction is equivalent to changing the inclination angle of extension (defined as the angle between the extension direction and the normal direction of the rift) during the rifting process [23, 27, 33]. Model 1 had an extension rate and direction of 6.67×10^{-3} m/s and N315°E–N135°E, respectively. In model 2, the extension rate was changed to 3.35×10^{-2} m/s. In model 4, the extension direction was changed to N330°E–N150°E, which corresponds to a change in the extension inclination angle of $\alpha = 0°$, 25° compared with model 1 (extension angle $\alpha = 15°$, 40°).

Table 1: Parameter table of each sand box simulation experiment model.

Mode	Experimental series	Velocity of extension (mm/min)	Thickness of basement layers (mm)	Thickness of brittle layers (mm)	Extension direction	Syndeposition
1	Reference model	0.4	0.2	4.3	N315°E-N135°E	-
2	Variable extension velocity	2.0	0.2	4.3	N330°E-N150°E	-
3	Syndeposition	0.4	0.2	2.5	N315°E-N135°E°	+
4	Variable extension direction	0.4	0.2	4.3	N315°E-N135°E	-

Table 2: Material parameters of physical simulation experiments.

	Density (g/cm^3)	Particle size (mm)	Internal friction angle (°)	Kinetic friction coefficient	Static friction coefficient	Cohesion (Pa)
Quartz sand	1.43	0.25–0.3	30-31	0.65	0.59	80

3.2. Material Properties. We employed loosely dried quartz sand, which follows the Mohr-coulomb yielding criteria with a particle size of 0.25–0.3 mm, a density of 1.43 g/cm^3, an internal friction angle of 30–31°, a kinetic friction coefficient of 0.65, and a cohesion force close to 80 Pa (Table 2). It is an ideal analog material for simulating shallow structural deformation of the crust [34]. Rubber is widely used in experiments simulating the extensional structure of the rift basin due to its flexible elasticity [29, 35, 36]. This experiment employed the quasi-kinematic retractable eraser to simulate the highly ductile weak basement zone [36]. This weak deformation area was overlain with nonstretchable canvas to transfer the displacement.

3.3. Scaling. The model size ratio is 1×10^{-5}, as 1 cm in the model represents 1 km in reality; thus, the standard model simulates a brittle layer 4 km thick and 60 km long (Table 2). Values for the density, angle of internal friction, and cohesive force of brittle material of the geologic entity are derived from Zhou et al. [37]. The cohesive force of the brittle material in the model is 80 Pa [38], giving a cohesive force ratio of 2×10^{-6} (Table 3).

We apply standard formulas to scale the proportions of our model and actual geologic entity. The brittle sand follows the Mohr-Coulomb yielding criteria, and the stress ratio ($\sigma*$, constant: $\sigma* = \sigma_m/\sigma_n$, subscripts m and n, respectively, represent the model and geologic entity) is as follows [39]:

$$\sigma^* = \rho^* \times h^* \times g^*. \quad (1)$$

The density ratio ($\rho*$) is $\rho_m = 1430\ kg/m^3$ and $\rho_n = 2400\ kg/m^3$. The length ratio ($h*$) is $h_m = 4 \times 10^{-2}$ m and $h_n = 4 \times 10^3$ m. The gravity ratio ($g*$) is $g_m = g_n = 9.81\ m/s^2$. The stress ratio of the model brittle layer is 3×10^{-6}. The above proportions have the same order of magnitude, which indicates that our model satisfies the kinetic similarity criterion [40].

We also determined the ratio, R_s, between the gravity and cohesion force of the brittle region to ensure kinetic similarity between our experiments and the geologic entity [41]:

Table 3: Scaling of models and geologic entity.

Parameter	Model	Nature	Model/nature ratio (*)
Density, ρ (g/cm^3)	1.43	2.40	0.60
Internal friction angle, u	0.65	2.20	0.43
Cohesion, c (Pa)	80	7×10^7	1.14×10^{-6}
Gravity, g (m/s^2)	9.81	9.81	1.00
Length, l (m)	0.01	1000	1.00×10^{-5}
Stress, σ (Pa)	561	9.42×10^7	3.00×10^{-6}
R_s	7.01	2.35	/

$$R_S = \frac{\text{gravity}}{\text{cohesion}} = \frac{\rho.g.h}{c}. \quad (2)$$

The R_s values are 7.01 and 2.35 for the model and geologic entity, respectively ($c_{\text{geologic entity}} = 6 \times 10^7$, according to [42]).

4. Results

4.1. Reference Model (Model 1). The tectonic deformation evolution process of model 1 is shown in Figure 3 (extension rate 2 mm/min, extension direction NE315°–N135°E, and no syndeposition). Similar to the results of previous experiments [43–45], the initial stage of extension involves formation of a trunk boundary fault in the northern part of the model from the ductile and brittle base, forming a sinking rift zone (Figure 3(a)). Together with the antithetic secondary fault, they form a marginal graben. At this stage, all deformation is concentrated in the trunk boundary fault and the antithetic faults. Further stable extension promotes

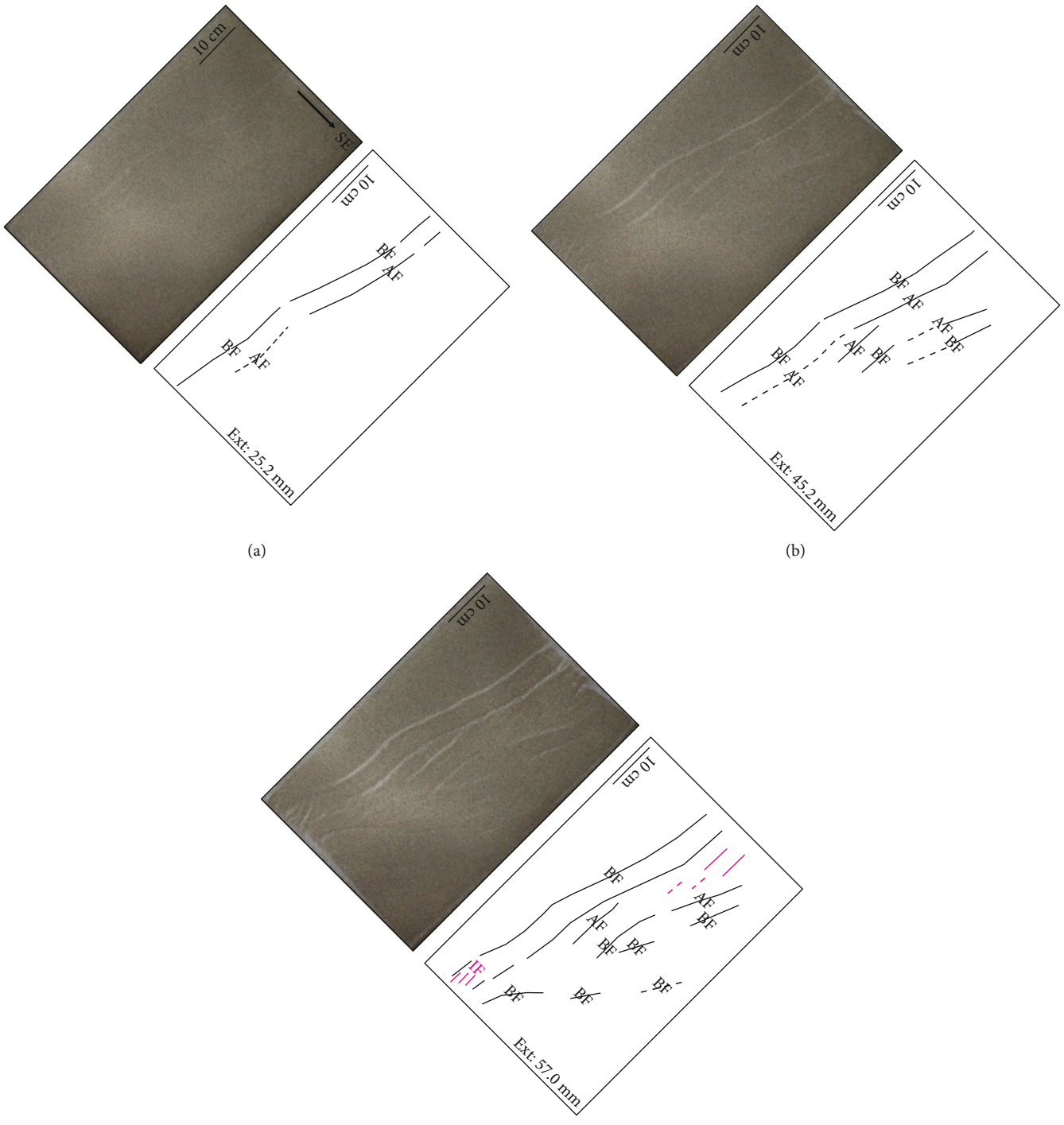

Figure 3: Continued.

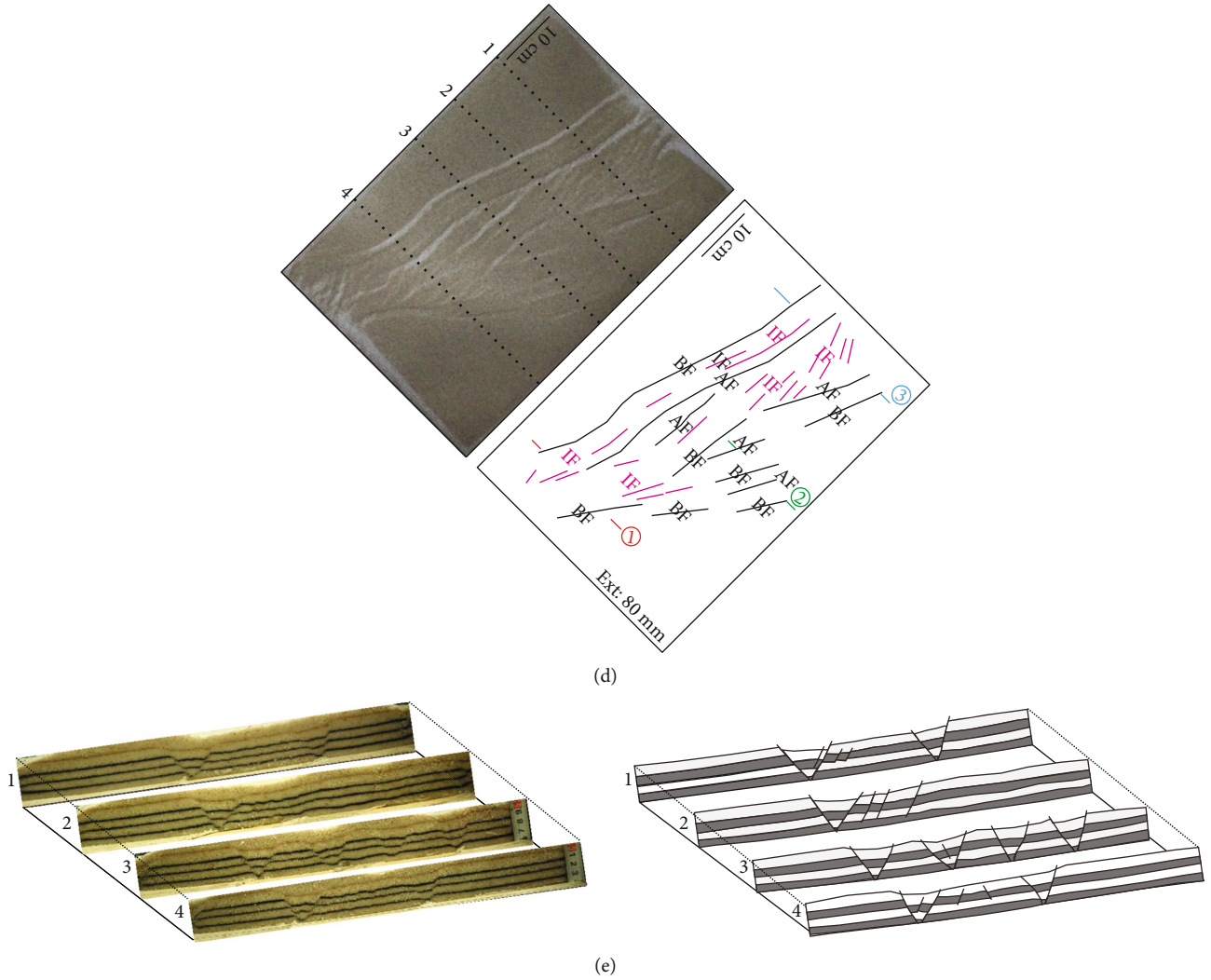

Figure 3: Evolution and characteristics of deformation in reference model 1. (a–d) Top-view photos (left panels) and schematic line-drawings of structures (right panels), illustrating boundary faults (BF), antithetic faults (AF), and internal faults (IF). (e) Vertical cross sections corresponding to locations in (d).

a change in the deformation pattern with extension of 57 mm (Figure 3(c)). The second master fault is formed at the boundary between the ductile base and the brittle base of the central horst zone, and the antithetic faults formed in the south of the model constitutes the second larger marginal graben, which undergoes further extension (Figures 3(c) and 3(d)) in the central horst zone to form a large number of secondary faults (the critical extension of the secondary fault when it first appears is determined by observing deformation of the model surface) [43–45]. Conversely, activity on the trunk boundary faults is reduced, eventually forming a structure in which the graben is arranged separately under steep boundary fault control. The final section clearly shows that four narrow grabens are juxtaposed in the center (Figure 3(e), slice 3). Close to the sides of the baffle, and these become two narrow grabens; thus, the closer to the baffle sides, the larger the interval between the grabens (Figure 3(e), slices 2, 4, and 5).

4.2. Effect of Extension Rate (Model 2). Model 2 has an extension rate of 4.0 mm/min, which is twice that of the reference model. The evolution of deformation still involves the initial boundary fault formation stage and the internal secondary fault formation and movement stage. As shown in Figure 4, the formation and movement of internal secondary faults occur when the amount of extension is 48 mm. This indicates that the rate of extension determines the amount of extension required for the evolution of internal secondary faults; a higher rate of extension leads to more rapid formation of internal secondary faults in the rift basin, thus requiring less amount of extension (Figure 5). However, the extension rate has little effect on the evolution of rift zone width (widest value in the vertical extension direction); all of them start at 20 mm extension and exhibit a positive correlation (Figure 6). The final cross section shows that the rifting system, in which the compound complex graben developed by a broad internal domino fault under the

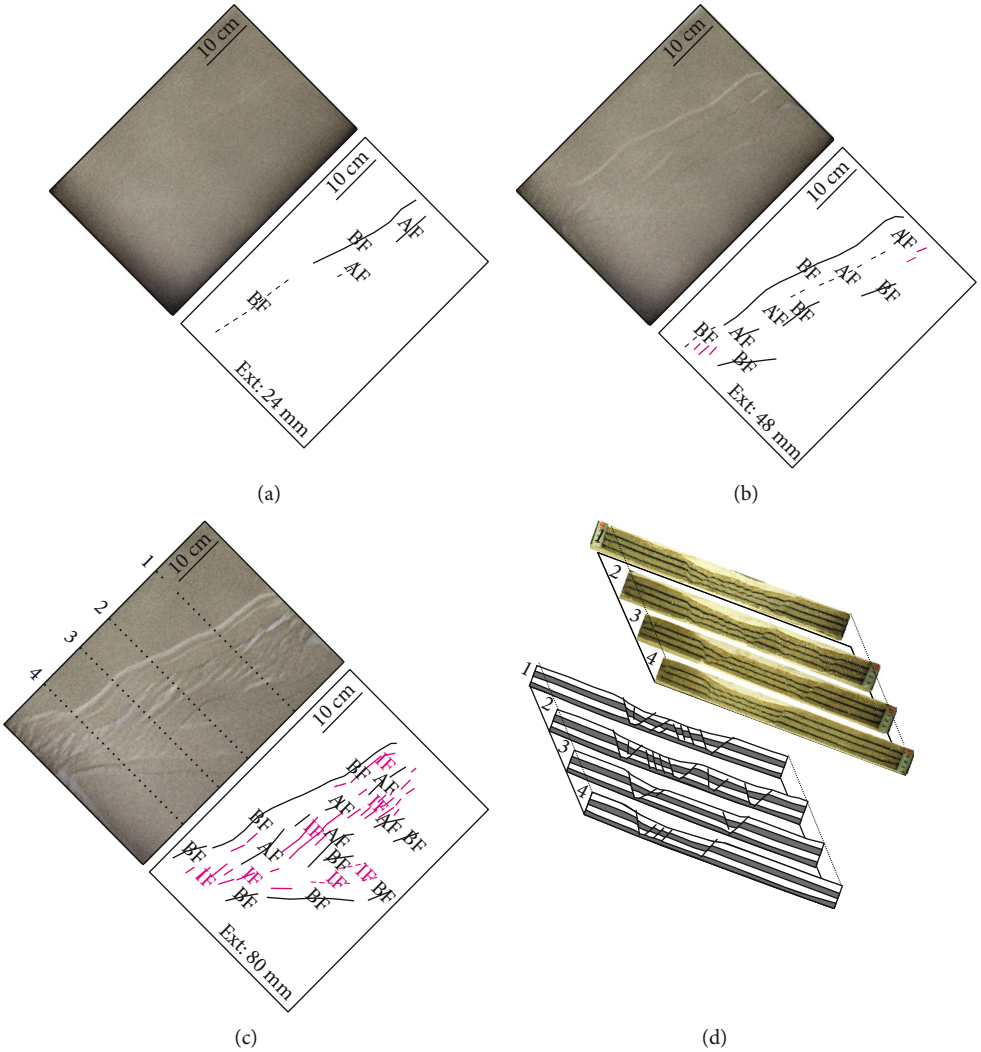

Figure 4: Evolution and characteristics of deformation in model 2, with a higher extension rate. (a–c) Top-view photos (left panels) and schematic line-drawings of structures (right panels), illustrating boundary faults (BF), antithetic faults (AF), and internal faults (IF). (d) Vertical cross sections corresponding to locations in (c).

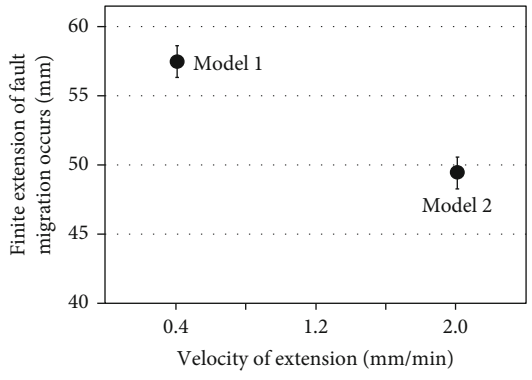

Figure 5: Summary of series 2 experiments (variable extension rate) illustrated as plots of the bulk extension corresponding to the first appearance of internal faults as a function of extension rate.

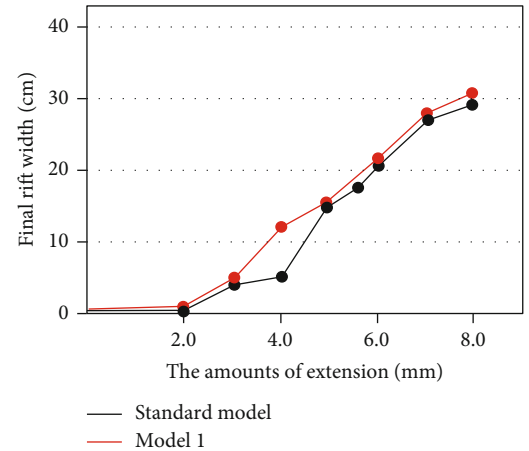

Figure 6: Final rift segment width as a function of extension, measured from the model surface views in Figures 4 and 5.

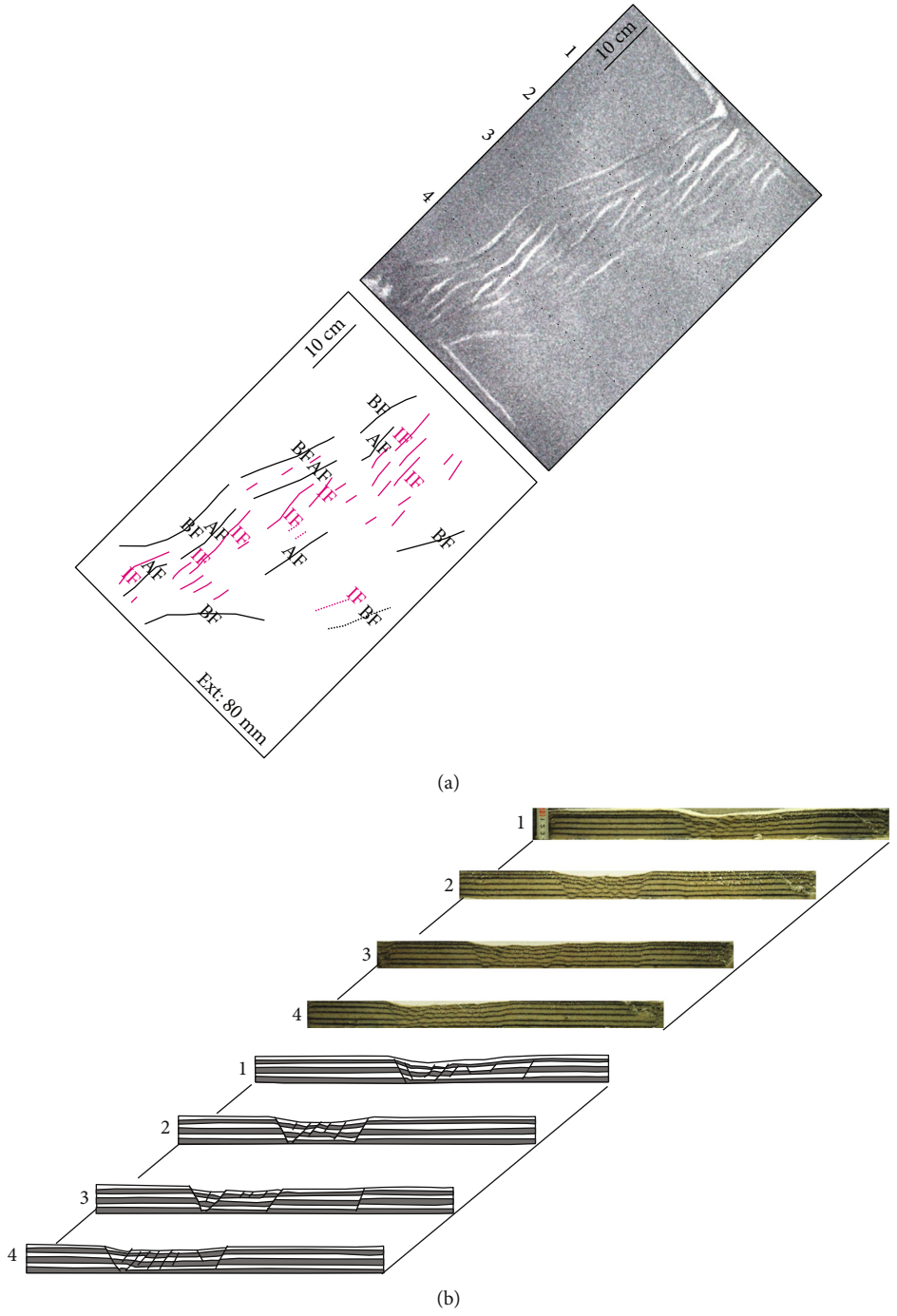

Figure 7: Evolution and characteristics of deformation in model 3, with thicker strata. (a) Top-view photo (upper panel) and schematic line-drawing of structures (lower panel), illustrating boundary faults (BF), antithetic faults (BF), and internal faults (IF). (b) Vertical cross sections corresponding to locations in (a).

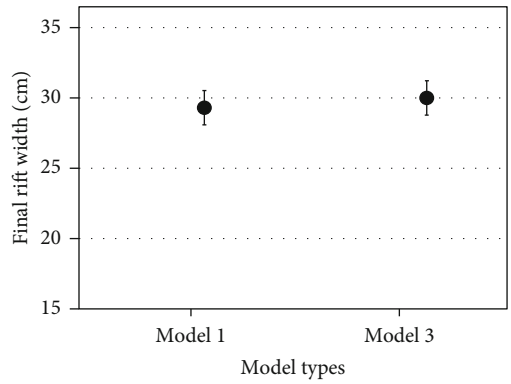

Figure 8: Final rift segment width as a function of extension, measured from the model surface.

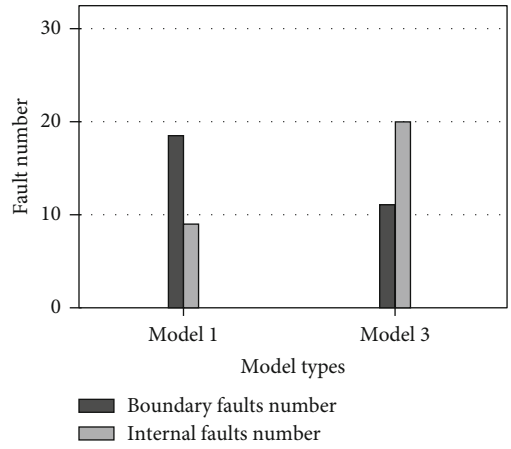

Figure 9: Number of faults in the reference model and model 3, where the number of faults is the sum of sections 1–4.

control of a trunk boundary fault and the simple graben are arranged separately, differs between models 1 and 2. That is, model 2 has more secondary faults for the same amount of extension (80 mm) (Figures 3(d) and 4(c)).

4.3. Effect of Syndeposition (Model 3). The evolution of deformation shown by model 3 is similar to that of the reference model; both exhibit complex rifting with internal secondary faults under the control of the master fault (Figure 7). Model 3 has a rift (30 cm) that is 2 cm wider after extension of 8 cm than the rift of the reference model (28 cm) (Figure 8). The deformation pattern observed in the cross section of model 3 is also similar to the reference model (Figure 7), but the number of internal faults (quantified by the total number of faults in the four sections) is 12 for the trunk boundary fault and 20 for the secondary fault. The reference model therefore has more master faults (18) and fewer secondary faults (9) (Figure 9), as well as fewer total faults. The experimental results show that syndeposition is equivalent to the thickness of the overlying brittle layer gradually increasing to the thickness of the reference model brittle layer and the strength of the overlying brittle

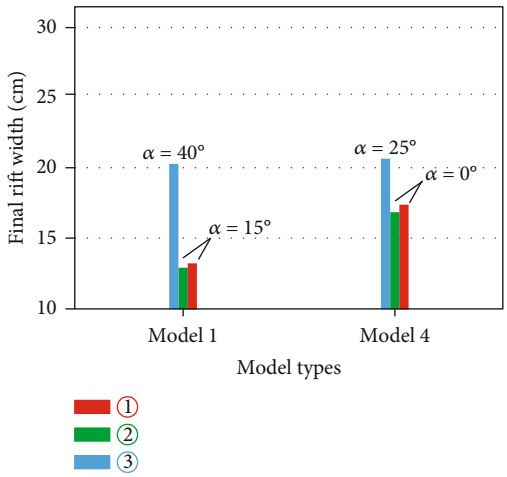

Figure 10: Relationship between different inclination angles and rifting width.

layer increasing to that of the reference model brittle layer. In this case, the width of the rift is greater, the number of trunk boundary faults is reduced, and the number of secondary faults is increased.

4.4. Effect of Extension Direction (Model 4). Model 4 exhibits a wider rift (35 cm) at 8 cm of extension, which is 7 cm wider than that of the reference model (28 cm). The rifting width of the three different cross sections is negatively correlated with the angle of extension obliquity (Figure 10). The dominant strike of the secondary fault of cross sections 1 and 2 of the model 4 is N62 E, which differs by 8 from the dominant strike (N70 E) of the reference model. The dominant strike of the secondary fault of cross-section 3 is N58 E, 15 of the dominant strike (N43 E) of the reference model (Figure 11). The experimental results show that extension obliquity at different angles controls the width of rifting and the strike of the internal secondary fault. The larger the inclination angle of oblique rifting, the wider the rift. The fault strike near the ductile rifting boundary is controlled by this oblique angle, which is approximately parallel to the strike of the master fault. The strike of the secondary fault inside the rift is predominantly controlled by the extension direction, which is almost perpendicular to the extension direction.

5. Discussion

5.1. Major Controlling Factors of Tectonic Deformation. The rate of extension of the lithosphere affects the tectonic evolution of rift basins ([45–47] for reviews). Our physical simulation results show that different extension rates control the amount of extension required for secondary fault appearance, in that a high extension rate corresponds to more rapid movement of the internal deformation in the rift basin. This is similar to the results of a physical simulation experiment conducted by Corti et al. [45]. We use retractable rubber instead of different viscosity silica gels in the base ductile

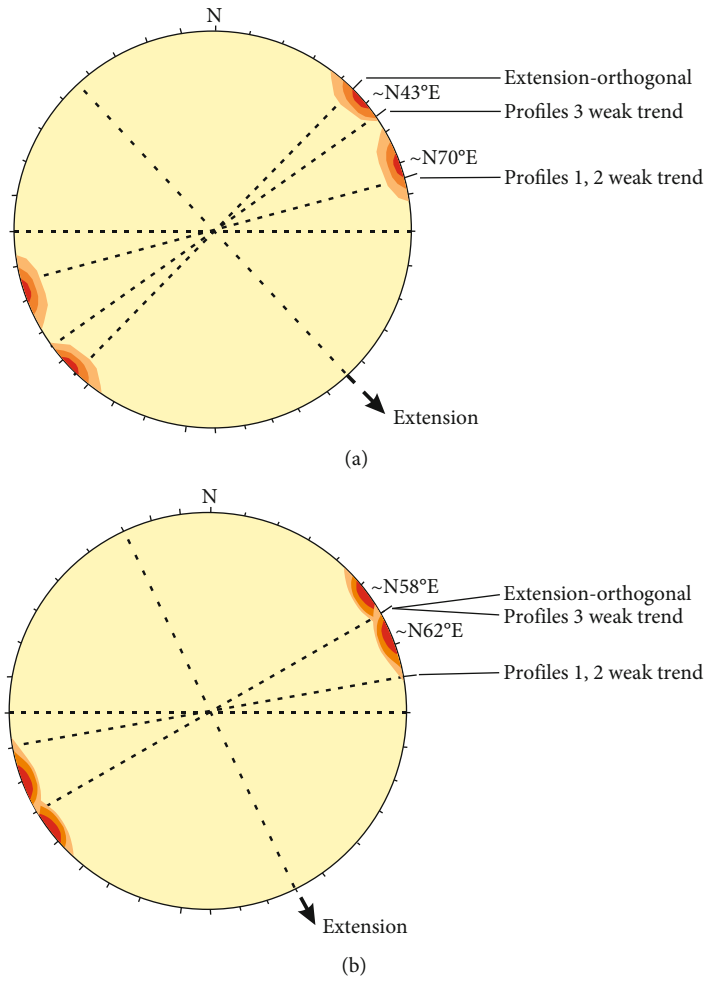

Figure 11: Rift zone fault dominant strike orientation map for the reference model and model 4.

layer [44, 45]. This may explain why our experiments exhibited more rapid deformation evolution. Due to the heterogeneity of extension rate and amount in different areas of the Erlian Basin [48], our physical simulation results show that, even if the extension rate and magnitude are small, it will lead to differences in rifting width and development of secondary faults (Figures 3 and 4).

The syndeposition is equivalent to increasing the thickness of the upper layer, thereby increasing the strength of the overlying brittle layer. An increase in the thickness of the overlying brittle layer (and thus strength of the brittle layer) inhibits the formation of axial faults [45]. This is the same as our research.

The direction of extension (equivalent to changing the angle of the oblique rift) is the main factor controlling the pattern of the rift structure [19, 21, 23, 27, 49]. Experimental results show that positive rifting forms a narrow positive rift zone dominated by normal faults with steep dip angles. Oblique rifting forms a broad oblique rifting zone dominated by "domino-type" faults. The larger the angle of rifting, the more developed the "domino-type" fault (Figures 4 and 12), which is similar to the experimental results of previous physical models [23, 50]. The larger the oblique angle of rifting (angle between the direction of extension and the normal direction of the rift strike), the more rapid the evolution of internal secondary faults [43].

5.2. Comparison with Nature. The Mesozoic rifting basin of Erlian in northeast China has the typical features of a continental rifting basin. Since the early Cretaceous, it has experienced a long period of intracontinental extensional rifting, recording the long-term extension process from early rifting to late depression. The Mesozoic rift zone is controlled by the early preexisting structural style of the basement lithosphere comprising; (1) the weak deformation zone of the basement formed by Paleozoic magmatic rock or the anticlinorium uplift zone, whose core is the Lower Paleozoic and (2) the strong deformation zone of the basement formed by the fold thrust belt or the synclinorium, whose core is the Carboniferous-Permian, and Erlian-Hegenshan melange belt and the Solon Obo-Xar Moron suture zone. In particular, the weak and strong basement boundary forms a number of trunk boundary faults that control the rift basin group. Continued extension and thinning of the lithosphere

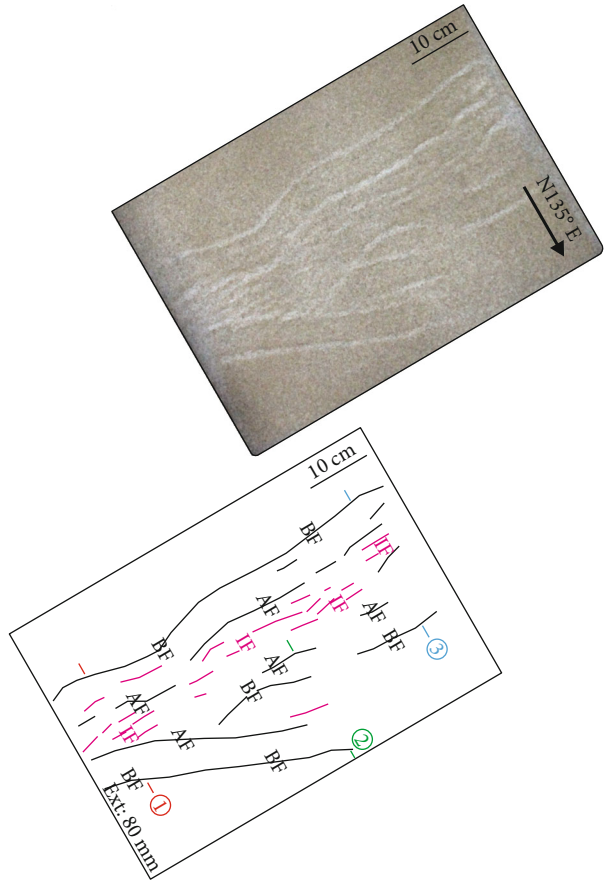

Figure 12: Evolution and characteristics of deformation in model 4, with a different extension direction. (a) Top-view photo (upper panel) and schematic line-drawing of structures (lower panel), illustrating boundary faults (BF), antithetic faults (AF), and internal faults (IF).

lead to central rifting, accompanied by the formation of a central secondary fault and cessation of the trunk boundary fault. The internal secondary fault of the rift formed in the early Cretaceous, and the central internal secondary fault formed later. Seismic data show that the rift obliquity of the secondary rift in the Erlian Basin is characterized by small inclinational angles (the angle between the extension direction and the axis of the rifting) in the north and central regions and large inclinational angles in the west and south. This indicates that trunk boundary fault activity and evolution of the internal secondary fault along the axial direction are strictly controlled by the thickness of the brittle and ductile layer (the increase in the thickness of the brittle layer is equivalent to the syndeposition) and the obliquity of rifting. Specifically, the narrow weak zone and the small angle of obliquity in the central part of the Erlian Basin make the boundary fault more active, and the central secondary fault is formed later.

Compared with the actual structural features of the Erlian Basin, except for the poor similarity of model 3, all models show good similarity in the deformation patterns (Figure 13). These models reproduce the overall structural pattern of the "5 depressions, 3 uplifts" in the basin: (1) Chuanjing Sag of NEE and EW faults, (2) Wulanchabu Sag and Sunite Sag of NNE and NE faults with longer extension, (3) Sunite Sag of NNE and near NS faults with large intervals between faults, and (4) Tenggeer Sag of NE and NNE faults; relatively underdeveloped faults in this area may be due to the depression being close to the direction of extension and the rubber being less stretched.

Although the extension direction of model 3 is only 15° different from that of other models, it exhibits very low similarity in its structural pattern. The strike of internally developed faults is NEE and EW (Figure 11), which is similar to the dominant orientation of fault strike developed in Chuanjing Sag and Tenggeer Sag. Other factors such as fault combination and extension length display low similarity. In addition, when the extension is small, the deformation pattern of model 3 is not as good as that of the actual structure of Erlian Basin (Figure 13), which indicates that the magnitude of extension is not the cause of the lack of similarity.

Figure 11 reflects that the dominant orientation of the secondary fault strike of the standard model is similar to that of the actual master fault of Erlian Basin. However, the dominant orientation of the master fault of model 3 is less similar to the actual situation, which also indicates that inconsistency of the fault strike inside the rift basin and the complex kinematic mechanism is not necessarily inevitable. The fault strike inside the basin far from the boundary is mainly controlled by the direction of structural extension [51]. By

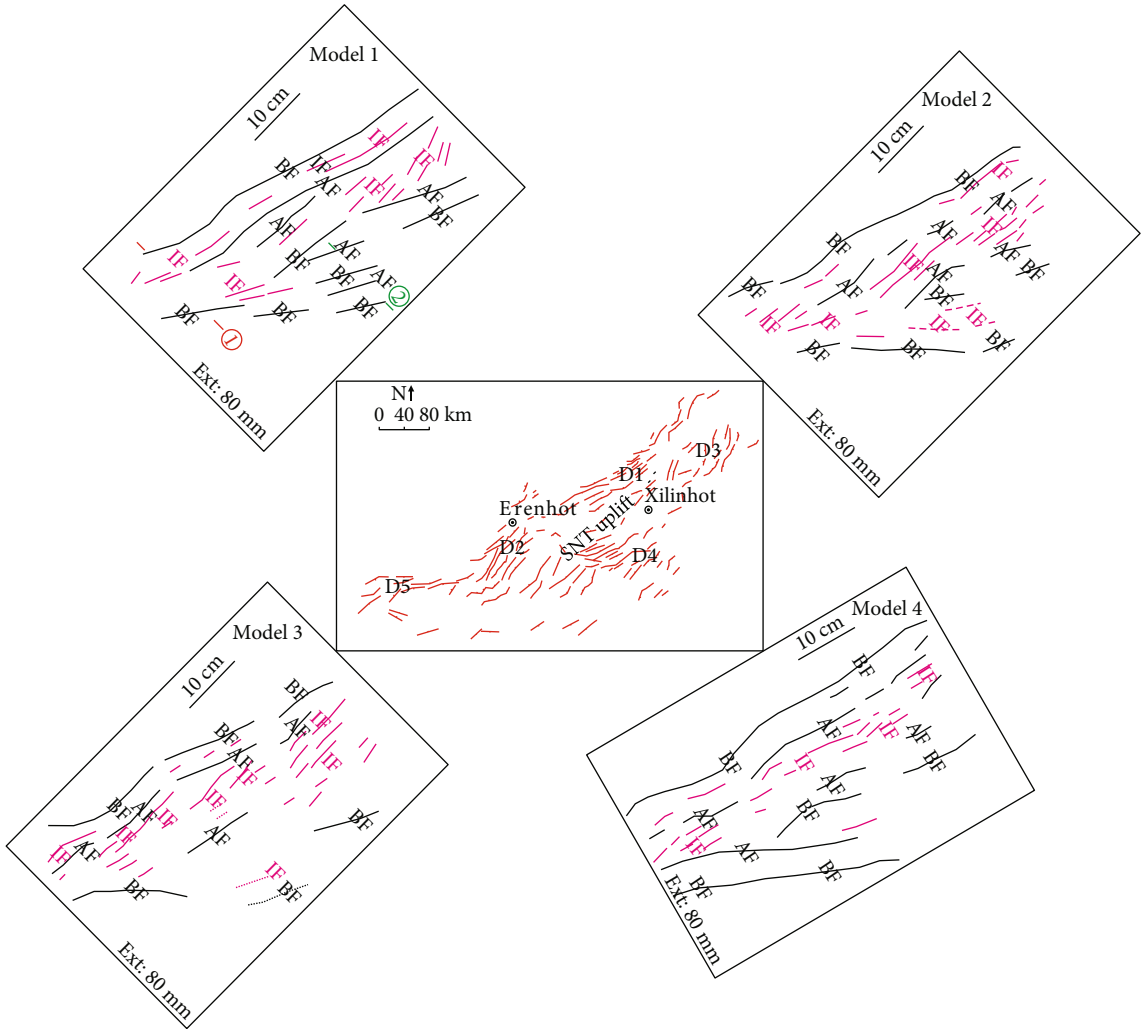

Figure 13: Comparison between experimental models and the actual geologic structure of Erlian Basin.

comparing the physical simulation experiments of different extension directions, we propose that Erlian Basin was formed by extension in the direction N315°E–N135°E. Strike-slip deformation of the boundary faults in the western and eastern of the basin is therefore the result of uniform N315°–135E° extension and different angles of the basement ductile zone ($\alpha = 0°$, 10°), which plays a role in lateral conversion. We suggest that the "N315°E–N135°E direction extension mode" provides a good kinematic explanation for the formation of the Erlian Basin and similar rift basins in northeastern China.

6. Conclusions

We applied the physical simulation method to study the effects of extension rate, extension direction, and syndeposition on the Mesozoic tectonic deformation of the Erlian Basin and obtained the following conclusions:

(1) The results of extension models with different extension rates and syndeposition are similar to the actual geological structure of the basin, but there are differences in the deformation evolution process and deformation patterns. An increase of the extension rate promotes earlier appearance of secondary faults inside the rift and increases the width of the rift

(2) Syndeposition is equivalent to increasing the strength of the overlying brittle layer, which promotes the development of internal secondary faults, favors a wider rift, and conversely suppresses the development of master faults

(3) The similarity between the experimental results of the N330°E–N150°E extension model and the actual geologic structure is poor. However, the experimental results show that the magnitude of extension is not the cause of the lack of similarity. When the angle of rifting is small, a narrow positive rifting zone is formed. When the angle is large, a gentle oblique rifting zone is formed. Extension direction controls faults inside the rift zone far from the extension boundary. Good similarities between the

different extension models and the actual geologic structure indicate that the Erlian Basin was formed by extension in the southeast direction. The physical simulation experimental model designed in this study can provide some reference for the research on the tectonic evolution of similar basins

Data Availability

The data used to support the findings of this study are included within the article.

Conflicts of Interest

The authors declare that they have no conflicts of interest.

Acknowledgments

This work was supported by the China National 973 Project (2015CB453000) and China Geological Survey Project (12120115009801).

References

[1] S. T. Li, S. G. Yang, C. L. Wu et al., "Late Mesozoic rift in Northeast China and Northeast Asian Fault Basin," *Science in China Series B Chemistry*, vol. 2, pp. 185–195, 1987.

[2] S. T. Li, *Evolution of the Mesozoic and Cenozoic Basins in the Eastern and Adjacent Areas of China and the Geodynamic Background*, China University of Geosciences, Wuhan, 1997.

[3] Q. R. Meng, J. M. Hu, X. J. Yuan, and J. Q. Jin, "Structure evolution and origin of Late Mesozoic extensional basins in the China-Mongolia border region," *Geological Bulletin of China*, vol. 21, pp. 224–231, 2002.

[4] Q. R. Meng, "What drove late Mesozoic extension of the northern China-Mongolia tract," *Tectonophysics*, vol. 369, no. 3-4, pp. 155–174, 2003.

[5] J. Y. Ren, S. T. Li, and G. H. Jiao, "Extensional tectonic system of Erlian fault basin group and its deep background," *Earth Science*, vol. 23, pp. 567–572, 1998.

[6] J. A. Shao, *Northeast China Terrain and Northeast Asian Continent Evolution*, Seismological Press, 1995.

[7] T. T. Yan, Y. B. Yao, and D. M. Liu, "Critical tectonic events and their geological controls on gas generation, migration, and accumulation in the Weibei coalbed methane field, southeast Ordos basin," *Journal of Natural Gas Science and Engineering*, vol. 27, pp. 1367–1380, 2015.

[8] T. T. Yan, S. He, Y. Bai et al., "A study on the heterogeneity characteristics of geological controls on coalbed methane accumulation in Gujiao coalbed methane field, Xishan Coalfield, China," *Geofluids*, vol. 3, 20 pages, 2021.

[9] A. C. Xiao, S. F. Yang, and H. L. Chen, "Geodynamic background on formation of Erlian basin," *Oil and Gas Geology*, vol. 22, pp. 137–140, 2001.

[10] Y. Q. Zhang, Y. Zhao, S. W. Dong, and N. Yang, "Tectonic evolution stages of the Early Cretaceous rift basins in Eastern China and adjacent areas and their geodynamic background," *Geoscience Frontiers*, vol. 11, pp. 123–133, 2004.

[11] C. L. Zhao, "Formation mechanism of reservoir space and oil possibility of volcanic reservoirs," *Geological Review*, vol. 42, pp. 37–43, 1996.

[12] Z. Y. Tian, P. Han, and K. D. Xu, "The Mesozoic-Cenozoic East China rift system," *Tectonophysics*, vol. 208, no. 1-3, pp. 341–363, 1992.

[13] Z. Y. Tian and B. Q. Shi, "Geological features and petroleum reservoir formation in Meso-Cenozoic sedimentary basins in China," *Geotectonica et Metallogenia*, vol. 26, pp. 1–5, 2002.

[14] Y. Q. Cui, X. H. Liu, Z. H. Sun, H. Yao, and C. Y. Han, "The deep physical geographic characteristics and Neopaleozoic geological structural exploration of Erlian basin, Inner Mongolia," *Geological Bulletin of China*, vol. 30, pp. 235–242, 2011.

[15] X. P. Li, S. H. Zhang, L. B. Li et al., "Coupling of faulted sags to basement in the Early Cretaceous Erlian Basin," *Chinese Journal of Geology*, vol. 50, pp. 88–99, 2015.

[16] J. F. Qi, X. Z. Zhao, X. P. Li et al., "The distribution of Early Cretaceous faulted-sags and their relationship with basement structure within Erlian Basin," *Geoscience Frontiers*, vol. 22, pp. 118–128, 2015.

[17] Z. Cai, Q. Huang, B. Xia, and J. Xiang, "Differences in shale gas exploration prospects of the upper Yangtze Platform and the lower Yangtze Platform: insights from computer modelling of tectonic development," *Journal of Natural Gas Science and Engineering*, vol. 36, pp. 42–53, 2016.

[18] L. Wang, S. Wang, R. Zhang et al., "Review of multi-scale and multi-physical simulation technologies for shale and tight gas reservoirs," *Journal of Natural Gas Science and Engineering*, vol. 37, pp. 560–578, 2017.

[19] M. Bonini, T. Souriot, M. Boccaletti, and J. P. Brun, "Successive orthogonal and oblique extension episodes in a rift zone: laboratory experiments with application to the Ethiopian rift," *Tectonics*, vol. 16, no. 2, pp. 347–362, 1997.

[20] Y. Mart and O. Dauteuil, "Analogue experiments of propagation of oblique rifts," *Tectonophysics*, vol. 316, no. 1-2, pp. 121–132, 2000.

[21] K. R. McClay and M. J. White, "Analogue modelling of orthogonal and oblique rifting," *Marine and Petroleum Geology*, vol. 12, no. 2, pp. 137–151, 1995.

[22] J. X. Zhou and J. S. Zhou, "Cenozoic tectonic deformation mechanism in the Bohai Bay Basin: physical simulation and discussion," *Science China Earth Sciences*, vol. 36, pp. 507–519, 2006.

[23] F. Zwaan, G. Schreurs, J. Naliboff, and S. J. H. Buiter, "Insights into the effects of oblique extension on continental rift interaction from 3D analogue and numerical models," *Tectonophysics*, vol. 693, pp. 239–260, 2016.

[24] A. Chemenda, J. Déverchère, and E. Calais, "Three-dimensional laboratory modelling of rifting: application to the Baikal Rift," *Russia. Tectonophysics*, vol. 356, no. 4, pp. 253–273, 2002.

[25] K. McClay and T. Dooley, "Analogue models of pull-apart basins," *Geology*, vol. 23, no. 8, pp. 711–714, 1995.

[26] D. Paul and S. Mitra, "Experimental models of transfer zones in rift systems," *AAPG Bulletin*, vol. 97, no. 5, pp. 759–780, 2013.

[27] J. Autin, N. Bellahsen, S. Leroy, L. Husson, M. O. Beslier, and E. Acremont, "The role of structural inheritance in oblique rifting: insights from analogue models and application to the Gulf of Aden," *Tectonophysics*, vol. 607, pp. 51–64, 2013.

[28] T. Dooley and K. McClay, "Analog modeling of pull-apart basins," *AAPG Bulletin*, vol. 81, pp. 1804–1826, 1997.

[29] H. M. Tong, L. J. Meng, D. S. Cai, Y. P. Wu, X. S. Li, and M. Q. Liu, "Fault formation and evolution in rift basins-sandbox

modeling and cognition," *ACTA Geol Sin*, vol. 6, pp. 759–774, 2009.

[30] X. Z. Zhao, F. M. Jin, J. F. Qi et al., "The structural types and petroleum geological significance of Early Cretaceous complex faulted sag in Erlian Basin," *Natural Gas Geoscience*, vol. 26, pp. 1289–1298, 2015.

[31] J. B. Zhou, X. Z. Zhang, Z. H. Ma et al., "Tectonic framework and basin evolution in Northeast China," *Oil and Gas Geology*, vol. 30, pp. 530–538, 2009.

[32] X. Z. Zhang, B. J. Yang, F. Y. Wu, and G. X. Liu, "The lithosphere structure in the Hingmong-Jihei (Hinggan-Mongolia-Jilin-Heilongjiang) region, northeastern China," *Geologyin-China*, vol. 33, pp. 816–823, 2006.

[33] G. Corti, G. Ranalli, and D. Sokoutis, "Quantitative modelling of geological processes preface," *Tectonophysics*, vol. 484, no. 1-4, pp. 1–3, 2010.

[34] K. McClay and M. Bonora, "Analog models of restraining stepovers in strike-slip fault systems," *AAPG Bulletin*, vol. 85, no. 2, pp. 233–260, 2001.

[35] H. M. Tong, D. S. Cai, Y. P. Wu, X. G. Li, X. S. Li, and L. J. Meng, "Determination of pre-existing tectonic activity in non-uniform deformation," *Science China Earth Sciences*, vol. 41, pp. 158–168, 2011.

[36] J. X. Zhou, F. Y. Xu, C. G. Weia, G. Li, F. S. Yua, and H. M. Tong, "Shortening of analogue models with contractive substrata: insights into the origin of purely landward-vergent thrusting wedge along the Cascadia subduction zone and the deformation evolution of Himalayan-Tibetan orogen," *Earth and Planetary Science Letters*, vol. 260, no. 1-2, pp. 313–327, 2007.

[37] J. X. Zhou, B. Zhang, and Q. Xu, "Effects of lateral friction on the structural evolution of fold-andthrust belts: insights from sandbox experiments with implications for the origin of landward-vergent thrust wedges in Cascadia," *Geological Society of America Bulletin*, vol. 128, no. 3-4, pp. 669–683, 2016.

[38] F. Nilfouroushan, R. Pysklywec, and A. Cruden, "Sensitivity analysis of numerical scaled models of fold-and-thrust belts to granular material cohesion variation and comparison with analog experiments," *Tectonophysics*, vol. 526-529, pp. 196–206, 2012.

[39] H. Ramberg, *Gravity, Deformation and the Earth's Crust*, Academic Press, London, 1981.

[40] M. Bonini, F. Sani, and B. Antonielli, "Basin inversion and contractional reactivation of inherited normal faults: a review based on previous and new experimental models," *Tectonophysics*, vol. 522, pp. 55–88, 2012.

[41] G. Mulugeta, "Squeeze box in the centrifuge," *Tectonophysics*, vol. 148, no. 3-4, pp. 323–335, 1988.

[42] G. Corti, "Centrifuge modelling of the influence of crustal fabrics on the development of transfer zones: insights into the mechanics of continental rifting architecture," *Tectonophysics*, vol. 384, no. 1-4, pp. 191–208, 2004.

[43] A. Agostini, G. Corti, A. Zeoli, and G. Mulugeta, "Evolution, pattern and partitioning of deformation during oblique continental rifting: inferences from lithospheric-scale centrifuge models," *Geochemistry, Geophysics, Geosystems*, vol. 10, no. 11, pp. 1–23, 2009.

[44] G. Corti, "Control of rift obliquity on the evolution and segmentation of the main Ethiopian rift," *Nature Geoscience*, vol. 1, no. 4, pp. 258–262, 2008.

[45] G. Corti, G. Ranalli, A. Agostini, and D. Sokoutis, "Inward migration of faulting during continental rifting: effects of pre-existing lithospheric structure and extension rate," *Tectonophysics*, vol. 594, pp. 137–148, 2013.

[46] J. P. Brun, "Narrow rifts versus wide rifts: inferences for the mechanics of rifting from laboratory experiments," *Philosophical Transactions of the Royal Society of London. Series A: Mathematical, Physical and Engineering Sciences*, vol. 357, no. 1753, pp. 695–712, 1999.

[47] L. Michon and O. Merle, "Mode of lithospheric extension: conceptual models from analogue modeling," *Tectonics*, vol. 22, no. 4, 2003.

[48] J. Y. Ren, K. Tamaki, S. T. Li, and Z. Junxia, "Late Mesozoic and Cenozoic rifting and its dynamic setting in Eastern China and adjacent areas," *Tectonophysics*, vol. 344, no. 3-4, pp. 175–205, 2002.

[49] L. Michon and D. Sokoutis, "Interaction between structural inheritance and extension direction during graben and depocentre formation: an experimental approach," *Tectonophysics*, vol. 409, no. 1-4, pp. 125–146, 2005.

[50] M. Philippon, E. Willingshofer, D. Sokoutis, M. Bonini, and S. Cloetingh, "Slip re-orientation in oblique rifts," *Geology*, vol. 43, no. 2, pp. 147–150, 2015.

[51] J. X. Zhou and J. F. Qi, "Sandbox experimental modeling of oblique extensional rifting with kink boundary," *Journal of Earth ScienceChina*, vol. 24, pp. 630–634, 1999.

Hindawi
Geofluids
Volume 2022, Article ID 4549153, 12 pages
https://doi.org/10.1155/2022/4549153

Research Article

Multiscale Fracturing in Medium- to Low-Rank Coals and Its Implications on Coalbed Methane Production in the Baode Area, Eastern Ordos Basin, China

Wei Zhang, Baoshan Zhao, Qingfeng Zhang, Jikun Zhang, Ziling Li, Xiaoguang Sun, and Mingming Yan

PetroChina Coalbed Methane Company Limited, Beijing, China 100028

Correspondence should be addressed to Ziling Li; lzl_cbm@petrochina.com.cn

Received 1 March 2022; Revised 24 March 2022; Accepted 29 March 2022; Published 20 April 2022

Academic Editor: Yong Li

Coal fractures are crucial in affecting the production of methane from coal. Multiscale fracturing and its implications on coalbed methane production have still not been fully understood. Herein, we present a case study, combining underground coal mine surveying and specimen, thin section, and scanning electron microscope observations for illustrating the ~m-, ~cm-, ~mm-, and ~μm-scale fractures present in the Baode area, eastern Ordos Basin, China. Then, the fracture connectivity is evaluated by helium permeability and mercury porosimetry measurement. The coals are mainly of semibright, semidull, and dull macrolithotypes. And main maceral composition is vitrinite, accounting for 73%~95%, with around 26% inertinite. The coals are ultralow-ash and low-ash content, belonging to high-volatile bituminous coal. The ~m scale fractures can penetrate the whole coal seams, dominant by S-N and following E-W direction, which were generated during the Yanshanian and Himalayan movements. The ~cm fractures are generally parallel to the lamina, influenced by the bright and dull coal band extension caused by the depositional differences. The ~mm fractures are mainly shown as endogenous fractures perpendicular to the lamina restricted within bright macrolithotypes. There are also ~mm fractures that are perpendicular to the lamina while penetrating dull components and fractures parallel to the lamina. The ~μm fractures are widely distributed and connect each other. Some of the fractures are filled with carbonate and clay minerals and are beneficial for methane migration, caused by hydraulic fracturing. The average mercury withdrawal efficiency of the coals was 75%. The helium permeability of the coals was between 10×10^{-3} and 50×10^{-3} μm^2, indicating good fracture connectivity. The study findings, which indicated the presence of fractures of different scales in the coals studied, can be used for fully understanding the coalbed methane performance of medium- and low-rank coals.

1. Introduction

The total coalbed methane (CBM) resources in China that are within 2000 m from the ground are estimated to be 36.81 trillion cubic meters of which medium- and low-rank coals accounted for 7.8 and 14.7 trillion cubic meters, respectively [1, 2]. The CBM production in China is currently dominated by medium (maximum vitrinite reflectance, $R_{o,max}$, = 0.7% – 2.0%)-to-high ($R_{o,max}$ > 2.0%) rank coals; most of the production wells are located in the southern Qinshui Basin and eastern Ordos Basin [3, 4]. Low-rank CBM has not yet been widely developed in China despite its huge production potential. The coals used from the Powder River Basin in the United States and Surat Basin in Australia for commercial production of CBM are typically low-rank coals [5–7]. The Baode area is the most successful middle-to-low rank–CBM production area in China. The coal reservoir characteristics have not been widely explored thus far.

Coal permeability is critical in influencing CBM migration and production, which are both affected by coal matrix pores and fractures [8–10]. Even though hydraulic fracturing is typically used during CBM production, the initial permeability of coal is still a dominant controlling factor of CBM well performance [11, 12]. The permeability of coal

is mainly influenced by its fractures, including intrageneric cleats and exogenous joints. The fracture size and connectivity are the main factors affecting the permeability of coal reservoirs [13, 14]. Extensive studies using methods, such as gas adsorption and desorption experiments with N_2, CO_2, or Ar, as the medium; three-dimensional imaging, such as micro- and nano-X-ray computed-tomography, focused ion beam scanning electron microscopy, and helium ion microscopy; and fluid intrusion techniques, such as mercury intrusion porosimetry and nuclear magnetic resonance, have been conducted for exploring micropore occurrence in coal [15–20]. However, as for the traditional and direct observation of the fracture developed in the coals, it is still lacking clear recognition [21]. The calculation of the number of fractures is difficult because of the complexity and heterogeneity of the fractures. Mechanical parameters are used to estimate coal fracture, fracture occurrence, and fracture numbers [22–24]. Coal fractures have to be studied using coal core and coal mining surface observations and geophysical methods.

The Baode area, one of the most successful CBM production areas in China, was selected as the study area. A series of comprehensive studies were conducted for investigating fracture occurrence in coal, followed by a discussion on its influence on CBM production. The key purpose of the study was to identify the fracture extension in low-to-middle rank coals, which could help understand methane migration and production. The results would help understand low rank–CBM production in other basins where coals with similar properties are present.

2. Geological Setting

The Baode area in Shanxi is on the eastern margin of the Ordos Basin, and its tectonic location is along the northern segment of the Jinxi fold [25]. The area, which has a stable structure, is located in the transitional area between the basin margin and the inner basin (Figure 1). Large faults and folds are less developed, with most small fault strikes along the near north-south direction. The coal exhibits a monoclinic structure along the near north-south direction with a westward inclination. The dip angle of the coal seam is small. The coal measure mainly comprises fine gravel sandstone, siltstone, and carbonaceous mudstone. It has small amounts of medium-grained and coarse-grained sandstones. The coal-bearing strata comprise the Upper Carboniferous-to-Permian Benxi, Taiyuan, and Shanxi Formations. Ordovician limestone is below the coal measure, whereas Triassic fluvial deposits are above it.

3. Materials and Methods

3.1. Coal Seams and Specimen Observation. Exogenous fractures in the coal seams of the Baode Coal Mine were observed via underground observations. The anatomical points were mainly concentrated on the coal wall of the excavation roadway. The 240 m wide 308 working face of the Baode Coal Mine was continuously tracked and observed while focusing on the development of small structures and microstructures, such as exogenous joints and small faults. The roadway excavation was straight, and small folds were not apparent. The occurrence of exogenous fractures was observed, and their density was estimated. The location and partial filling characteristics of the exogenous fractures associated with the coal seam were marked.

All of the samples were collected from the No. 8 coal seam of the study area. The hand specimen samples could be described using features, such as sample color, structure, composition, macroscopic coal type, luster, fracture, hardness, firmness coefficient, endogenous fracture development characteristics, exogenous fracture development characteristics, and filling characteristics. Coal macrolithotypes can be classified as dull, semidull, semibright, and bright coal. Furthermore, the ~μm scale fracture was detected by a scanning electronic microscope (SEM) [4].

3.2. Proximate, Maceral Composition, and Vitrinite Reflectance Analyses. Proximate analysis, including moisture, ash yield, volatile matter, and fixed carbon content analysis, was performed on 12 samples based on GB/T 212-2001 [26]. Maceral composition analysis was conducted according to ISO 7404–3 : 2009, and the total maceral composition was measured by counting all the macerals present using volume percentages [27, 28]. The R_o values were analyzed using a Leitz MPV3-SP microscope in accordance with the international standard ISO17246: 2010 and China Petroleum Industry Standard SY/T 5124-2012. At least 50 readings from each sample were recorded [29].

3.3. Helium Permeability. Coal permeability was tested using coal columns of 25 mm diameter. It was determined using Darcy's formula, which says that the flow rate of a fluid passing through a rock sample will be directly proportional to the cross-sectional area A of the core and pressure difference ΔP between core inlet and outlet and inversely proportional to the length L of the rock sample, and viscosity μ of the fluid as given in

$$K_g = \frac{2Qp_o\mu L}{A\left(p_{\text{in}}^2 - p_{\text{out}}^2\right)} \times 1000, \tag{1}$$

where K_g is the gas permeability, 10^{-3} μm^2; A is the cross-sectional area of the core, cm^2; L is the length of the tested core, cm; μ is fluid viscosity, mPa·s; Q is the flow rate at the core outlet under atmospheric pressure, cm^3/s; P_0 is the atmospheric pressure, 0.1 MPa; P_{in} is the pressure at the core inlet, MPa; and P_{out} is the pressure at the core outlet, MPa. The helium viscosity was found to be 0.017 mPa·s when tested.

3.4. Mercury Intrusion Porosimetry. Mercury intrusion porosimetry analysis was performed only on six selected samples because other samples had either quality- or quantity-related issues. The experiment was conducted using a Micromeritics 9310 porosimeter. It was based on the Chinese Oil and Gas Industry Standard SY/T 5346-1994. Before performing the analysis, all samples were dried at 75°C for 48 h. The average pore radius, mercury saturation, and mercury

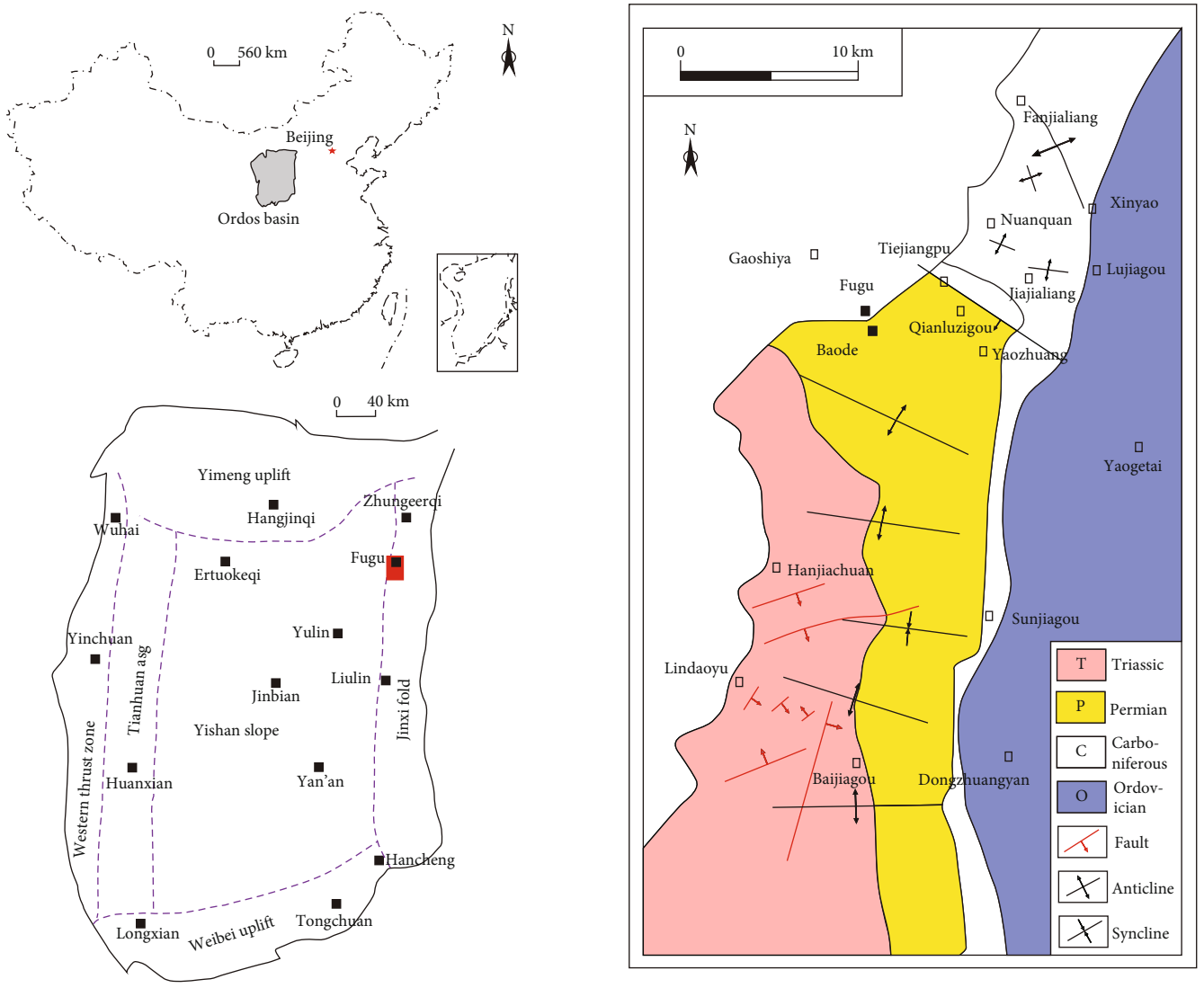

Figure 1: Geological setting of the study area.

withdrawal efficiency of the coal in the samples were all recorded [8, 30].

4. Results

4.1. Maceral Composition. Coal has a high vitrinite content of approximately 73%–95% (Table 1). Its inertinite content is low (<26%). The gelovitrinite content in vitrinite is high, mainly comprising homogeneous vitrinite and collodetrinite. Furthermore, a few samples contained telovitrinite. Vitrodetrinite was present in the samples, and small amounts of collodetrinite and telinite were observed (Figure 2(a)). The inertinite group was dominated by semifusinite and inertodetrinite. Well-preserved fusinite was rarely detected. The interlayers of collodetrinite and homogeneous vitrinite strips and corpogelinite could be observed, as shown in Figure 2(b). Collotelinite is commonly developed with internal pores, and pore deformation occurred during the coalification process (Figures 2(c) and 2(d)).

Table 1: Maceral composition of coal in the Baode area in the eastern Ordos Basin of China.

Sample No.	*T* (%)	*G* (%)	VD (%)	*V* (%)	Sf (%)	ID (%)	*I* (%)	*E* (%)
BD1	0.13	0.4	0.11	0.64	0.15	0.16	0.31	0.05
BD2	0.52	0.42	0.01	0.95	0.02	0.03	0.05	0.01
BD4	0.17	0.57	0.03	0.77	0.19	0.04	0.23	0
BD7	0.26	0.42	0.05	0.73	0.19	0.07	0.26	0.01
BD8	0.41	0.53	0.01	0.95	0.03	0.01	0.04	0
BD9	0.38	0.33	0.04	0.76	0.14	0.1	0.24	0
BD10	0.34	0.58	0.02	0.94	0.04	0.02	0.06	0.01
BD11	0.29	0.5	0.07	0.86	0.07	0.06	0.13	0
BD12	0.64	0.24	0.03	0.90	0.06	0.03	0.09	0.01
BD14	0.24	0.31	0.16	0.71	0.10	0.16	0.26	0.03

T: telovitrinite; *G*: gelovitrinite; VD: vitrodetrinite; *V*: vitrinite; Sf: semifusinite; ID: inertodetrinite; *I*: inertinite; *E*: exinite.

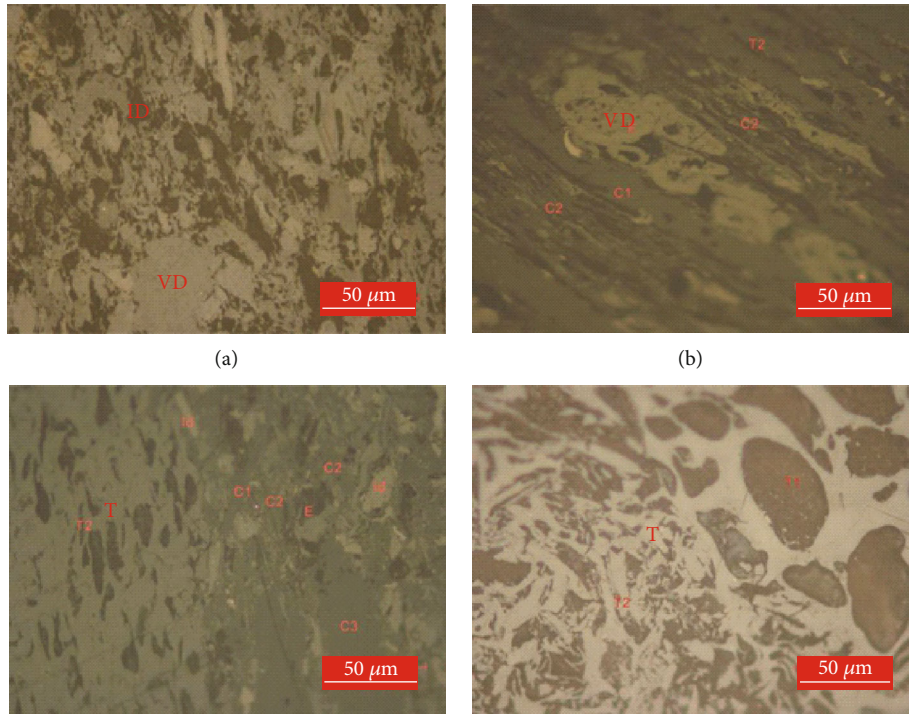

Figure 2: Photomicrographs of macerals present in the samples (T: telovitrinite; VD: vitrodetrinite; ID: inertodetrinite).

Table 2: Proximate analysis results and vitrinite reflectances of the samples.

Sample No.	M_{ad} (%)	A_{ad} (%)	V_{ad} (%)	V_{daf} (%)	FC_{ad} (%)	$R_{o,max}$ (%)
BD1	2.16	12.65	23.89	28.04	61.30	1.21
BD2	3.63	9.13	35.09	40.22	52.15	0.85
BD4	3.45	7.72	32.40	36.47	56.43	0.80
BD6	3.19	5.78	36.61	40.22	54.41	0.57
BD7	2.60	16.59	30.88	38.21	49.93	0.99
BD8	3.47	5.12	37.30	40.80	54.12	0.83
BD9	2.65	14.56	32.85	39.68	49.94	0.77
BD10	3.20	5.39	35.22	38.53	56.19	0.86
BD11	2.77	7.86	36.40	40.73	52.97	0.59
BD12	2.70	10.05	34.79	39.87	52.46	0.81
BD13	3.08	7.08	35.57	39.60	54.27	0.76
BD14	2.06	29.52	20.93	30.59	47.49	1.40
Average value	2.91	10.95	32.66	37.75	53.47	0.78

M_{ad}: moisture, air dry basis, %; A_{ad}: ash yield content, air dry basis, %; V_{ad}: volatile, air dry basis, %; daf: dry ash free basis; FC_{ad}: fixed carbon, air dry basis, %; $R_{o,max}$: maximum vitrinite reflectance, %.

4.2. Proximate Analysis. The results of the proximate analysis of the samples indicated that they had stable moisture content of 2%–4% (Table 2). Thus, the coal could be classified as low-moisture coal. The ash yield of the coal varied depending on the constituent minerals. The highest and lowest ash yields were 29.52% and 5.1%, respectively. Thus, the coals found in the study area could be generally classified as ultralow-ash and low-ash coals. The volatile-matter content of the coal was between 28% and 41%. Most of the samples had volatile-matter content between 36% and 41%, indicating that the samples comprised high-volatile bituminous coal. Two samples comprised a volatile-matter content of 28.04% and 30.59%, respectively, belonging to medium volatile bituminous coal. The $\%R_o$ values of most samples were between 0.7% and 0.9% with an average of 0.78%. Two samples had a $\%R_o$ of 1.21% and 1.40%, which indicated an abnormally high thermal maturity. Most samples contained gas coal and fat coal. A few samples comprised long flame coal.

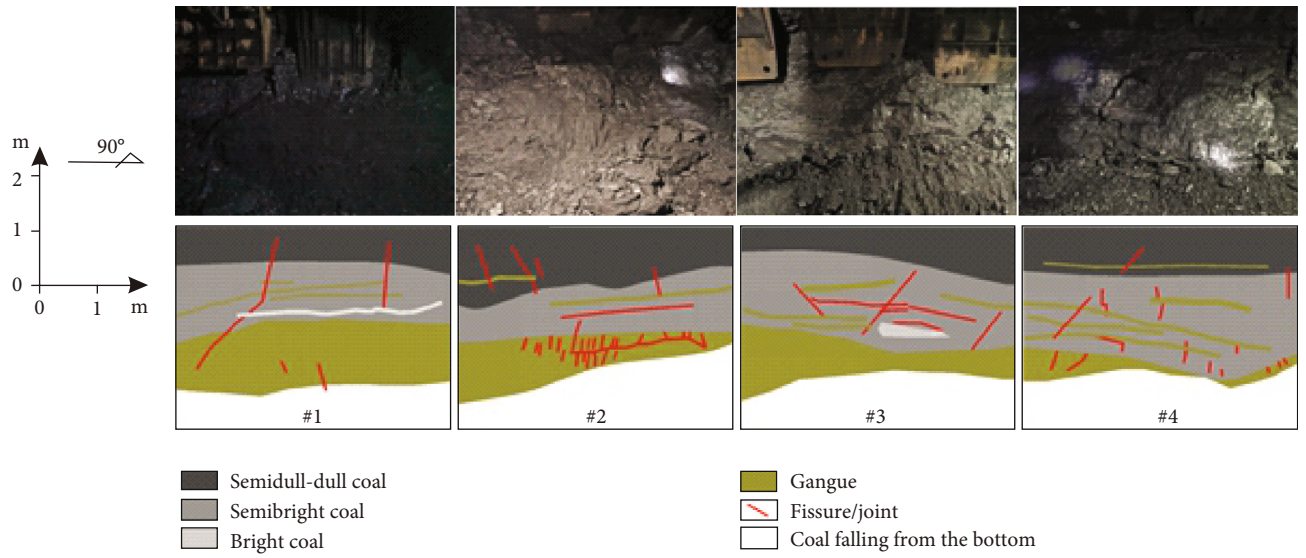

Figure 3: Fractures developed in underground coal seams in different locations. The lower figure is a schematic, where white areas represent coal falling out from the bottom, red lines represent exogenous joints, gray-yellow areas represent mudstone gangue, and other colors represent coal stratification of different macroscopic coal types.

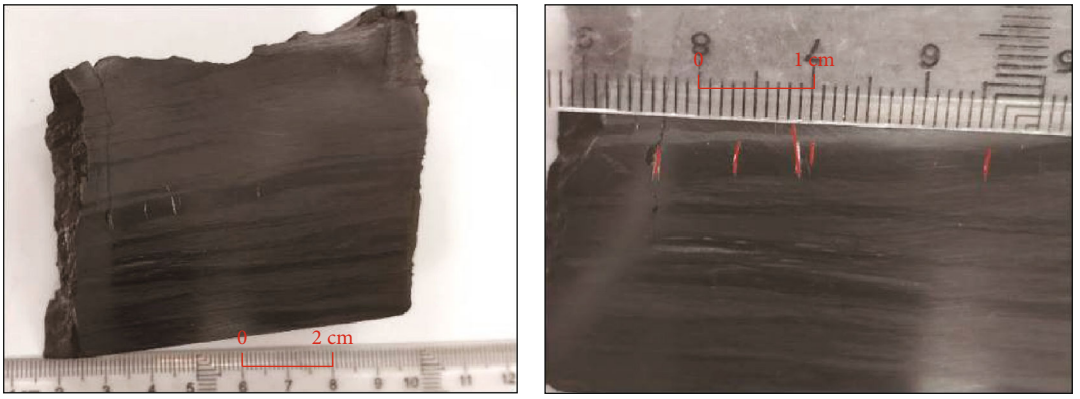

(a) (b)

Figure 4: Fractures (cm-scale) developed in coal cores.

4.3. Occurrence of m-Scale Fractures. The orientation of most of the exogenous fractures in the coal seam of the Baode Coal Mine was along the south-north direction, while the orientation of the other fractures was along the east-west direction. Most of the natural exogenous fractures that had large cross-beds were steeply inclined and tended to dip westward (Figure 3). The linear density of the fractures was 0.7–1.3 strips/10 m, and the distribution of single strips was dominant. Exogenous joints and endogenous fractures were present. Exogenous joints can pass through adjacent macroscopic coal rock-type layers. It is difficult for them to pass through thick gangue layers. The mechanically strong gangue lithology mostly comprises carbonaceous and sandy mudstones. Gangue can develop network joints. Horizontal natural fractures develop in coal reservoirs, mainly in the layers between the coal seam and roof and between the layers within the coal seam.

4.4. Occurrence of cm-Scale Fractures. The samples collected were mainly made of dull coal, semidull coal, and semibright coal, with some bright coal present. The coal in most of the samples had a unified structure or ribbon structure, influenced by peat deposition intervals. The endogenous fractures in the samples were present mainly in bright coal. Yellow-to-white minerals were observed mostly in the endogenous fractures. Four continuous bright coal bands with uneven thicknesses can be observed in Figure 4(a). Their average thicknesses were 4, 3, 1.5, and 0.5 mm. Most of the bright bands had discontinuous fracture distributions. Dull coal bands, with a thickness of approximately 2–6 mm, were present between continuous bright coal bands and discontinuous bright coal bands. Microfractures were well developed in the bright coal bands and were perpendicular to the lamina (Figure 4(b)). They were parallel to each other. At the center of the sample, the fracture density was

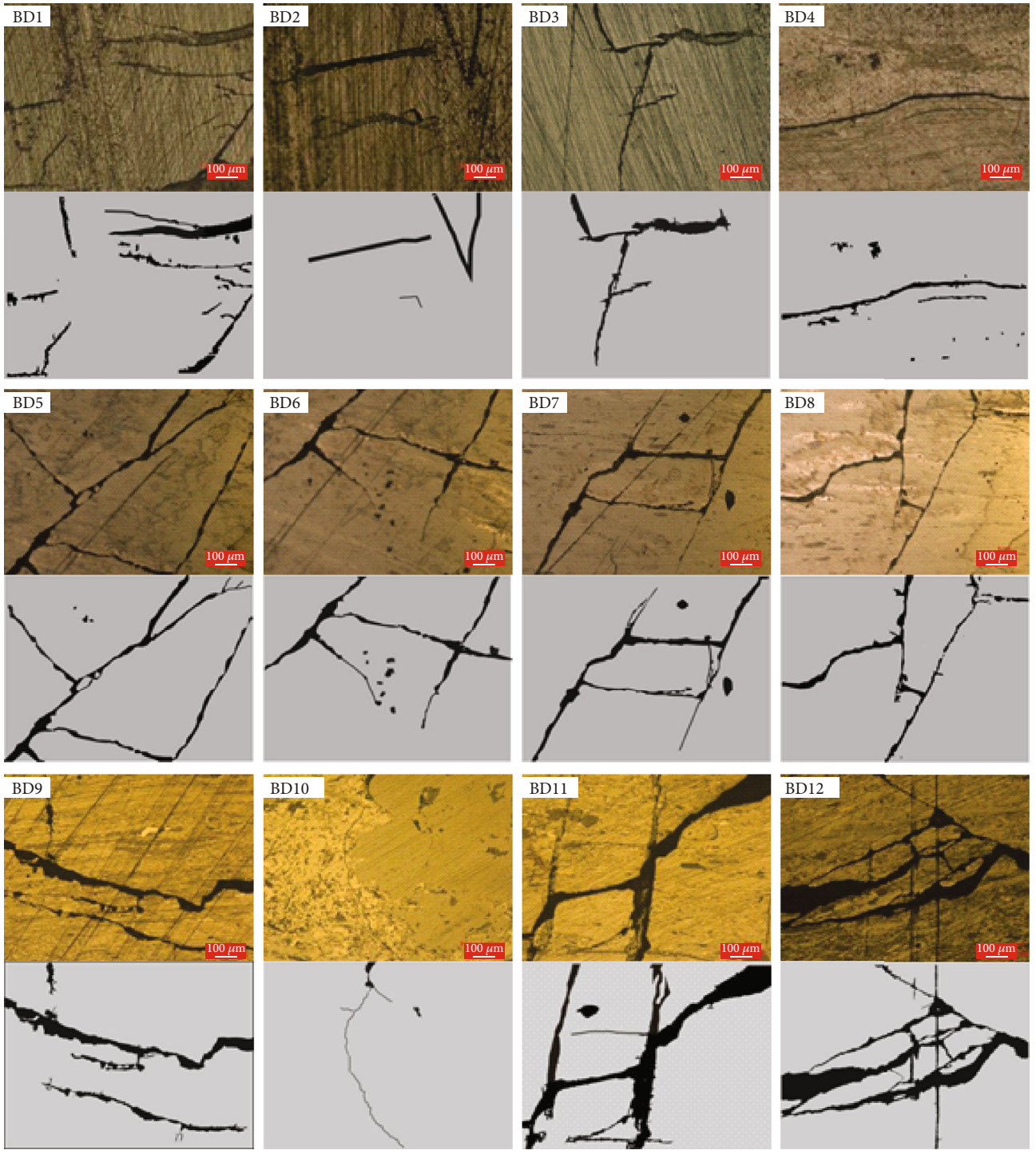

Figure 5: Coal fracture distribution in the samples.

approximately 5 over a length of 7 cm. Some fractures were connected to one another. The fractures intersected the bright coal bands at a high angle. However, these fractures generally cannot penetrate the dull bands.

Microcracks were prominent in the continuous bright coal bands. A few microfractures are present in the discontinuous bright coal strips. Microcracks are developed perpendicular to the layers and are parallel to one another. Yellow-white fillings can be seen in the bright coal strip in the middle. The mineral-filled fissures have a density of 5-7 cm with a spacing of 1.5–11 mm and penetrated the bright coal strip and extended into the dark coal layer. The density of the microcracks that are filled with minerals is 1/cm, and their spacing is between 2 and 5 mm. The dark coal layers have not been penetrated, and there are parallel fractures between the two parallel fractures to connect them.

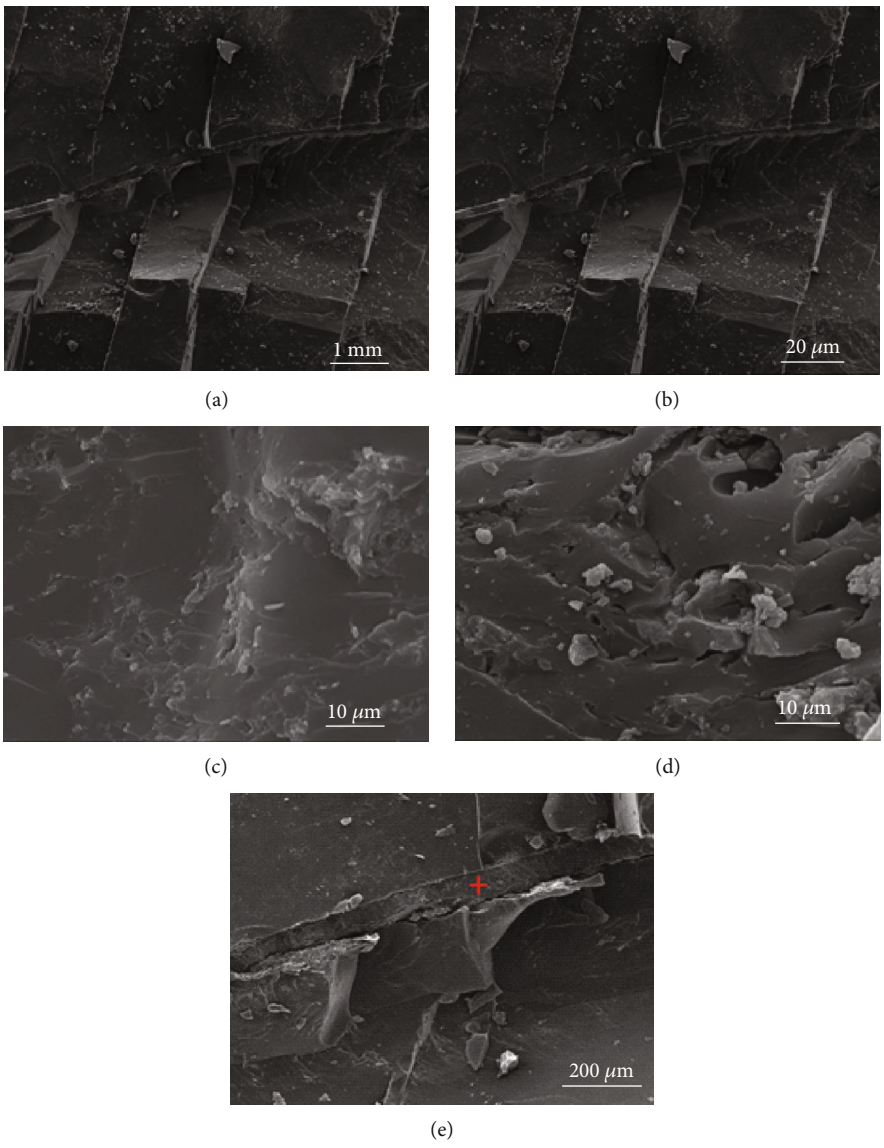

(a) (b) (c) (d) (e)

Figure 6: Continued.

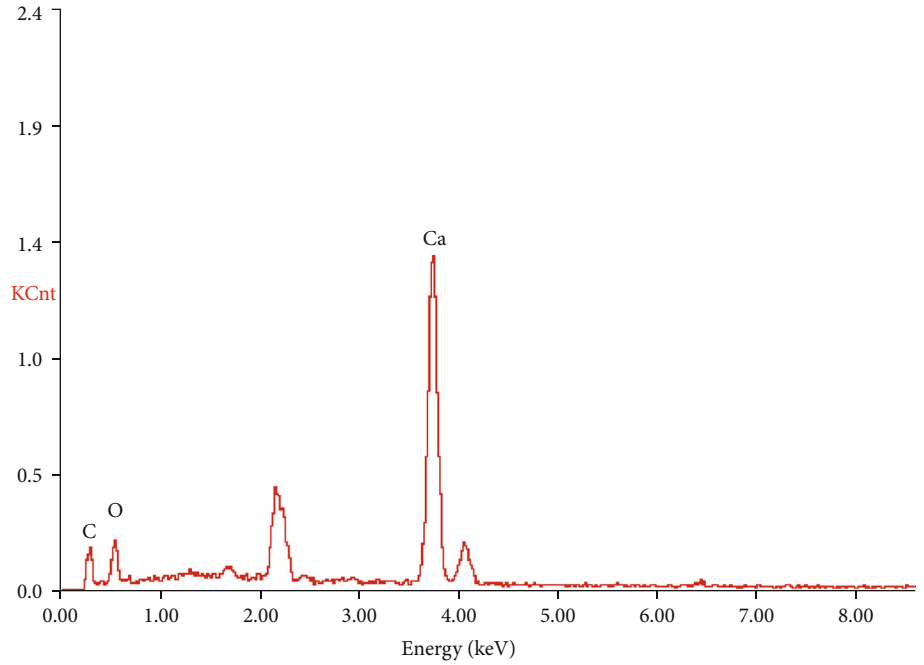

(f)

Figure 6: Fractures and minerals in coal. (a) Endogenous fractures, (b, d) endogenous fissures filled with clay minerals, (c, d) clay minerals, (e) endogenous fractures filled with carbonate minerals, and (f) results of the elemental analysis of the point marked by the red cross in (e).

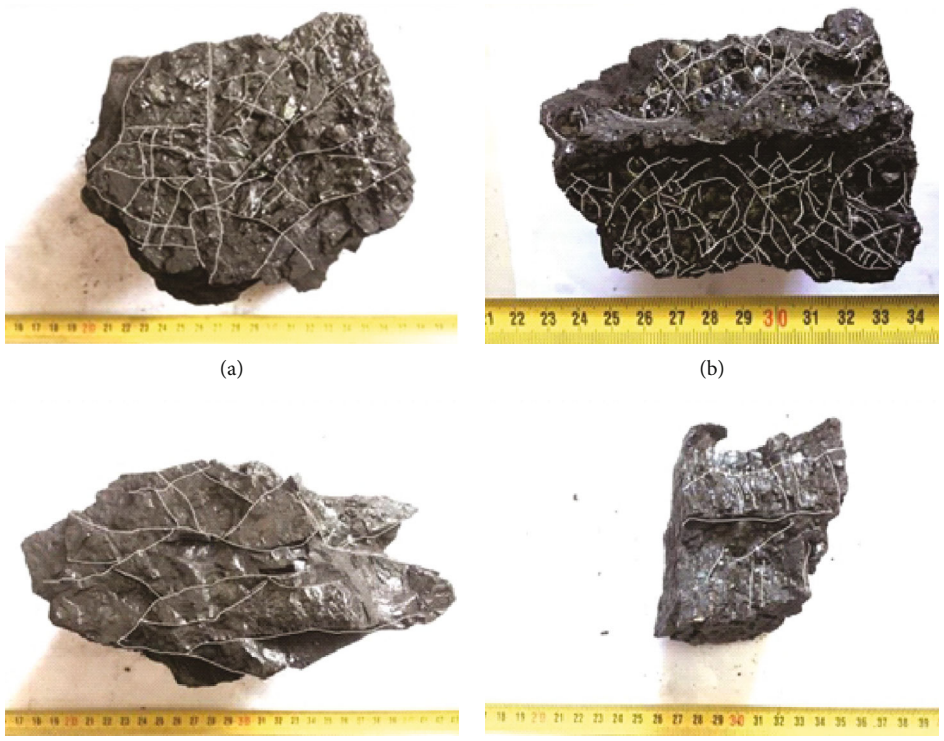

(a) (b)

(c) (d)

Figure 7: Endogenous fractures and their distribution in coal. (a, b) Interconnected endogenous fractures filled with minerals and (c, d) endogenous fractures without mineral fillings.

Mineral-filled fractures are less developed in the rest of the belts, and the fractures not filled with minerals are similarly developed with a density of approximately 1/cm.

4.5. Occurrence of mm-Scale Fractures. In the thin section, microfractures are widely distributed, penetrating bright and dull coal bands. The fractures are generally unstable

Table 3: Mercury porosimetry results of the samples.

Samples	Porosity (%)	Average pore radius (nm)	Mercury saturation (%)	Mercury withdrawal efficiency (%)
BD01	3.82	6.63	37.42	90.12
BD02	6.12	6.73	57	64.58
BD03	5.95	6.53	55.79	71.93
BD08	6.37	9.36	60.22	57.16
BD09	2.8	6.98	34.8	92.15
BD10	4.14	11.18	60.41	71.51

Table 4: Helium permeability test results of the samples.

Samples	Fractures	Confining pressure (MPa)	Inlet pressure (MPa)	Outlet pressure MPa)	Flow rate (cm^3/s)	Permeability (10^{-3} μm^2)
1	Developed	7.0	1.5	1.0	3.58	40.78
		9.0	1.5	1.0	3.17	36.04
		11.0	1.5	1.0	2.92	33.19
		13.0	1.5	1.0	2.58	29.40
		15.0	1.5	1.0	2.42	27.50
		17.0	1.5	1.0	2.08	23.71
2	Developed	7.0	2.0	1.0	6.67	31.61
		9.0	2.0	1.0	5.33	25.29
		11.0	2.0	1.0	5.00	23.71
		13.0	2.0	1.0	4.33	20.55
		15.0	2.0	1.0	3.83	18.18
		17.0	2.0	1.0	3.50	16.60
3	Developed	7.0	1.5	1.0	1.00	8.88
		9.0	1.5	1.0	0.92	8.14
		11.0	1.5	1.0	0.72	6.37
		13.0	1.5	1.0	0.58	5.18
		15.0	1.5	1.0	0.33	2.96
		17.0	1.5	1.0	0.29	2.59
4	Developed	7.0	2.0	1.0	2.25	8.33
		9.0	2.0	1.0	2.12	7.83
		11.0	2.0	1.0	1.92	7.09
		13.0	2.0	1.0	1.45	5.37
		15.0	2.0	1.0	1.17	4.32
		17.0	2.0	1.0	1.08	4.01

and are root-shaped, geese-shaped, cone-shaped, and side column-shaped with coarse fracture surfaces. These fractures are not fully filled, and some of the broken coal matrix particles could be seen. The fractures are connected even though most of the fractures are confined to the bright coal band (Figure 5).

The mm-scale fractures can be divided into three categories. The first type of fractures is perpendicular to the lamina and confined to the bright coal bands. A few have small openings and are filled with minerals. They are not connected to other fractures. The second type of fractures, which are either root-shaped or brush-shaped, is perpendicular to the lamina. They extend into bright and dull coal bands. Most of these fractures have large openings filled with minerals. The minerals and coal components are quite apart from each other, not completely filled. The fractures generated during the geological evolution of coal are connected together, which benefits methane migration and production. The third type of fractures is parallel to the lamina, and they are mainly at the junctions of the bright coal bands and silk charcoal or within silk charcoal itself.

4.6. Occurrence of μm-Scale Fractures. The SEM images indicated that endogenous fractures were widely distributed in the samples tested. Some fractures were parallel to each other, with some being closed while some are open, as shown in Figures 6(a) and 6(b). The fractures indicated that the inner connectivity of the coal in the study area was

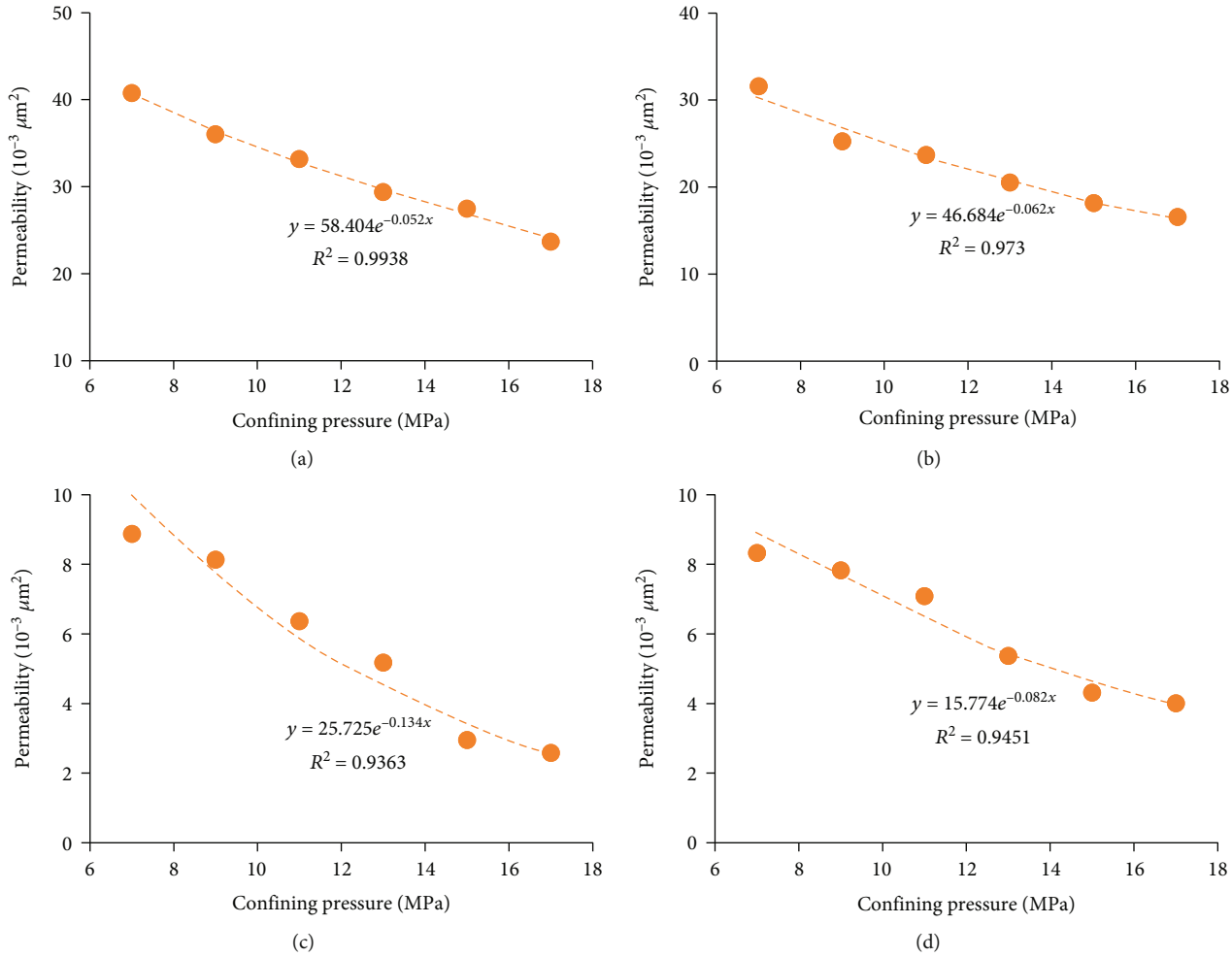

Figure 8: Permeability influenced by the confining pressure.

satisfactory, which is beneficial for methane migration. Similar to the fractures, the pores, namely, gas pores and residual plant tissue pores, were well developed, as shown in Figures 6(c) and 6(d). The coals had been generating methane as indicated by their thermal maturity (Table 2). The coals, however, were in their early coalification stage with residual pores apparent, which is favorable for methane migration and production.

5. Discussion

5.1. Fracture Connectivity and Its Influences. The formation of endogenous fractures in coal depends on the type of coal. Endogenous fractures often develop in bright coal bands (Figure 7). They are irregularly distributed, and the directions of some fractures were visible. One group of fractures was perpendicular to the lamina, whereas the fractures in the other two groups were parallel to the lamina, and some of the fractures in the first group were connected to the fractures in the other group at a certain angle, as shown in Figures 7(a) and 7(c). The fracture surfaces were flat, and some fractures were filled with minerals. The endogenous fissures on the hand specimens formed an irregular network and were filled with minerals. SEM energy spectrum analysis revealed that the endogenous fractures were filled mostly with carbonate minerals, followed by clay minerals (Figure 6(f)). The closure of the fractures can decrease coal permeability, and the existence of closed fractures can be beneficial for methane production. The fractures that are not filled with minerals can get easily extended during hydraulic fracturing. Thus, the development of both forms of fractures is advantageous for CBM production [31].

Mercury porosimetry can indicate the presence of fractures and help determine pore connectivity of coal. Table 3 shows that the mercury intrusion porosity of the sample ranges from 2.8% to 6.37% (average porosity = 4.87%). The pore throat diameter of the coal ranges from 6.53 to 16.18 nm, with an average of 7.9 nm. The approximate average mercury saturation is 50.94%, and the approximate average mercury withdrawal efficiency is 74.58%. The samples exhibit high mercury withdrawal efficiency, implying satisfactory pore and fracture connectivity. The amount of mercury injected gradually increases at first; the mercury injection saturation is within 10%. When the pressure reaches 20–50 MPa, the amount of mercury injected increases rapidly until mercury injection saturation is achieved, indicating that the micropores are rich in the sample. The mercury withdrawal curve is roughly similar to the

mercury injection curve. The high mercury withdrawal efficiency indicates that the pores are mostly open and that they have good connectivity—favorable for CBM production [32, 33].

5.2. Influence of Fractures on Coal Permeability. Two series of coal permeability tests were conducted under different confining stresses to determine the influence of the fractures on the permeability of the coal (Table 4). The original permeabilities of the two series of coals with fractures were 40.78 and 31.61×10^{-3} μm^2 while the permeabilities of the coals that did not have fractures were only 8.88×10^{-3} and 8.33×10^{-3} μm^2. Coal permeability was tested under a confining pressure of 7 MPa and at a coal burial depth of 700–800 m. Coal permeability was influenced by the confining pressure and decreased exponentially as the pressure was increased from 7 to 17 MPa (Figure 8). As the burial depth increased, the fractures started to influence coal permeability. Coals with a high initial permeability can improve the channel flow in the coal mine. The permeabilities of the two coals with fractures were 23.71 and 16.60×10^{-3} μm^2 at 17 MPa while the permeabilities of the two coals without fractures were only 2.59 and 4.01×10^{-3} μm^2 at 17 MPa. Compared with the permeability of the coals at other CBM production blocks, such as the Shizhuang Block, the permeability of the coals in the study area was high, which benefits CBM production [31].

6. Conclusions

Coal macrolithotypes contain mostly semibright, semidull, and dull coals. The main maceral group found in coal is vitrinite (73%–95%). The inertinite content in coal is approximately 26%. Collodetrinite and corpogelinite are the dominant subgroups of vitrinite, whereas semifusinite and inertodetrinite are the dominant subgroups of inertinite. High-volatile bituminous coal has ultralow-ash or low-ash content.

The m-scale fractures in coal seams are mostly in the south-north direction. Some fractures are in the east-west direction. The fractures can penetrate entire coal seams while was blocked the coal gauge. These fractures have been generated during the Yanshanian and Himalayan movements.

The cm-scale fractures are parallel to the lamina and are influenced by the bright and dull coal bands. The mm-scale fractures are of three types. Most of them are endogenous fractures perpendicular to the lamina and are confined to the bright coal bands. The other two types are the fractures perpendicular to the lamina, penetrating the dull coal bands and the fractures parallel to the lamina. The μm-scale fractures are widely distributed and connect coal matrix pores.

Some fractures are filled with carbonate and clay minerals and are arranged as connected networks, which are beneficial for methane production after fracturing. Mercury porosimetry measurements and helium tests show that the coal in the study area has high permeability in the wide range of $10 \times 10^{-3} - 50 \times 10^{-3}$ μm^2. Coal permeability is exponentially related to the confining stress and is influenced by the fracture closure under high confining pressures.

Data Availability

The data has been included in the ms.

Conflicts of Interest

The authors declare that they have no conflicts of interest.

Acknowledgments

This research was funded by the National Major Science and Technology Projects of China (2016ZX05042). We would like to thank Yuan Zhang for helping in data curation and Prof. Shengwei Wang in China University of Geosciences (Wuhan) for conducting the original research.

References

[1] R. M. Flores, *Coal and Coalbed Gas: Fueling the Future*, Elsevier Science Publishing Co Inc, United States, 2014.

[2] Y. Qin, T. A. Moore, J. Shen, Z. Yang, Y. Shen, and G. Wang, "Resources and geology of coalbed methane in China: a review," *International Geology Review*, vol. 60, pp. 1–36, 2017.

[3] Y. Li, J. Yang, Z. Pan, S. Meng, K. Wang, and X. Niu, "Unconventional natural gas accumulations in stacked deposits: a discussion of Upper Paleozoic coal-bearing strata in the east margin of the Ordos Basin, China," *Acta Geologica Sinica-English Edition*, vol. 93, no. 1, pp. 111–129, 2019.

[4] Y. Li, Z. Wang, Z. Pan, X. Niu, Y. Yu, and S. Meng, "Pore structure and its fractal dimensions of transitional shale: a cross-section from east margin of the Ordos Basin, China," *Fuel*, vol. 241, pp. 417–431, 2019.

[5] B. Walter, "Coalbed gas systems, resources, and production and a review of contrasting cases from the San Juan and Powder River basins," *AAPG Bulletin*, vol. 86, no. 11, pp. 1853–1890, 2002.

[6] C. A. Rice, R. M. Flores, G. D. Stricker, and M. S. Ellis, "Chemical and stable isotopic evidence for water/rock interaction and biogenic origin of coalbed methane, Fort Union Formation, Powder River Basin, Wyoming and Montana U.S.A.," *International Geology Review*, vol. 76, no. 1-2, pp. 76–85, 2008.

[7] L. H. Hamilton, J. S. Estrela, and S. D. Golding, "Geological interpretation of gas content trends, Walloon Subgroup, eastern Surat Basin, Queensland, Australia," *International Journal of Coal Geology*, vol. 101, pp. 21–35, 2012.

[8] T. A. Moore, "Coalbed methane: a review," *International Journal of Coal Geology*, vol. 101, pp. 36–81, 2012.

[9] Y. Li, J. Yang, Z. Pan, and W. Tong, "Nanoscale pore structure and mechanical property analysis of coal: an insight combining AFM and SEM images," *Fuel*, vol. 260, p. 116352, 2020.

[10] S. Karimpouli, P. Tahmesbi, and H. L. Ramandi, "A review of experimental and numerical modeling of digital coalbed methane: imaging, segmentation, fracture modeling and permeability prediction," *International Journal of Coal Geology*, vol. 228, article 103552, 2020.

[11] C. Clarkson, N. Solano, R. Bustin et al., "Pore structure characterization of north American shale gas reservoirs using

USANS/SANS, gas adsorption, and mercury intrusion," *Fuel*, vol. 103, pp. 606–616, 2013.

[12] Y. Li, C. Zhang, D. Tang, Q. Gan, X. Niu, and R. Shen, "Coal pore size distributions controlled by the coalification process: an experimental study of coals from the Junggar, Ordos and Qinshui basins in China," *Fuel*, vol. 206, pp. 352–363, 2017.

[13] W. Xu, J. Li, X. Wu, D. Liu, and Z. Wang, "Desorption hysteresis of coalbed methane and its controlling factors: a brief review," *Front Earth Sci-Prc.*, vol. 15, no. 2, pp. 224–236, 2021.

[14] H. Hou, G. Liang, L. Shao, Y. Tang, and G. Mu, "Coalbed methane enrichment model of low-rank coals in multi-coals superimposed regions: a case study in the middle section of southern Junggar Basin," *Front Earth Sci-Prc.*, vol. 15, no. 2, pp. 256–271, 2021.

[15] Y. Ma, M. Wang, R. Ma, and J. Li, "Micropore characteristics and gas-bearing characteristics of marine- continental transitional shale reservoirs in the east margin of Ordos Basin," *Adsorption Science and Technology*, vol. 8, pp. 1–15, 2021.

[16] C. Chen, D. Hu, D. Westacott, and D. Loveless, "Nanometer-scale characterization of microscopic pores in shale kerogen by image analysis and pore-scale modeling," *Geochemistry, Geophysics, Geosystems*, vol. 14, no. 10, pp. 4066–4075, 2013.

[17] M. Blunt, B. Bijeljic, H. Dong et al., "Pore-scale imaging and modelling," *Advances in Water Resources*, vol. 51, pp. 197–216, 2013.

[18] S. Kelly, H. El-Sobky, C. Torres-Verdín, and M. Balhoff, "Assessing the utility of FIB-SEM images for shale digital rock physics," *Advances in Water Resources*, vol. 95, pp. 302–316, 2016.

[19] T. Wu, X. Li, J. Zhao, and D. Zhang, "Multiscale pore structure and its effect on gas transport in organic-rich shale," *Water Resources*, vol. 53, no. 7, pp. 5438–5450, 2017.

[20] S. Zhao, Y. Li, Y. Wang, Z. Ma, and X. Huang, "Quantitative study on coal and shale pore structure and surface roughness based on atomic force microscopy and image processing," *Fuel*, vol. 244, pp. 78–90, 2019.

[21] K. Jiao, S. Yao, W. Hu, and K. Zhang, "The evolution of nanopores and surface roughness in naturally matured coals in South China: an atomic force microscopy and image processing study," *Fuel*, vol. 234, pp. 1123–1131, 2018.

[22] Y. Wang, D. Liu, Y. Cai, Y. Yao, and Z. Pan, "Constraining coalbed methane reservoir petrophysical and mechanical properties through a new coal structure index in the southern Qinshui Basin, northern China: implications for hydraulic fracturing," *AAPG*, vol. 2020, p. 104, 2020.

[23] Y. Cai, D. Liu, J. P. Mathews et al., "Permeability evolution in fractured coal – combining triaxial confinement with X-ray computed tomography, acoustic emission and ultrasonic techniques," *International Journal of Coal Geology*, vol. 122, pp. 91–104, 2014.

[24] S. E. Laubach, R. A. Marrett, J. E. Olson, and A. R. Scott, "Characteristics and origins of coal cleat: a review," *International Journal of Coal Geology*, vol. 35, no. 1-4, pp. 175–207, 1998.

[25] Y. Li, D. Tang, D. Elsworth, and H. Xu, "Characterization of coalbed methane reservoirs at multiple length scales: a cross-section from southeastern Ordos Basin, China," *Energy Fuel.*, vol. 28, no. 9, pp. 5587–5595, 2014.

[26] C. Guo, Y. Xia, D. Ma et al., "Geological conditions of coalbed methane accumulation in the Hancheng area, southeastern Ordos Basin, China: implications for coalbed methane high-yield potential," *Energy Exploration & Exploitation*, vol. 37, no. 3, article 014459871983811, pp. 922–944, 2019.

[27] G. H. Taylor, M. Teichmuller, A. Davis, C. F. K. Diessel, R. Littke, and P. Robert, *Organic Petrology*, Gebruder Borntraeger, Berlin, Germany, 1998.

[28] International Committee for Coal and Organic Petrology (ICCP), "The new vitrinite classification (ICCP System 1994)," *Fuel*, vol. 77, pp. 349–358, 1998.

[29] W. Zhao, X. Li, T. Wang, and X. Fu, "Pore size distribution of high volatile bituminous coal of the southern Junggar Basin: a full-scale characterization applying multiple methods," *Frontiers in Earth Science*, vol. 15, no. 2, pp. 237–255, 2021.

[30] M. Zou, C. Wei, M. Zhang, J. Shen, Y. Chen, and Y. Qi, "Classifying coal pores and estimating reservoir parameters by nuclear magnetic resonance and mercury intrusion porosimetry," *Energy & Fuels*, vol. 27, no. 7, pp. 3699–3708, 2013.

[31] W. Han, Y. Wang, and Y. Li, "Recognizing fracture distribution within the coalbed methane reservoir and its implication for hydraulic fracturing: a method combining field observation, well logging, and micro-seismic detection," *Journal of Natural Gas Science and Engineering*, vol. 92, article 103986, 2021.

[32] Y. Yao and D. Liu, "Comparison of low-field NMR and mercury intrusion porosimetry in characterizing pore size distributions of coals," *Fuel*, vol. 95, pp. 152–158, 2012.

[33] C. R. Clarkson, M. Freeman, L. He et al., "Characterization of tight gas reservoir pore structure using USANS/SANS and gas adsorption analysis," *Fuel*, vol. 95, no. 1, pp. 371–385, 2012.